



저작자표시-비영리-변경금지 2.0 대한민국

이용자는 아래의 조건을 따르는 경우에 한하여 자유롭게

- 이 저작물을 복제, 배포, 전송, 전시, 공연 및 방송할 수 있습니다.

다음과 같은 조건을 따라야 합니다:



저작자표시. 귀하는 원저작자를 표시하여야 합니다.



비영리. 귀하는 이 저작물을 영리 목적으로 이용할 수 없습니다.



변경금지. 귀하는 이 저작물을 개작, 변형 또는 가공할 수 없습니다.

- 귀하는, 이 저작물의 재이용이나 배포의 경우, 이 저작물에 적용된 이용허락조건을 명확하게 나타내어야 합니다.
- 저작권자로부터 별도의 허가를 받으면 이러한 조건들은 적용되지 않습니다.

저작권법에 따른 이용자의 권리는 위의 내용에 의하여 영향을 받지 않습니다.

이것은 [이용허락규약\(Legal Code\)](#)을 이해하기 쉽게 요약한 것입니다.

[Disclaimer](#)

공학박사학위논문

가솔린 엔진에서 실린더 벽면 온도가  
노킹 현상에 미치는 영향에 관한 연구

**Study on the Effect of Cylinder Wall Temperatures  
on Knock Characteristics in Spark-Ignited Engine**

2018 년 8 월

서울대학교 대학원

기계항공공학부

조 석 원

**Study on the Effect of Cylinder Wall Temperatures  
on Knock Characteristics in Spark-Ignited Engine**

지도교수 민 경 덕

이 논문을 공학박사 학위논문으로 제출함

2018 년 4 월

서울대학교 대학원

기계항공공학부

조 석 원

조석원의 공학박사 학위논문을 인준함

2018 년 6 월

위원장	고 상 근	
부위원장	민 경 덕	
위원	송 한 호	
위원	도 형 립	
위원	최 회 명	

知之为知之，不知为不知，是知也。

- 孔子

*True knowledge exists in knowing you know nothing.*

- Socrates

## Acknowledgement

Above all things, I would like to express my deepest thanks to Professor Kyoungdoug Min for his guidance, knowledge and patience. Without doubt, I am benefited from his insight and wisdom for not only in my research are but also non-academic area of life. Also sincere appreciation goes to Professor Han Ho Song and Professor Hoimyoung Choi who gave me precious advices.

I sincerely appreciate to research fellow Dr. Kyoung-pyo Ha, senior research engineers Backsik Kim and Ingee Suh of Hyundai for their unconditional support. Without them, this study could not be established. I'm also thankful to senior research engineers Byeongseok Lee and Jinwook Son for engine setup of research project. I'm also indebted to their immediate responses of Mr. ByungGi Kim of Han-il precision and Mr. Seokju Lee of Samsung high-pressure tech.

I appreciate all of the laboratory people, especially, endlessly thank to Chiheon Song and Sechul Oh who showed enormous passions to this research and shared me a lot of discussions. I'm very thankful to Professor Minjae Kim for optimization and Professor Sangyeol Lee for deep learning. I'm also appreciate to ByungGun Song who was my writing mate for dissertation.

And I'm grateful to my friends: Changbum Choi, Hoseok Jeong, Young-oh Jang and Gilyeon Jeon for our invaluable friendship, and either 'Budwoo(友)' members: Gwanghwan Kim, Seungheon Jeon, Sunghee Jung, Junmin Lee and Yongseok Lee as they cheered me up a lot during my PhD period.

My parents Keejong Cho and Jeewon Kim and my sister Ahyung Cho, I am undoubtedly indebted to their support and help. Last but not least, my thanks go to my dearest, Luna, who gave me an extraordinary comfort.



## **Abstract**

# **Study on the Effect of Cylinder Wall Temperatures on Knock Characteristics in Spark-Ignited Engine**

**Seokwon Cho**

Department of Mechanical and Aerospace Engineering  
The Graduate School  
Seoul National University

To cope with stringent regulations of fuel economy and emission, development of high efficiency gasoline engine is getting urgent than ever before. Due to its intrinsic characteristics, the increment of compression ratio has a direct relationship to efficiency enhancement. However, increasing compression ratio provokes knock-prone in-cylinder condition. The temperature and pressure of the end gas area increase during the combustion period, and this may cause spontaneous ignition of air-fuel mixture which is known as knocking phenomena.

Knock phenomena has to be avoided because of the engine failure and its unfavorable noise during engine operation. Numbers of attempts have been made to reduce the temperature of end-gas to mitigate knock. Exhaust gas recirculation and water injection studies are now actively being introduced, and there have been experimental suggestions on cooling optimization, dual-loop cooling and introduction of insulated intake port. It has been shown by a simulation study that the intake port has a great effect on gas temperature reduction, however, quantification and in-depth study of effects of other wall components has not been

investigated. Furthermore, reflection of temperature variation on control is needed for future utilization of knock or auto-ignition for higher efficiency.

In this study, a systematic investigation was conducted to observe how wall temperatures affect the overall knock behavior. Therefore, study for experimental methodology of knocking combustion was conducted according to the necessity of exquisite test and analysis. It was found that decreasing coolant temperature shows a significant effect on knock mitigation.

With the segregation of the head and liner coolants and the introduction of the piston oil cooling gallery, the wall temperature of each component was controlled. Temperature measurement including piston surface facilitated by designing an optimized linkage system, showed that independent temperature control was achieved. Individual impact of each wall component on knocking behavior was assessed using refined experimental techniques. As a result, the effect of head temperature reduction was found to be greater than that of the liner temperature reduction under various conditions such as different engine geometry. Also piston cooling showed a remarkable effect by reducing its surface temperature.

In addition, 3D simulation analysis was conducted for deeper understanding. As a result, it was confirmed that the effect of temperature decrease on heat transfer from the combustion gas to the wall was restrictive due to originally large temperature difference. Reducing wall temperature showed a large knock mitigation effect due to reduction the gas temperature during the intake and compression process. The intake port has the greatest effect during the intake process, and after insulation of intake port, temperature reduction by the liner wall was found to be more effective in reducing temperature than that of head wall. The liner cooling effect was higher in long-stroke engine, and intensified tumble

flow showed a potential of gas temperature decrease by increasing the heat transfer from gas to wall during compression stroke.

To establish a cooling strategy of liner wall cooling depending on knock position, knock localization was demonstrated by PCB ion-probe gasket. No significant change in knock location was observed while chilling the liner wall. Knock was mainly occurred in intake and exhaust side under weak knock condition and occurred simultaneously around the cylinder bore with multiple spots regardless of wall temperature variation. This confirms that the knock location was not heavily affected by wall temperature, but rather critically affected by flame propagation.

Lastly, for a future control of auto-ignition and knock phenomena under transient engine operation, a fast 0D knock prediction model was established based on ignition delay correlation and individual cycle analysis including improved knock onset determination. The validity under variation of coolant temperature was identified, and the robustness was thoroughly secured.

**Keywords: Spark-Ignited Engine, Knock, Auto-ignition, 0D (zero-dimensional), Cycle Analysis, Coolant Temperature, Wall Temperature, Knock Prediction Model**

**Student Number: 2012-20703**

# Contents

<b>Abstract .....</b>	<b>i</b>
<b>Contents .....</b>	<b>iv</b>
<b>List of Tables .....</b>	<b>vii</b>
<b>List of Figures .....</b>	<b>viii</b>
<b>Nomenclature .....</b>	<b>xvii</b>
<b>Chapter 1. Introduction .....</b>	<b>1</b>
<b>1.1 Backgrounds and Motivations .....</b>	<b>1</b>
1.1.1 Major issues in internal combustion engine .....	1
1.1.2 Knock and efficiency .....	4
<b>1.2 Literature Review .....</b>	<b>10</b>
1.2.1 Auto-ignition fundamentals .....	10
1.2.2 Knock measurement and analysis .....	15
1.2.3 Knock mitigation methods .....	28
<b>1.3 Research Objectives.....</b>	<b>34</b>
<b>Chapter 2. Analysis and Modeling of Knock .....</b>	<b>35</b>
<b>2.1 Knock Metric.....</b>	<b>35</b>
2.1.1 Detection of knock occurrence.....	35

2.1.2 Knock incidence.....	41
2.1.3 Knock onset determination.....	44
<b>2.2 Individual Cycle Analysis .....</b>	<b>53</b>
2.2.1 Heat release calculation.....	53
2.2.2 Estimation of unburned gas temperature .....	62
2.2.3 0D Ignition delay model for fast prediction .....	67
<b>Chapter 3. Configuration for Test and Simulation .....</b>	<b>68</b>
<b>3.1 Experimental configuration .....</b>	<b>68</b>
3.1.1 Single cylinder gasoline engines .....	68
3.1.2 Test facility and equipment .....	69
3.1.3 Experimental conditions.....	78
<b>3.2 Detection of Knock Location.....</b>	<b>82</b>
3.2.1 Visio-Knock system .....	82
3.2.2 PCB Ion-probe head gasket.....	83
<b>3.3 Wall Temperature Measurement .....</b>	<b>93</b>
3.3.1 Linkage system for piston measurement .....	93
3.3.2 Method for thermocouple installation .....	107
<b>3.4 3D CFD simulation .....</b>	<b>112</b>
<b>Chapter 4. Results and Discussion .....</b>	<b>116</b>
<b>4.1 Wall Temperature Effect on Knock Mitigation .....</b>	<b>116</b>
4.1.1 Feasibility of thermal boundary temperature reduction .....	116
4.1.2 Independent temperature control by segregated cooling .....	119
4.1.3 Thermal effect of oil-cooling gallery .....	123

4.1.4 Load limit expansion.....	126
4.1.5 Efficiency increase by ignition advance.....	134
4.1.6 Effect under different conditions.....	150
<b>4.2 Knock Mitigation Effect of Independent Cooling .....</b>	<b>159</b>
4.2.1 Comparison of coolant temperature effects.....	159
4.2.2 Effect in different engine type.....	167
<b>4.3 Heat Transfer between Gas Mixture and Wall .....</b>	<b>170</b>
4.3.1 Heat transfer during combustion.....	171
4.3.2 Heat transfer until ignition timing.....	175
<b>4.4 Strategic Knock Suppression .....</b>	<b>180</b>
4.4.1 Intake port insulation.....	180
4.4.2 Effect of intensified intake flow.....	183
4.4.3 Knock suppression effect using liner cooling.....	188
4.4.4 Knock position under liner cooling.....	192
<b>4.5 Evaluation of Knock Prediction Model.....</b>	<b>199</b>
 <b>Chapter 5. Conclusions .....</b>	 <b>207</b>
 <b>Bibliography.....</b>	 <b>211</b>
 <b>국 문 초 록.....</b>	 <b>230</b>

## List of Tables

Table 1.1 Common knock intensity metrics using in-cylinder pressure.....	23
Table 2.1 Oscillation frequencies of pressure wave .....	39
Table 3.1 Engine specifications.....	77
Table 3.2 Fuel specifications .....	80
Table 3.3 Experimental conditions for cylinder wall temperature effect .....	80
Table 3.4 Test conditions for knock prediction modeling .....	81
Table 3.5 Result linkage system optimization.....	103
Table 3.6 Configuration of CFD simulation.....	113
Table 3.7 Boundary conditions for CFD simulation (combustion) .....	114
Table 3.8 Boundary conditions for simulation (motoring) .....	115

## List of Figures

Figure 1.1 CO <sub>2</sub> regulations in global markets.....	6
Figure 1.2 Fuel economy test modes: NEDC, FTP-75 and WLTC .....	7
Figure 1.3 Outlook of future market share of vehicles [9] .....	8
Figure 1.4 In-cylinder pressure of knocking cycle.....	9
Figure 1.5 Determination of knock onset by Kim's TVE method, from [32]. ...	27
Figure 1.6 Determination of knock onset by Shahlari's method, from [19].....	27
Figure 2.1 Oscillation modes of pressure wave (3D images from [100]) .....	39
Figure 2.2 FFT and PSD analysis of knocking combustion .....	40
Figure 2.3 Phase shifting in low-pass filtered signal.....	40
Figure 2.4 Comparison of MAPO knock incidence and ISPO knock intensity .	43
Figure 2.5 An example of incorrect knock onset determination.....	48
Figure 2.6 Improved knock onset determination at 1500 rpm, WOT, ign=2.5 CA bTDC, $\lambda=1$ , cycle number 865, 1329.....	49
Figure 2.7 Improved knock onset determination at 1500 rpm, WOT, ign=2.5 CA bTDC, $\lambda=1$ , cycle number 2486, 4467.....	50
Figure 2.8 Improved knock onset determination at 1750 rpm, IMEP 7.69 bar, ign=12.5 CA bTDC, $\lambda=1.1$ , cycle number 203, 1807.....	51

Figure 2.9 Improved knock onset determination at 1750 rpm, IMEP 7.69 bar, ign=12.5 CA bTDC, $\lambda=1.1$ , cycle number 2775, 4830.....	52
Figure 2.10 Mass fraction burned of individual knocking cycle.....	60
Figure 2.11 EOC determination methods.....	60
Figure 2.12 Filtering in-cylinder pressure signal in low pressure region.....	61
Figure 2.13 Mass fraction burned with Wiebe-fitting method in knocking cycle .....	61
Figure 2.14 Single-zone based in-cylinder temperature.....	66
Figure 2.15 Two-zone based unburned gas temperature .....	66
Figure 3.1 Valve profiles at standard valve timing: PFI and GDI.....	72
Figure 3.2 Engine test facility .....	73
Figure 3.3 Schematic diagram of experimental system.....	74
Figure 3.4 Design of segregated cooling passages.....	75
Figure 3.5 Oil-cooling gallery piston .....	76
Figure 3.6 Schematic of AVL Visio-Knock system, from [60, 64].....	87
Figure 3.7 Visio-Knock test result under liner cooling condition .....	88
Figure 3.8 Light intensity of eight optical probes in Visio-Knock.....	88
Figure 3.9 PCB ion-probe head gasket installation .....	89

Figure 3.10 Motoring pressures with normal gasket and PCB ion-probe gasket at 2000 rpm .....	90
Figure 3.11 Engine setup of PCB ion-probe head gasket.....	91
Figure 3.12 Flame arrival and knock onset using PCB ion-probe gasket .....	92
Figure 3.13 Speed and acceleration of piston at 6000 rpm. ....	101
Figure 3.14 Schematic diagram of the linkage system.....	102
Figure 3.15 Method for thermocouple wiring on the linkage.....	102
Figure 3.16 3D stress analysis of original linkage design at 2000 rpm.....	104
Figure 3.17 3D stress analysis of piston at 2000 rpm.....	104
Figure 3.18 Stress on link 2 of original design at 2000 rpm .....	105
Figure 3.19 Maximum stress of improved linkage design at 2000 rpm.....	105
Figure 3.20 Stress analysis of improved linkage design at 6000 rpm .....	106
Figure 3.21 Original concept design and improved design of linkage system.	106
Figure 3.22 Temperature measurement points on the combustion wall .....	109
Figure 3.23 Temperature measurement points of cylinder head and piston .....	109
Figure 3.24 Thermocouple installation on piston.....	110
Figure 3.25 Special thermocouple wires for moving linkage system (left: Alumel, right: Chromel).....	110

Figure 3.26 Positions of thermocouple installation on liner wall.....	111
Figure 3.27 PFI Engine mesh generated at BDC .....	113
Figure 4.1 Effect of intake temperature and coolant temperature .....	118
Figure 4.2 Wall temperature variation of head and liner at head cooling.....	121
Figure 4.3 Wall temperature variation of head and liner at liner cooling.....	121
Figure 4.4 Wall temperature variation at simultaneous cooling of head and liner .....	122
Figure 4.5 Piston surface temperature variation at each cooling condition.....	122
Figure 4.6 Piston temperature distribution during the oil jet injection at 1500 rpm, 7.2 bar, knock incidence: 10%.....	125
Figure 4.7 In-cylinder pressure during oil-jet injection at 1500 rpm, 7.2 bar, knock incidence: 10% .....	125
Figure 4.8 Load limit under coolant temperature decrease at 1500 and 2000 rpm .....	130
Figure 4.9 In-cylinder pressure of load limit increase at 2000 rpm .....	130
Figure 4.10 Load limit expansion under different knock incidence.....	131
Figure 4.11 Head and piston surface temperature distribution, left: 80°C Tcoolant w/o oil-jet injection right: 40°C Tcoolant w/ oil-jet injection .....	132
Figure 4.12 Effect of oil-jet injection in load expansion at 1500 rpm.....	133

Figure 4.13 Effect of oil-jet injection in load expansion at 2000 rpm.....	133
Figure 4.14 In-cylinder pressure at 1500 rpm under cooling .....	138
Figure 4.15 Intake pressure at 1500 rpm under cooling.....	138
Figure 4.16 Load increase at 1500 rpm under cooling.....	139
Figure 4.17 Efficiency increase at 1500 rpm under cooling.....	139
Figure 4.18 Combustion efficiency at 1500 rpm under cooling.....	140
Figure 4.19 NO <sub>x</sub> and THC emission at 1500 rpm under cooling.....	140
Figure 4.20 P-V diagram at 1500 rpm under cooling.....	141
Figure 4.21 Percent fuel heating values at 1500 rpm under cooling .....	142
Figure 4.22 Comparison of in-cylinder temperature under cooling .....	142
Figure 4.23 KLSA and efficiency increase at 1500 rpm, 6.9 bar under cooling .....	146
Figure 4.24 KLSA and efficiency increase at 2000 rpm, 7.3 bar under cooling .....	146
Figure 4.25 NO <sub>x</sub> and THC emissions at 1500 rpm, 6.9 bar under cooling .....	147
Figure 4.26 NO <sub>x</sub> and THC emissions at 2000 rpm, 7.2 bar under cooling .....	147
Figure 4.27 Exhaust temperature variation at 1500 and 2000 rpm under cooling .....	148
Figure 4.28 Effect of oil-jet injection to piston at 1500 rpm.....	149

Figure 4.29 Effect of oil-jet injection to piston at 2000 rpm.....	149
Figure 4.30 Load limit of PFI/GDI engines at 1500 and 2000 rpm .....	152
Figure 4.31 Load increase in GDI engine at 1500 rpm under cooling .....	153
Figure 4.32 Efficiency increase in GDI engine at 1500 rpm under cooling.....	153
Figure 4.33 Engine designs for three bore-to-stroke ratio: B/S = 1.0, 0.84 and 0.68 .....	156
Figure 4.34 Load limit expansion at 1500 rpm, different B/S ratio under cooling .....	157
Figure 4.35 Load limit expansion at 2000 rpm, different B/S ratio under cooling .....	157
Figure 4.36 Burn duration of different B/S ratio at 1500 rpm.....	158
Figure 4.37 Burn duration of different B/S ratio at 2000 rpm.....	158
Figure 4.38 IVC temperature at different coolant temperature .....	164
Figure 4.39 Load limit expansion at 1500 rpm under independent cooling.....	165
Figure 4.40 Load limit expansion at 2000 rpm under independent cooling.....	165
Figure 4.41 KLSA under the same load condition at 1500 rpm.....	166
Figure 4.42 KLSA under the same load condition at 2000 rpm.....	166
Figure 4.43 Load limit expansion at 1500 rpm (GDI) under independent cooling .....	169

Figure 4.44 Load limit expansion at 2000 rpm (GDI) under independent cooling .....	169
Figure 4.45 Decrease of heat transfer during combustion, case 1-5.....	174
Figure 4.46 Unburned gas temperature at 20 CA aTDC: case 1 (w/o cooling) and case 5 (w/cooling) .....	174
Figure 4.47 Total heat transfer from walls at 1500 rpm (case 6).....	178
Figure 4.48 Total heat transfer from walls at 2000 rpm (case 7).....	178
Figure 4.49 Total heat transfer from gas to wall at 1500 rpm (case 6).....	179
Figure 4.50 Total heat transfer from gas to wall at 2000 rpm (case 7).....	179
Figure 4.51 Heat transfer during gas induction phase with heat-insulated intake port at 1500 rpm, WOT (case 6, 8-10) .....	182
Figure 4.52 Heat transfer during gas induction phase with heat-insulated intake port at 2000 rpm, WOT (case 7, 11-13).....	182
Figure 4.53 Design modification of intake port for intensified tumble flow....	185
Figure 4.54 Turbulent intensity of base and intensified intake ports at 1500 rpm, WOT (case 6 and case 14).....	185
Figure 4.55 Total heat transfer from walls w/intensified port at 1500 rpm, WOT (case 14) .....	186
Figure 4.56 Total heat transfer from walls w/intensified port at 2000 rpm, WOT (case 15) .....	186

Figure 4.57 Total heat transfer from gas to wall w/ intensified port at 1500 rpm, WOT (case 14) .....	187
Figure 4.58 Total heat transfer from gas to wall w/ intensified port at 2000 rpm, WOT (case 15) .....	187
Figure 4.59 Improvement on knock resistance by liner cooling in different B/S ratio.....	190
Figure 4.60 Efficiency increase rate in different B/S ratio under liner cooling	191
Figure 4.61 Knock locations in weak knock condition (20%)  at Tcoolant (liner) = 80°C, 1500 rpm, 6.2 bar, ign = 21 CA bTDC.....	194
Figure 4.62 Effect of squish to air motion during compression (w/ combustion) at 1500 rpm, 6 bar, ign = 21 CA bTDC .....	195
Figure 4.63 Knock locations in weak knock condition (20%) at Tcoolant (liner) = 40°C, 1500 rpm, 6.5 bar, ign = 21 CA bTDC .....	196
Figure 4.64 Knock locations in heavy knock condition (60%) at Tcoolant (liner) = 80°C, 1500 rpm, 6.3 bar, ign = 23 CA bTDC .....	197
Figure 4.65 Knock locations in heavy knock condition (60%) at Tcoolant (liner) = 40°C, 1500 rpm, 6.6 bar, ign = 23 CA bTDC .....	198
Figure 4.66 Knock prediction model (Chen).....	204
Figure 4.67 Knock prediction model (Douaud-Eyzat) .....	204
Figure 4.68 Knock prediction model validation under various conditions: Engine speed, load, air-fuel ratio and coolant temperature .....	205

Figure 4.69 Knock prediction model with adiabatic unburned temperature .... 206

Figure 4.70 Validation of knock prediction model at different coolant temperature  
..... 206

## Nomenclature

A	area [m <sup>2</sup> ]
$h_w$	convective heat transfer coefficient [W m <sup>-2</sup> K <sup>-1</sup> ]
k	polytropic coefficient
m	mass [kg]
n	mole number [-]
N	number [-]
P	Pressure [bar]
Q	heat [J]
$Q_{LHV}$	low heating value [J kg <sup>-1</sup> ]
R	ideal gas constant [J mol <sup>-1</sup> K <sup>-1</sup> ]
$r_c$	Compression ratio [-]
$R_s$	specific ideal gas constant [J kg <sup>-1</sup> K <sup>-1</sup> ]
$S_p$	piston speed [m s <sup>-1</sup> ]
t	time [s]
T	Temperature [K]
V	volume [m <sup>3</sup> ]
$x$	mass fraction burned [-]

## Greek Letters

$\eta$	efficiency [-]
$\gamma$	specific heat ratio [-]
$\rho$	gas density [kg m <sup>-3</sup> ]
$\tau$	ignition delay time [ms]
$\lambda$	Lambda [-]

## Subscripts/Superscripts

a	air
b	burned zone
c	combustion
f	fuel
filt	filtered
ht	heat transfer
ign	ignition
in	intake
m	motoring
max	maximum
n	net
p	piston
r	residual
sat	saturation
u	unburned
w	Woschni

## Acronyms

0D	zero-dimensional
1D	one-dimensional
3D	three-dimensional
aBDC	after bottom dead center
AEPO	average energy of pressure oscillation
AHHR	accumulated heat release rate
ASTM	American Society for Testing and Materials
aTDC	after top dead center
AWG	American wire gauge
bBDC	before bottom dead center

BDC	bottom dead center
BDC	bottom dead center
B/S	bore-to-stroke ratio
bTDC	before top dead center
CA	crank angle
CA10	crank angle at mass fraction burned 10%
CA50	crank angle at mass fraction burned 50%
CA90	crank angle at mass fraction burned 90%
CAI	controlled auto-ignition
CARB	Californian Air Resources Board
CFD	computational fluid dynamics
CO	carbon dioxide
CVVT	continuous variable valve timing
DISI	direct injection spark ignition
DKI	dimensionless knock indicator
DOHC	double over-head cam
ECU	engine control unit
EGR	exhaust gas recirculation
EOC	end of combustion
EU	European Union
EV	electric vehicle
EVC	exhaust valve closing
EVO	exhaust valve opening
FFT	fast Fourier transform
FID	flame ionization detection
GDI	gasoline direct injection
HCCI	homogeneous charge compression ignition
HEV	hybrid electric vehicle
HPF	high-pass filter

ICE	internal combustion engine
IMEP	indicated mean effective pressure
IMPO	integral of modulus of pressure oscillation
ISPO	integral of signal pressure oscillation
IVC	intake valve closing
KI	knock intensity
KLSA	knock limit spark advance
LHV	low heating value
LIVC	late intake valve closing
LKI	logarithmic knock intensity
LLNL	Lawrence Livermore National Laboratory
MAPO	maximum amplitude of pressure oscillation
MBT	maximum brake torque
MFB50	mass fraction burned 50%
MON	motor octane number
NEDC	new European driving cycle
NMOG	non-methane organic gas
NO <sub>x</sub>	nitrogen oxide
NVH	noise, vibration and harshness
OI	octane index
ON	octane number
PCB	printed circuit board
PDF	power density function
PEMS	portable emissions measurement system
PFI	port fuel injection
PHEV	plug-in hybrid electric vehicle
PMEP	pumping mean effective pressure
PN	particulate number
PPR	pressure rise rate

PRF	primary reference fuel
PSD	power spectral density
RDE	real driving emission
RHS	right hand side
RMSE	root mean square error
RON	research octane number
rpm	revolution per minute
SD	standard deviation
SEPO	signal energy of pressure oscillation
SER	signal energy ratio
SOC	start of combustion
TDC	top dead center
THC	total hydrocarbon
TVE	threshold value exceed
USD	United States dollar
WOT	wide open throttle



# **Chapter 1. Introduction**

## **1.1 Backgrounds and Motivations**

### **1.1.1 Major issues in internal combustion engine**

An internal combustion engine is defined as a heat engine which combusts the fuel in a combustion chamber, converts the heat energy into mechanical energy for power propulsion [1, 2]. Since the first continuous rotary motioned steam engine was developed by a James Watt in 1781, reciprocating type engine has been the majority of power source among the industry. By J. J. Lenoir in late 1858, the internal combustion engine was successfully become commercialized. Until now, it has been used as a power source for many fields, especially transportation and automotive field and has made remarkable developments in conjunction with the qualitative development of fossil fuels.

Internal combustion engine can be categorized [2] in several ways such as application target, engine design, fuel and ignition system, etc. Among these categories, the four-stroke, DOHC (double over-head cam) water-cooled engine is now used most in automotive industry to cope with various technical and environmental regulations.

While developing an internal combustion engine, the most important things are its marketability, emission and efficiency. Marketability already contains the other two things, however, it also includes consumer-oriented value such as performance and by NVH (noise, vibration and harshness) problem. The goal and objectives of the development may vary widely.

Secondly, emissions have become increasingly stringent in recent years due to environmental issues around the world. Since the European Union introduced EURO1 regulations in 1990, the regulations have become stricter. From 2014, EURO6 regulations became effective, and the restriction on PN (particulate number) was also introduced for gasoline vehicles equipped with GDI (gasoline direct injection) type engines. Detailed regulations for light duty vehicles are shown in figure 1.1 [3]. In the United States, from September, 2017, the WLTC (Worldwide harmonized light vehicles test cycles) was applied to all types of vehicles with harsher conditions compared to a previous monotonous NEDC (new European driving cycle). And RDE (real driving emission) regulation using PEMS (portable emissions measurement system) on-road equipment was also introduced. From U.S. EPA Tier 3 (2017-2025) regulation, Tier 3 emissions standards were adopted in March 2014 and phase-in 2017-2025. The regulation also tightens sulfur limits for gasoline. The United States CARB (California air resources board) LEV III (2017-2025) has phase-in standards from NMGO (non-methane organic gas) + NO<sub>x</sub> (nitrogen oxides) emissions [4]. China will soon begin to implement the CN 6b in 2019 and the CN 6b in 2022, which is 50 percent HC, 40 percent of NO<sub>x</sub> and 33 percent of PM (particulate matter) emission limit level of EURO6 regulation. This will also include the N<sub>2</sub>O and RDE regulation [5]. Not only these three major markets, but other governments are also joining in strengthening emissions regulations to improve the environment, and it has become the biggest challenge for automakers.

In the last, the fuel efficiency regulation, CO<sub>2</sub>, is also being strongly enforced annually. CO<sub>2</sub> is known to be the main contributor to greenhouse gases and it is known to be produced in the transportation field (23 percent). Global pressures to control the CO<sub>2</sub> production are forcing automakers to invest aggressively in innovative technology development. The EU regulates 130 g/km in 2015, 118 g/km in 2016 and 96 g/km in 2021 [6]. Recently, more stringent regulation is

getting applied as the EU announced that 15% less CO<sub>2</sub> will be required in 2025 and 30% less in 2030 compared to 2021. For the United States, the average industry-fleet wide level had to be lower than 25.5 mpg in phase 1 from 2012 to 2016, and must meet 54.5mpg level in phase 2 by 2025 [7, 8].

Thus, many outlooks had predicted that by 2015, the internal combustion engine's market sharers would be reduced by up to 30 percent, replaced by fuel cells, electric cars or hybrids. However, nowadays the outlooks still show the majority of internal combustion engine. Figure. 2 shows the market share prediction in 2025 in major markets [9]. The rise of HEV market share is noteworthy, however, it is expected that the internal combustion engine will still be the mainstream of powertrain in the future as HEVs also require internal combustion engines [10].

In Japan, the Research Association of Automotive Internal Engineers (AICE) launched in April 2014. The consortium consists of nine automaker companies and two research institute and aimed at making internal combustion engines highly efficient and reducing emissions, funded 750 million yen (6.8 million USD) with government investments [11]. In addition, through the SIP (Cross-Ministerial strategic invocation promotion) program, the government strengthens the inter-ministerial linkage for scientific and technology-related policies. Of total 11 projects, 2 billion yen (18 million USD) is being funded for internal combustion engine and targeting 50% of efficiency and 30% reduction of CO<sub>2</sub> emission [12]. Europe also has 14 European carmakers forming a research organization called EUCAR [13], which is actively supporting internal combustion engine research in a sustainable propulsion in HORIZON 2020 project. In the United States, the overall budget for automotive R&D is increasing, and the budget for Advanced Combustion Engine (ACE) is also continuously increasing.

Over 60% of vehicles in the world are equipped with spark-ignited engine [14] and recent major scandals related to Diesel emission problem have caused the bad influence to public on the image of the Diesel powertrain vehicles. Diesel powertrain systems are now also struggling on the cost increase of additional after-treatment system to meet the future stringent regulations. For that reason, in the meantime, thanks to the low cost, industrial automakers and researchers are again putting efforts and capital into maximizing the efficiency of spark-ignited engine.

### **1.1.2 Knock and efficiency**

The compression ratio has a direct relationship with the efficiency in an ideal engine [2]. Its theoretical characteristic is shown in equation 1.1. However, a higher compression ratio provokes the knock-prone in-cylinder conditions because of the increased pressure and temperature in the unburned end-gas region.

$$\eta = 1 - \frac{1}{r_c^{k-1}}$$

(where  $r_c$  is the compression ratio, and  $k$  is the polytropic coefficient)

(1.1)

Knock is a kind of spontaneous ignition that occurs in the unburned end-gas region in the cylinder [15]. In spark-ignited engine, as the in-cylinder pressure is increased due to combustion, the temperature of the unburned end-gas ahead of the flame is increased. Hot spots in the end-gas located in front of the flame are auto-ignited before the flame is arrived and causes a spontaneous heat release of all end-gas. Pressure wave generated by the hot spot hits the wall inside of the cylinder which causes the pinging sound. If the heat release amount is rapid and large enough, it causes the erosion and damage such as piston crown melting, ring

cranking, head gasket leakage, bore scuffing [14, 16, 17]. Knock occurrence in spark-ignited engine must be avoided during operation because it can cause serious engine failure and damage and this is the main hindrance of increasing the compression ratio for developing future high efficiency engine. An example for pressure traces of knocking cycle and ensemble averages cycle are shown in figure 1.4.

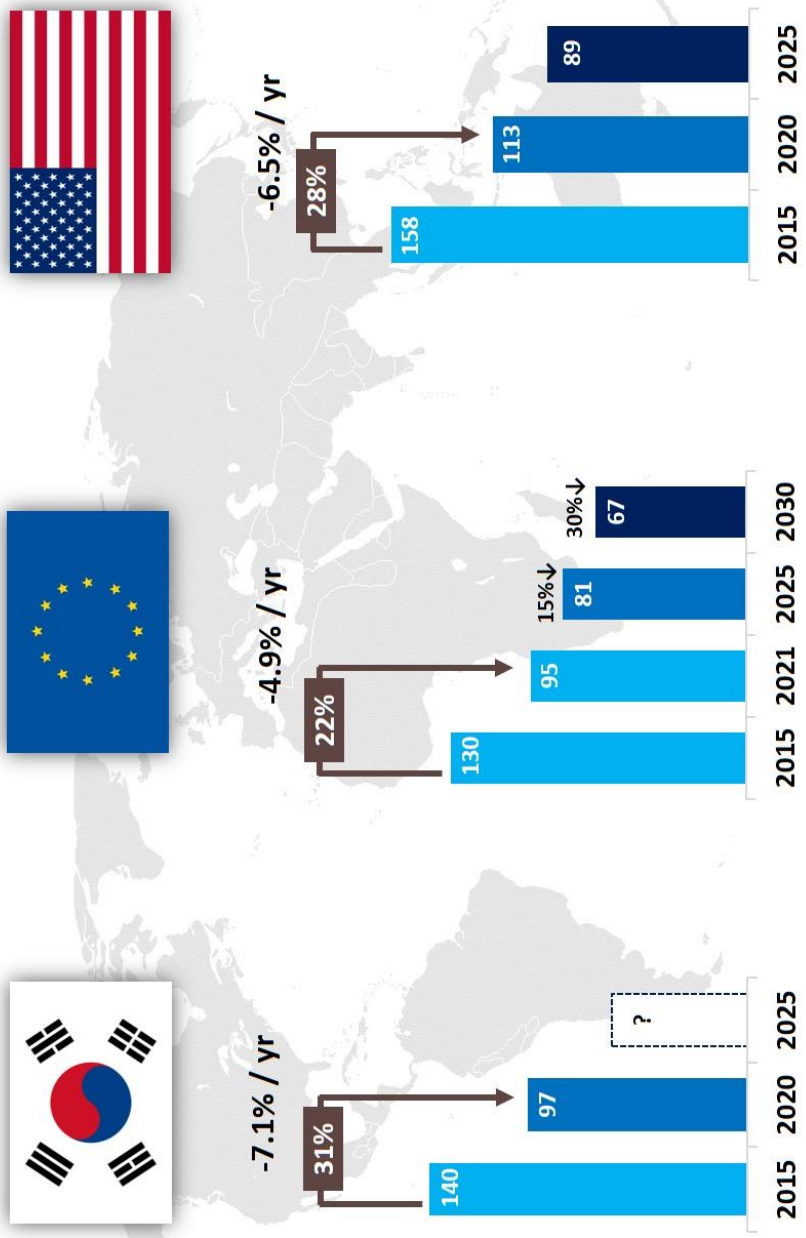


Figure 1.1 CO<sub>2</sub> regulations in global markets

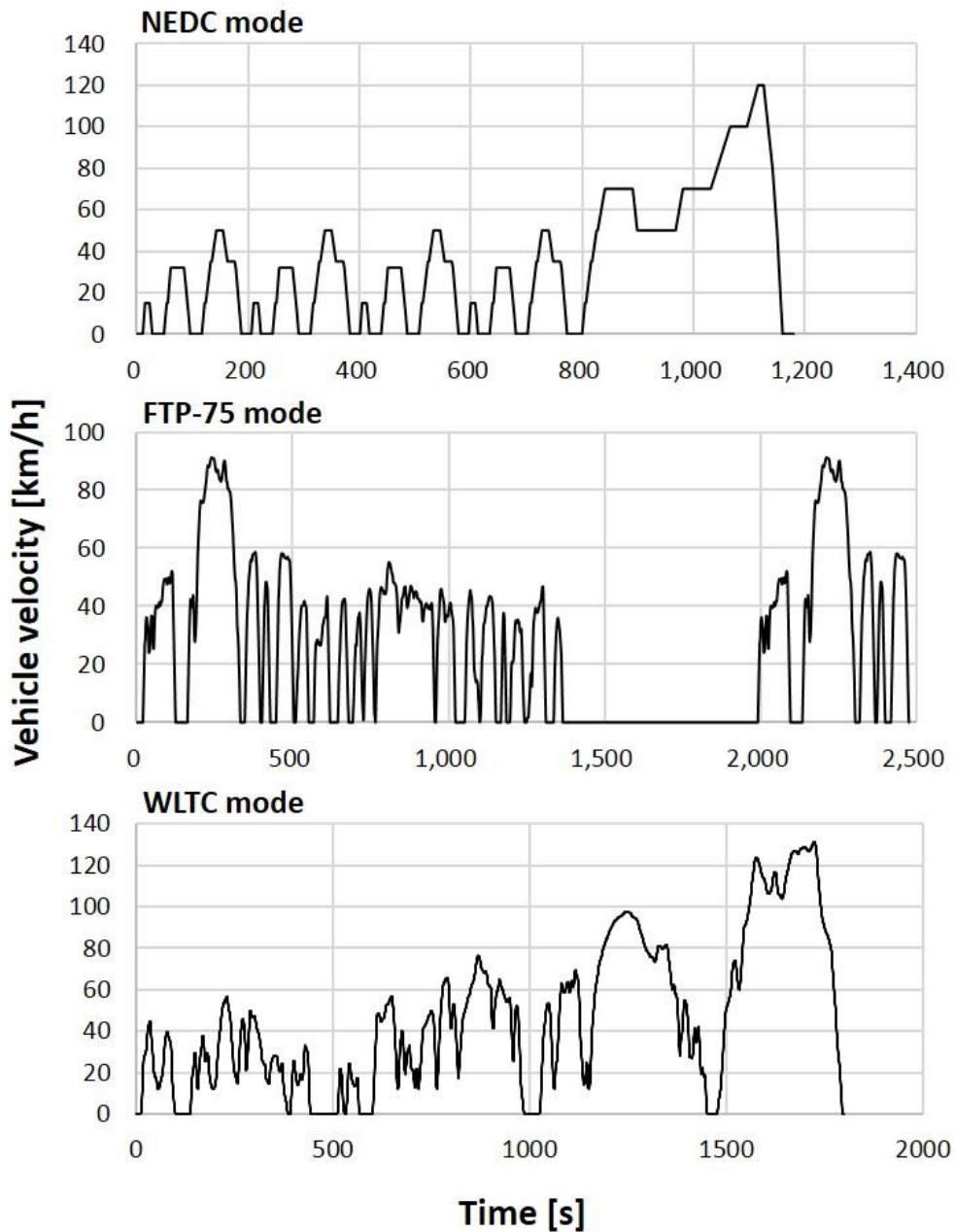


Figure 1.2 Fuel economy test modes: NEDC, FTP-75 and WLTC

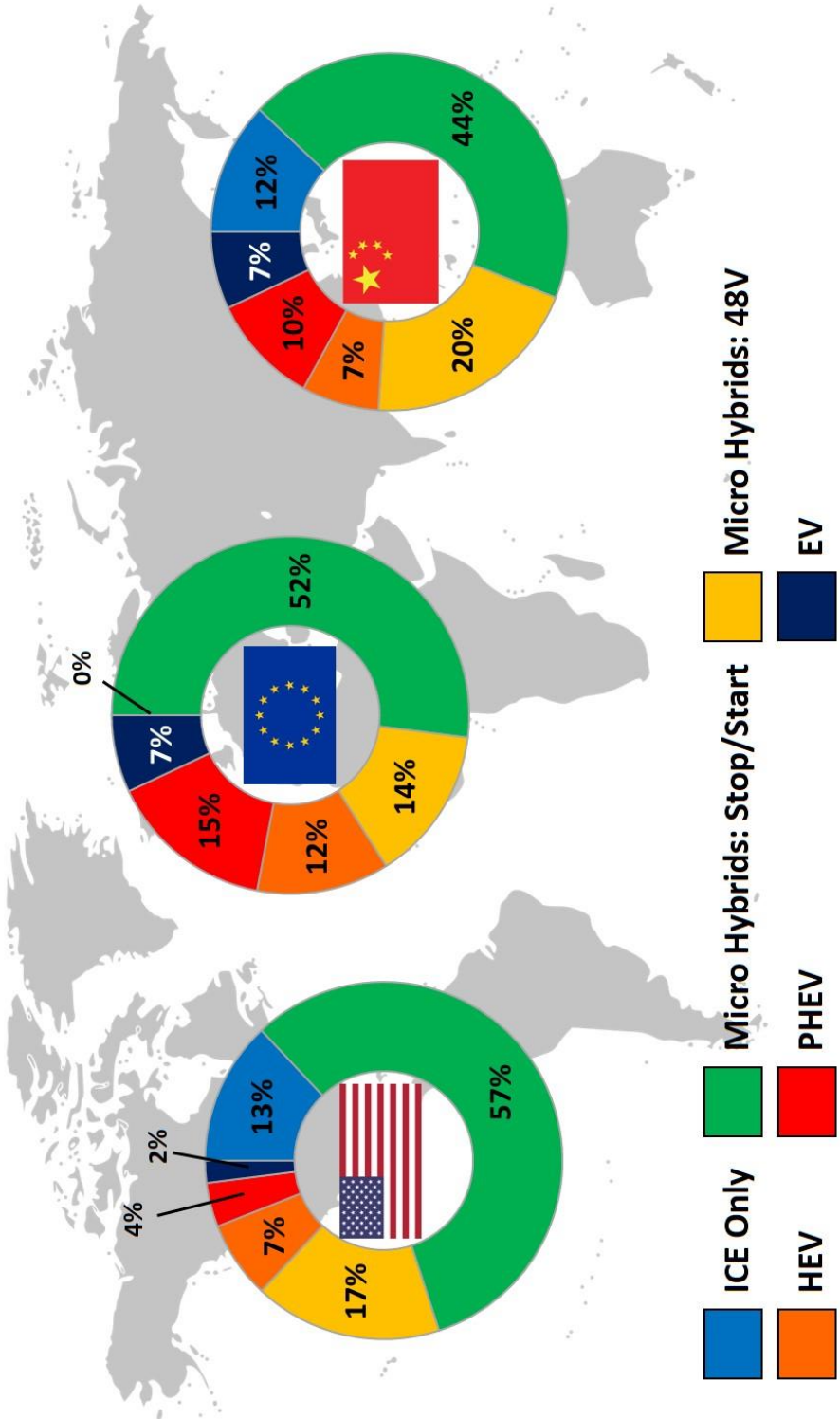


Figure 1.3 Outlook of future market share of vehicles [9]

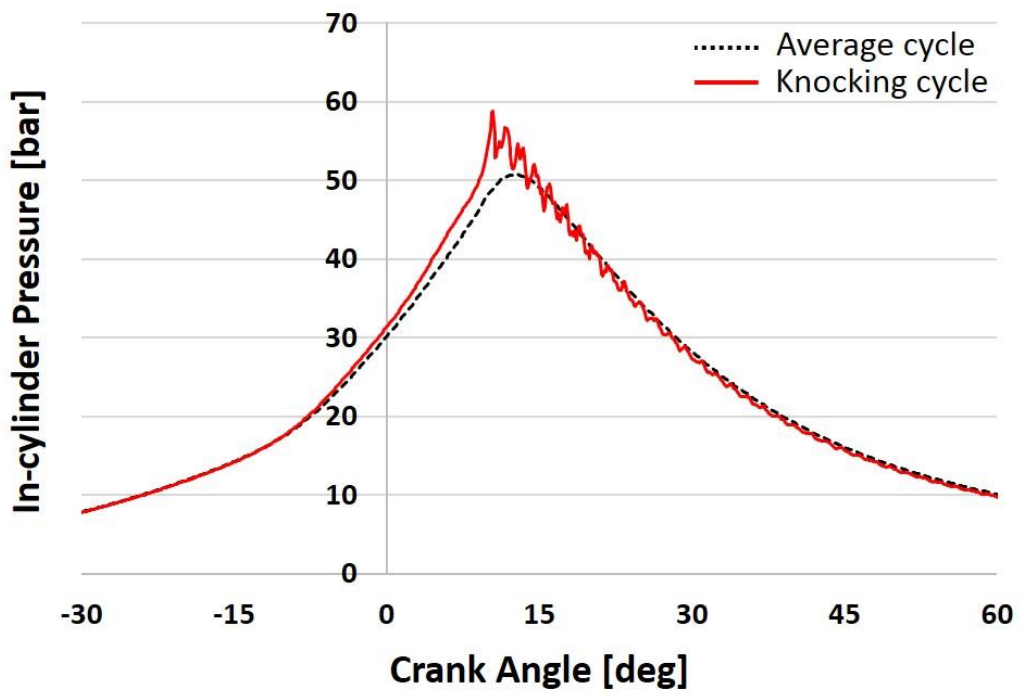


Figure 1.4 In-cylinder pressure of knocking cycle

## 1.2 Literature Review

### 1.2.1 Auto-ignition fundamentals

#### 1.2.1.1 Auto-ignition classification

Knock is auto-ignition in the unburned end-gas zone, as the flame propagation in the unburned end-gas zone is non-uniform and can be classified as three modes: deflagration, thermal explosion, or developing detonation [14, 15, 18-20]. From the numerical and experimental studies, Zeldovich et al. [21] and König et al. [22] identified these modes and showed that auto-ignition of the hot-spot can lead to pressure spikes. Temperature gradient or reactivity gradient in the end-gas region is a standard for the classification, and it is as the follows.

- 1) Deflagration: large spacial temperature gradient, hot spot triggers the reaction of the rest of the end-gas.
- 2) Thermal explosion: low spacial temperature gradient, spontaneous ignition of entire homogeneous end-gas.
- 3) Developing detonation: inhomogeneity in the end-gas ultimately generates a strong shock wave (exceed Chapman-Jouget velocity) leading to detonation.

Pressure oscillation can be predicted with comparing pressure increase by an auto-ignition and pressure decrease by expansion of a burned gas. If an end gas is supposed to be as sphere shape, a numerical expression of pressure rise of the end gas can be write as in below [18, 23].

$$\frac{dP}{dt} = \frac{\gamma-1}{V} \frac{dQ}{dt} - \frac{\gamma P}{V} \frac{dV}{dt} \quad (1.2)$$

$$\frac{dq}{dt} > \frac{3\gamma}{\rho(\gamma-1)} \frac{P}{r} \frac{dr}{dt} = \frac{3\gamma}{\rho(\gamma-1)} \frac{Pa}{r} \quad (1.3)$$

In equations 1.2 and 1.3,  $\gamma$  is the heat capacity ratio and  $r$  is the radius of sphere, and  $a$  is the speed of sound in such condition. In the small  $r$  case, the end gas has a steep temperature gradient. Therefore, auto-ignition is started at small region that has the highest temperature among the region. However, because of small pressure of the end gas, significant shock wave will not be detected. This regime is classified as deflagration or flame initiation. If the  $r$  is large enough to satisfy the upper equation, minor shock wave that can interrupt combustion chamber will be occurred. In this case, flame propagation speed is subsonic, therefore there is no relationship between heat release and pressure wave. This is thermal explosion and also frequently referred as acoustic knock. When the  $r$  is so large that pressure build up is significantly large, pressure wave accompanying fast chemical reaction comes through the combustion chamber. In this case combustion wave has a similar speed of pressure wave's and it induces the large interaction of heat release and pressure wave. This phenomenon is called developing detonation. Developing detonation is considered as physically damaging. However, deflagration mode doesn't give a damage to the engine and it can be thought as a favorable phenomenon by increasing the burn rate leading to higher combustion efficiency.

#### 1.2.1.2 Octane Number

RON (research octane number) and MON (motor octane number) are the evaluation factors of test fuel for determination of knock characteristics. There are two PRFs (primary reference fuels): iso-octane that has 100% ON (octane number) and n-heptane that has 0% ON. ON of the test fuel can be evaluated by comparing the knock resistance of the fuel and the mixture of two PRFs.

RON and MON are tested under different specific engine running conditions. However, it is well known that both indexes don't represent the fuel characteristics property. Introduction of road octane number and fuel sensitivity shows better performance for evaluation. Road octane number is expressed as mean value of RON and MON, and fuel sensitivity is the difference of RON and MON.

The fact that spark-ignited engine runs with premixed fuel and air, certain condition can guarantee good homogeneity theoretically. However, in compression stage, the homogeneity cannot be good as of theoretical condition because of region that has high temperature locally. Auto ignition is initiated in certain pressure and temperature condition and it is not desirable in combustion chamber as it could make knock that intimidate the combustion chamber physically. There are several fuels and those fuels have different chemical structure. Therefore, the condition that initiates auto ignition differs among the fuels. To prevent the phenomenon, knock propensity index has to be evaluated for practical using of several fuels in SI engines.

Kalghatgi [24] introduced a new index: Octane Index (OI). OI can describe fuel knock tendency more accurate than road octane number or sensitivity and it is defined as equation 1.4. Here, S is the sensitivity and K is a constant that is defined by hysteresis of pressure and temperature in certain combustion cycle. The fact that K is calculated in real condition guarantees that OI is the best index to describe the fuel's knock tendency.

$$OI = (1 - K)RON + KMON = RON - KS \quad (1.4)$$

### 1.2.1.3 Livengood and Wu correlation

To predict the timing that knock occurs, auto-ignition prediction models are being used in many studies. There are mainly three types of prediction model [25]: models that are using detailed chemical kinetic mechanism, models using simplified mechanisms such as Shell Knock model [26, 27] and phenomenological models [15, 25] based on Arrhenius equation. Among various models, phenomenological models are widely used with convenience and fast calculation speed. Assuming a one-step reaction mechanism, the auto-ignition delay time can be described as the Arrhenius equation. The first attempt of this method was conducted by Livengood and Wu [15, 28]. Assuming the reaction is zero-order and the reaction rate does not change, the relationship between concentration and auto-ignition delay can be expressed as equation 1.5, where  $\tau$  is the ignition delay,  $(x)/(x_c)$  is the concentration ratio.

$$\frac{(x)}{(x_c)} = \int_{t=0}^{t=t_e} \frac{1}{\tau} dt \quad (1.5)$$

Auto-ignition may be occurred as RHS reaches to the unity. Douaud and Eyzat [29] proposed a chemical reaction based ignition delay time calculation as expression 1.6 and calculated the coefficients by experimental studies using primary reference fuels (iso-octane and n-heptane mixture).

$$\tau = 18.69 \left( \frac{ON}{100} \right)^{3.4017} p^{-1.7} \exp \left( \frac{3800}{T} \right) \quad (1.6)$$

A lot of researchers has been developed empirical-typed ignition delay correlation since this study [30-32]. Worret et al. [33], Berluka et al. [34] and Siokos et al. [35] used Douaud-Eyzat model for their knock prediction studies, Wayne et al. [36] re-calibrated the coefficients.

Pipitone et al. [37] assumed the temperature at IVC (intake valve close) timing is 35K higher than manifold temperature for individual cycle temperature calculation and used downhill simplex optimization method to calibrate the coefficients of the equation except the octane number under operating condition of gasoline-natural gas mixture combustion.

Hoepke et al. [38] developed a new form of knock prediction model including the effects of cooled-EGR (exhaust gas recirculation) in condition of boosted operation. As the EGR diluent increases the frequency of the quenching collisions, thus the empirical term for EGR was newly introduced, and the term of molar density (P/T) was also introduced due to its direct relationship to the chemical reaction. The proposed model is shown in equation 1.7 where  $x_{egr}$  is the EGR rate.

$$\tau = 8.449 \times 10^{-5} \left(\frac{P}{T}\right)^{-1.343} (1 - x_{egr})^{-0.8881} \exp\left(\frac{5266}{T}\right) \quad (1.7)$$

Chen [25] et al., introduced a new model based on Hoepke model, containing  $\lambda$  to include the impact of air-fuel ratio because it affects not only the pressure and temperature but chemical reactions during auto-ignition. The coefficients were calibrated with optimization using genetic algorithm, and the expression is shown in equation 1.8. The temperatures at IVC timing was assumed to be the same regardless of cyclic variation and was calculated with 1D (one-dimensional) simulation tool, GT-Power.

$$\tau = 5.35 \times 10^{-5} \left(\frac{P}{T}\right)^{-2.374} (1 - x_{egr})^{-3.013} \lambda^{-1.927} \exp\left(\frac{3167}{T}\right) \quad (1.8)$$

The latest study was conducted by McKenzie [39] et al., proposed a correlation of equation 1.9 which can be included the impacts of cooled-EGR, residual gas fraction and air-fuel ratio for modern SI engine by introducing an additional term of dilution factor as expressed in equation 1.10. A nice correlation was shown in the speed range of 1250 to 2000 rpm, EGR of 0 to 12.5% and  $\lambda$  of 0.8 to 1.3. The temperature at IVC was also assumed to be the average temperature calculated by 1D simulation.

$$\tau = 2.71 \times 10^{-5} \left(\frac{P}{T}\right)^{-1.73} \exp\left(\frac{5190}{T}\right) (1 - w_d)^{-0.618} \quad (1.9)$$

$$w_d = x_{egr} + x_{residual} + 0.95 \left| \frac{\lambda - 1}{\lambda + (A/F)_{stoi}} \right| \quad (1.10)$$

## 1.2.2 Knock measurement and analysis

Knock accompanies a sudden pressure increase because it is an auto-ignition phenomenon of air-fuel mixture in the unburned end-gas [40]. Bradley et al. [20] showed that up to 40% of air-fuel mixture of the original charge can be auto-ignited in the most severe condition.

Knock phenomena shows a stochastic behavior due to the cyclic variation during operation, thus it is not easy to define the status or level of knocking combustion. There are various approaches for knock detection and analysis that highly depend on the tester. This was already described as a dilemma by Kalghatgi

et al. in a recent study [41]. However, it is necessary to establish the techniques not only to accurately understand the knock phenomena, also to ensure the repeatability of the test and to carry out an assessment of knock robustness.

There are various methods to detect the knock occurrence [14, 15, 19, 32]: In-cylinder pressure sensor, optical measurement using endoscope or transparent engine, ion-current signal, engine vibration including knock sensor, and other methods such as exhaust temperature measurement. Among these various methods, it is well known the measurement with the in-cylinder pressure sensor is the most accurate and versatile for engine knock measurement. [19, 42]

#### 1.2.2.1 Knock frequency and harmonic wave

Draper [43] solved the wave equation and suggested the in-cylinder pressure oscillation mode that has been widely used in knock studies. Millo et al. [44] and Eng et al. [45] also introduced the equation and showed the relationship between cylinder bore, sound speed and the radius of the cylinder bore. Gaeta et al. [46] implemented advanced modeling of in-cylinder pressure oscillation under knocking condition including the damping mechanism, which can be from friction, heat transfer and expansion of the fluid. The solution and principle of the wave equation is well-written in many studies [43-48]. The frequency of pressure oscillation can be expressed as equation 1.11 [46], where sound speed is shown in equation 1.12.

$$f = \frac{\bar{a}}{2\pi} \cdot \sqrt{\left(\frac{u^* \lambda m}{B/2}\right)^2 + \left(\frac{\pi g}{Z_0}\right)^2} \quad [\text{Hz}] \quad (1.11)$$

$$\bar{a} = \sqrt{\gamma RT} \quad (1.12)$$

$\mu_{\lambda m}^*$  is the  $m^{\text{th}}$  root of the first derivative of Bessel's equation ( $J'_{\lambda}(\mu_{\lambda m}^*)=0$ ), where ( $m = 1, 2, \dots$ ) and ( $\lambda = 0, 1, \dots$ ).  $\lambda$  is the number of the circumferential mode,  $m$  is radial mode number and  $g$  is the axial mode number.  $\bar{a}$  is the speed of sound,  $B$  is the radius of the cylinder bore and  $Z_0$  is the height assuming the volume between the piston top and engine head at knock onset is cylindrical,  $Z_0 = V_0 / \pi B^2$ .

### 1.2.2.2 Knock detection of occurrence and location

It is very important how to install the pressure transducer into the cylinder to measure the knock phenomena precisely. Brunt et al. [49] and Bertola et al. [50] investigated the difference of sensor location resulted in the discrepancy of measured in-cylinder pressure values. Also, if the sensor is installed in the center of the cylinder, as the pressure oscillation occurs from the hot spot in the end-gas, knock may not be detected precisely. In addition, flush-mounting is highly recommended because other methods including recessed mounting may cause the unwanted pipe oscillation which can affect the original frequency of knock signal.

Ando et al. [51] showed a good representativeness for the auto-ignition phase of the time interval between 50% to 10% of maximum heat release during the decay. Kirsten et al. [52] proposed a new detection method and dimensionless indices for dual fuel combustion (Diesel/natural gas) using SOC (start of combustion) determination from heat release calculation, which showed a good agreement.

Sjöberg et al. [53] defined 'strong end-gas auto-ignition' if the heat release of auto-ignition exceeds 75% of maximum heat release through the 1<sup>st</sup> law heat release calculation method. Very fast decay of heat release at the end of combustion was shown in the strong auto-ignition condition. From this

observation, using ignition timing shaking method (maximum 5 CA), the auto-ignition combustion was clearly separated from the normal combustion under various fuel types.

In most recent studies, McKenzie et al. [18] defined if the MAPO (maximum amplitude of pressure oscillation)-derived knock intensity exceeded 1 bar of threshold. Kalghatgi [41] used a 0.5 bar threshold, defined as twice the maximum amplitude of the pressure pulse.

Many researchers have tried to find the location of knock occurrence. Hettinger and Kulzer [54] introduced triangulation method to detect the auto-ignition hot spot and knock onset. Six pressure sensors have been used and the analysis from the pressure sensors found that some of the cycles had multiple hotspots. However, inserting additional pressure sensors to identify the knocking spot would also lead to significant increases in the cost during the engine development.

Kawahara et al. [55] used an optical engine to record the chemiluminescence images of OH, CH<sub>2</sub> radicals of knocking combustion. It was found that the explosion of the auto-ignition kernel produced the pressure oscillation, and knock intensity and mass fraction of unburned mixture showed a big relationship. Furthermore, weak signal of OH and HCHO radicals were measured before the auto-ignition occurred, thus it was verified that the OH radical can be used as an indicator of transition from low temperature reaction to high temperature reaction.

Ma et al. [56] investigated the evolution of intermediate species during knocking combustion using an optical engine with imaging of CH<sub>2</sub>O and OH chemiluminescence. As a result, second stage flame which has the flame speed of 160m/s was observed ahead of normal SI flame front. They also verified a

significant pressure gradient was generated by the end-gas auto-ignition, resulting in the pressure oscillation in the cylinder.

Suzuki et al. [57] showed the cool flame reaction in the end-gas region with measurement of  $\text{CH}_2\text{O}$  and Merola et al. [58] used spectroscopic approach with an optical engine and investigated the location of knock occurrences. As a result, for all tested fuels, the possibility for hot-spot existence was the largest in the area near the exhaust valves.

Many optical techniques have been being used for knock measurement and investigation of auto-ignition mechanism [14]. However, optical engine has walls with quartz or sapphire for its transparency, therefore, even though it has a great advantage on measurement of hot spot size or filming the in-cylinder chemical reaction, the temperature and gas composition still have differences from that of actual metal engine due to the discrepancy of thermal boundary conditions, may leading to different measurement of knock location.

Spicher [59] inserted a large number of optic fibers in the cylinder head to detect the flame propagation inside the cylinder. By introducing this method, knock intensity was quantified and flame front velocity was measure as high as approximately 1,300 m/s in high knock intensity cycle.

AVL Visio-Knock [60] equipment provides an easy access to measurement of flame propagation and knock location under real engine operating condition. [61-64] It is designed to view the end-gas area by inserting optical fibers and installing windows around the spark plug. Depending on the probe, it has eight to forty and more windows. As the flame propagates, light intensity is increased and shows the perturbation if the pressure oscillation occurs. By high-pass filtering the light intensity signals, the knock spot is determined as the place where the first variation of light intensity occurs.

Witze and Green [65] introduced a detection method of knock location using ion-probe head gasket. Flame ionization detection has been widely used in modern society for flame detectors and this is the basic principle of the ion-probe gasket. It measures the ionization of the reaction in the flame, which facilitates the measurement of arrival of flame when it reaches the end of the cylinder bore. And then it is analyzed combined with the in-cylinder pressure sensor, the flame shape can be identified when the knock occurs. It has the great advantage of being able to detect without making major configuration changes. The head gasket ion-probe used in this study will be described in the Chapter. 3.

#### 1.2.2.3 Calculation of knock intensity

For knock intensity calculations, the method also largely depends on the individual and operating conditions such as load, speed, and shape of the engine. Borg et al. [66] showed a good comparison of various methods for knock intensity calculation. And it was investigated that time-domain calculations and frequency-domain calculations do not differ thanks to Parseval's identity [67]. Most common metrics are shown in Table. 1.1, and they are also well summarized in previous studies [19, 66].

Generally, researchers have investigated knock behavior using their own methods. It is generally accepted to use IMPO (integral of modulus of pressure oscillation), MAPO and ISPO (integral of signal pressure oscillation) methods for intensity calculations due to their simplicity and intuitiveness. Among the various methods, MAPO is the most commonly used [68] and has the advantage of using in both software and hardware due to its simplicity [66].

Brunt et al. [49] defined KI (knock intensity) as in equation 1.13 where  $N_c$  is the number of knocking cycle. A one-bar offset is applied so a knock pressure less than 1.0 bar does not contribute to the intensity calculation. This offset also has the advantage of zero being achievable when the ignition timing is retarded.

$$KI = \frac{20}{N_c} \sum (P_k - 1) \quad (1.13)$$

Amann et al. [69] used IMPO to calculate knock intensity in their study. Brecq et al. [70] established a new index, DKI (dimensionless knock indicator), which is a combination of IMPO and MAPO, as shown in equation 1.14. ( $W$  = window size)

$$DKI = \frac{IMPO}{MAPO \times W} \quad (1.14)$$

Hudson et al. [71] introduced a new index called LKI (logarithmic knock intensity) using the energy concept as shown in equation 1.15. (where  $C$  is a constant determined by trials) Then, a 6~25 kHz band-pass filtered data was used for the average energy (which is ISPO) calculation. This was verified in the time and frequency domains. Additionally, it was shown that an analysis for knock intensity needs more than 1,000 units of cycle data.

$$LKI = \ln\left(C \times \frac{1}{N} \sum_{n=0}^{N-1} x^2(n)\right) \quad (1.15)$$

In very recent studies, Sjöberg et al. [53] calculated knock intensity using a 4~28 kHz frequency range of the signal to quantify the auto-ignition level. This filter range can include multiple modes of the acoustic waves. In the study, an average of 500 cycles was used. Bradley et al. [40] and Kalghatgi et al. [41] established knock intensity as twice the maximum amplitude of the pressure pulse.

McKenzie et al. [18] used MAPO-calculated knock intensity. Mutzke et al. [72] validated MAPO, IMPO and LKI with measured heat flux. Kim [32] investigated knock intensity with cyclic variability with MAPO method. Szybist et al. [73] determined a knocking cycle as if the peak-to-peak knock intensity exceed 1 bar.

A new method was developed by Shahlari [19] for determining knock intensity that can eliminate the potential bias from the transducer shock period, which is derived from a new method for knock onset determination. This seems to be the most progressive method for intensity calculation to date. However, this also requires post-processing after the experiment.

Table 1.1 Common knock intensity metrics using in-cylinder pressure

MAPO	Maximum Amplitude of Pressure Oscillation	$\max  P_{filt} _{\theta_0}^{\theta_0+\Delta\theta}$
IMPO	Integral of the Modulus of Pressure Oscillation	$\int_{\theta_0}^{\theta_0+\Delta\theta}  P_{filt}  d\theta$
ISPO (SEPO)	Integral of Squared Pressure Oscillation (Signal Energy of Pressure Oscillation)	$\int_{\theta_0}^{\theta_0+\Delta\theta} P_{filt}^2 d\theta$
AEPO	Average Energy of Pressure Oscillation	$\frac{1}{\Delta\theta} \int_{\theta_0}^{\theta_0+\Delta\theta} P_{filt}^2 d\theta$
RI	Ringing Intensity	$\frac{1}{2\gamma} \frac{\left(\beta \frac{dP}{dt}\right)^2}{P_{max}} \sqrt{\gamma RT_{max}}$
PRR	Pressure Rise Rate	$\text{Max} \left( \frac{dp}{d\theta} \right)$

#### 1.2.2.4 Knock onset determination

There have been two general ways to locate the knock onset during testing; one is the threshold value exceed method (TVE), and the other one is the signal energy ratio method (SER) [32]. The TVE method defines the knock onset as the crank angle when the amplitude of the high-pass filtered pressure signal exceeds the set threshold. Generally, this method has an error of 0.5 CA (crank angle) if the threshold is properly set [32]. Worret et al.[33] have found that the simple TVE method can possibly determine knock onset later than the actual onset. To mitigate this defect, Lee et al. [74] compensated for a few crank angles earlier to reduce the difference. Chen et al. [25] used mouse-clicking method of massive data for precise determination.

Shahlari and Ghandhi [67] presented the SER (signal energy ratio) method using ISPO, as shown in equation 1.16, to compensate for the limitations of the TVE method. In their research, knock onset was defined as the timing when SER has the highest value, while a proper window size was suggested as 5 CA, and various filters were used for comparison.

$$SER = \frac{ISPO_{fwd}^2}{ISPO_{bwd}^{0.5}} = \frac{(\int_{\theta_0}^{\theta_0+\Delta\theta} P_{filt}^2 d\theta)^2}{(\int_{\theta_0-\Delta\theta}^{\theta_0} P_{filt}^2 d\theta)^{0.5}} \quad (1.16)$$

On the other hand, Kim [32] had found that the SER method can possibly determine knock onset earlier than the actual onset. Under these circumstances, Kim conducted an investigation on the TVE method to increase the accuracy of determining knock onset in the research.

To avoid the bias by Butterworth filter, median and smoothing filters were applied for 10 data points corresponding to 1 CA in 0.1 CA resolution data. After high-pass filtering with the new filter, a threshold ( $\mu + 5\sigma$ ) was set as the five

times of the standard deviation ( $\sigma$ ) added with the mean value ( $\mu$ ) from 5 CA before the guessed point of knock onset. It was concluded as knock onset if the value of the data point exceeded the threshold. An example of this Kim's modified TVE method is shown in figure 1.5.

In a recent study, Shahlari et al. [19, 48] developed a new algorithm for determining the knock onset using an iteration method with very high accuracy, and the explanation is shown in figure 1.6.

- 1) An initial guess for knock onset is found; this can be from the TVE method or any other reasonable estimation method.
- 2) Data points from 136 to 40  $\mu\text{s}$  before the knock onset were isolated; and a line was fit to these data points using a weighting function based linearly on the time from knock onset, i.e. a value of 1 was assigned to the point at the earliest point, and a value of 100 was assigned to the point 40  $\mu\text{s}$  before knock onset.
- 3) The slope of the fit line was projected forward starting from the point 40  $\mu\text{s}$  before the knock onset and ending at 196  $\mu\text{s}$  after the knock onset (i.e. the y intercept is the point at 40  $\mu\text{s}$  before the knock onset).
- 4) The difference between the raw pressure and the projected line is calculated. The data point where this difference first exceeds 10 kPa is assigned as the new knock onset, given all of the following conditions are met.
  - 4-1) This difference at knock onset is below 100 kPa
  - 4-2) This difference at the following data point (knock onset + 4  $\mu\text{s}$  for this study) is greater than 0 kPa.
  - 4-3) The raw pressure at the following data point (knock onset + 4  $\mu\text{s}$  for this study) is greater than that at knock onset.

- 5) If the conditions in the previous step are not met at any points in the projected line, the knock onset is set 30  $\mu\text{s}$  earlier than that in step 1.
- 6) The knock onset from steps 4 and 5 are used as new guesses for the next iteration of this procedure.
- 7) These steps (1-6) are repeated 5 times.
- 8) For any cycle that entered step 5 in every iteration (i.e. the knock onset was cumulatively moved 150  $\mu\text{s}$  earlier), the knock onset is set 100  $\mu\text{s}$  after the initial knock onset guess.
- 9) Steps 1 through 6 are repeated 5 more times.
- 10) The cycles for which the knock onset is never determined (i.e. the cycles that enter step 5 at the final iteration of the process) are marked as special cases. For all other cycles, the knock onset calculated in step 4 of the last iteration is reported.

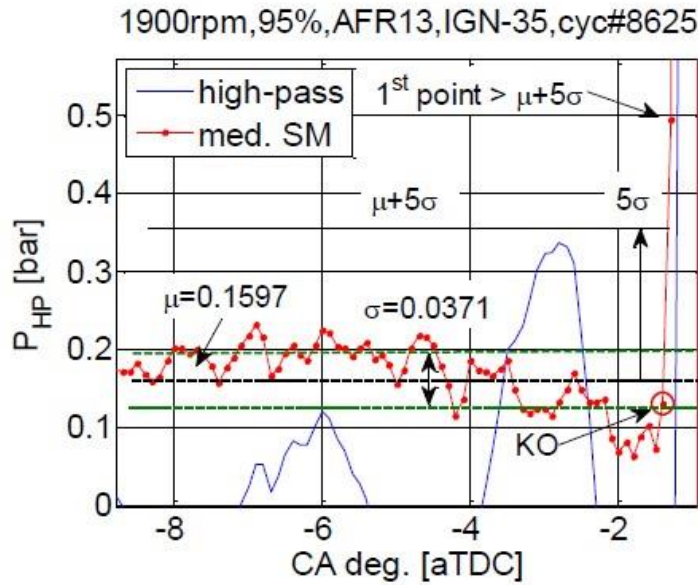


Figure 1.5 Determination of knock onset by Kim's TVE method, from [32].

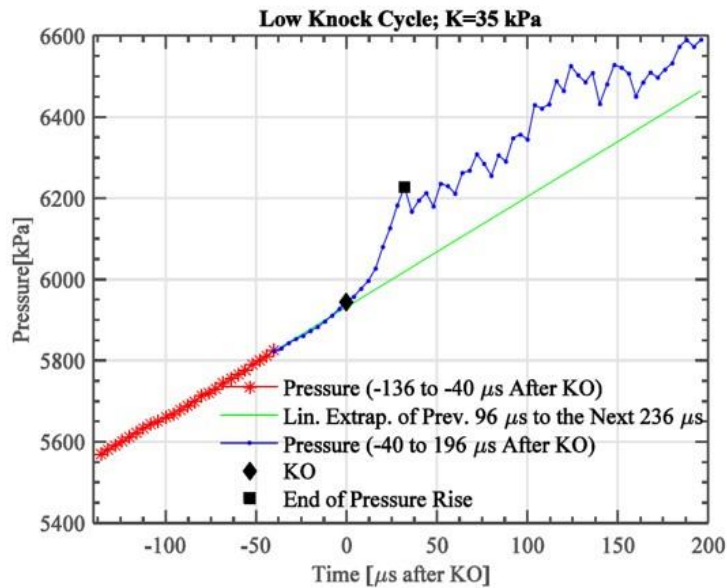


Figure 1.6 Determination of knock onset by Shahlari's method, from [19]

### **1.2.3 Knock mitigation methods**

For knock mitigation or control during operation, car manufacturers previously utilized spark timing strategies. However, this method decreases efficiency and increases the exhaust temperature excessively, which may deteriorate the durability of downstream components. To solve this problem, over-fueling has been frequently adapted [42]. However, this also decreases the engine efficiency and increases CO and THC emissions.

More practical and fundamental methods of reducing knock occurrence in very recent studies are as the followings. First one is the enhancement of flame speed during the combustion process [75-77]. Under the enhanced flame speed, the air-fuel mixture in the unburned end-gas area can be consumed before the in-cylinder condition reaches the auto-ignition point. Use of advanced ignition systems not only can increase the efficiency but also has an effect of knock suppression [78, 79]. Introducing a high-tumble port design [61, 80-84] is also one of the most effective ways to produce fast combustion, which is attributed to increased flame speed by higher turbulent intensity.

Another method is the improvement using an EGR system. EGR is a very promising method for knock mitigation by the reactivity reduction of unburned end-gas and decrement of in-cylinder temperature [83, 85]. A number of automakers put a great deal of effort into EGR systems because of its potential. Matsuo et al. [86] improved the manifold design to enhance the EGR distribution of each cylinder. Cooled EGR [75] and improved EGR cooling units [85] have recently been adapted to mass production engines.

In the last, engine cooling strategy is also a very efficient method. This method is applicable without significant changes to engine features and does not

result in a high cost increase. Knock suppression with this method is attributed to decreasing temperature of the air-fuel mixture in the cylinder. Lowering the cylinder wall temperature reduces the amount of initial heat transfer to the mixture from the wall before the start of combustion and increases the heat transfer to the cylinder wall during the expansion stroke (heat loss). This eventually leads to the end-gas temperature decrement which allows the unburned end-gas to be consumed before auto-ignition occurs. Improving the temperature distribution by structural changes using a water jacket [85, 86], enhancement of combustion chamber cooling such as the introduction of hollow valves [75], split cooling or dual-loop cooling system [86] have been shown in recent studies.

Kobayashi et al. [87] introduced a dual circuit cooling system into a four-cylinder, compression ratio of 9.0 1.3L engine and showed that the operating condition was affected more by the cylinder head coolant temperature than the block coolant temperature. The effect by lowering head coolant temperature was twice as much as that by lowering the cylinder block coolant temperature. Authors in the study elucidated that it is due to the lowering of cylinder head coolant temperature led to a larger decrease of unburnt gas temperature during the combustion process, and this is attributed to the larger wall temperature decrease.

Finlay et al. [88] demonstrated a precision cooling system to small automotive engines. Higher velocities of coolant showed higher heat flux through the combustion chamber wall, which resulted in up to 50K decrease of surface temperatures. Iwashita et al. [89] also investigated the effect of coolant flow. Their research showed higher velocities of the coolants can effectively reduce the wall temperatures which enabled 2-4 CA additional advance of ignition timing.

Kubozuka et al. [90] developed an evaporative cooling system which has a superior cooling effect than a conventional liquid cooling system. Wall temperature could be controlled accurately by controlling the vapor pressure in

the system. Using this system, 1 CA KLSA (knock limit spark advance) advance was achieved for every 10K drop in coolant temperature (corresponding to 0.1 CA/K). Knocking characteristics for liquid cooling of 85°C were similar to those for evaporative cooling at 90 to 100 °C.

Russ [91] investigated the effect of various engine operating conditions on borderline knock including the coolant temperature. In this study, the effect of each operating parameter was quantified as a function of octane number. In terms of coolant, effects of coolant temperature variation were investigated and 10 K decrease of coolant temperature led to the corresponding effect of increasing one octane number of fuel. Independent cooling effect of the cylinder head and liner were also observed. It was found that volumetric efficiency was slightly more affected by the cylinder head temperature while the KLSA was more sensitive to the block temperature. It was shown the effects of head coolant and liner coolant were almost similar. The author explained the effect of engine block temperature on the unburned charge temperature was similar to that of engine head temperature by the end of compression while the engine head temperature largely affects through heat transfer during air induction. Furthermore, the effect of lowering the coolant temperature was more significant at the lower engine speed due to dilated time for heat transfer to the charge.

Fukuda et al. [92] employed a dual control direct cooling system with individual thermostats for cylinder head and block to 2.4 L DOHC engine. As a result, the temperature of cooling water in water jacket was lowered 23°C average under similar conditions at WOT (wide open throttle), 6000 rpm. Knock limit was evaluated by using the system and observed an improvement of 6.3 CA ignition timing advance compared to the baseline of single control cooling system.

Takahashi et al. [93], in their 3D (three-dimensional) CFD (computational fluid dynamics) simulation, showed the potential of the liner temperature

distribution affecting the auto-ignition in the cylinder. In their paper, they expounded that the in-cylinder air mixture temperature is affected by the exhaust side of the cylinder liner rather than the intake side due to intake air flow motion at the beginning of the intake process. Therefore, to reduce the ring friction loss of the piston, they proposed a strategic cooling that increases the liner temperature on the intake side while decrease the exhaust side temperature to reduce the piston ring friction loss.

Imaoka et al. [94] investigated the effect of wall temperature on knocking combustion under high compression ratio conditions. Through extensive experimental and computational approaches, it has been shown that the heat transfer towards the intake air charge from the intake port is dominant in the temperature increase. Furthermore, a few independent coolant passages were designed for the test, and as a result, ignition timing could be advanced by decreasing the coolant temperature. Furthermore, the authors introduced the optical method and, through CFD work, found the squish in the chamber has an effect on knock mitigation due to its large heat transfer effect to the wall from the unburned gas.

Asif et al. [42] investigated the effect of coolant on KLSA using a multi-cylinder DISI (direct injection spark ignition) engine with dual CVVT (continuous variable valve timing) system. They showed in their recent study that the temperature between the exhaust valve bridge decreases by only 1K, while the coolant flow decreases by 20%. KLSA also was not significantly affected by the flow reduction. Moreover, they observed KLSA was retarded from approximately 0.5 CA to 1 CA while the coolant temperature increased from 90°C to 100°C. They explained this variation cannot be considered a significant change.

Cho et al. [62] have observed the effect of coolant experimentally in a wider temperature range. With a steady-state experiment using a single-cylinder SI

engine, it was shown that by decreasing the coolant temperature, knock can be mitigated during operation effectively. Using a segregated cooling system for the cylinder head and the liner, and maintaining MBT (maximum brake torque) timing at every operating condition, the expansion of the maximum operable load was achieved. While maintaining the same load, it was shown that approximately 0.2 CA of ignition timing advance was achieved for every 1°C decrease of the coolant temperature. Furthermore, using the optical method and a PCB (printed circuit board) flame ionization gasket, location search of the knock occurrence spot was facilitated. As a result, under the operating conditions, the intake and exhaust side in the cylinder were found to be the main locations where auto-ignition occurs. It was also shown that coolant temperature variation does not have a significant influence on knock location.

Matsura et al. [63] proposed the knock mitigation method through enhancement of local heat transfer. It was identified the knock location with optical measurement, and it was concluded that auto ignition ignites frequently at between exhaust and front side in the combustion chamber. A path-guided piston was newly designed based on the result. It allowed higher flow velocity and turbulence intensity near knock onset position and timing. The heat transfer from the end gas to the wall was promoted, so the temperature of the end gas could be decreased, resulted in knock mitigation. This enhancement enabled 2.2 CA advance of combustion phasing, and load was increased by 17.2 kPa and the efficiency was also increased by 0.7%, However, slight increase of carbon monoxide emission mainly thought to be the lower temperature of the end gas was observed.

Inoue et al. [95, 96] and Morioka et al. [96] conducted extensive experimental studies on heat transfer effect in the intake port. Resin-coated intake port wall could decrease 6-10°C of air temperature in combustion chamber

compared to conventional aluminum surface. Based on the test result with 1.2 L 3-cylinder engine, heat insulation in the intake port granted 3.5kW higher power at high speed region and approximately 1% of fuel efficiency improvement in NEDC and JC08 driving cycle. However, the effect was not significant under cooled-EGR condition.

Uozumi et al. [97] studied the effect of in-cylinder surface roughness on the knock phenomena. They investigated the correlation between the surface roughness parameters and heat transfer coefficient and exploited the higher angle and height of surface roughness could lead to higher heat transfer, mainly thought to because of higher possibility of collision of air molecules. They concluded that reduced heat transfer by the improvement unevenness could result in reduction of unburned gas temperature which facilitated the ignition timing advance. In addition, the piston showed the biggest effect during the test compared to other components such as head, exhaust and intake valve.

## 1.3 Research Objectives

Knock mitigation is inevitably essential for development of future high efficiency engine. Decreasing unburned end-gas temperature is one of the key factors for further knock suppression, thus, wall temperature decrease have been studied.

However, quantification of knock level is not easy to be determined due to its stochastic behavior, and it has not been investigated that which component affects to knocking behavior and how. For this, precise combustion analysis is needed. Furthermore, knock prediction model is necessary for future engine control which will utilize auto-ignition phenomena for higher efficiency. Therefore, the objectives of this study are:

- 1) Refined experimental methodology for knocking combustion  
: Experimental method and quantification of knock test result will be achieved.
- 2) Approach for individual cycle analysis  
: Precise cycle analysis of knocking condition will be available.
- 3) Investigations on relationships between coolant temperature and engine walls, and knock behavior  
: Strategic cooling strategy for knock mitigation will be proposed.
- 4) Development of knock prediction model  
: A robust model for cycle-by-cycle knock prediction will be established and verified under different thermal boundary conditions.

## **Chapter 2. Analysis and Modeling of Knock**

### **2.1 Knock Metric**

#### **2.1.1 Detection of knock occurrence**

As previously described, during the engine operation, it is the most accurate way to use in-cylinder pressure sensor for characterization of knocking combustion. However, the test environment is critical for the precise measurement of in-cylinder pressure sensor. Highly filtered signal for reducing noise may cause distortion of original signal such as phase shift, resulting in a large error during the analysis. For a proper usage of pressure signal, it is advisable to observe the following. However, there's no certain answer for noise reduction.

- 1) Assured earth grounding for all equipment is needed.
- 2) Qualitative wire with ground is recommended.
- 3) The sensor should be located farther away from high-voltage, high-current components such as ignition coil or injector. Sensor wire also should be isolated from the components.
- 4) Use stable power sources such as linear power for equipment. Especially SMPS (switching mode power supply) is not recommended: switching frequency causes the signal noise and superposition.
- 5) Installation of reactor is recommended if there is a high capacity motor or pump. Noise can be generated from phase shifting from the inverter depending on the method of grounding and setup. Active harmonic filter is also recommended but cost-consuming.

In this study, the method with an in-cylinder pressure sensor was adapted. This is the most accurate and direct method among the various methods to detect knocking behavior. However, this type of measurement highly depends on the mounting position of the in-cylinder pressure sensor [49, 50] as it is described in Chapter 1. Therefore, the sensor was mounted flush and bias-positioned to one side of the cylinder head. This has already been shown as the most proper way to observe the in-cylinder pressure oscillation in previous studies.

The first six pressure oscillation modes of the used engine in this study are shown in figure 2.1 and table 2.1 under a cylinder bore radius equal to 81 mm, assuming that there is no axial mode., and the gas temperature is 2500 K, the polytropic coefficient is 1.4 and the sound speed was calculated with equation 1.9.

Figure 2.2 shows the FFT (Fast Fourier Transform) result and PSD (power density spectral density). 3kHz high-pass filter was used to eliminate the frequency of normal combustion, and 30 cycles which have the highest MAPO intensity were used for calculation and ensemble averaged. The first mode shows the highest value in FFT and PSD. From this result, it was concluded that signal processing regarding more than first three or four modes can represent the knock intensity of knocking cycle.

Knock detection with heat release calculation is not sensitive for especially weak knock detection and must rely on post-processing. This paper focuses on the thermal boundary condition, which obviously has a strong relationship with auto-ignition and knock. Thus, lots of time for the experiment was required to achieve the steady state condition, especially for the temperature, and this can cause engine failure under knocking combustion. Thus, every operating point was under weak knock condition, i.e., the method to detect the knock occurrence had to be sufficiently sensitive to perform the correct statistics.

For the calculation of pressure oscillation frequency and frequency analysis, a 4~28 kHz 5th order Butterworth band-pass filter was chosen for the test in this study to cover the first six modes of oscillation frequency. Instead of calculation of heat release rate, the MAPO TVE method was used – a cycle was determined as a knocking cycle if the maximum amplitude of the filtered pressure signal exceeded the 0.5 bar of threshold. The 0.5 bar threshold of MAPO TVE can detect the knock at a lower intensity than a normal acoustic knock. (Brunt et al. [49] determined the acoustic knock for a knock intensity greater than two in equation 1.10) This sensitive MAPO method still requires a high signal-to-noise ratio but can secure the engine durability during operation and results in more precise steady-state data.

To analyze the knock phenomena precisely, a high sampling rate is required to be able to measure the pressure oscillations. Therefore, an encoder with 0.1 CA resolution was used. This was already shown to be sufficient for proper measurement [98, 99]. Combustion data was logged with an AVL Indi-module device.

Knock phenomena accompany cyclic variations and exhibit stochastic behavior [41]. For example, even if the same ignition timing is maintained, due to the variation of in-cylinder conditions, there is a considerable cyclic variation on the occurrence timing (knock onset), frequency and intensity. For that reason, results of knock research are frequently shown with PDF (power density function) or other probabilistic terms. Accordingly, it is important to decide how to measure and analyze the knocking phenomena precisely. Therefore, for the calculations related to knock measurement, 1,000 consecutive cycle data were used to satisfy quantitative requirement. For combustion metrics, such as calculation for IMEP (indicated mean effective pressure) and MFB50 (mass fraction burned 50%), 300

cycle data were used. This number of cycle data is necessary for proper combustion analysis [49, 99].

However, band-pass filtering, which is the most widely used, induces phase-shifting problem during signal conditioning of in-cylinder pressure as shown in figure 2.3. Therefore, this method is only suitable for detection of knock occurrence such as MAPO method and it is highly recommended to use different type of filters for additional post-processing. This will be described in Chapter. 2 where the signal handling techniques are interpreted.

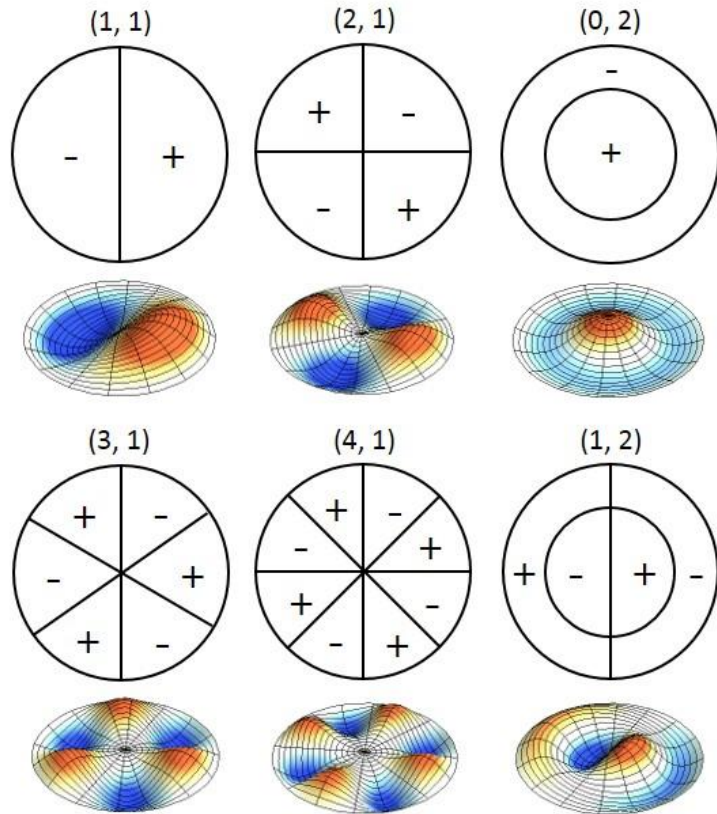


Figure 2.1 Oscillation modes of pressure wave (3D images from [100])

Table 2.1 Oscillation frequencies of pressure wave

$\lambda, m$	1, 1	2, 1	0, 2	3, 1	4, 1	1, 2
$\mu^*_{\lambda m}$	1.841	3.054	3.832	4.201	5.318	5.332
Frequency [kHz]	7.26	12.03	15.11	16.55	20.95	21.0

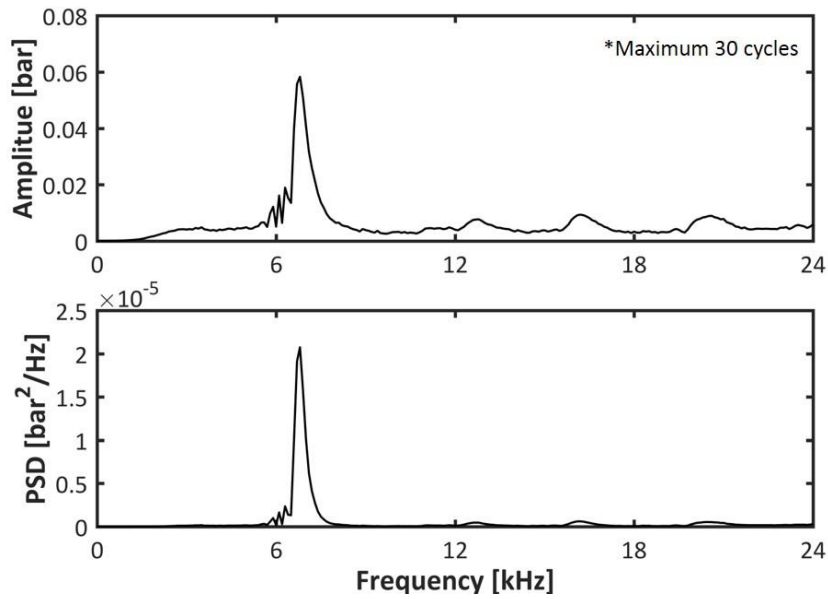


Figure 2.2 FFT and PSD analysis of knocking combustion

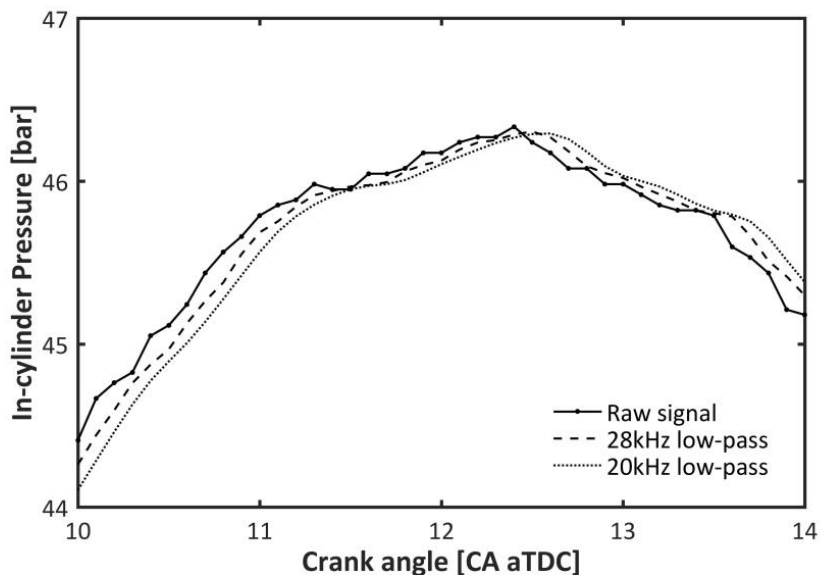


Figure 2.3 Phase shifting in low-pass filtered signal

### 2.1.2 Knock incidence

To quantify the level of knock occurrence under a certain steady state condition, a representative index value is needed such as mean knock intensity. Furthermore, simpler logic leads to reduction of time and cost for installing system for tester. Therefore, in this study, knock incidence method, shown in equation 2.1, was proposed and its validity was verified. This method can be easily adapted to any engine test facility with simple electronic circuit or computational code.

$$\textit{Knock Incidence} = \frac{N_{knock}}{N_{total}} \times 100 \quad [\%] \quad (2.1)$$

For calculation of knock incidence, one thousand cycle running average value was used ( $N_{total} = 1000$ ) in order to minimize the effect of stochastic behavior during the engine operation. From consecutive cycle data, it was observed that the standard deviation is less than unity while sometimes it's over than five if a hundred cycle data was used during steady-state operation.

Knock intensity calculation under weak knock condition has a large error due to its stochastic characteristics (not enough samples) if knocking cycles are calculated only. Thus, for ISPO knock intensity calculation, a thousand cycle overall value of the entire operating cycles was calculated as well. This was also proposed by previous studies for less error considering the stochastic behavior of knock [49, 71]. For example, Brunt et al. [98] showed that approximately 50% of error was possibly made if only 300 cycle data were used for the intensity calculation under weak knock conditions. A 40 CA calculation window ( $\Delta\theta$ ) was chosen, resulting in good performance.

$$Knock\ intensity = \frac{1}{1000} \sum_{i=N}^{N+1000} \int_{TDC}^{TDC+40CA} P_{filt}^2 d\theta \quad [\text{bar}^2 \cdot \text{deg}] \quad (2.2)$$

As previously mentioned, for validity of ISPO method, a correlation between ISPO method and other methods are thoroughly investigated and organized by Borg and Alkidas [66], which showed larger than 0.9 of correlation coefficient with other indices under various conditions.

The correlation between knock incidence and all-cycle ISPO knock intensity is shown in figure 2.4. It has a substantial correlation ( $R^2=0.98$ ) with the conventionally calculated ISPO knock intensity value. Besides, it was found that two different engines used in this study all show good correlations.

From the validation result, it was concluded that the knock incidence method can represent the knocking behavior of engine operation. In this study, most of the test condition was maintained at 5% of knock incidence, which means 5% of total operating cycles were classified as knocking conditions. However, it varied depending on the implementation in this study (10% for oil-gallery cooling and 5% for effect verification of segregated cooling). Even though the target knock incidence value varied, the tendency of the results didn't change, and this will be discussed later in this study. From this method, observation under weak knock condition with steady-state condition is well achieved. However, due to the stochastic behaviour of knock, a thousand running-averaged value of the knock incidence was also varied. Thus, in this study, a tolerance was set as 0.5% for all operating condition. (target incidence  $\pm 0.5\%$ )

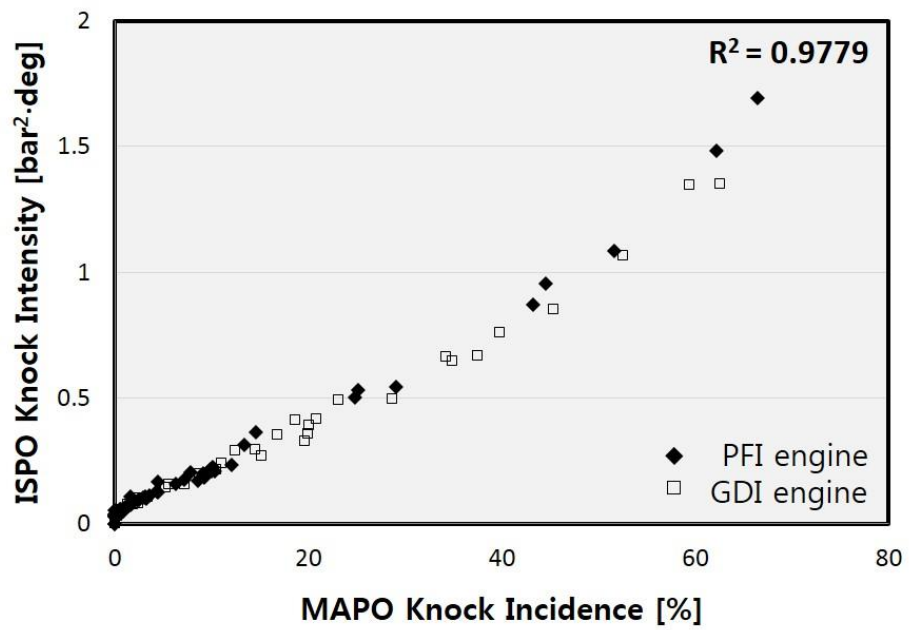


Figure 2.4 Comparison of MAPO knock incidence and ISPO knock intensity

### **2.1.3 Knock onset determination**

The determination of knock onset is a critical aspect of knock analysis because a small error in knock onset can lead to a misunderstanding of combustion [32]. For example, as shown in figure 2.5, approximately 3 CA late determination of knock onset can result in an error of 3 bar for in-cylinder pressure.

Many researchers have normally used high-pass (band-pass) filters for signal processing. There are a few ways to filter the signal; usually, Butterworth or median filtering methods are commonly adapted as previously described. The former has the advantage of its characteristic for noise reduction but generates a bias after filtering so that the knock onset is determined incorrectly [32].

As it is described in previous section, Butterworth band-pass filtering and MAPO TVE method was adapted to detect the knock occurrence in this study. However, for more sophisticated analysis for knock onset determination, to prevent the aforementioned bias after band-pass filtering, a 9-point (corresponding to 0.9 CA) median filter with Savitzky-Golay [101] smooth-filtering was adapted.

Kim's modified TVE method finds the knock onset with a high accuracy, but the logic is not appropriate for weak knock condition because this logic was validated under heavy knock condition, where the value of MAPO was over two. Shahlari method, described in section 1.2.2.4, showed the most advanced logic, but also not appropriate for weak knock condition and data of normal test condition which uses a rotary encoder.

Therefore, in this study, based on Shahlari's method, a new method of 0.1 CA rotary encoder resolution based under weak knock condition was developed.

For the filtering to avoid the bias, based on Kim's filtering method, 9 data points were initially averaged (median filtering) from the raw in-cylinder pressure signal and trimmed using a Savitzky-Golay smoothing filter (2<sup>nd</sup> order, 7 frame-length). Then, a filtered signal was obtained by subtracting the trimmed signal from the original signal. This logic can be used under various test condition and can be easily adapted. The logic is as the follows:

1. Modified TVE method based on Kim's method [32] is used for first finding.
  - 1) Filter the pressure: 9 points median filter with Savitzky-Golay smoothing filter are used. Filtered signal is obtained by subtracting smoothed signal from original signal.
  - 2) Find the peak values (local maxima) and indexes of absolute filtered signal from 15 CA after the ignition to 90 CA aTDC.
  - 3) Calculate the standard deviation (SD:  $\sigma$ ) of peak values from 11th value with ten-point values corresponding to 1 CA. Until 10th value, SD is fixed to zero to avoid the large deviation during calculation.
  - 4) Timing (CA) at which SD exceeds SD Threshold is found. SD Threshold is set by 0.03.
    - 4-1) if no timing was found, multiply 0.9 to SD Threshold.
    - 4-2) Repeat until index is found.
  - 5) From before 10 CA to 5 CA of the timing found in 4), mean value ( $\mu$ ) and standard deviation ( $\sigma$ ) of the filtered signal is calculated.

In weak knock condition, dip is not easily found by band-pass filtered signal on account of comparatively large deviation. Thus, the calculation window for  $\mu$  and  $\sigma$  has to be more advanced than Kim's method.

6) from 2 CA before the timing in 4), a timing is found at which filtered pressure exceeds  $\mu + 5\sigma$ .

6-1) If the timing is not found, threshold is adjusted to  $\mu + 3\sigma$ .

6-2) If the timing is still not found, threshold is adjusted to  $\mu + 2\sigma$ .

2. Modified fitting method is applied. The method is basically Shahlari's method [48], and it's slightly modified to crank angle domain.

1) Guess initial knock onset. Timing from 1-6) is used.

2) 2.5 CA before to 0.5 CA before the timing 1) is set as fitting window.

3) Raw pressure signal is fit with 2nd order polynomial fitting giving the weighting factor linearly heavier as timing goes to window end.

In weak knock and part-load condition, linear fitting by Shahlari is not appropriate to capture the separation point. For that reason, polynomial fitting is introduced.

4) From timing of 1), timing is found given all the following are met.

4-1)  $0.1 \text{ bar} < P_{raw}(n) - P_{poly}(n) < 1 \text{ bar}$  : A timing at which the pressure starts to rise, being separated from polynomial fit curve.

4-2)  $P_{raw}(n + 1) - P_{poly}(n + 1) > 0$ : Still separated at next timing.

4-3)  $P_{raw}(n + 1) - P_{raw}(n) > 0$ : Still pressure increasing at next timing

5) If the conditions in the previous step are not satisfied at any points in the projected line, the knock onset is set 0.3 CA earlier than that in step 1).

6) The finding from steps 4) and 5) are used as new guesses for the next iteration of this procedure.

7) These steps (1-6) are repeated 5 times.

- 8) For any cycle that entered step 5) five times, i.e. the finding was cumulatively moved 1.5 CA earlier, the finding is set 10 CA after the initial knock onset guess.
- 9) Steps 1 through 6 are repeated 5 more times.
- 10) If it is not found, use the timing from initial guess, 1-6) is used.

From figures 2.6-9, the results of knock onset determination of this study are shown. Various conditions were tested; however, two conditions are shown in the figures including variations of air-fuel ratio, load, ignition timing and engine speed. Determined knock onsets were indicated with black arrows and proper results were obtained with the modified logic with stochastic knocking cycles.

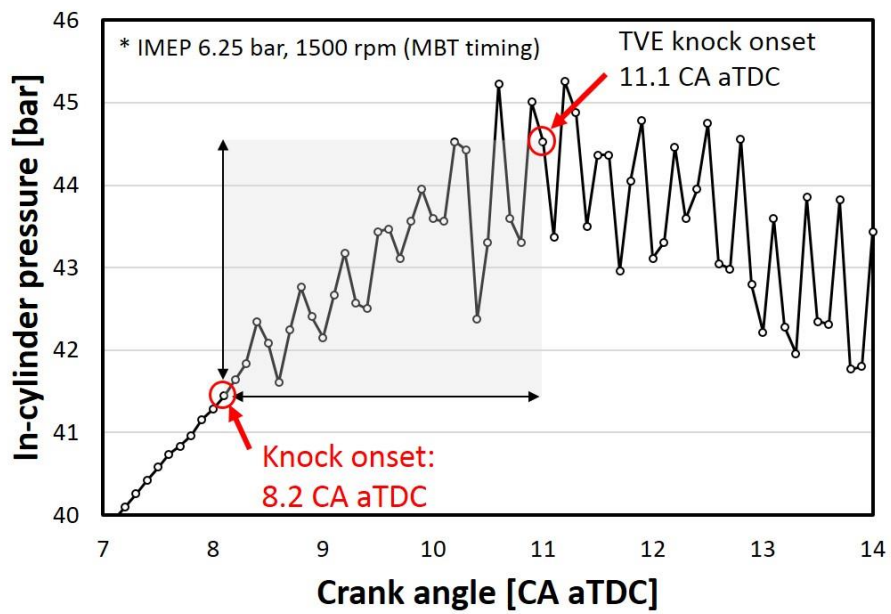


Figure 2.5 An example of incorrect knock onset determination

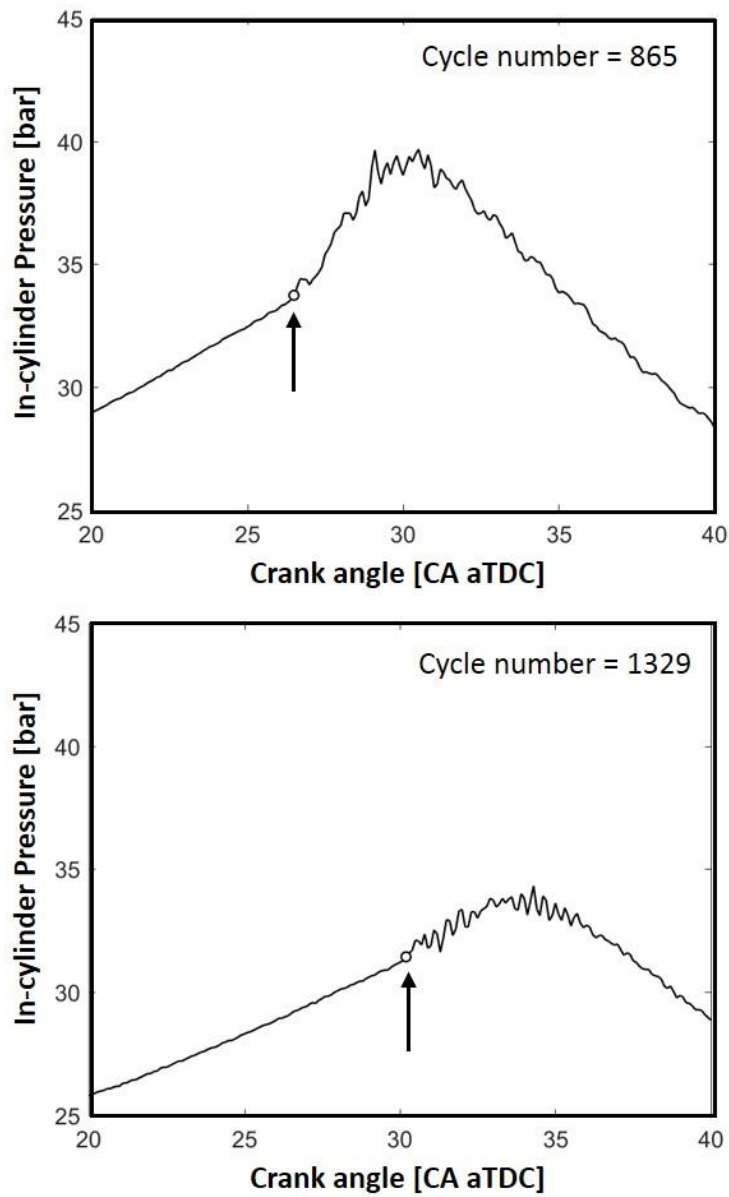


Figure 2.6 Improved knock onset determination at 1500 rpm, WOT, ign=2.5  
CA bTDC,  $\lambda=1$ , cycle number 865, 1329

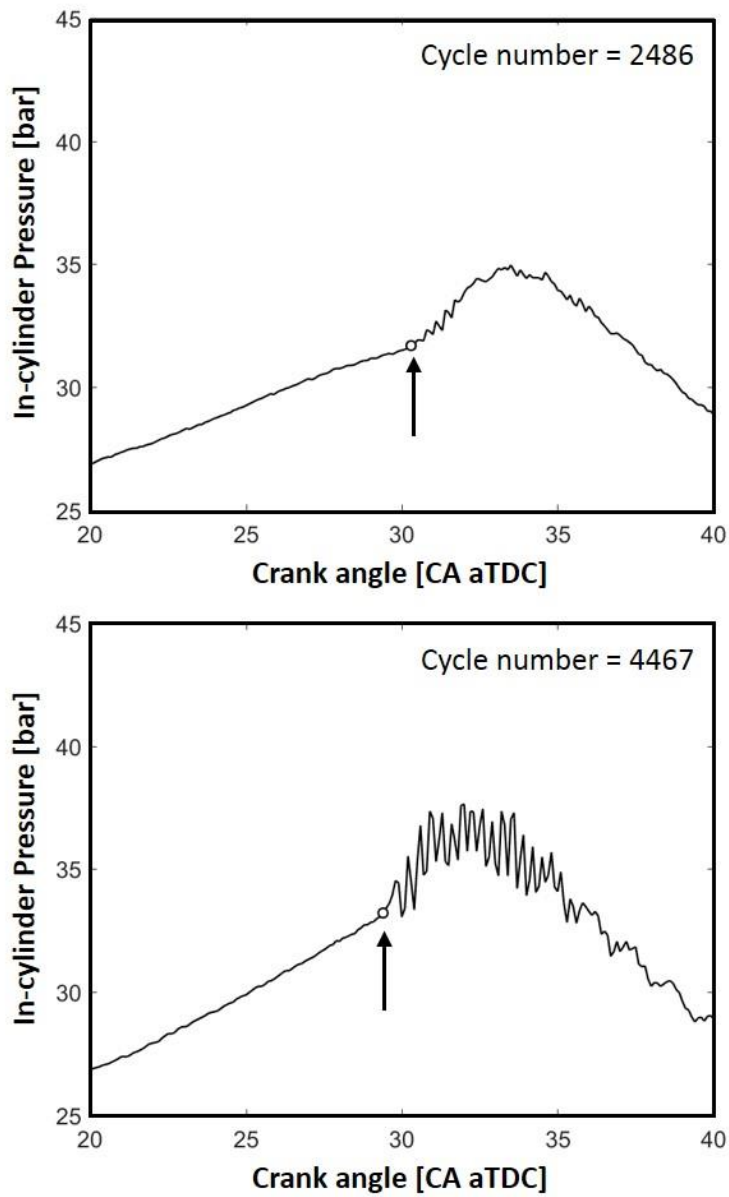


Figure 2.7 Improved knock onset determination at 1500 rpm, WOT, ign=2.5  
CA bTDC,  $\lambda=1$ , cycle number 2486, 4467

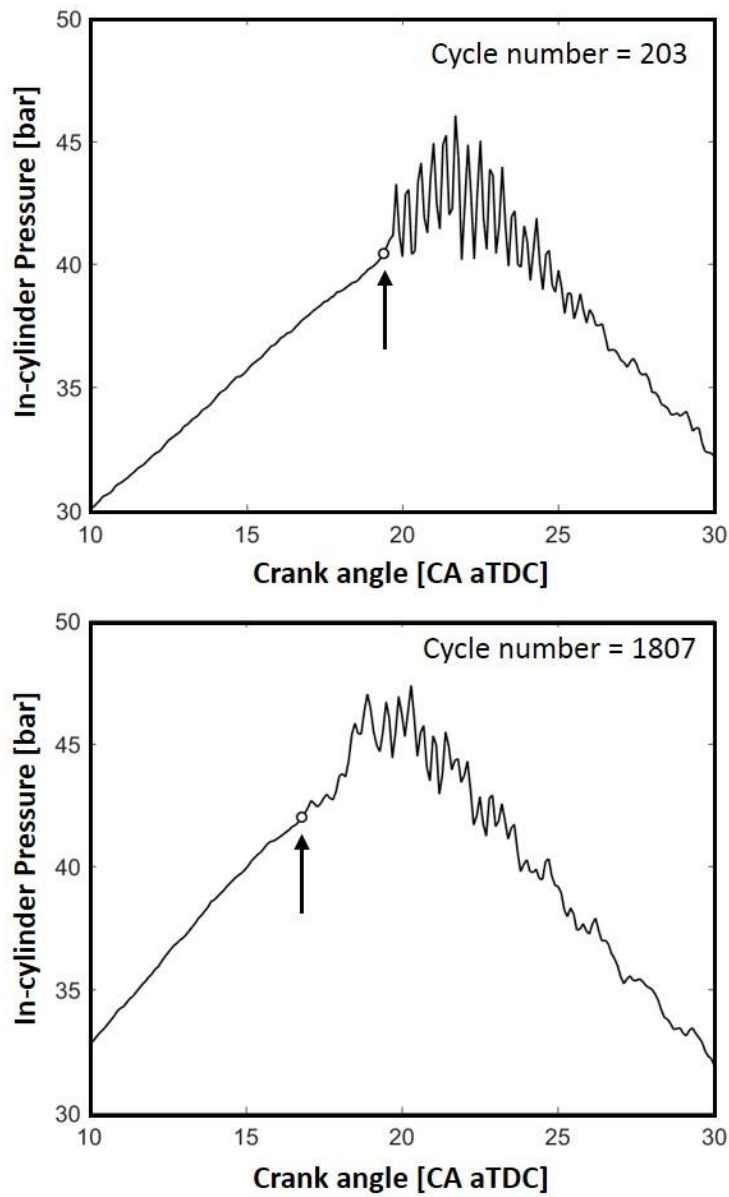


Figure 2.8 Improved knock onset determination at 1750 rpm, IMEP 7.69 bar,  $\text{ign}=12.5$  CA bTDC,  $\lambda=1.1$ , cycle number 203, 1807

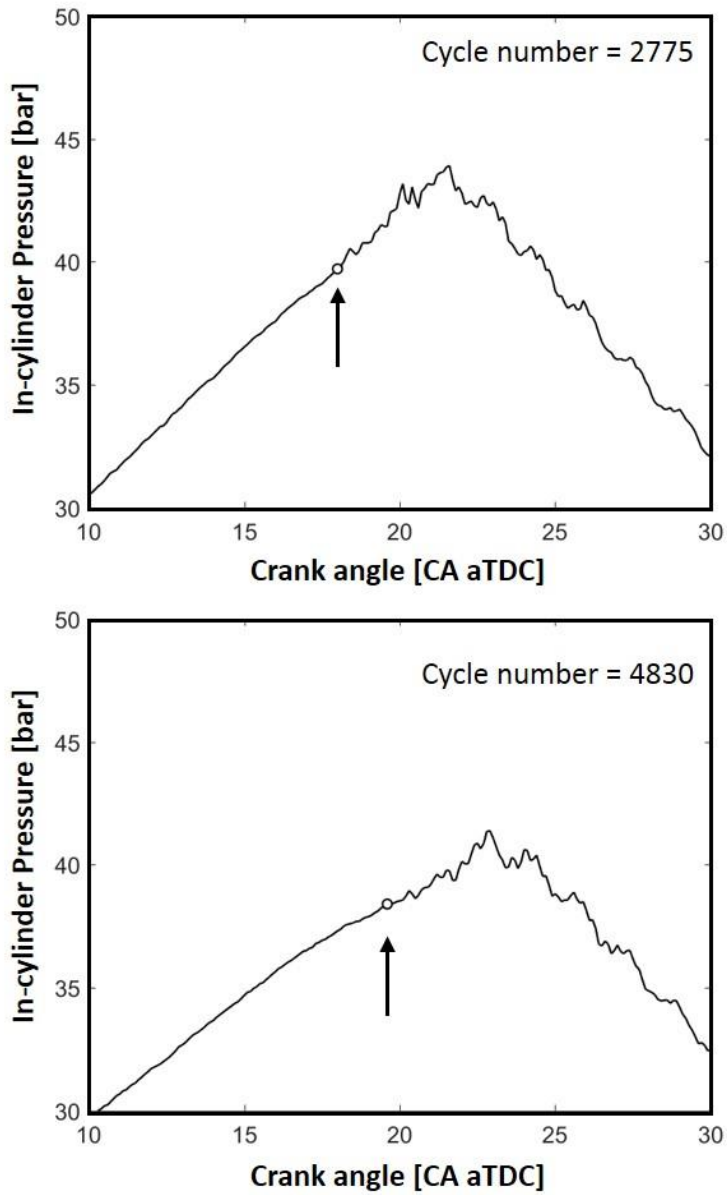


Figure 2.9 Improved knock onset determination at 1750 rpm, IMEP 7.69 bar, ign=12.5 CA bTDC,  $\lambda=1.1$ , cycle number 2775, 4830

## 2.2 Individual Cycle Analysis

### 2.2.1 Heat release calculation

Heat release analysis is very important to analyze the combustion phenomena. Especially parameters or indexes such as burn duration or CA50 (crank angle at mass fraction burned 50%) are very widely used for definition of the combustion state. However, in knocking cycles, it is not easy to analyze the in-cylinder pressure trace due to the pressure oscillation after knock onset.

Figure 2.10 shows the mass fraction burned (MFB) calculation result of a knock cycle. Simple calculation without consideration of heat transfer was applied, and the polytropic coefficient was set to 1.32. As it is shown, with simply normalizing with the maximum accumulated heat release value, it is hard to recognize the combustion indexes such as EOC (end of combustion) and CA90 especially after knock onset.

Also, because knock has stochastic behavior, in steady state operation, there are not only cycles with knock occurrence but also cycles without knock occurrence. Furthermore, even though it is knock occurring cycle, the timing and in-cylinder condition is all different as it is demonstrated in previous section. Hence, it is important to analyze the cycle individually. However, there is an issue of determination on end of combustion for individual cycle to calculate the MFB.

Mass fraction burned means amount of fuel burned throughout the combustion process and indicated within the value from zero to one. Mass fraction burned  $x_b$  is shown in equation 2.3, where  $n_c$  is combustion efficiency,  $m_{fuel}$  is fuel input mass,  $Q_{LHV}$  is low heating value of fuel and  $t_{ign}$  is ignition timing.

$$x_b = \frac{1}{n_c m_f Q_{LHV}} \int_{t_{ign}}^t (dQ_n + dQ_{ht}) \quad (2.3)$$

This value is important because this leads to calculations of other combustion indexes such as CA. CA value is widely used in spark-ignited engine field. CA10 and CA90 indicate the crank angle timings of 10% mass fraction burned and 90% mass fraction burned, respectively.  $Q_n$  and  $Q_{ht}$  are net heat release and heat transfer to the wall, respectively, and net heat release rate is written as equation 2.4.

$$dQ_n = \frac{\gamma}{\gamma-1} PdV + \frac{1}{\gamma-1} VdP \quad (2.4)$$

For precise calculation of individual mass fraction burned by processing in-cylinder pressure, the follows should be determined or calculated: 1) Specific heat value, 2) Combustion efficiency, 3) End of combustion, 4) Heat transfer.

### 2.2.1.1 Calculation of specific heat value

For calculation of specific heat ratio ( $\gamma$ ), various methods have been proposed. In this study, big combustion data such as 3,000 to 10,000 cycles were analyzed. For the calculation speed, single-zone model method was introduced for heat release calculation which is the most critical factor.

Gatowski et al. [102] developed a single-zone heat release model based on the first law of thermodynamics and proposed the specific heat as a linear function of mean in-cylinder temperature. Chun et al. [103] proposed the correlated single-zone specific heat value by analyzing different specific heat values for burned and unburned area using mixture theory. By calculation of uniform cylinder

temperature with two-zone analysis, single-zone based correlation value was obtained. Brunt et al. [104] also developed temperature dependent specific heat ratio model by fitting the curve using single-zone temperature.

$$\gamma_{Gatowski} = 1.392 - 8.13 * 10^{-5}T \quad (2.5)$$

$$\gamma_{Brunt} = 1.338 - 6 * 10^{-5}T + 1 * 10^{-8}T^2 \quad (2.6)$$

Ghandhi [105], in a recent study, developed a single-zone model based gamma for heat release calculation regarding the air-fuel ratio with a good correspondence based on Chun's constant gamma method. This method was used in this study for single-zone based calculation.

$$\gamma_{Ghandhi} = \max \left\{ \begin{array}{l} \gamma_0 + \gamma_1 T \\ \gamma_{ht} \end{array} \right\}, \text{ where } \left\{ \begin{array}{l} \gamma_0 = 1.426 - 0.0459\phi \\ \gamma_1 = 10^{-5}(1.02\phi^2 - 3.3\phi - 9.44) \\ \gamma_{ht} = 0.0386\phi^2 - 0.0838\phi + 1.33 \end{array} \right. \quad (2.7)$$

### 2.2.1.2 Combustion efficiency

Combustion efficiency was calculated by equation 2.8 in this study. By using the measured mass flow of the fuel and exhaust gas emission result, the calculation of combustion efficiency was conducted including the relative humidity.

$$\eta_c = \frac{m_f Q_{LHV} - \sum_{prod} Q_{LHV_i}}{m_f Q_{LHV}} \quad (2.8)$$

The fuel was assumed as iso-octane in the calculation of combustion efficiency ( $x=8$ ,  $y=18$ ), however, the low heating value (LHV) was used the

value of actual test result, 42.825 MJ/Kg. It was assumed there is no residual gas in reactants, and the valve timing of experiment was fixed to negative valve overlap in order to minimize the residual gas fraction.

### 2.2.1.3 End of combustion

Determination of EOC is important to calculate MFB and CA during combustion, as the AHRR (accumulated heat release rate) should be normalized by the value at EOC. However, it is not noticing in in-cylinder pressure trace; therefore, methodologies for EOC determination have been proposed by previous studies.

Brunt et al. [106] tested various models for precise calculation of heat release rate and burn rate. Data of 150 cycles at minimum and 1.0 degree of resolution was proposed for adequate analysis. An algorithm for EOC determination was also proposed and it was concluded that EOC locates at the 10 CA after the crank angle at which  $PV^{1.15}$  reached the maximum value while analyzing the ensemble averaged cycle data as expressed in equation 2.9.

$$EOC_{Brunt} = CA \text{ at } PV^{1.15}_{max} + 10 \text{ CA} \quad (2.9)$$

Kim [32] investigated the EOC using thermodynamic engine model and experimental validation data under knocking condition. As described in equation 2.10, it was suggested that EOC locates at the 10 CA after the crank angle at which  $PV^1$  reaches to maximum. It was shown to be highly valid under ensemble averaged pressure data.

$$EOC_{Kim} = CA \text{ at } PV^1_{max} + 10 \text{ CA} \quad (2.10)$$

For EOC determination of individual cycle, Kim proposed a method fitting the model-generated pressure trace based on Wiebe function heat release to experimental data. The crank angle at which sum of squared errors between Wiebe curve-fitted heat release and the heat release curve normalized at the crank angle reached a minimum value. This method finds the EOC which makes the MFB curve to be similar with the Wiebe function the most; however, this assumption implies that the assumed heat transfer multiplier to normalize the AHRR at EOC in every individual cycle is different.

Therefore, in this study, regarding the EOC of ensemble averaged cycle, heat transfer multiplier value was calculated and adapted for all cycles. Woschni's correlation [107] was used in this study and it is shown in equation 2.11. Since recent engines have shorter combustion duration, EOC is getting faster, EOC of ensemble averaged cycle was determined by Kim's method, 10 CA after at which  $PV^1$  reaches to maximum. Figure 2.11 shows the understanding of the concept in an example of ensemble averaged cycle pressure data.

$$h_w = 3.26B^{-0.2}P^{-0.8}T^{-0.53} \left( C_1 \bar{S}_p + C_2 \frac{V_d T_{IVC}}{P_{IVC} V_{IVC}} (P - P_m) \right)^{0.8} \quad (2.11)$$

For analysis of in-cylinder pressures at valve timings such as IVC, EVC, EVO, in-cylinder pressure data should be trimmed due to the sensitivity problem of pressure transducer. As it is described in section 2.1.1, the pressure trace will be shifted if a simple band-pass filter is used. The shifting in low pressure region is more critical and this is one of the biggest reason to make error during the individual cycle analysis. Incorrect in-cylinder pressure at IVC leads to incorrect calculation for everything in OD based combustion analysis including specific heat, in-cylinder temperature, mass fraction burned, etc. In practice, for signal processing knock during the combustion, researchers recently use median type filters [41, 53]. Likewise, in this study, to eliminate the error of phase shifting and

sensitivity problem simultaneously, nine points median with additional 3<sup>rd</sup>-order was applied. However, for the processing of low pressure region, only median filtering insufficient, thus, 151 frame length Savitzky-Golay [101] filtering was additionally applied. Figure 2.12 shows an example and raw and filtered signals of individual cycle near IVC timing. The difference due to the sensitivity error reaches to approximate 10% of cylinder pressure measurement. This corresponds to 10% of IVC temperature difference in single-zone based calculation, leading to the larger error for unburned gas temperature estimation after compression stroke. Thus, a clean and reliable pressure values could be obtained with less measurement resolution-based error by new filtering method.

#### 2.2.1.4 Heat transfer

Heat transfer multiplier was calculated with the assumption of EOC of ensemble averaged cycle. In order to calculate net heat release ( $Q_n$ ) in equation 2.4 and motoring pressure in equation 2.11, Gandhi's correlation of specific heat ratio in equation 2.7 should be calculated. On top of that, in-cylinder temperature is necessary. Temperature at IVC was first calculated and in-cylinder temperature was calculated as equation 2.12 with assumption of single-zone and ideal gas law. Residual gas fraction of individual cycle was calculated with Yun's [32, 108, 109] method shown in equation 2.14, however, without knowing the specific heat ratio before the calculation, constant of 1.32 was applied. Molar mass of the residual gas was calculated using Cantera with the emission measurement data. Heat transfer multiplier ( $C_{ht}$ ), shown in equation 2.15 was calculated from ensemble averaged cycle analysis and was applied to all of the cycles for Woschni heat transfer as shown in equation 2.16.

$$T_{IVC} = \frac{P_{IVC}V_{IVC}}{(n_{fuel}+n_{air}+n_{residual})R} \quad (2.12)$$

$$T = T_{IVC} \frac{PV}{P_{IVC}V_{IVC}} \quad (2.13)$$

$$m_r = (m_a + m_f + m_{egr}) \frac{V_{EVC}}{V_{EVO}} \left( \frac{P_{EVC}}{P_{EVO}} \right)^{\frac{1}{\gamma}} \left( 1 - \frac{V_{EVC}}{V_{EVO}} \left( \frac{P_{EVC}}{P_{EVO}} \right)^{\frac{1}{\gamma}} \right)^{-1} \quad (2.14)$$

$$C_{ht} = 1 - \frac{\int_{IGN}^{EOC} dQ_n}{n_c m_f Q_{LHV}} \quad (2.15)$$

$$dQ_{ht} = C_{ht} h_w A (T - T_{wall}) dt \quad (2.16)$$

By applying the multiplier, EOC of individual cycle could be newly calculated to the crank angle at which  $x_b$  in equation 2.3 reached to unity. However, in a knocking cycle, due to the picky pressure trace and rapid heat release, determination parameters after knock onset (e.g. CA90) is not easy. Therefore, with the idea of Wiebe curve fitting by Kim [32], the mass burned fraction curve was fit in knock cycles from initial state (CA02) to knock onset using *lsqcurvefit* function in MATLAB (CA99 for non-knocking cycle). From fitting data, calculation of combustion parameters such as burn duration was possible.

$$Burn\ duration = CA90 - CA10 \quad (2.17)$$

Figure 2.13 shows the comparison of Wiebe-fit based MBF and calculated MBF from individual EOC determination by heat transfer estimation.

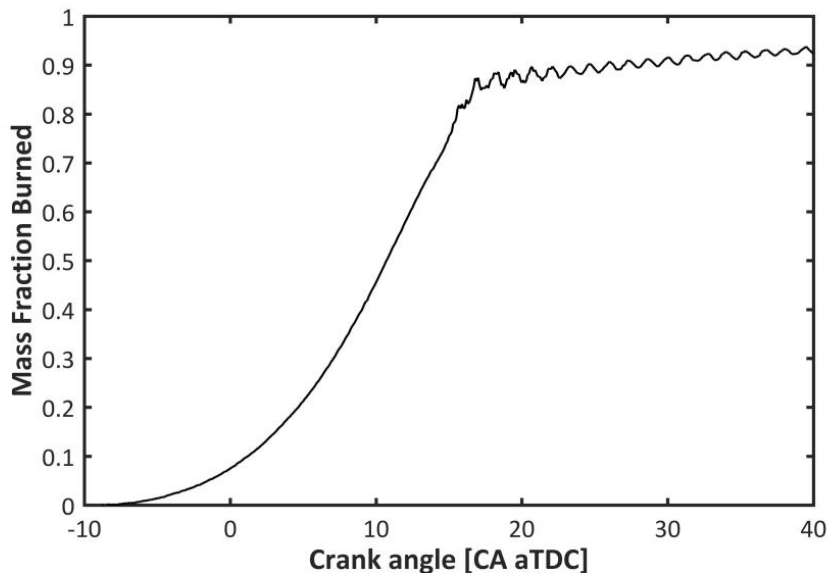


Figure 2.10 Mass fraction burned of individual knocking cycle

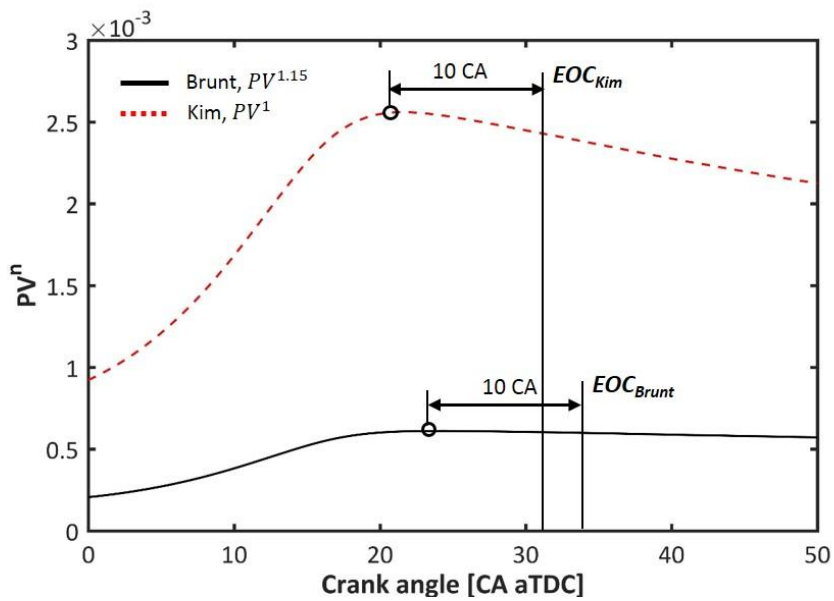


Figure 2.11 EOC determination methods

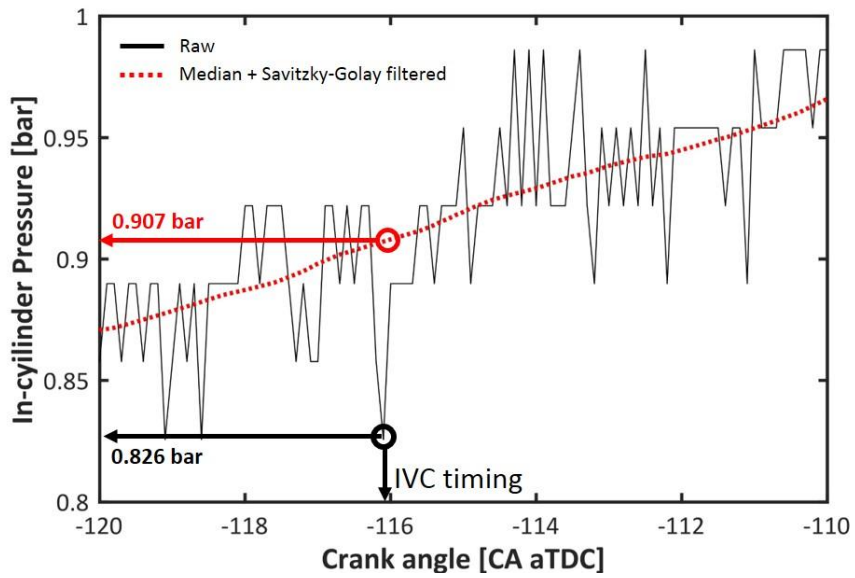


Figure 2.12 Filtering in-cylinder pressure signal in low pressure region

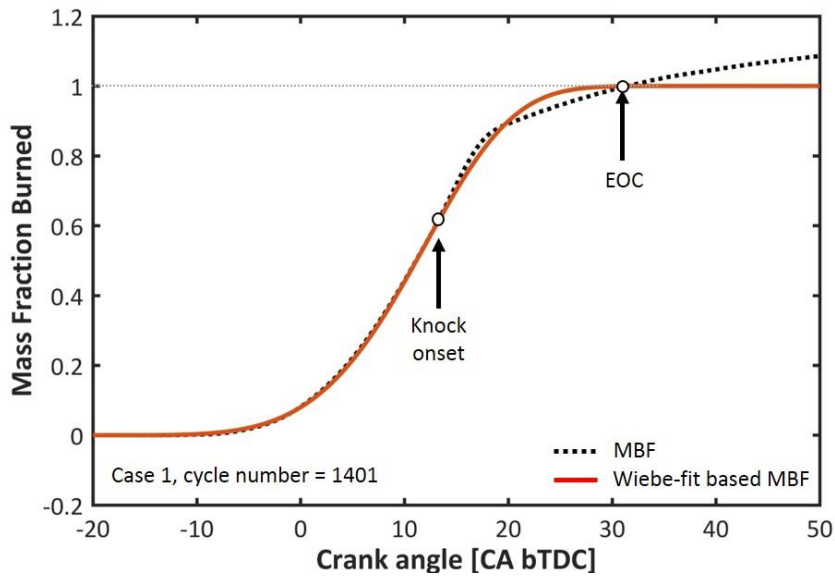


Figure 2.13 Mass fraction burned with Wiebe-fitting method in knocking cycle

### **2.2.2 Estimation of unburned gas temperature**

For further understanding of knock phenomena, the condition of unburned gas has to be investigated because knock is occurred in unburned end-gas region during combustion process. Several parameters are required: pressure, temperature, and mixture properties such as composition. Under test circumstances, pressure is easily obtained using in-cylinder pressure transducer and data acquisition system. In addition, since pressure wave travels by sonic speed, it can be assumed the pressure of unburned gas region is the same with the measured in-cylinder pressure.

However, it is not simple to measure the in-cylinder temperature due to the harsh condition. Flame temperatures are usually known as approximately 2500 K, and mean in-cylinder temperature is also high. It is possible to measure dynamic in-cylinder temperature with fast response thermocouples such as Gardon type [110] or co-axial thermocouples which have extremely low thermal capacity. However, it needs a modification of combustion chamber component to insert the thermocouples, and also has some issue that it measures the temperature of thermal boundary layer instead of auto-ignition exothermic center. Therefore, estimations with modeling are commonly used. In this section, OD analysis approach with experimental data will be interpreted.

During the combustion process, because the flame is initiated by the spark plug in spark ignited engine, gas mixture is divided into two zones: burned and unburned. While regarding the pressure is the same for both zones, temperature and mixture property are apparently different. Therefore, two-zone based approach is needed.

Conventional two-zone approach is that considering the crevice effect is extremely small, mass and energy conservation laws to both zones, perfect ideal gas law are applied.

$$dV_u + dV_b = dV \quad (2.18)$$

$$dm = dm_u + dm_b = 0 \quad (2.19)$$

$$\delta Q - PdV = dU \quad (2.20)$$

Neglecting high-order terms and substituting equation to another and assuming the composition of unburned gas has no change, equations for unburned zone is as the follows [111]:

$$V_u = (1 - x_b)m \frac{R_u T_u}{P} \quad (2.21)$$

$$-q_u A_u dt = (1 - x_b) \left( c_{p_u} dT_u - R_{s,u} T_u \frac{dP}{P} \right) \quad (2.22)$$

Equation 2.22 is the equation for unburned temperature calculation where  $T_u$  is the averaged unburned end-gas temperature,  $P$  is the pressure which can be considered known value by measurement,  $m$  is the total mass,  $R_{s,u}$  is specific ideal gas constant or unburned gas and  $q_u$  is the heat transfer rate of unburned gas to the wall. For calculation of heat transfer, as described in previous section 2.2.1.4, multiplier was applied with Woschni's correlation followed by the determination of EOC. It is shown in equation 2.16.

$$q_u = C_{ht} h_w (T - T_{wall}) \quad (2.23)$$

$$A_u = \left( 1 - x_b^{1/2} \right) A \quad (2.24)$$

$A_u$  is the surface area contact of unburned gas to cylinder walls, Ferguson approximation method [112] was used as expressed in 2.24 [112-114]. Equation 2.22 and 2.24 need the MFB ( $x_b$ ) for their calculations, and it was calculated with the sing-zone based method described in previous section. For reference, equation 2.29 also can be written in different form, equation 2.25 [32].

$$\frac{dT_u}{dt} = \left(\frac{\gamma-1}{\gamma}\right) \left(\frac{T_u}{P} \frac{dP}{dt} + \frac{q_u}{m_u R_u}\right) \quad (2.25)$$

Calculation was conducted from IVC to EVO. *ode45* function (Runge-Kutta method) in MATLAB was used and the tolerance was set as 1e-4. However, the specific heat value of unburned gas is unknown. MATLAB based Cantera 2.3.0 with PRF detailed mechanism of LLNL (Lawrence Livermore National Laboratory) was used for calculation of gas property at every state. Initial gas composition was defined as mixture of intake air and residual gas, proportion was calculated by equation 2.21 and emission measurement.

As it is previously discussed. band-pass filtering in-cylinder pressure provokes the phase-shifting, thus, median with Savitzky-Golay filtering was introduced for low pressure value region. In combustion process, because sensitivity problem of pressure transducer is relatively less. Therefore, Savitzky-Golay frame-length was adjusted to 71 for combustion period.

For precise calculation of specific heat value and temperature, iteration method was used. Initial unburned gas temperature was assumed the same with IVC temperature as written in equation 2.19. Single-zone based gamma from previous section was used for first iteration. Temperature and specific heat ratio by specific heat values were calculated and iteration stopped when RMSE (root mean square error) between  $n^{\text{th}}$  and  $n-1^{\text{th}}$  specific heat ratio values from IVC to

EVO was under  $1e-3$ . It was found that less than five iterations were usually enough.

$$T_{IVC} = T_{IVC,u} \quad (2.26)$$

By assuming the heat transfer occurs between thermal boundary layer and walls in unburned gas region, core gas of unburned mixture can be considered adiabatically compressed. Regarding the heat transfer is zero, the core gas temperature can be expressed as equation 2.27. Auto-ignition can be thought possibly occurs in the core gas where has the highest temperature in the unburned end gas, however, both of equations 2.22 and 2.27 are widely used for the calculation.

$$T = T_{IVC} \left( \frac{P}{P_{IVC}} \right)^{1-\frac{1}{\gamma}} \quad (2.27)$$

For calculation with precise specific heat ratio value in cycle analysis, equation 2.28 is used from initial calculation of  $T_{IVC}$  from equation 2.19.

$$T_{n+1} = T_n \left( \frac{P_{n+1}}{P_n} \right)^{1-\frac{1}{\gamma_n}} \quad (2.28)$$

Figure 2.14 shows the in-cylinder temperature by single-zone based method and figure 2.15 shows a result of two-zone based unburned gas temperature. It is clearly from the lower temperature if the heat transfer is included to calculation.

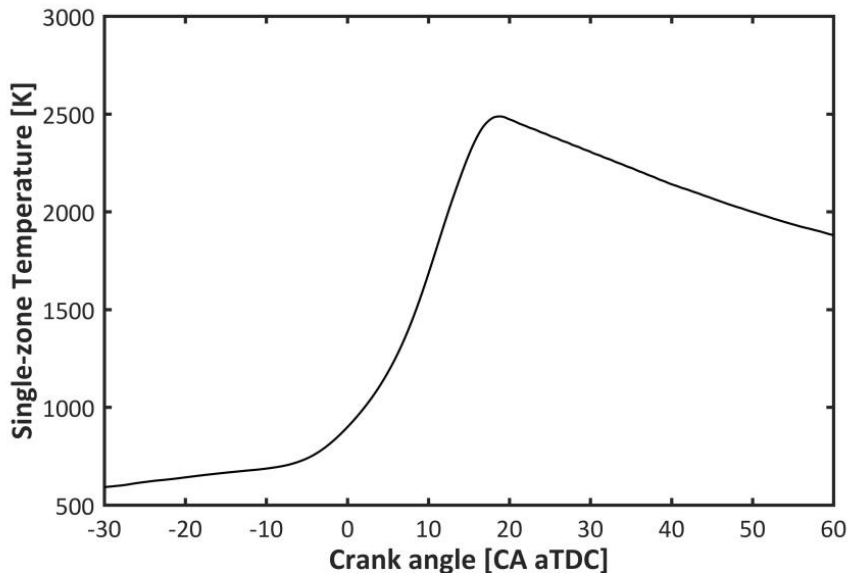


Figure 2.14 Single-zone based in-cylinder temperature

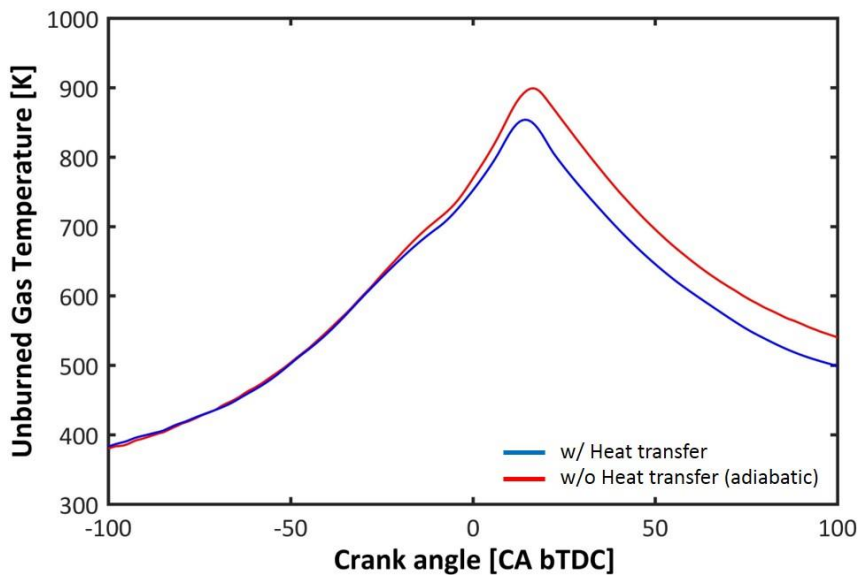


Figure 2.15 Two-zone based unburned gas temperature

### 2.2.3 0D Ignition delay model for fast prediction

The knock prediction model is based on auto-ignition delay theory that auto-ignition occurs when the fuel consumption is end. Thus, ignition delay can be approximated as equation 2.30, from the reverse form of gas reaction rate expressed in equation 2.29.

$$r = A[Fuel]^m [O_2]^n \exp\left(-\frac{E_a}{RT}\right) \quad (2.29)$$

$$\tau \sim [Fuel]^{-p} [O_2]^{-q} \exp\left(\frac{E_a}{RT}\right) \quad (2.30)$$

The molar concentrations can be substituted to pressure and temperature expressed as equation 2.31, and the molar fractions are expressed in equations 2.32 and 2.33, and they were approximated assuming the mole number of air is overwhelming. Thus, the ignition delay can be expressed as equation 2.34. This implies that the ignition delay is a function of air density, and the air-fuel ratio. Chen model [25] and McKenzie model [39] are also based on this concept.

$$[Fuel] = \frac{P}{RT} x_f, \quad [O_2] = \frac{P}{RT} x_{O_2} \quad (2.31)$$

$$x_f = \frac{n_f}{n_{fuel} + n_{air} + n_r + n_{egr}} \sim \frac{C}{\lambda} \quad (2.32)$$

$$x_{O_2} = \frac{n_a}{n_f + n_a + n_r + n_{egr}} \approx C \quad (2.33)$$

$$\tau = C_1 \left(\frac{P}{T}\right)^{-C_2} \lambda^{-C_3} \exp\left(\frac{C_4}{T}\right) \quad (2.34)$$

## **Chapter 3. Configuration for Test and Simulation**

### **3.1 Experimental configuration**

#### **3.1.1 Single cylinder gasoline engines**

Two types of 0.5 L single cylinder engines were used, and both engines were equipped with dual CVVT system which facilitates the 50 CA advance for intake cam shaft and 40 CA retardant for exhaust cam shaft from their standard parking timing, respectively. Both engines are shown in figure 3.1, and the detailed engine specifications are shown in table 3.1.

PFI (port fuel injection) engine is a naturally aspirated engine with DPI (double port fuel injection) system. GDI Engine is a LIVC (late intake valve closing) Atkinson cycled engine with side-mounted GDI injector, which has 280 degrees of intake valve duration and 240 degrees of exhaust valve duration, respectively. Most of the implementations in this study including CFD simulation was conducted using PFI engine, GDI engine was tested for verification and the effects under different bore-to-stroke ratio. PFI engine has compression ratio of 12, however, some of implementations were tested under 12.5. The valve profiles of two engines are shown in figure 3.1.

Since four different types of engines (including different bore-to-stroke ratio in GDI engine) were tested in this study, conditional similarity was necessary. Thus, to minimize the effect of different engine types (PFI: normal cam, GDI: LIVC cam), GDI engine was operated under the intake cam timing which makes the motoring peak pressure to the same as PFI engine's, while the exhaust cam

timing was fully advanced. This resulted in the effective compression ratio being the same.

### **3.1.2 Test facility and equipment**

190 kW ELIN AC dynamometer was used for the test. This dynamometer is a double-sided dynamometer, so two engines are connected at each side. By designing the intermediate shaft changer, if necessary, the shaft was swapped immediately to the other side and the dynamometer was operated reverse. Air, oil and coolant temperatures were controlled. An oil pump with inverter was used for oil pressure control and supply the oil into the engines. The temperature controllers for liner coolant and head coolant were used independently. The facility is shown in figure 3.2.

It is important to mount the in-cylinder pressure sensor properly to obtain a fine signal to analyze knocking combustion. The pressure sensor was mounted flush in the cylinder head to minimize the cavity resonance and obtain higher sensitivity for pressure oscillation measurement. A Kistler 6056A piezoelectric in-cylinder pressure sensor was used and was positioned biased from the centerline of the cylinder to measure pressure oscillation as much as possible.

The schematic diagram of the engine testing system is shown in figure 3.3. AVL IndiMicro IFEM amplifier was used to amplify the in-cylinder pressure signal, and intake manifold pressure was measured with a Kistler 4045A2 absolute pressure sensor and the signal was amplified by a Kistler 4603 piezo-resistive amplifier. Pressure pegging was conducted at  $BDC \pm 2CA$  during the intake process before combustion. To reduce the error caused by the TDC calibration

using an in-cylinder pressure sensor, TDC was calibrated at mid-speed range (2500 rpm) and introduced 0.3 CA of heat loss angle under 40°C coolant temperature condition. This method still can generate errors, especially while the engine is changed to different bore-to-stroke ratio; however, the compression ratio was held constant ( $\pm 0.1$ ), so it was assumed that the loss angle is the same in this study.

Horiba MEXA-110 $\lambda$  and ETAS ES631.1 were used to monitor the air-fuel ratio during operation to obtain the stoichiometric condition (also rich and lean conditions). A Horiba MEXA-7100DEGR exhaust gas analyzer was used not only to measure emissions but also to validate the air-fuel ratio. For engine control, CVVT modules and the throttles were controlled by an ECU (engine control unit) with ETAS INCA 7.0 software. However, due to not only the shortage of resolution for ignition timing control and its uncertainty but also for control and further data acquisition for pressure signal and temperatures, National Instrument cRIO-9039 platform and a few modules were used with developed code using LabVIEW software (Modules: NI-9758: DRIVEN based injection and PWM control, NI-9401: sync, ignition control, NI-9222: pressure signals, NI-9214: temperatures). National instrument PXI-8119 platform and PXI-7342R FPGA board were used for measurement of amplified flame signal from PCB ion probe gasket with 0.1 CA resolution.

To obtain accurate fuel flow measurements using OVAL CA001, frequency output of the pulse signal was used instead of analog output to minimize signal loss and three-minute ensemble averaged value was used for calculation. This can achieve higher signal-to-noise ratios ( $S/N \sim n^{0.5}$ , n: number of repetitions [115]). Consequently, the error, except for the steady-state error of fuel flow measurement, was less than 0.3% in all operating conditions. The fuel used in this study is the conventional gasoline fuel of Korea, which has 42.825 MJ/kg of low heating value

(ASTM D 240-14) and 91.5 or research octane number (ASTM D 2699). The detailed specification and test methods of the fuel is shown in table 3.2.

In this study, to verify the individual effect, the coolant passages were segregated to each other, as shown in figure 3.4. Furthermore, the oil-cooling gallery piston, shown in figure 3.5, was introduced, thus cooling piston surface temperature was facilitated.

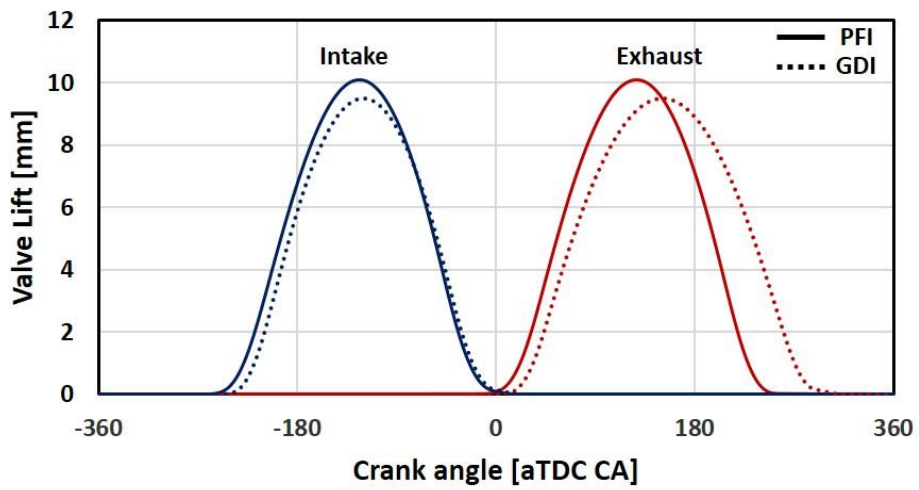


Figure 3.1 Valve profiles at standard valve timing: PFI and GDI

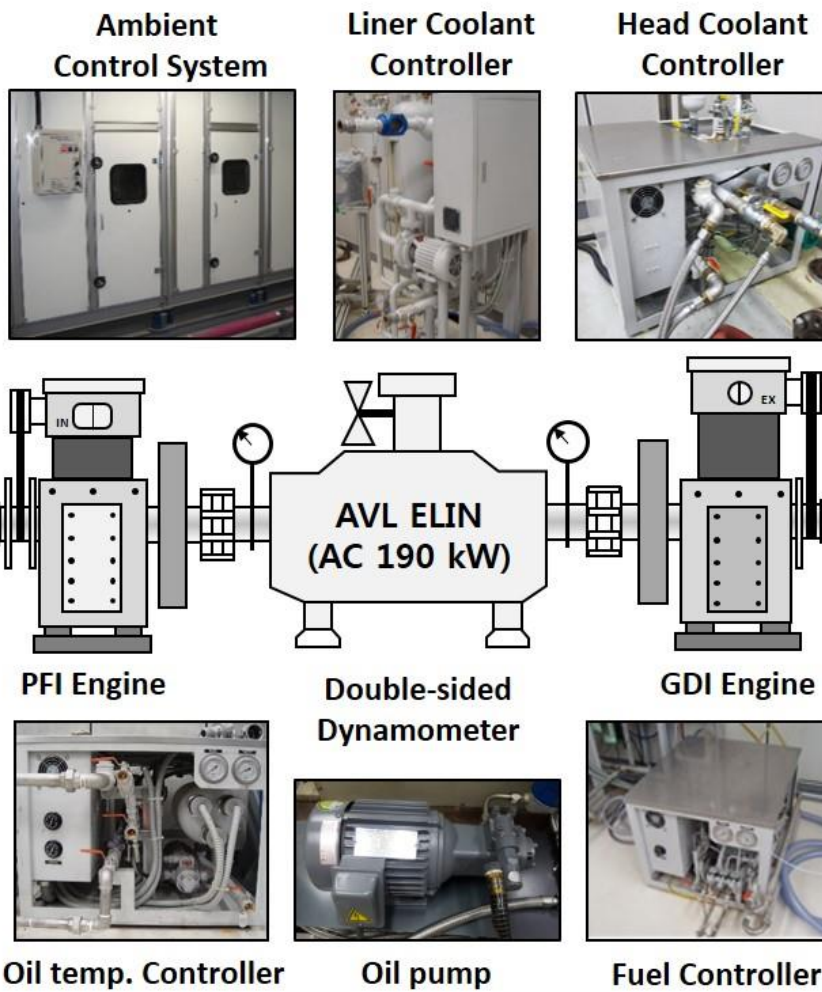


Figure 3.2 Engine test facility

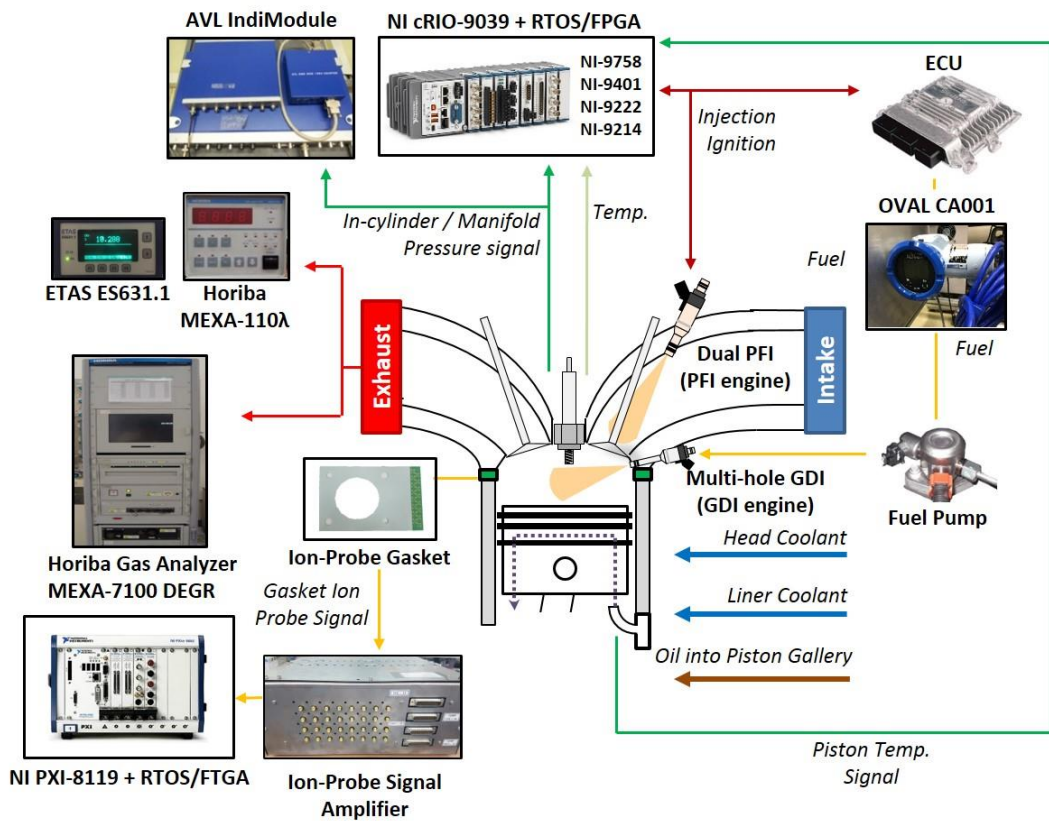


Figure 3.3 Schematic diagram of experimental system

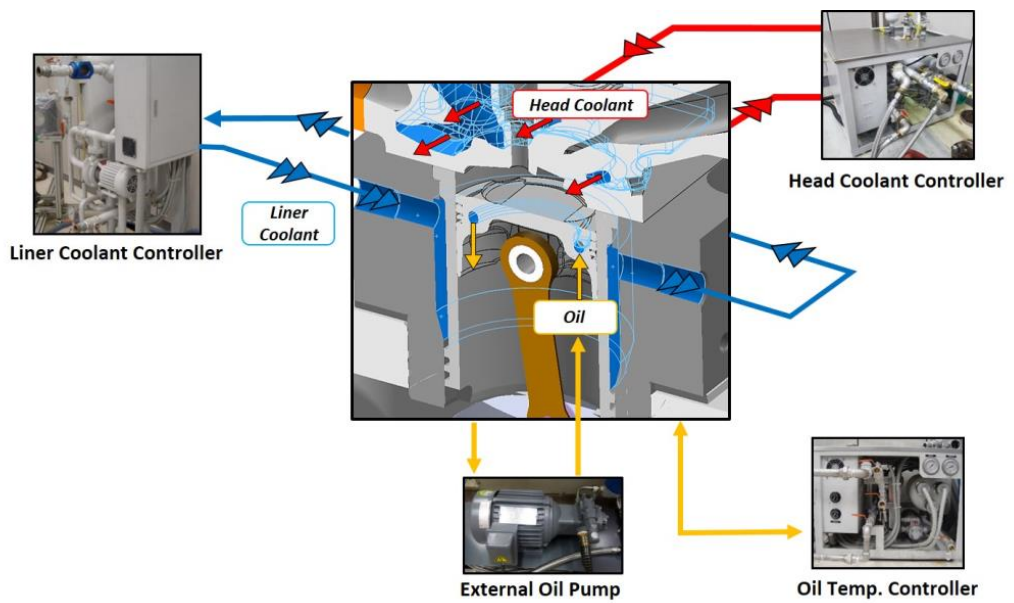


Figure 3.4 Design of segregated cooling passages

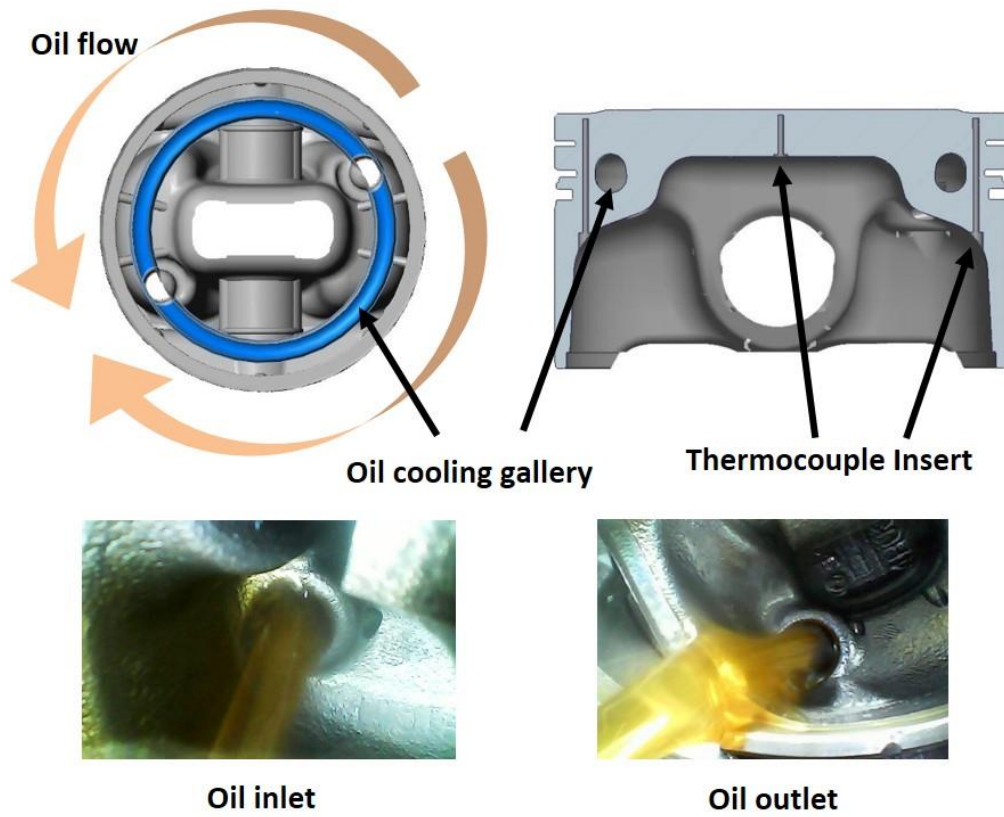


Figure 3.5 Oil-cooling gallery piston

Table 3.1 Engine specifications

Engine		PFI	GDI		
Type of engine		Single-cylinder N/A dual CVVT	Single-cylinder Atkinson-cycled dual CVVT		
Displacement [cc]		499.8	499.6	499.8	498
Stroke [mm]		97	86	97	111
Bore [mm]		81	86	81	75.6
Bore-to-stroke ratio		0.84	1.0	0.84	0.68
CR <sub>design</sub>		12 / 12.5	12		
CR <sub>actual</sub>		11.89 / 12.5	11.95	12.05	11.90
Injection system		Dual PFI (3.5 bar)	Multi-hole GDI (100 bar)		
Injection timing		540 CA bTDC	330 CA bTDC		
Valve Timing (@ 0.1 mm)	EVO	68 CA bBDC	59 CA bBDC		
	EVC	1 CA aTDC	1 CA aTDC		
	IVO	10 CA aTDC	34.5 CA bTDC		
	IVC	67CA aBDC	65.5° CA aBDC		
Number of valves		4			
Maximum valve lift		10 mm	9.5 mm		

### 3.1.3 Experimental conditions

Experiments were conducted in two parts in this study. First, investigation of wall temperature effect on engine knock was performed. Conditions are summarized in table 3.3. In practice, the cooling water temperature has been tested from 85°C to 40°C, but excessive cooling in 40°C condition, coolant temperature may decrease the brake thermal efficiency since it requires more accessory work in actual engine operation. Therefore, this study mainly focused on the conditions until down to 60°C condition. In addition, to maintain a uniform thermal boundary temperature, coolant flow was maximized in normal conditions. Consequently, the coolant temperature discrepancy between the inlet and outlet was less than 2°C for all operating conditions. The piston surface temperature was controlled by the oil flow injected from the oil-jet, and it was tried controlling the oil temperature to cool down more excessively with 20°C-oil but heat transfer was occurred in the oil passage before the injection. Thus, there was no significant difference of excessive cooling of oil injection to oil-cooling gallery of the piston.

Second, the experiments for knock prediction modeling was conducted. The test was performed mainly at 1500, 1750 and 2000 rpm, and the intake pressure of 0.9, 1.0 (WOT), and 1.1 bar. 0.9 and WOT conditions were selected due to the most knock-prone condition during the N/A engine operation, and 1.1 bar was selected for verification of validity under boosted condition. The boosted air was induced using a belt-driven auxiliary supercharger with an inverter-controlled motor. The experimental condition for knock prediction modeling is summarized in table 3.4. Ignition timing was adjusted depending on the condition to generate the knock behavior. Because it was conducted under steady-state condition, knock incidence was not extremely high to prevent the engine failure problem. However, it was approximately from 15 to 50% depending on the operating condition. To

validate the model reliability under different thermal boundary condition, coolant temperatures of the head and liner were changed in WOT condition from 85°C to 60°C.

Table 3.2 Fuel specifications

Conventional gasoline	Value	Test Method
H/C ratio	2.064	ASTM D 5291
Density [kg/m <sup>3</sup> ] @ 15°C	724.5	ASTM D 1298
Research Octane Number	91.5	ASTM D 2699
LHV [MJ/kg]	42.825	ASTM D 240-14
Oxygen [% in mass]	1.53	ASTM D 4815
Methanol [% in mass]	< 0.05	ASTM D 4815

Table 3.3 Experimental conditions for cylinder wall temperature effect

Engine speed [rpm]		1500, 2000
Air-fuel ratio		Stoichiometric ( $\lambda = 1$ )
Coolant Temperature	Head [°C]	85 ~ 40
	Liner [°C]	85 ~ 40
Piston oil-jet		On / Off
Oil temperature [°C]		75 ± 1
Ambient temperature [°C]		30 ± 0.5
Fuel inlet temperature [°C]		35 ± 2

Table 3.4 Test conditions for knock prediction modeling

Case	Parameter	Engine Speed [rpm]	Intake Pressure [bar]	Ignition Timing [CA bTDC]	Coolant Temperature [°C]	Lambda
1	Load & Speed	1500	Part load, 0.9	16	85	1
2		↑	WOT, 1	4	↑	↑
3		↑	Boosted, 1.1	-1	↑	↑
4		1750	Part load, 0.9	19.5	↑	↑
5		↑	WOT, 1	7.5	↑	↑
6		↑	Boosted, 1.1	5.5	↑	↑
7		2000	Part load, 0.9	23	↑	↑
8		↑	WOT, 1	8.5	↑	↑
9		↑	Boosted, 1.1	4.5	↑	↑
10	Lambda	1750	Part load, 0.95	15	↑	↑
11		↑	Part load, 0.98	12.5	↑	1.1
12		↑	Part load, 0.88	21	↑	0.9
13	Wall Temperature	1500	WOT, 1	7	60	↑
14		1750	WOT, 1	10	↑	↑
15		2000	WOT, 1	10	↑	↑

## 3.2 Detection of Knock Location

### 3.2.1 Visio-Knock system

In Visio-Knock system [60, 64] optical windows are attached around the spark plug, watching the inside of the combustion chamber 30 degree down from the horizontal line. It has 45 angle degree of the window for sensitive light intensity measurement of light intensity in end-gas region. The system used in this study has eight windows, however, there are options of 32 windows or more. The schematic of this apparatus is shown in figure 3.6.

Figure 3.7 shows the statistical comparison of the knock locations while the liner coolant temperature was decreased. Bright area shows more knock occurred region and knock spot was detected by analysing light intensity HPF (high-pass filter) signals. As the temperature of the liner decreased, it seems that the possibility of knock occurrence on the air intake side was increased.

However, this device uses the light intensity signals by the flame propagation. As shown in figure 3.8, eight light windows all show the rise of the light intensity as the flame propagates and all show the oscillation of the intensity. This implies that this device doesn't capture the light intensity of auto-ignition hot spot, but uses the light intensity perturbation of the original flame provoked by the pressure wave oscillation. And if the light intensity of original flame is affected by the pressure oscillation, the pressure increase ( $\Delta P$ ) (can be said as knock intensity) of auto-ignition has to be high enough. For this, the ignition timing has to be more advanced.

Under conditions that can give clarity for analysis of light intensity signal, it is already considered as heavy knock condition which has multiple hot spots in the cylinder. Therefore, it can be thought that the results of analysis using Visio-Knock system tells that the local possibility of the first knock occurrence in a cycle, not the knock occurrence of all the hot spots. Furthermore, it cannot be used in weak knock condition. Thus, in this study, PCB ion-probe gasket was used.

### **3.2.2 PCB Ion-probe head gasket**

There have been various approaches using ion-probe method for investigations of flame detection, flame speed and knock location [117-122]. Installation of ion-probe electrodes inside the combustion chamber is not easy work, however, there are a few methods for insertion. Making pathways on the bottom surface of the head and insulating the electrode wire in it, inserting the electrodes around the spark plug, etc. In this study, the ion-probe head gasket concept, which was first interpreted by Witze and Green [65, 123], was used for easy installation and modification.

For implementation, PCB (printed circuit board) type ion-probe head gasket was produced. It is much less cost-consuming than making a special gasket and is also capable of obtaining heat resistance and flexibility at the same time thanks to the recent remarkable developments of Korean PCB technology. The gasket was designed to have 16 ion probes around the cylinder bore, which had 22.5 degree spacing to each other.

Various materials and designs had been tried for production. Rig testing was performed before the fabrication of the ion probe gasket. Using the same material

of metals with the engine head and liner, the test was conducted and it was found the head or liner could substitute the cathode electrode in normal PCB thicknesses under 3 mm. Therefore, it was concluded the only via hole (through hole) without ground electrode can act as a probe. There are some types of high heat durability materials for PCB such as polyimide (usually well known as flexible PCB), however, the thicknesses of PCBs made of these materials were not enough to capture the flame under normal conditions, and even though it was possible, still not enough for steady-state flame measurement due to the signal loss by carbon deposit.

As the result, in this study, High TG (temperature of glass transition) material PCB was used which can stand over 170°C of temperature condition. Both-sided for easy connection of signal wires to amplifier, and insulated coating was applied on the surface to prevent the direct electrical conduction with the engine or metal gasket. For installation, it was inserted between the head and the liner as normal head gasket does, replacing the original head gasket as shown in figure 3.9. But two additional metal gaskets were inserted as well on the above and beneath to prevent the combustion gas leakage. The final thickness was 2.36 mm. In order to maintain the compression ratio as the same level of original status, the thickness of the shim plates was modified. The motoring pressures at WOT, 2000 rpm are shown in figure 3.10 for both of normal gasket and PCB ion-probe gasket conditions. The difference of the peak pressure was less than 0.1%.

A special amplifier was designed for amplification of the ion probe signal which has the signal intensity level of dozens of microamperes. Based on the design of Lee et al. [124] and Han et al. [125], the circuit was modified. For cleaner flame signal, filtering system was adjusted and LPF (low-pass filter) was added in front of signal output. There was a possibility for carbon deposit on the ion probe which can makes the circuit short problem, the protective circuit was

additionally applied. Additionally, there is a structural difficulty for inserting the electrode into the combustion chamber while making the PCB ion-probe head gasket, thus for sensitive detection of the flame arrival, the bias voltage of ion-probe electrode (anode) was designed to be high enough. 48V of SMPS (switching mode power supply) powered the main power source, and LM3481 DC-DC step-up was added for high voltage power input (300 V) to the ion-probes. MC7815 and MC7915 were used for power input of the amplifier. Two-channel OP (operational) amp, AD8672, was used as the voltage follower and the amplifier. LM6511 was used for voltage comparator, which returns the digital signal when the analogue voltage of ion-probe head gasket signal exceeds the set threshold. Threshold was adjusted with TL783 and was set as 1V in this study. The amplifier totally has 32 multiple amplifying circuits, however, for ion probe head gasket, 16 circuits were used. To carry out the signals from ion-probes to the amplifier, it was connected using SMA connectors and RG-316 wires for low noise problem. Figure 3.11 shows the final appearance of used ion-probe head gasket during the engine experiment.

Figure 3.12 shows the example of cycle-by-cycle results. In the figure, the radius from the center indicates the crank angle from ignition timing, 10 CA for each scale. Red line with rectangle indicates the splined flame arrival timing and blue line indicates the knock onset timing at the cycle with in-cylinder pressure analysis. Considering the pressure travel time from end-gas region to the sensor position, line of knock onset minus 1 CA is also indicated, therefore it has double line. Knock usually occurred 30 to 40 CA after the ignition in this condition. Because the ion probes on PCB gasket are located at the end of cylinder bore, if the radius of red line is longer than that of blue line, it means the flame was arrived after knock onset in that certain position. In contrast, if the radius of red line is shorter, the flame arrived earlier to the cylinder bore end before the knock onset. This implies that if the red line is outer than blue line in certain direction, there

might be the auto-ignition hot spot. Therefore, knock position can be both intake side and exhaust side in this example.

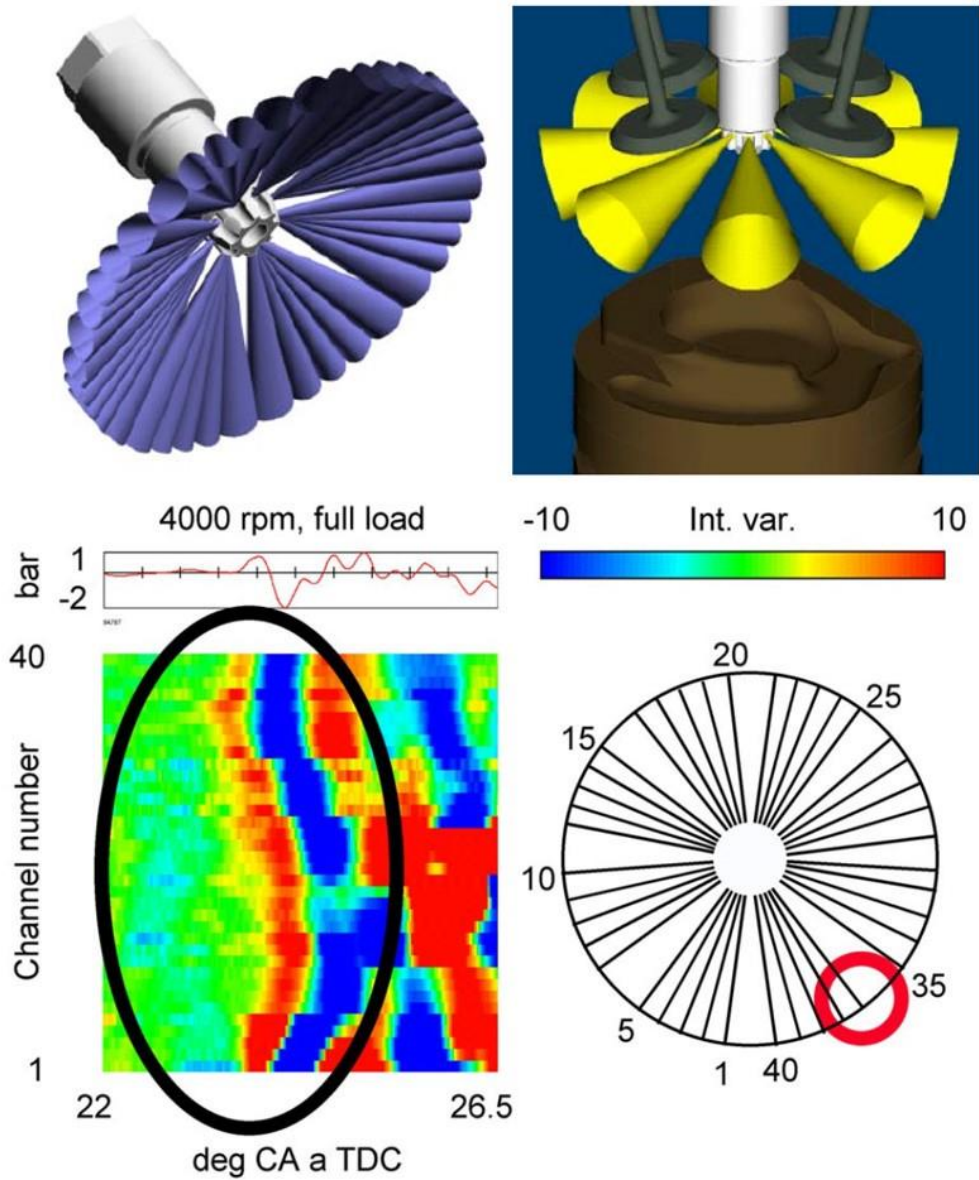


Figure 3.6 Schematic of AVL Visio-Knock system, from [60, 64].

Head coolant = 80°C  
 Knock 40%, IGN 23 CA (Heavy-knock)

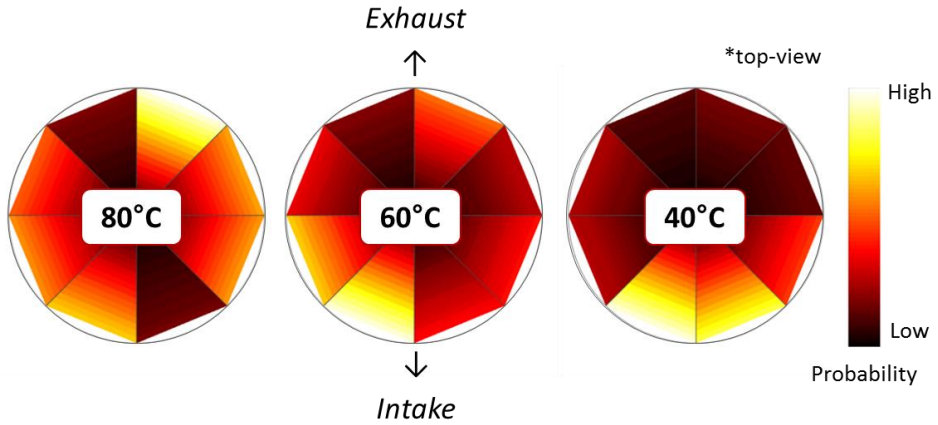


Figure 3.7 Visio-Knock test result under liner cooling condition

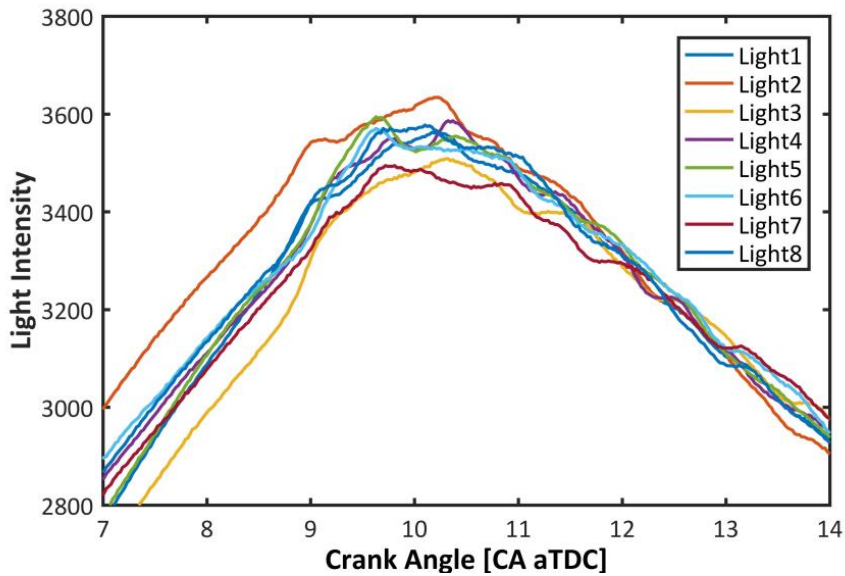


Figure 3.8 Light intensity of eight optical probes in Visio-Knock

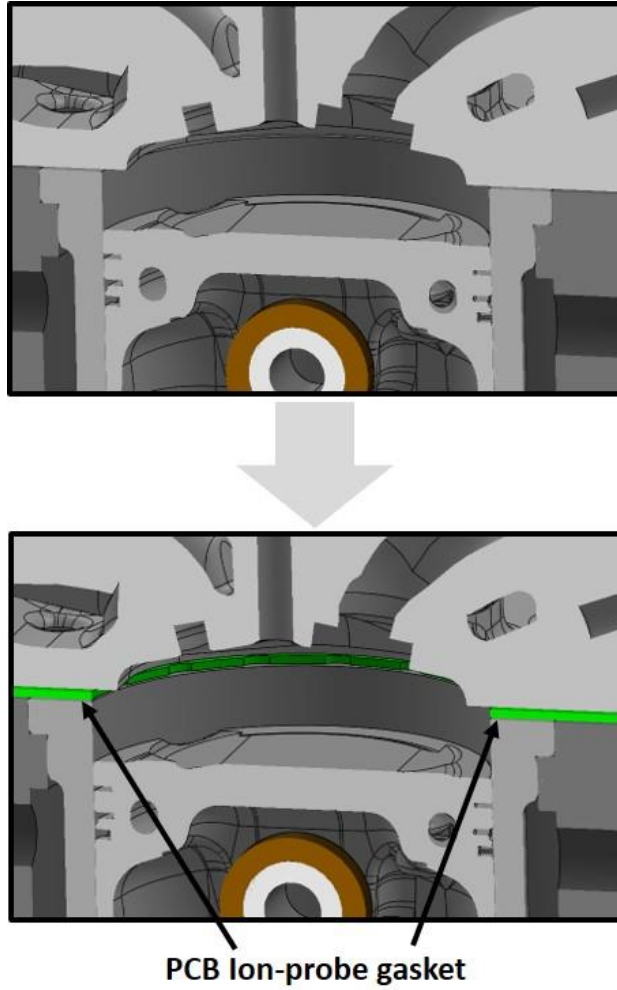


Figure 3.9 PCB ion-probe head gasket installation

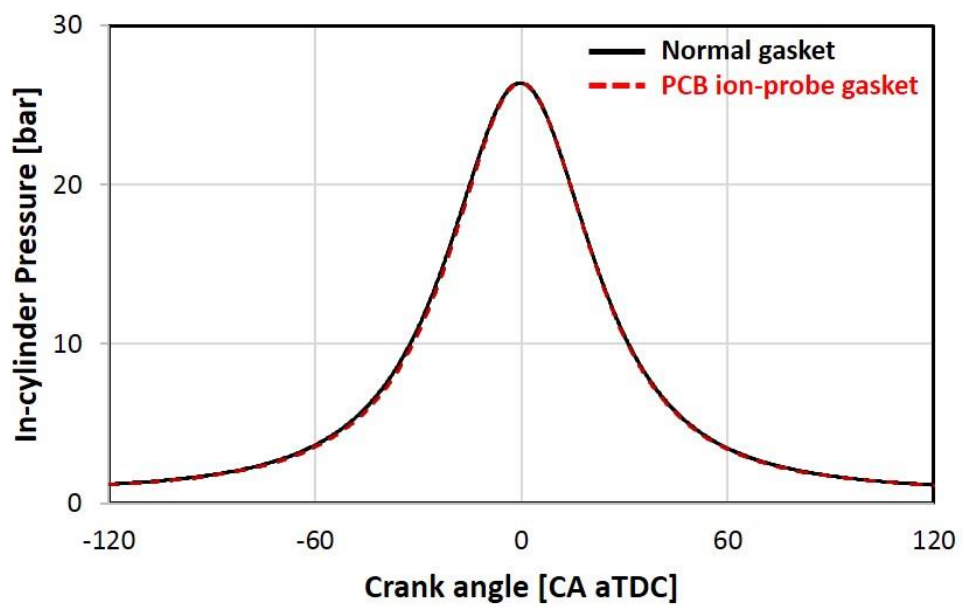


Figure 3.10 Motoring pressures with normal gasket and PCB ion-probe gasket at 2000 rpm

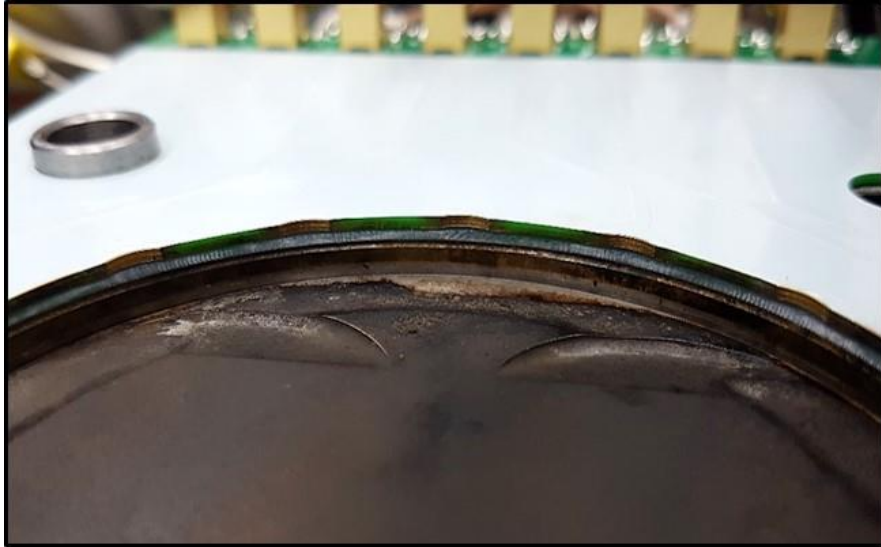


Figure 3.11 Engine setup of PCB ion-probe head gasket

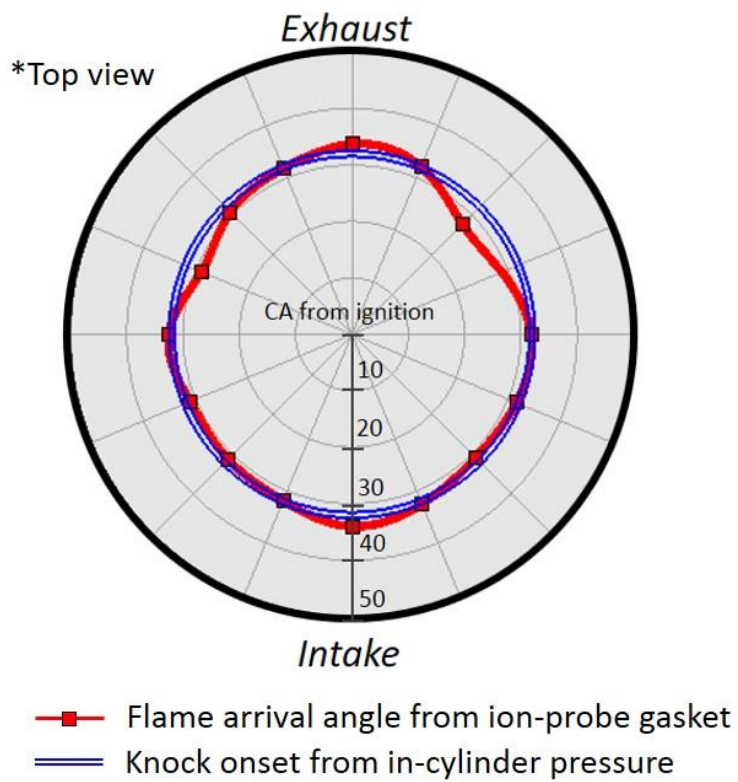


Figure 3.12 Flame arrival and knock onset using PCB ion-probe gasket

## **3.3 Wall Temperature Measurement**

### **3.3.1 Linkage system for piston measurement**

During the combustion period, the combustion chamber mainly consists of down surface of the head and the upper surface of the piston. The ratio of piston area to liner area is usually ten times larger than during the combustion, which means the piston surface temperature has a significant role on the heat transfer in internal combustion engine. Therefore, measuring the piston temperature and understanding the effect is undoubtedly important.

However, practically, it's not easy to measure not only the temperature but also data related to the piston due to its dynamic movement. Figure 3.13 shows the piston speed and acceleration of the test engine at 6000 rpm. As it is shown, maximum speed exceeds 30 m/s and acceleration is approximately 2,500 times of acceleration of the gravity. This harsh condition precipitates durability or fatigue problem on the sensors and apparatus for piston measurement.

A lot of method have been proposed to measure the piston temperature [126]. Furuhashi et al. [127] introduced a mechanical device to measure the piston temperature and proposed methods for installing thermocouples. Thermal plugs are made of material having a linear relationship between temperature and hardness [128, 129]. By measuring the hardness of the plug surface, the subjected temperature could be easily measured. This method is usually used for measuring the maximum temperatures of the test, so it is suitable for durability test of the engine development process. There are also methods using telemetry systems [130-134] but highly cost-consuming. Contact-point method [129, 135] makes the

lead wire to be contacted during the reciprocating motion of the moving assembly including piston.

Linkage system allows direct and reliable measurement at a low cost, unlike other methods. In addition to temperature measurements, flame propagation can be also measured in a very high resolution by installing ion-probe sensors on the piston as interpreted by Jie et al. [119]. It is also able to use fast response thermocouples such as Gardon-type sensors [110, 136] and heat flux sensors [137, 138]. For high speed and high resolution measurement, linkage system is very reasonable while recent developed telemetry system is expensive and has comparatively slow transmission speed.

Taylor et al. [139] used a grasshopper type linkage system. They attached displacement sensors on the piston to measure secondary motion between the liner and the second piston ring. Cho et al. [136] measured dynamic temperatures of piston using fast response thermocouple attached on a linkage system. Tsutsumi et al. [128] installed thermocouples at various location in the piston and the signals were transmitted through a linkage. They showed the mirror-finished piston had 4-6°C lower temperature at 1600 rpm, full load. Chang et al. [137, 138] installed nine heat flux sensors including seven in the piston, and measured local instantaneous temperature and heat flux variations. Mufti et al. [140] calculated the load of piston assembly by load measurement of various positions on connecting rod. The measurement was facilitated by a grasshopper type linkage system.

Figure 3.14 shows the original conceptual design of the linkage system in this study. The model was simplified for the optimization. The linkage system consists of two links, link 1 and link 2. The link 2 was retrofitted to the revolution joint on the middle of connecting rod because the bottom side of the connecting rod cannot be used due to the design characteristics of the engine.

The wiring concept on the linkage is shown in figure 3.15. Because the piston and connecting rod moves very quickly, direct wiring was not appropriate. Instead, the wires were attached on the linkage to prevent the fatigue. Wires were inserted through the holes in the joints and this method made the wires only take the torsional force by the movement.

### 3.3.1.1 Optimization of linkage system

Optimization on the operating angle of each joint was implemented to minimize twist angles of signal wires which can lead to the wire fracture. Downhill simplex optimization method, which was first introduced by Nelder and Mead [141], was adapted mainly because of its simplicity and universality for an optimization of non-linear system. This method initiates using a polytope with N+1 of vertexes in N-dimensional space when there are N number of variables. The vertexes continuously move and create a new polytope to find the optimum. The summarized process is as the follows.

- 1) With an initial condition N+1 number of variable, creates a polytope consisting of N+1 of vertexes coordinated by initial conditions.
- 2) Evaluate the values of objective function at each vertex with variables consisting the coordinates of vertexes.
- 3) Reflect vertex  $x_h$ . (subscript h: high, subscript r: reflected)

$$\bar{x} = \Sigma x_i / N \quad (i \neq h),$$

$$x_r = \bar{x} + \alpha(x_h - \bar{x})$$

3-1) If  $f(x_r) < f(x_l)$ , expand the polytope to obtain the  $x_e$  with the relation.

$$x_e = \bar{x} + \gamma(x_r - \bar{x}), \quad \gamma > 1$$

3-1-1) If  $f(x_e) < f(x_r)$ , substitute  $x_h$  to  $x_e$ .

3-1-2) Else, substitute  $x_h$  to  $x_r$ .

3-2) If  $f(x_r) > f(x_i)$ ,  $i \neq h$ , contract the polytope to obtain the  $x_c$  with the relation.

$$x_c = \bar{x} + \beta(x_h - \bar{x}), \quad 0 < \beta < 1$$

3-2-1) If  $f(x_c) < \min(f(x_h), f(x_r))$ , substitute  $x_h$  to  $x_c$ .

3-2-2) Else, change all the  $x_i$ 's with the relation  $x_i = (x_i + x_l)/2$

4) If the convergence is within the criterion, end the optimization procedure.

$$\text{Nelder - Mead Convergence} = \sqrt{\Sigma\{f(x_i) - f(\Sigma x_j / (N + 1))\}^2 / N}$$

As appeared during the procedure, the proper values of coefficients  $\alpha$ ,  $\beta$  and  $\gamma$  should be specified to expand, contract and shrink the polytope. Nelder and Mead performed a parametric study with these values on some representative planes (Rosenbrock's parabolic valley, Powell's quartic function and Fletcher and Powell's helical valley). It was shown that 1, 0.5 and 2 for each value showed the best convergence characteristics. However, as it is mentioned in their study, the optimal value for the coefficients highly depends on the objective function. Therefore, in this study, revision of original method was conducted by application of one-dimensional optimization, golden section method. Also, an escape algorithm was adapted to avoid the local minimum point.

The golden section method, one of the 1D optimization technique, has its priority on fast bracketing of section where the optimal point may exist because this method searches critical point with weight value of golden ratio. The procedure is as followed.

1) Define initial search point as  $x_1$  and proper interval value, d. Then, let the  $x_2$  to be  $x_1 + d$  and  $x_4$  to be  $x_2 + d * 1.618$  (golden ratio).

1-1) If  $f(x_4) < f(x_2)$ , let  $x_4$  to be  $x_2$  and  $x_2$  to be  $x_1$ .

1-2) Else, bracketing is done. Let  $x_3 = \frac{c}{1+c}x_4 + \frac{1}{1+c}x_1$ , where  $c = 1.618$

2) Evaluate function value at  $x_3$ .

2-1) If  $f(x_2) < f(x_3)$ , change  $x_4$  to  $x_1$  and  $x_1$  to  $x_4$ .

2-2) Else, change  $x_3$  to  $x_2$  and  $x_2$  to  $x_1$ .

3) If the interval of bracketed section becomes lower than specific criterion, end the optimization procedure.

These two algorithms were combined and the final algorithm is as followed.

1) With N+1 of initial condition of optimization variables, creates a polytope consisting of N+1 of vertexes coordinated by initial conditions.

2) Evaluate the values of objective function at each vertex with variables consisting the coordinates of vertexes.

3) Reflect vertex  $x_h$  to  $x_r = \bar{x} + \alpha(x_h - \bar{x})$  with  $\bar{x} = \Sigma x_i / N$  ( $i \neq h$ ).

3-1) If  $f(x_r) < f(x_h)$ , Determine a direction  $\vec{n} = \|\bar{x} - x_h\|$  for 1D optimization.

3-1-1) Determine a value of  $\gamma$  which gives the lowest objective function value by 1D optimization.

$$\min(f(\gamma)), f(\gamma) = f(\bar{x} + \gamma(x_r - \bar{x}))$$

3-1-2) Change  $x_h = \bar{x} + \gamma_{opt}(x_r - \bar{x})$ .

3-2) If  $f(x_r) > f(x_h)$  contract the polytope to check inside to obtain the  $x_c$ .

$$x_c = \bar{x} + \beta(x_h - \bar{x}), \quad 0 < \beta < 1$$

3-2-1) If  $f(x_c) > f(x_h)$ , replace the  $\beta$  to be half of itself. Then, calculate and check  $f(x_c)$  again.

3-2-1-1) If  $\beta$  becomes small enough, change the  $x_h$  with a point of smallest function value near the  $x_h$  (distort the polytope).

3-2-2-2) If distortion occurs N+1 times, change all the  $x_i$ 's (it means no better point outside of the polytope).

$$x_i = (x_i + \bar{x})/1.5$$

3-2-2) If  $f(x_c) < f(x_h)$ , change  $x_h$  to  $x_c$ .

4) If it reaches to the convergence, end the optimization procedure.

Modified downhill simplex method has a strength on its calculation speed by combination with 1D optimization, golden section method. This method can not only be used only for this study, but also propose an optimization method for very

complex non-linear system. The minimal objective function and the result value is:

$$[x_1, x_2, x_3] = [87.4986, 160.60, 76.11], \text{ while } f = 62.12$$

However, this is the optimization problem for the torsional angle of wire. In actual engine, the stress on the linkage system is also a critical factor. Even though the wiring torsional angle is minimum, the stress has to be considered. Therefore, the optimization process was implemented in 27 sections dividing one link length into three ranges. Among 27 optimal points, top nine results are listed in table 3.5.

### 3.3.1.2 3D analysis of linkage system

Due to the feature of single cylinder engine used in this study, link 2 had to be bend. Therefore, the stress analysis was conducted for original conceptual design. Recurdyn V8R4 software was used for 3D dynamic stress simulation and RFlex (modal) method was applied for fast calculation on piston stress analysis. The in-cylinder pressure profile which had over 120 bar or peak pressure value was introduced to assume an extreme situation. Figures 3.16 to 3.17 shows the simulation result at 2000 rpm condition. As it is clearly shown approximately 140 MPa was applied on the bend area on the link 2 by the movement which may cause the failure, of course it was inoperable in higher speed than 2000 rpm. Moreover, it was found that the linkage system is not affected a lot by the in-cylinder pressure profile due to the indirectness while the stress on connecting rod and piston were affected a lot. However, the connecting rod was design to be thicker and stronger than normal mass produced one, therefore, the stress on mass-produced parts were not considered.

As it is described, not only the optimization of torsional movement of wire but also the mechanical stress on the linkage system are important. Therefore, from minimal objective function of previous section, 5% of excess was allowed and 3D (three-dimensional) simulation was applied for the conditions (table 3.5). As the result, a design of for minimal stress was selected, showed the safety factor of 25 at 2000 rpm (figure 3.19) and two at 6000 rpm (figure 3.20) conditions, respectively. The stress distribution on link 2 of final design is shown in figure 3.21.

Right side of figure 3.21 shows the improved design alternative from the original conceptual design on the left. This linkage system can afford not only measurements of the temperatures in this study, but various measurements such as fiction, heat flux and dynamic temperature in the future.

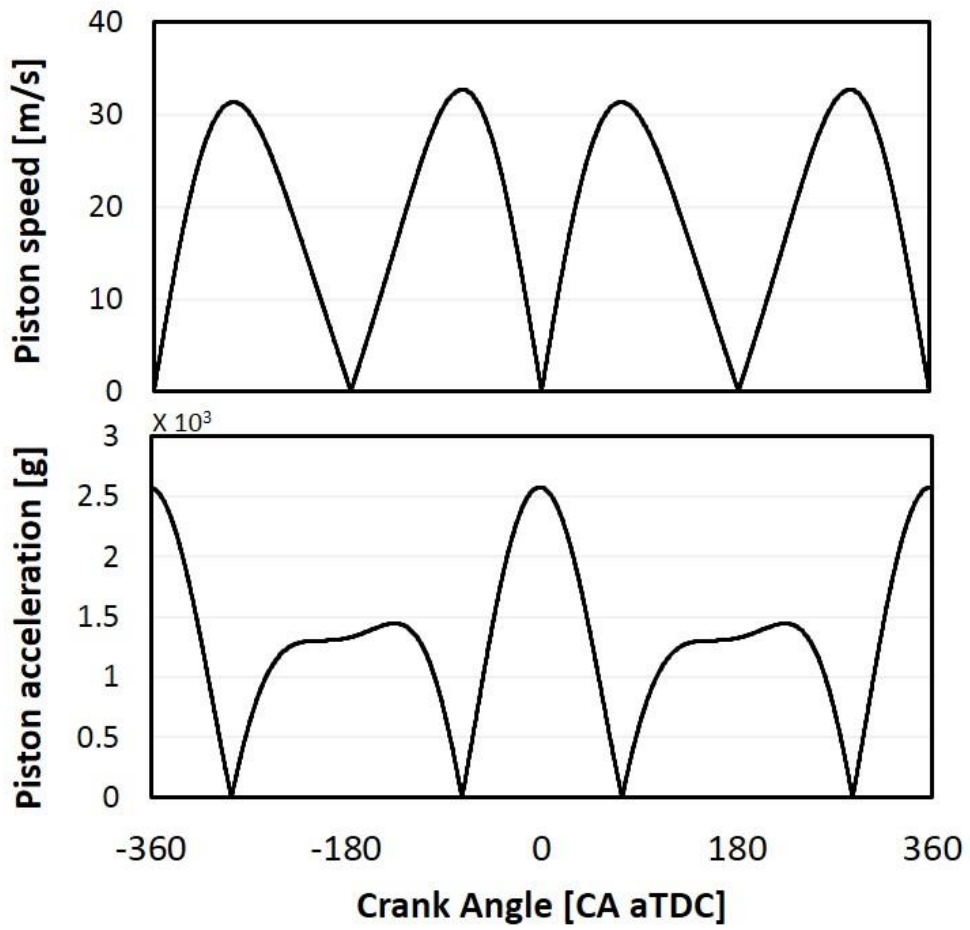


Figure 3.13 Speed and acceleration of piston at 6000 rpm.

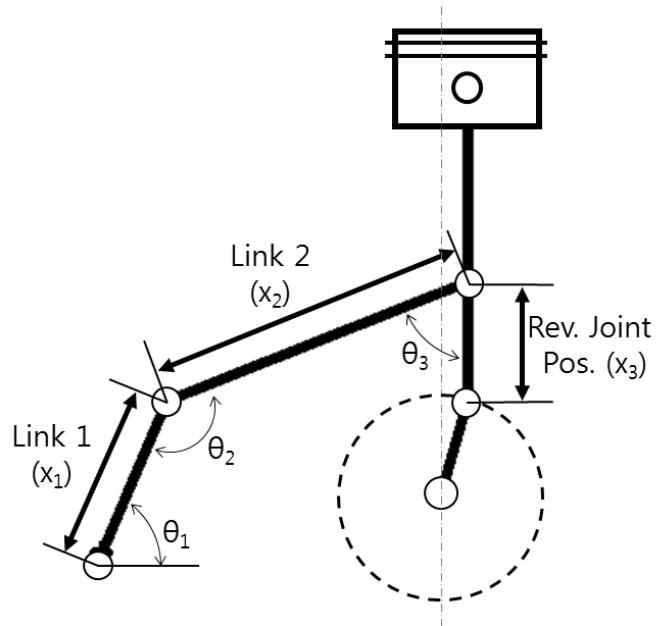


Figure 3.14 Schematic diagram of the linkage system

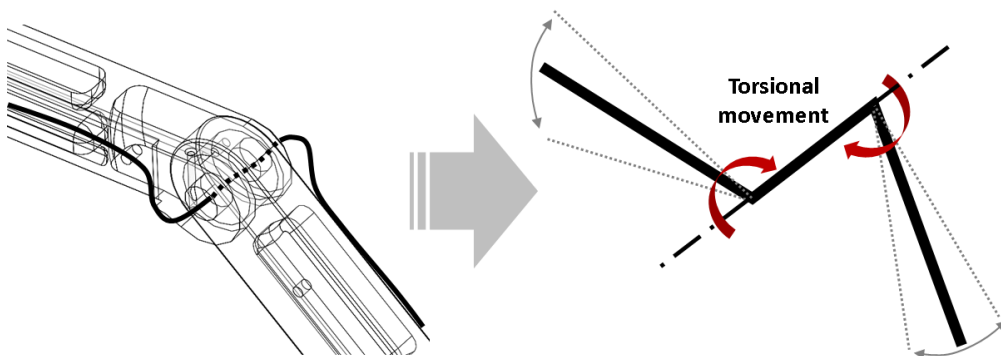


Figure 3.15 Method for thermocouple wiring on the linkage

Table 3.5 Result linkage system optimization

$X_1$ [mm]	$X_2$ [mm]	$X_3$ [mm]	Objective Function [deg]
87.4986	160.60	76.11	62.12
87.4997	163.77	82.87	62.29
87.4988	157.21	68.64	62.32
87.5000	165.40	86.25	62.49
86.9999	155.00	63.50	63.21
86.9986	167.30	90.02	63.38
87.4998	170.76	97.09	63.73
87.4989	156.25	71.25	64.08
87.0000	173.00	101.40	65.12

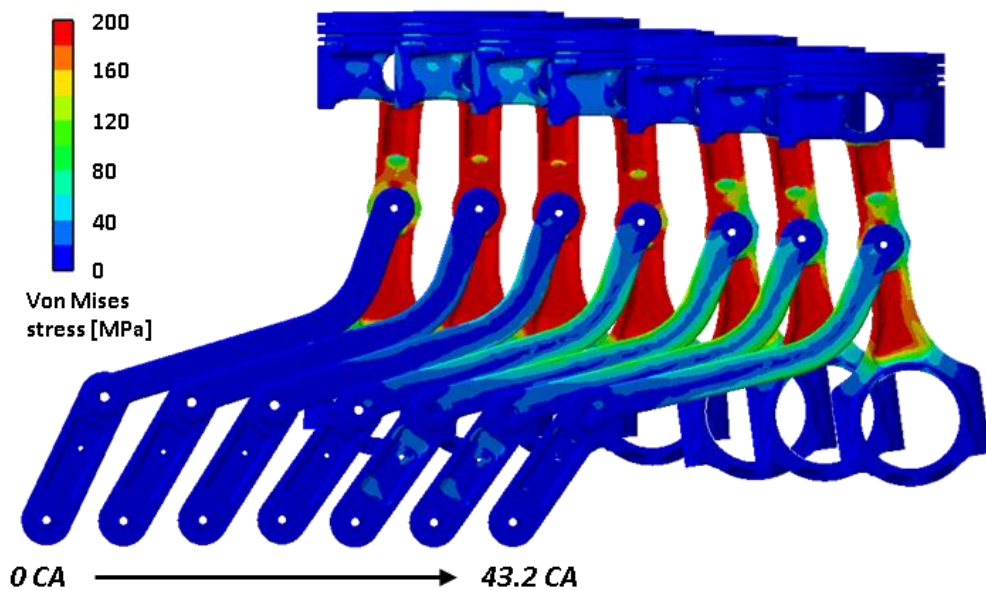


Figure 3.16 3D stress analysis of original linkage design at 2000 rpm

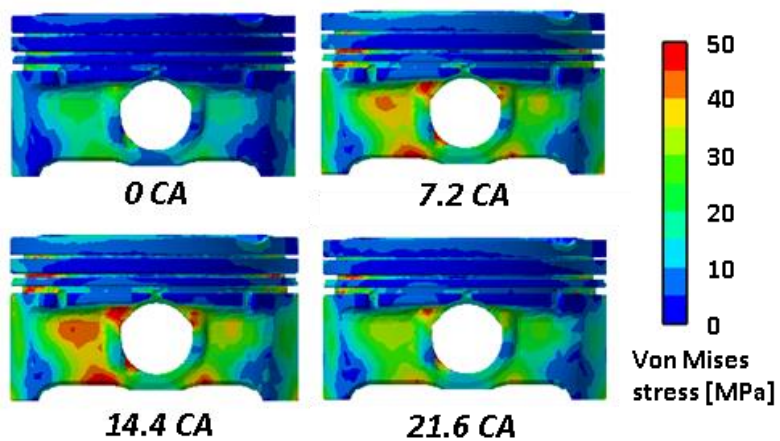


Figure 3.17 3D stress analysis of piston at 2000 rpm

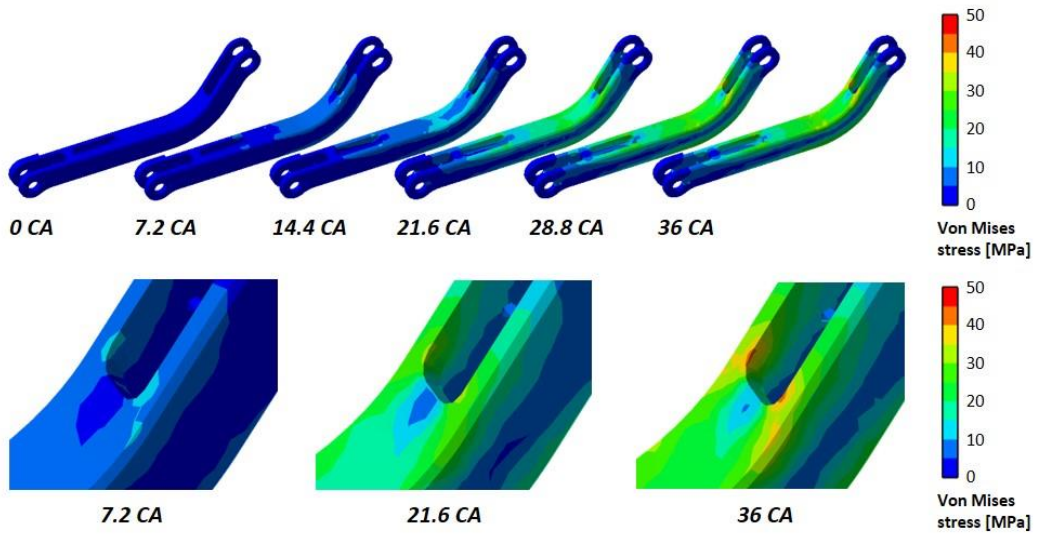


Figure 3.18 Stress on link 2 of original design at 2000 rpm

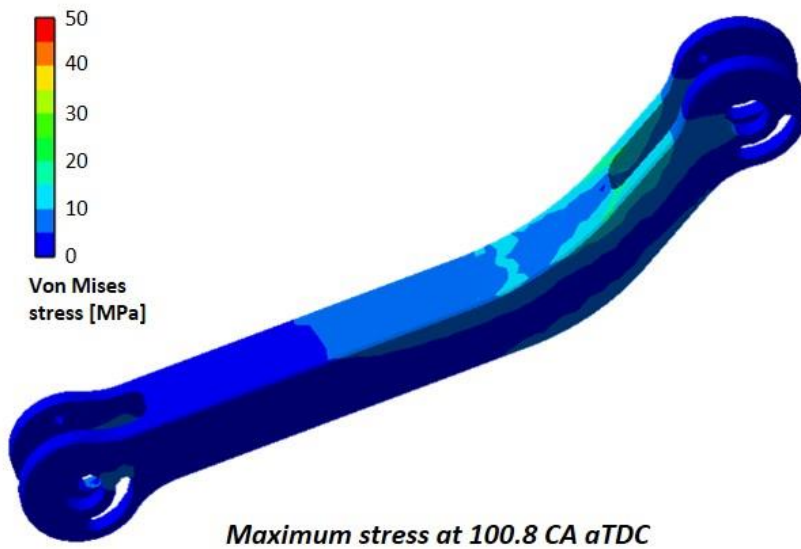


Figure 3.19 Maximum stress of improved linkage design at 2000 rpm

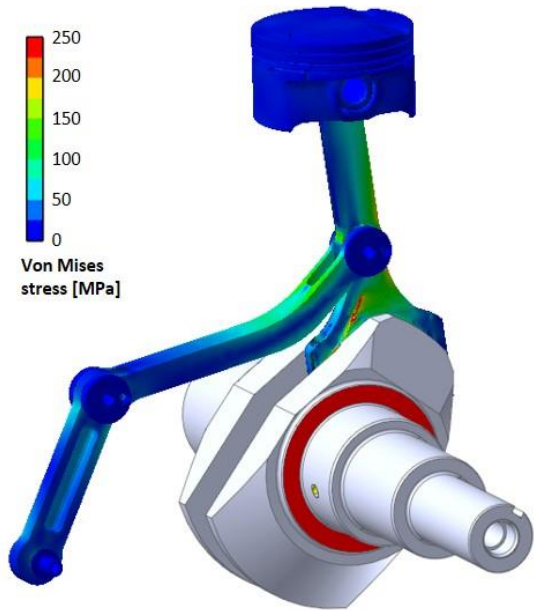


Figure 3.20 Stress analysis of improved linkage design at 6000 rpm



Figure 3.21 Original concept design and improved design of linkage system

### **3.3.2 Method for thermocouple installation**

The temperature measurement points for the thermal boundaries are shown in figure 3.22. All the points are located exactly 1 mm outside of the combustion chamber. Twenty-two total points were measured with K-type thermocouples: twelve points in the liner around the cylinder bore including inner wall and outer surfaces, five points beneath the top surface of the piston, five points in the cylinder head.

For measurement of wall temperatures of the cylinder head, five thermocouples were installed as shown in figure 3.23: one in right beside the spark plug, one between two intake valves, one between two exhaust valves, one in front side and one in rear side. The value shown in the results is averaged value of these five measurement points.

Five thermocouples were inserted into the piston (see figure 3.6) to measure the surface temperature during the operation. As shown in the right side of figure 3.23, one measured the temperature of the center and four thermocouples were inserted in the locations 34.5 mm away from the center for each direction. The thermocouples were inserted on the piston and glued with high temperature epoxy as shown in figure 3.24. In addition, to prevent disconnection of the thermocouple wires, aforementioned linkage system was used and the thermocouple wires were attached on it in a special way (see figure 3.12). Kapton insulated wires were used on the piston to prevent the melting problem of its sheath. However, from the connecting rod, the wire was changed in order to endure the torsional force. the wires were specially designed using silicon tube to be flexible. A hundred 23 AWG (American wire gauge) wires were twisted and inserted into each silicon tube. The custom-made Alumel and Chromel wires are magnified and shown in figure 3.25.

Totally twelve thermocouples were used for liner. As shown in figure 3.26, top measurement points were located 1 mm outside from the combustion chamber, 4.5 mm down from the liner top surface where contacts to the head gasket. Medium points were located 45 mm down from the liner top and have four points: inner surface and outer surface of intake side, inner surface and outer surface of exhaust side. Bottom four points were also measured in the same manner with medium points. However, the temperature showed as the liner wall temperature in this study was the average value of medium inner surface temperatures of both intake side and exhaust side. Electrical discharge machining facilitated the insertion of thermocouple wires from the bottom surface of liner inside the crankcase and the holes were insulated with high temperature epoxy.

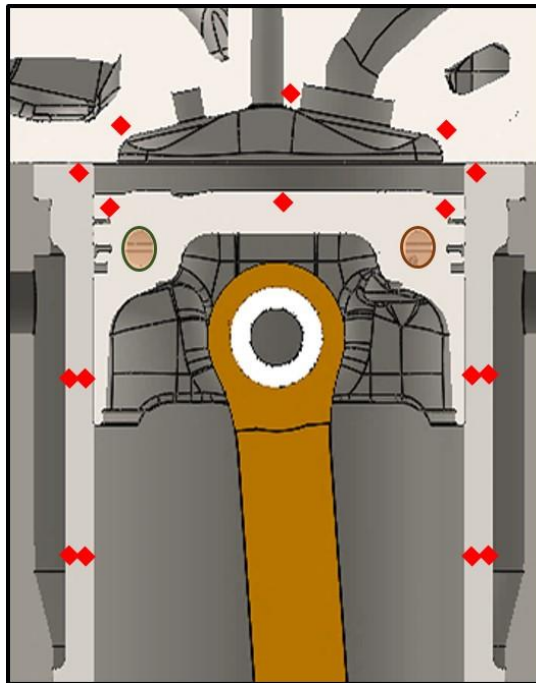


Figure 3.22 Temperature measurement points on the combustion wall

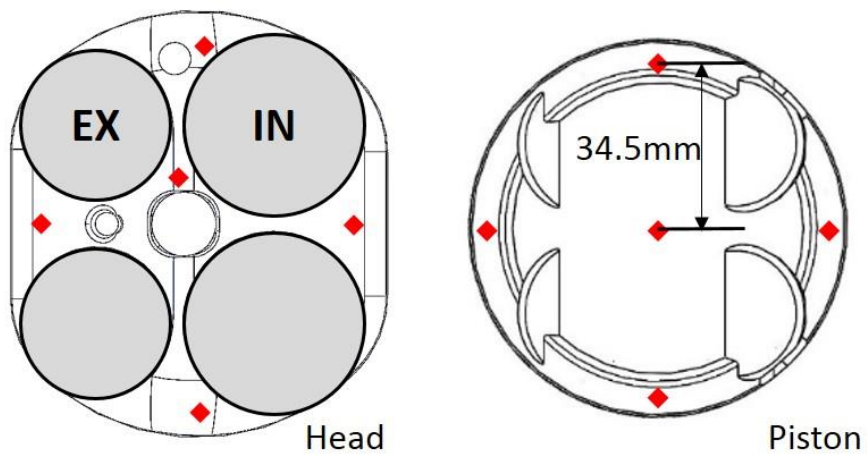


Figure 3.23 Temperature measurement points of cylinder head and piston



Figure 3.24 Thermocouple installation on piston

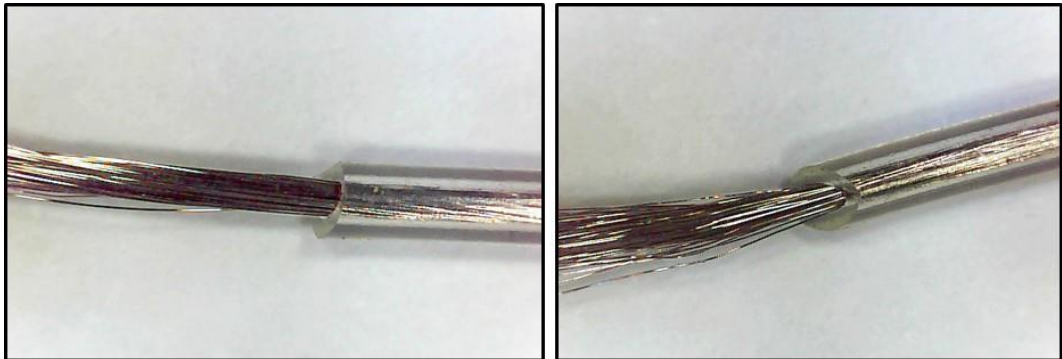


Figure 3.25 Special thermocouple wires for moving linkage system  
(left: Alumel, right: Chromel)

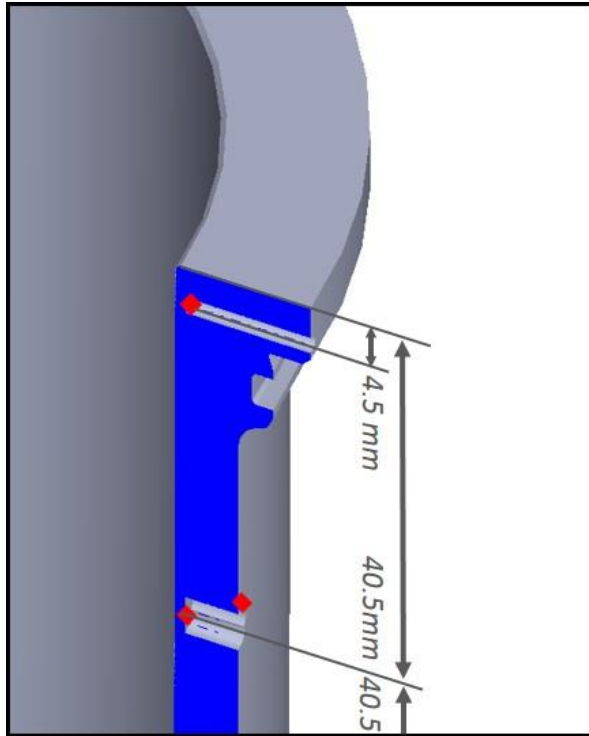


Figure 3.26 Positions of thermocouple installation on liner wall

### 3.4 3D CFD simulation

In order to investigate the heat transfer between walls and mixture gas, 3D CFD simulation was used in this study. STAR-CD V4.24 was used as a tool and mesh number was approximately one million at BDC. k- $\epsilon$ -RNG model and Angelberger model [142] were used to simulate the turbulence and heat transfer interaction, respectively. Mesh shape at BDC is shown in figure 3.27 and the specification is summarized in table 3.6.

In this study, 3D simulation was performed under both conditions of motoring and combustion. Table 3.7 shows the surface temperature conditions of combustion simulation. All the conditions were conducted in both engine speed, 1500 and 2000 rpm. The base temperature condition was determined by actual measurement data. From base condition, each surface temperature was reduced 20°C. And temperatures of valves and spark plug were considered not changing [2]. However, it was found that the liner coolant temperature has a large effect on piston surface temperature during the test. Therefore, for the liner cooling case, piston temperature decrement was included. To only separate the effect during combustion, data from calculation result of base condition 5 CA prior to ignition timing for subsequent calculation.

Table 3.8 shows the motoring conditions. In this study, because the effects of boundary wall temperatures were also investigated in intake process, the motoring conditions were used for comparison of boundary wall temperature effects.

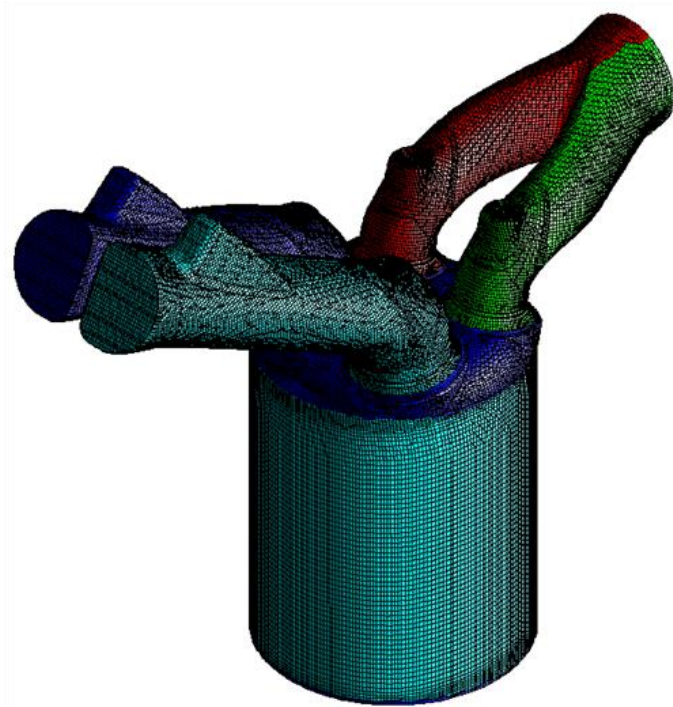


Figure 3.27 PFI Engine mesh generated at BDC

Table 3.6 Configuration of CFD simulation

Program	STAR-CD V4.24
Number of mesh	~ 1,120,000 at BDC
Turbulence model	k- $\epsilon$ -RNG
Heat transfer model	Angelberger [142]

Table 3.7 Boundary conditions for CFD simulation (combustion)

Case	Name	Head [°C]	Liner [°C]	Piston [°C]	Intake Port [°C]
1	Base	115	110	165	85
2	Head ↓	95	110	165	60
3	Piston ↓	115	110	145	85
4	Liner ↓	115	90	154	85
5	All ↓	95	90	154	60

Table 3.8 Boundary conditions for simulation (motoring)

Case	Engine Speed	Throttle	Head [°C]	Liner [°C]	Piston [°C]	Intake Port [°C]
6	1500	WOT	115	110	165	85
7	2000	↑	↑	↑	↑	↑
8	1500	↑	115	110	165	adiabatic
9	1500	↑	95	110	165	adiabatic
10	1500	↑	115	90	154	adiabatic
11	2000	↑	115	110	165	adiabatic
12	2000	↑	95	110	165	adiabatic
13	2000	↑	115	90	154	adiabatic
14	1500	↑	115	110	165	85 / intensified
15	2000	↑	115	110	165	85 / intensified

## Chapter 4. Results and Discussion

### 4.1 Wall Temperature Effect on Knock Mitigation

#### 4.1.1 Feasibility of thermal boundary temperature reduction

Because knock is auto-ignition phenomenon in the cylinder, the influence of intake gas temperature is inevitably large. In this section, knock mitigation effect of decreasing thermal boundary temperature was verified by comparison with that of intake temperature reduction.

Under the same condition, the effect of coolant temperature was investigated. The intake temperature was measured at the point in the intake manifold ahead of intake port. The load limit under 15°C and 30°C of intake temperature conditions were investigated using GDI engine while changing the coolant temperature. Knock incidence was maintained at 5%, and the ignition timing was adjusted to the timing that makes the CA50 to be 8 CA aTDC at which it is considered near MBT timing.

Figure 4.1 shows the comparison of knock limit under both intake temperatures. Blue line with rectangle indicates 15°C air temperature condition and red line with triangle indicates the 30°C condition. The knock limit load is indicated as a function of coolant temperature. In average, 8.2% of knock limit expansion was achieved, corresponding 0.55% per unit temperature decrease of intake air. It is shown 25°C simultaneous decrease of head and liner coolant temperatures corresponds to 15°C decrease of intake temperature. From this, it

can be indirectly thought the wall boundary temperature has a large effect on in-cylinder gas temperature.

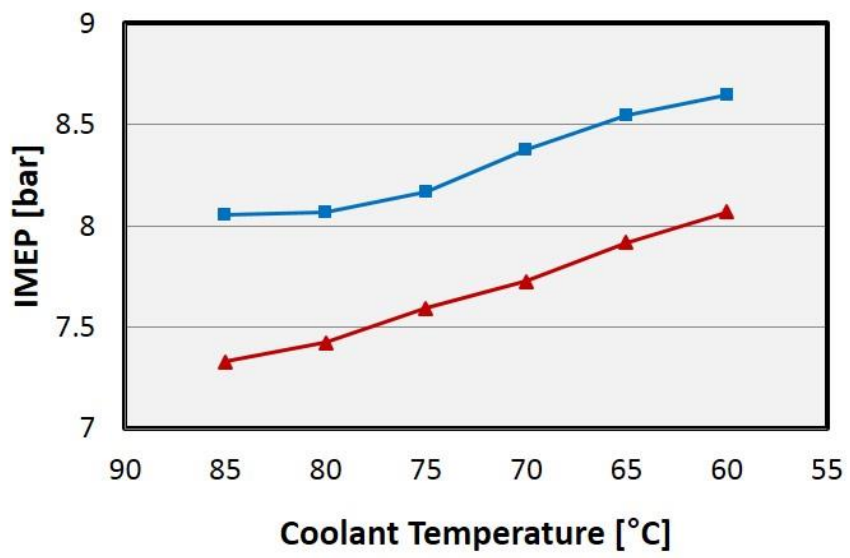


Figure 4.1 Effect of intake temperature and coolant temperature

### 4.1.2 Independent temperature control by segregated cooling

The wall temperature variation of the head and liner are shown in figures 4.2 to 4.4. Experimental condition was 1500 rpm, IMEP 6 bar. PFI engine was used for the test and while one of the two coolant temperatures were controlled, the other one was maintained at 85°C. In the figures, from left to right on the X-axis, the coolant temperature decreases from 85°C to 60°C.

It is clearly shown that independent temperature control was facilitated by segregated coolant passages. For example, in figure 4.2, the red line with diamond indicates the average head wall temperature against the head coolant temperature, while the liner coolant temperature remained constant at 85°C. The mean wall temperature of the liner didn't change remarkably while the head coolant temperature decreases. Likewise, in figure 4.3, the mean wall temperature of the head didn't change a lot while cooling the liner under liner cooling condition. It can be concluded that the wall temperature of each component is dominantly determined by the coolant temperature of itself. Figure 4.4 shows the result of simultaneous cooling of head and liner. The head surface temperature was dropped from 112.9°C to 90°C, and the liner surface temperature was dropped 94.7°C to 75.9°C. Head temperature was higher in overall cases and is mainly thought to be attributed to the larger surface area than that of liner during combustion period. The effect of coolant temperature decrement showed the similar temperature drop in both case, however, the head coolant temperature showed a slightly larger effect. Head surface showed 0.92°C decrease per unit temperature decrease of its coolant, and liner surface showed 0.74°C decrease.

In figure 4.5, the averaged piston temperature at 1500 rpm and IMEP 7 bar is shown. Simultaneous cooling indicates simultaneous decrease of the coolant temperatures for the head and the liner. Likewise, the red line with diamond

indicates the piston wall temperature variation while cooling only the head coolant to 60°C. It is obviously shown that piston wall temperature was mostly affected by the liner because it shows almost no change when only the head coolant temperature decreases. This is thought to be due to a large amount of conduction through the piston rings. There was no remarkable difference between liner cooling case and simultaneous cooling case which implied that the piston temperature is governed by liner wall temperature while considering the independent temperature control was already achieved.

It is also shown that piston wall temperature variation was smaller than that of the liner when the liner coolant temperature decreases. This fact supports that the large heat transfer takes place through the piston like the cylinder head as it also has a large surface area during the combustion period.

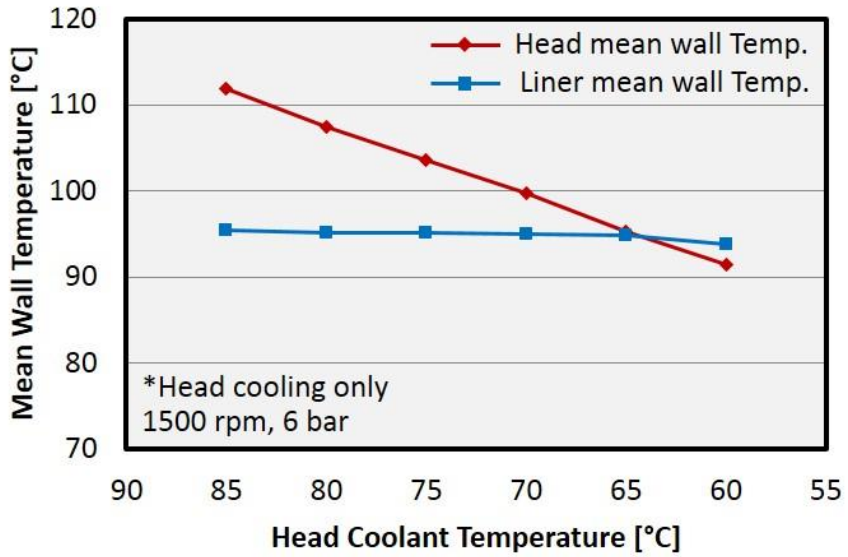


Figure 4.2 Wall temperature variation of head and liner at head cooling

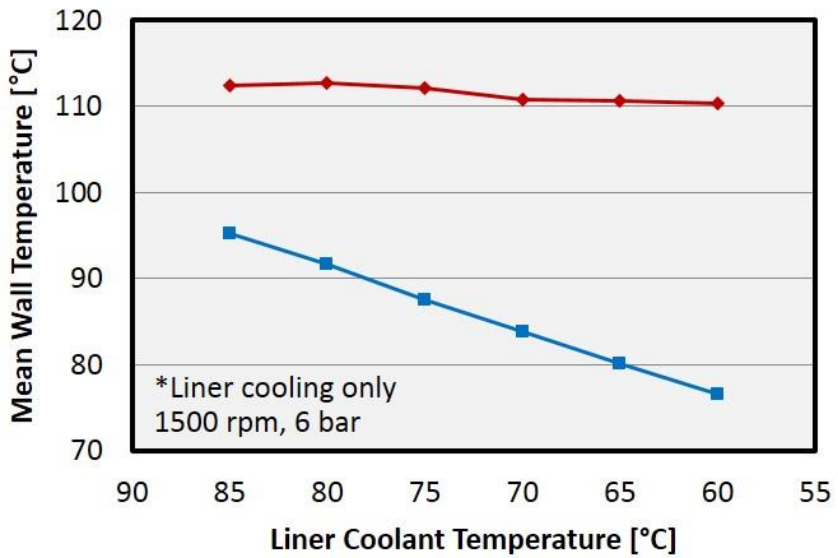


Figure 4.3 Wall temperature variation of head and liner at liner cooling

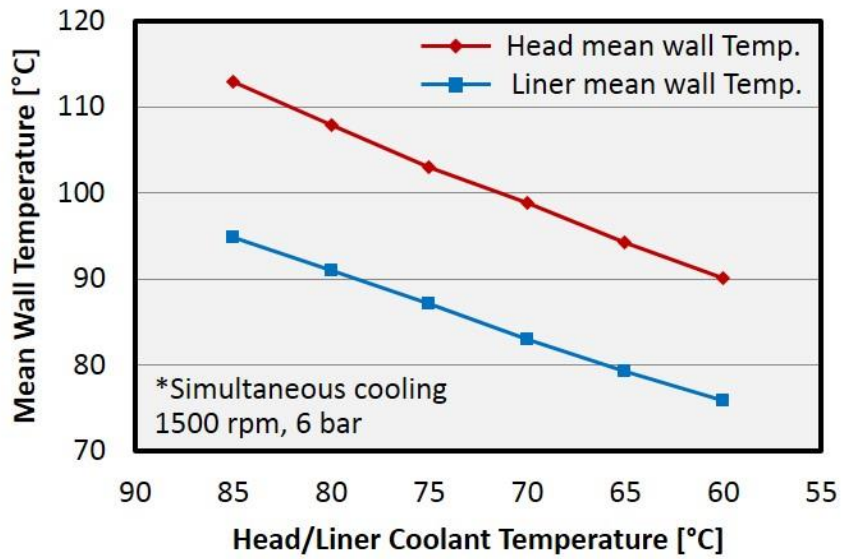


Figure 4.4 Wall temperature variation at simultaneous cooling of head and liner

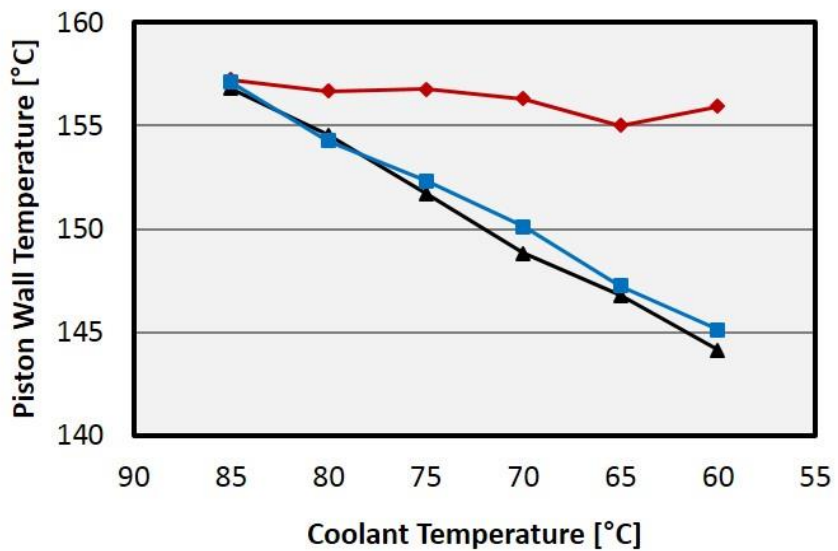


Figure 4.5 Piston surface temperature variation at each cooling condition

### 4.1.3 Thermal effect of oil-cooling gallery

The piston in this study has an oil-cooling gallery inside of it as it is described in Chapter 3.1 and shown in figure 3.5. By injecting oil towards the oil-cooling gallery, the piston surface temperature can be decreased and this leads to temperature decrease of unburned gas, which promotes knock mitigation.

Figure 4.6 shows the temperature distribution of the piston surface for the condition of both coolant temperatures of the head and the liner were maintained at 80°C. The right figure shows the oil injection case while the left one shows the result without the oil injection. The engine speed was 1500 rpm, and the load was the same as 7.2 bar of IMEP.

As it is apparently shown in the figure, the surface temperature was remarkably dropped. For the piston center, over 25°C of temperature drop was observed, and the side points also showed around 20°C of temperature drops. The exhaust side showed the minimum temperature drop among five measurement points which is considered due to the target position of oil-injection. In this engine, the oil was injected to the intake-rear side of the piston and flew out from the exhaust-front side. Therefore, it is shown that the oil injection case shows an eccentric distribution to the exhaust side.

Because the oil injection to piston shows knock mitigation, ignition timing could be advanced from 14.5 to 16.2 CA bTDC while maintaining the knock incidence at 10%, 7.2 bar of IMEP, and the coolant temperatures at 80°C. As the ignition timing advanced, CA50 was also advanced from 12.96 to 11.28 CA aTDC and burn duration was reduced from 17.2 to 16.9 CA. Figure 4.7 shows the change of in-cylinder pressure. There is an obvious increase of peak pressure when the ignition timing was advanced due to the knock mitigation effect by oil jet injection.

The exhaust temperature was decreased from 606.4 to 599.4°C which implies the energy conversion from exhaust enthalpy decrease to efficiency increase.

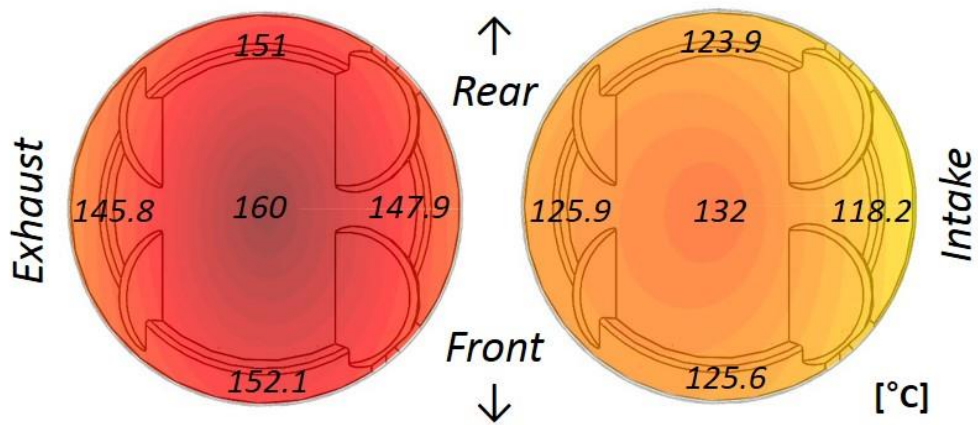


Figure 4.6 Piston temperature distribution during the oil jet injection at 1500 rpm, 7.2 bar, knock incidence: 10%

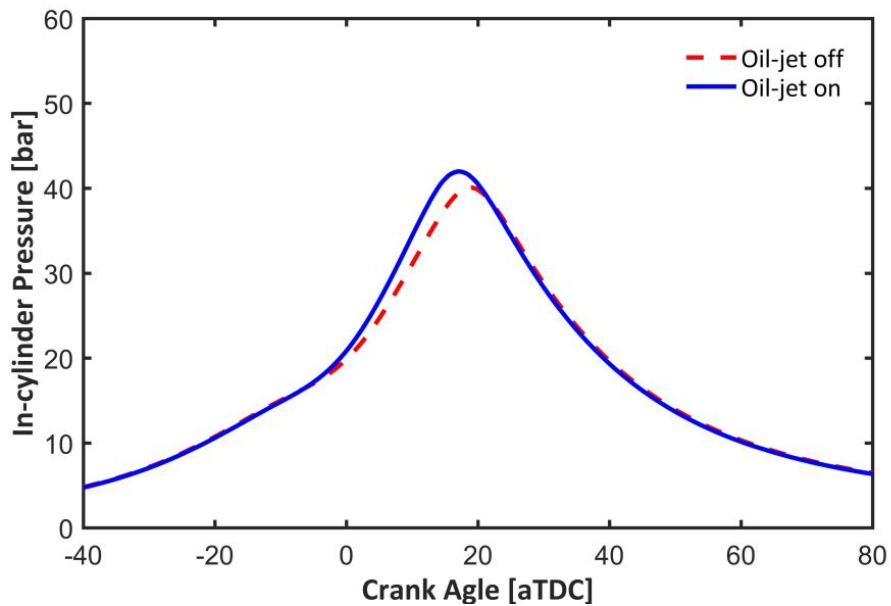


Figure 4.7 In-cylinder pressure during oil-jet injection at 1500 rpm, 7.2 bar, knock incidence: 10%

The knock mitigation effect was quantified in two different ways in this paper: ignition timing advance and load limit expansion. Ignition timing advance is more practical and axiomatic approach because it increases efficiency directly. However, every engine has different knock characteristics. For example, different maximum load, different combustion phasing for MBT, etc. produces difficulties for comparison when using the quantification of ignition timing advance method.

#### **4.1.4 Load limit expansion**

It is very important to improve the knock resistance for enhancing engine thermal efficiency. Cooling down the engine helps to increase anti-knock characteristics. In this study, knock mitigation effect was obtained and observed by controlling the temperatures of each component of the cylinder head, liner and the piston. In this section, the effect of coolant temperature decrease is observed.

PFI engine was used and the compression ratio was 12.5, knock incidence was maintained at 15% and the ignition timing was adjusted to the timing which makes CA50 to be 8 CA aTDC. The MBT timing might be slightly different depending on the engine operating condition such as load, speed, thermal boundary temperature, however, it was neglected in this study observing there was no remarkable difference.

As the coolant temperature was decreased, additional knock suppression was achieved. Therefore, while the combustion phasing was maintained, the expansion of load limit was possible. As the air-fuel amount increase, the pressure increases leading to the increase of in-cylinder temperature thus in-cylinder condition turns into more knock-prone condition. During the test, while maintaining the stoichiometric condition ( $\lambda=1$ ), the load was increased until the knock incidence reached to the target.

Figure 4.8 shows the load limit of each coolant temperature condition under 1500 rpm and 2000 rpm. The pressure curves are shown in figure 4.9, and it is confirmed the combustion phasing was maintained at the same timing. Both coolant temperatures of cylinder head and liner were decreased from 80°C to 60 simultaneously, and no oil injection to piston was applied. As it is apparently shown, the load limit was expanded as the coolant temperature decreased. At 1500 rpm, 17.8% and 26.9% of load limit expansion was achieved at 60°C and 40°C of coolant temperature conditions, respectively. Likewise, at 2000 rpm condition, 7.58% and 13.2% of load limit expansion was achieved in each condition.

The overall load limit was higher at 2000 rpm case than at 1500 rpm. In higher engine speed, due to the stronger intake air charge motion, the turbulence intensity is larger which makes the shorter burn duration. This helps the flame can be reached to the end-gas before the auto-ignition occurs. In addition, faster air flow motion enhances heat transfer between the unburned gas region and the cylinder wall during the compression and combustion process leading to further suppression of knock. However, faster air flow also may increase the heat transfer during the intake process that increases the overall gas temperature. There should be a trade-off on effect between increased convective heat transfer and decreased time in higher engine speed in this point of view. The experimental result, by observing the achievement of higher load limit in higher engine speed (2000 rpm), implies that the deterioration by increased convective coefficient was compensated. Increased flame speed, enlarged heat transfer during compression and less-timed heat transfer during intake might contribute to the knock suppression. This will be discussed with simulation result later in this study.

To verify the validity of knock incidence method, overall experiments under different knock incidence were conducted and the result is shown in figure 4.10. Knock incidence target was varied from 0% to 30%. The coolant temperature was

varied from 80°C to 40°C and the independent cooling cases were also tested. If one coolant temperature was decreased, the other one was fixed to 80°C. For example, 'Liner 60°C' in the figure means that the liner coolant temperature was decreased to 60°C while the head coolant temperature was maintained to 80°C.

Even though the load limit was expanded as the knock incidence target was increased from 0% to 15% till 30%, but the propensity was the same. Up to 31.44 % of the load increase was achieved with aggressive cooling, including the oil jet injection to the piston. Furthermore, it is shown that the cooling head coolant has the larger effect than cooling liner. The effect of oil injection to piston and the independent cooling will be discussed later in this study.

Figure 4.11 shows the temperature distributions of different thermal conditions. upper diagrams show the temperatures of the cylinder head and the lower diagrams are that of the piston. On the left side, the coolant temperature was 80°C for both the head and cylinder without oil jet injection to piston. And it is shown in the right side that the coolant temperature was 40°C for both and oil was injected to the piston. CA50 was maintained to 8 CA aTDC for both cases by adjusting the ignition timing, thus the load of right side was higher (7.83 bar) than the left side (5.95 bar) which are the last and the first cases of figure 4.10, at knock incidence of 15%.

Cylinder head surface shows 30 to 35°C of temperature decrement while the piston surface shows approximately 40°C drop. Because the piston temperature is largely affected by the conduction between the piston and the liner, the temperature decrease of the liner wall led to the further decrease of the piston surface temperature. On the cylinder head temperature, it was shown that the front side is hotter than the rear side and the exhaust side is hotter than the intake side. In this engine, the coolant flows from the rear side to front side, therefore the front side show the higher temperature. The temperature of the exhaust side is higher

mainly due to the exhaust gas. However, this distribution is not observed on the piston surface temperature. This also implies the temperature distribution of the piston surface is independent with the head surface. In addition, as it is previously described and shown the figure, the exhaust side shows the higher temperature than the intake side on the piston while the injecting the oil into the piston cooling gallery.

Piston cooling effect was verified with overall conditions. Figure 4.12 shows the load limit expansion under 1500 rpm. The blue line indicates the maximum load when oil jet injection was applied under various coolant temperatures. And the red line indicates the cases without oil jet injection. Effect was found to be similar in overall conditions under different coolant temperature. It was also verified in 2000 rpm as shown in figure 4.13. For all cases, 5.1% of load increase was achieved by oil jet injection, while the piston surface temperature was decreased 28°C in average, corresponding 0.18% knock limit expansion per unit temperature decrease of piston while there was no remarkable change in head, liner surface temperatures.

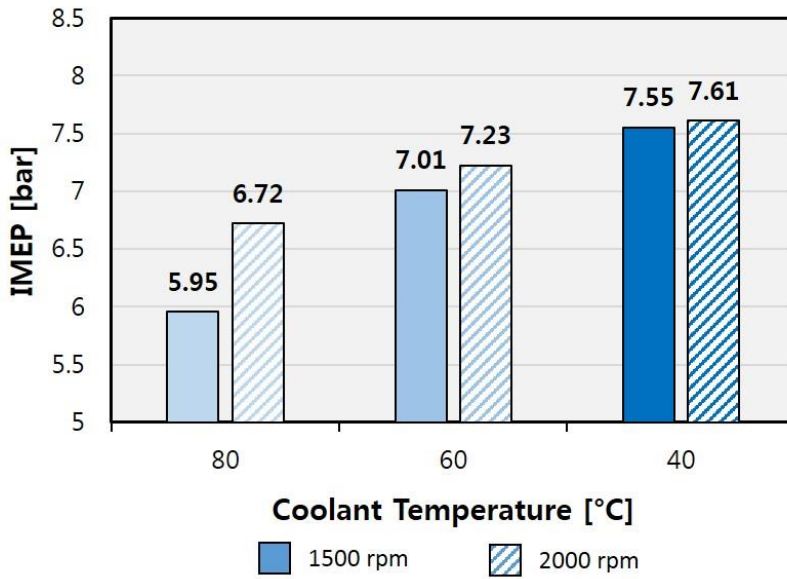


Figure 4.8 Load limit under coolant temperature decrease at 1500 and 2000 rpm

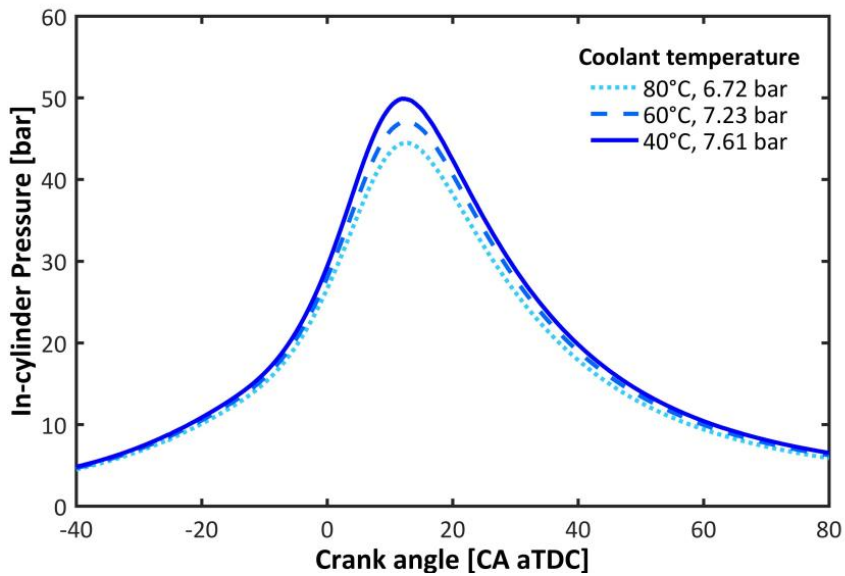


Figure 4.9 In-cylinder pressure of load limit increase at 2000 rpm

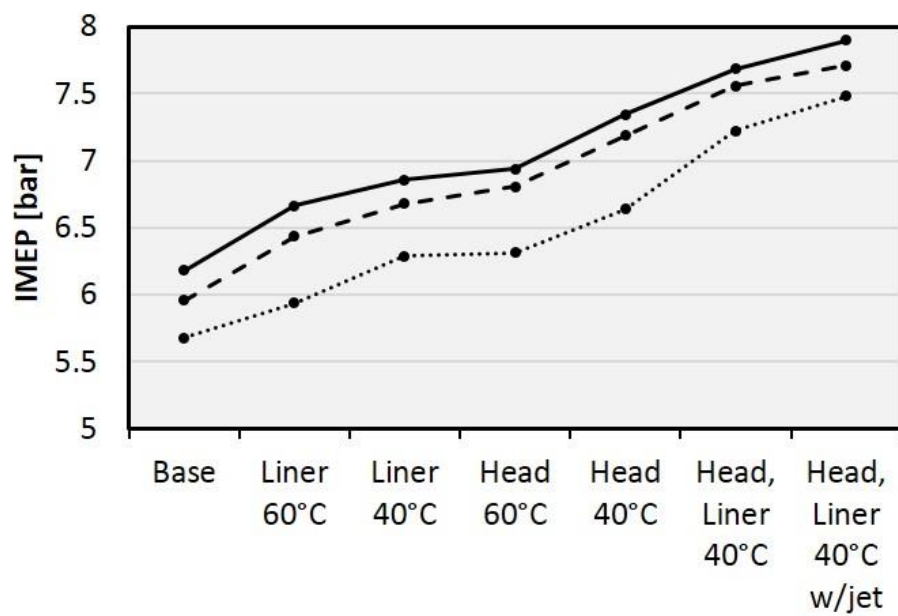


Figure 4.10 Load limit expansion under different knock incidence

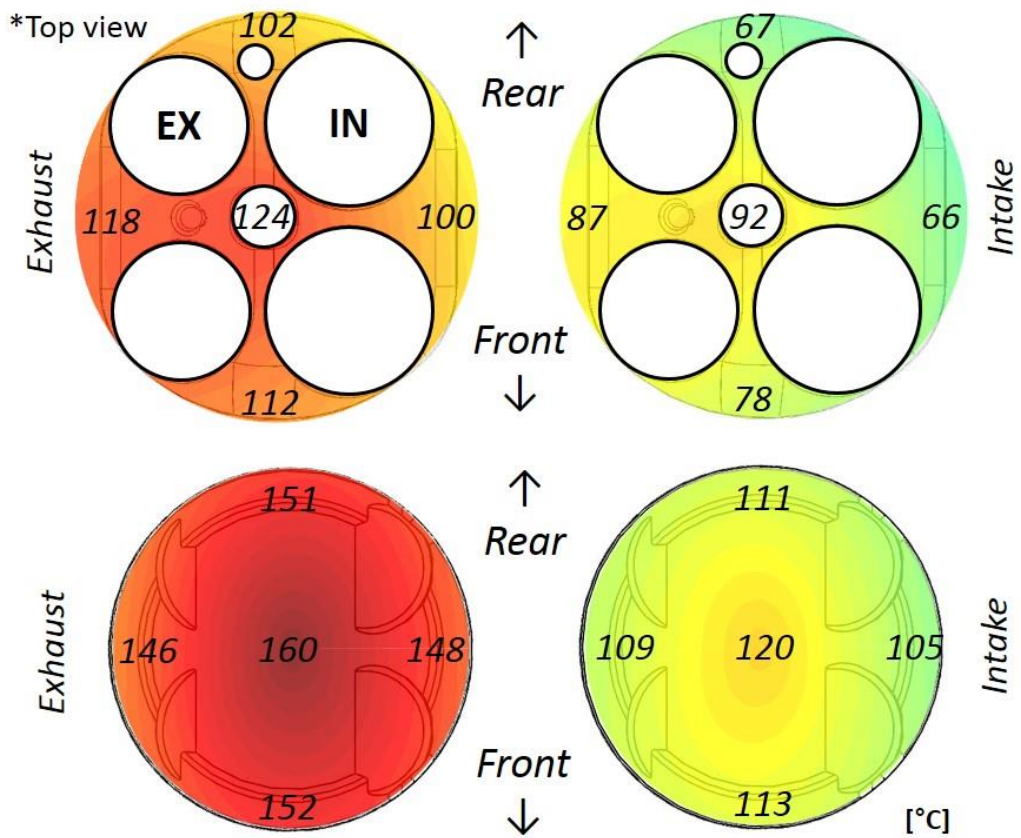


Figure 4.11 Head and piston surface temperature distribution,  
 left: 80°C Tcoolant w/o oil-jet injection  
 right: 40°C Tcoolant w/ oil-jet injection

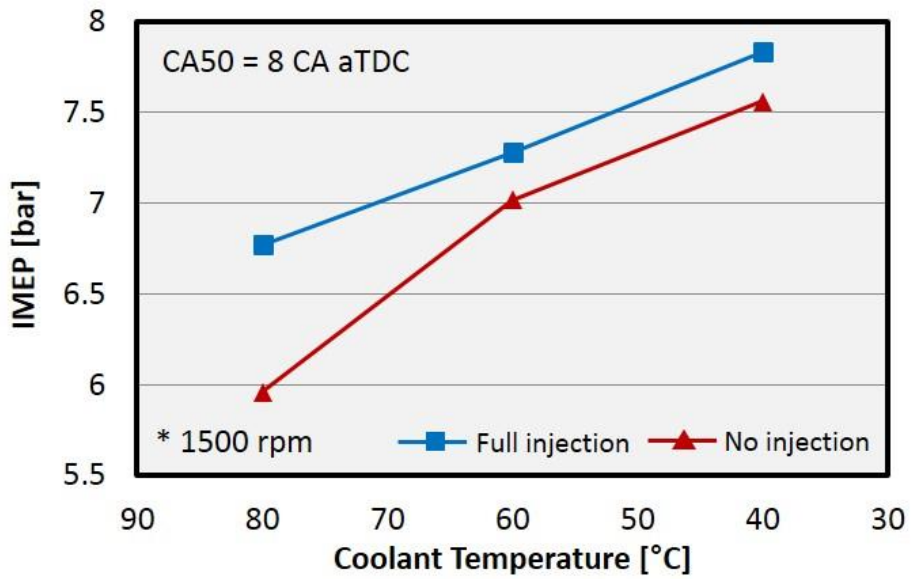


Figure 4.12 Effect of oil-jet injection in load expansion at 1500 rpm

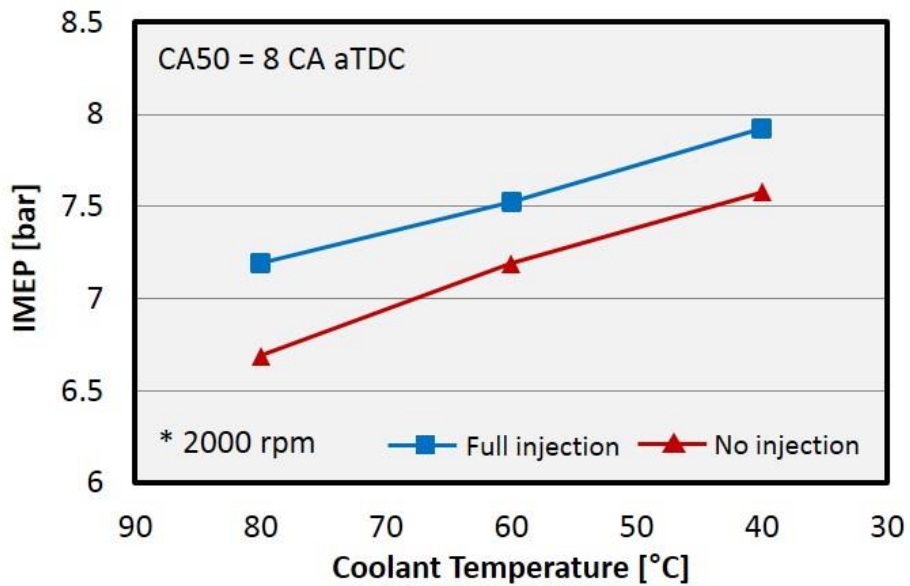


Figure 4.13 Effect of oil-jet injection in load expansion at 2000 rpm

## 4.1.5 Efficiency increase by ignition advance

### 4.1.5.1 Efficiency increase under constant fuel amount

Even though knock mitigation can utilize the expansion of the load limit, it doesn't imply knock mitigation can lead to the increase of efficiency. In general engine operating condition, knock occurs in the low-end torque region, where is already above of the sweet-spot of the specific fuel consumption map so the operation in increased load can deteriorate the efficiency.

Recently, a large amount of spark-ignited engines is equipped with turbochargers. Consequently, engine is frequently operated in boosted condition where ignition timing has to be retarded because of knocking behavior and so is naturally aspirated engine under higher load condition. This section describes the efficiency increase by knock mitigation. Under the constant amount of fuel input condition, if the ignition timing can be advanced in consequence of knock suppression, this clearly will increase the load which results in the increase of efficiency.

PFI engine was also used, the compression ratio was 12 and the coolant temperature was decreased from 85°C to 72.5°C until 60°C. The fuel injection amount was maintained at 24 mg/cycle under stoichiometric condition; lambda was maintained to unity in all operating conditions. As the coolant temperature decreased from 85 to 72.5 and 60°C, the ignition timing could be advanced from 11.8 to 13.7, and 15.3 CA bTDC, respectively, while maintaining the same knock incidence of 10%. These ignition timings are frequently called KLSA (knock limit spark advance). CA50 was advanced from 15.93 to 13.82 and 12.49 CA aTDC. The comparison of the in-cylinder pressure and the intake pressure are shown in figures 4.14 and 4.15, respectively.

As the ignition timing was advanced, under the same amount of fuel condition, the load was increased, which means the increase of the efficiency and decrease of the indicated specific fuel consumption. Figure 4.15 shows the KLSA and following load. In this condition, when the coolant temperature reached to 60°C, the KLSA was almost the same timing with MBT. Without additional oil jet injection, IMEP could be increased from 7.47 to 7.56, and 7.59 bar, respectively, as the coolant temperature was decreased from 85 to 60°C. Further knock mitigation with oil jet injection to piston cooling gallery was achieved. The ignition timing could be advanced to 16.5 CA bTDC, however, the load increase was not remarkable (7.6 bar) because the MBT timing was already achieved. Figure 4.17 shows ISFC of each case. Consequently, ISFC was decreased from 231 to 227.6 g/kWh corresponding to approximately 1.5% relative increase of indicated efficiency.

Combustion efficiency was 98.5%, 98.4% and 98.3% for each condition as shown in 4.18, respectively. The induced air mass was not measured due to the experimental uncertainty. However, because the combustion efficiency was the same level within the experimental error which grants the air mass can be assumed the same. As a result, decreasing the coolant temperature doesn't reduce the combustion efficiency. The calculation methods for combustion analysis is described in chapter 2.

Figure 4.19 shows the emission result at 1500 rpm. Slight increase, but not noteworthy, of CO and THC was noticed in both engine speeds, as the coolant temperature was decreased. However, even though the ignition timing was advanced, NO<sub>x</sub> emission was maintained at the same level. This implies the overall gas temperature during combustion could be decreased by wall temperature decrement. This can be also verified by the noticeable increased gas density by observing lower intake pressure in figure 4.15.

It was observed that the combustion duration was decreased (15.93 CA → 13.83 CA → 12.49 CA) followed by the ignition timing advance. In P-V diagram in figure 4.20, it is clearly shown that the engine was run within the negative valve overlap condition, and this was intended to exclude the residual gas effect as much as possible during the operation. As shown in the figure 4.15, the intake pressure was lower at 60°C condition, but PMEP (pumping mean effective pressure) showed no significant difference at 60°C condition (0.275 bar) and is within the experimental error: 0.279 bar at 72.5°C and 0.272 bar at 85°C. As it can be assumed that the induced air mass was the same in all three conditions, in lower coolant temperature condition, the heat transfer from the engine walls to the intake gas was reduced, resulted in the lower pressure value during the intake and compression stroke. Moreover, the advanced ignition timing leads to the conversion of exhaust enthalpy to work, thus, exhaust pressure was also lower than higher coolant temperature condition. Consequently, no significant increase of pumping loss was observed.

Figure 4.21 shows the energy balance of initial heating value of fuel. The method for analysis is well described in chapter 2. From the analysis, it was clearly shown that the exhaust loss converted into the work while the ignition timing was advanced by further knock mitigation. Cooling loss was increased very slightly for approximately 2.5 J/cycle (less than 0.7% of total energy) as the wall temperature decreased. This implies that decreasing coolant temperature not only decrease the wall temperatures, but also may decrease the gas mixture temperature and this can be verified with the no remarkable change in NO<sub>x</sub> emission. It reduces the heat transfer amount during the intake process and also reduce the heat transfer to the wall during compression and combustion process, therefore, the overall cooling loss was not significantly changed.

Figure 4.22 shows the temperature variation during combustion of 85°C and 60°C cases. The temperatures were calculated using 3D simulation. From dotted line, the case of 85°C coolant condition, as the ignition timing advanced from 11.8 to 15.3 CA bTDC, the in-cylinder pressure was increased, approximately resulted in 788 K increase of maximum temperature while maintaining the same intake pressure. However, in actual condition, intake pressure was decreased due to the increase of gas density by wall temperature decrease. This is indicated with blue line in the figure, 40K of temperature decrease was observed. This also supports the experimental result: peak temperature could be still low although the ignition timing was advanced.

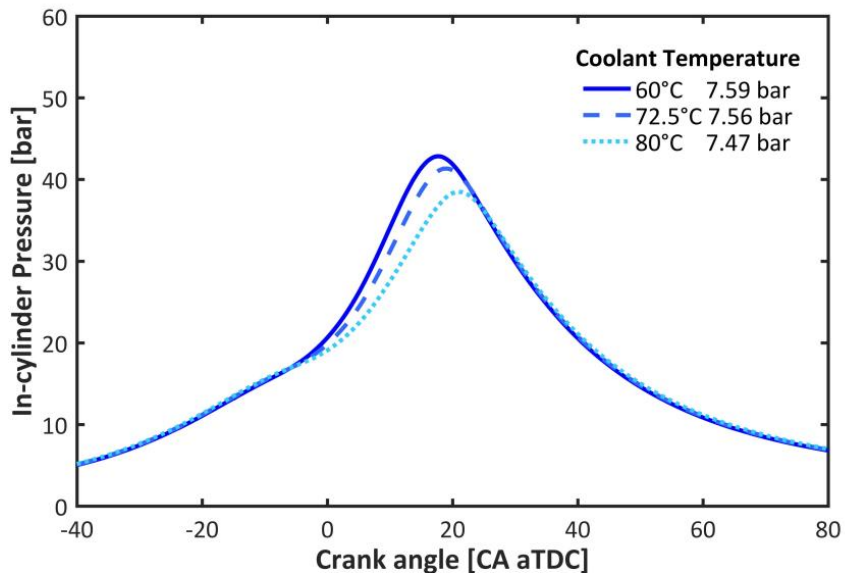


Figure 4.14 In-cylinder pressure at 1500 rpm under cooling

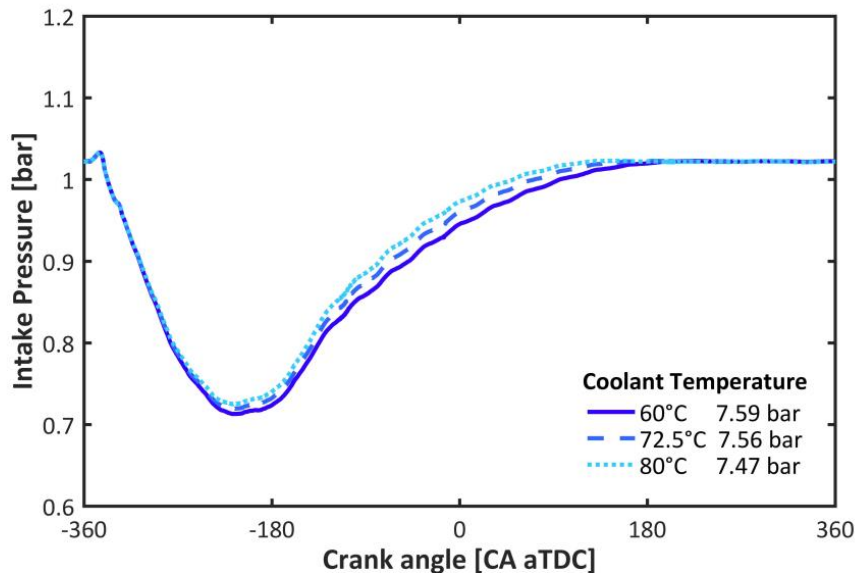


Figure 4.15 Intake pressure at 1500 rpm under cooling

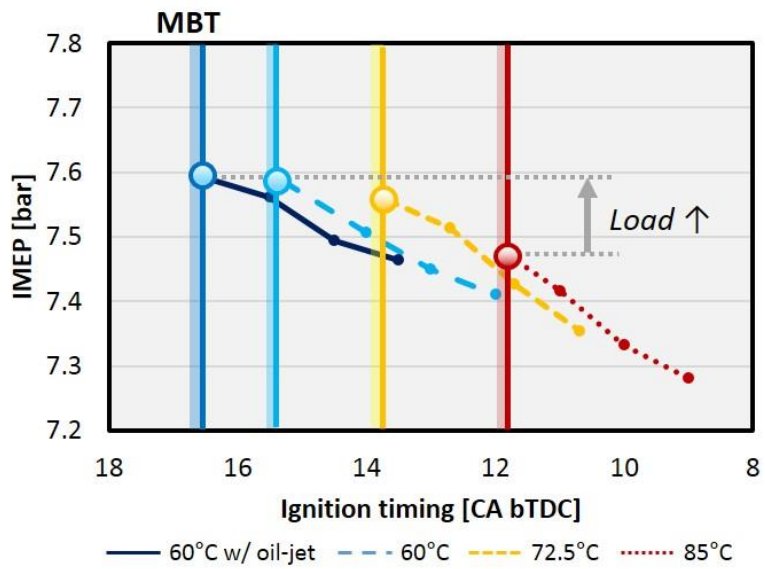


Figure 4.16 Load increase at 1500 rpm under cooling

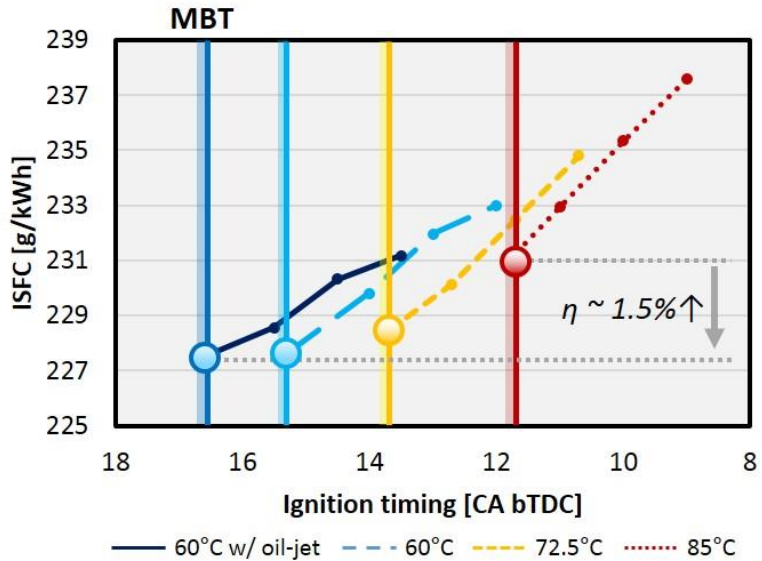


Figure 4.17 Efficiency increase at 1500 rpm under cooling

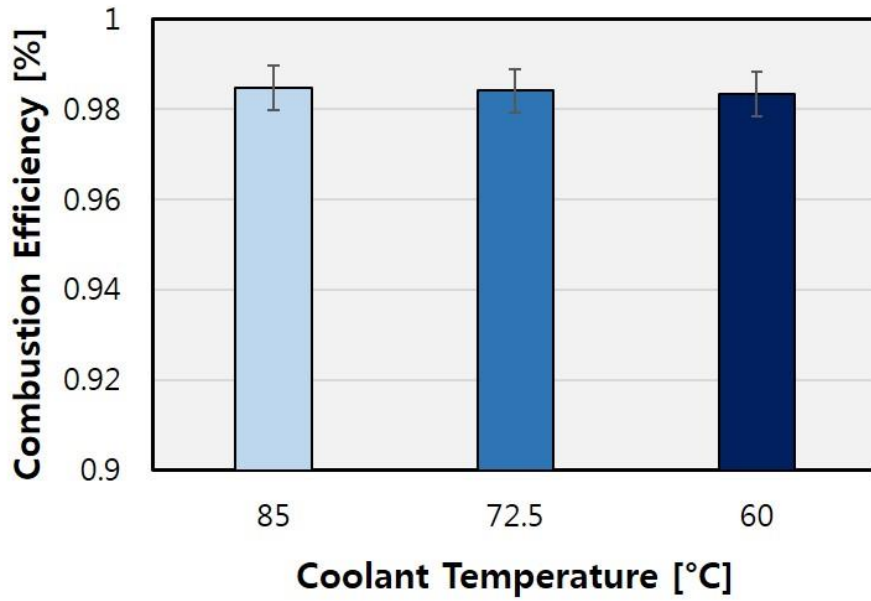


Figure 4.18 Combustion efficiency at 1500 rpm under cooling

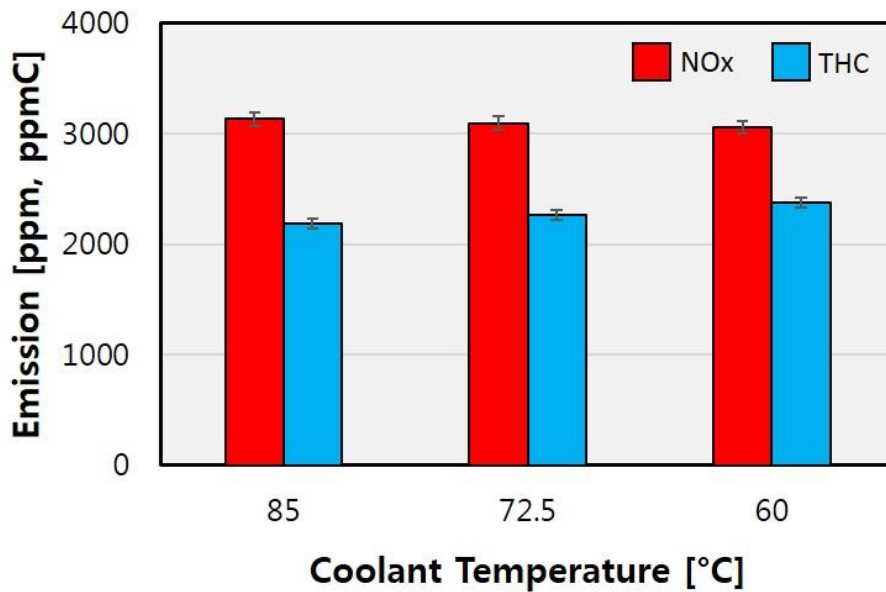


Figure 4.19 NOx and THC emission at 1500 rpm under cooling

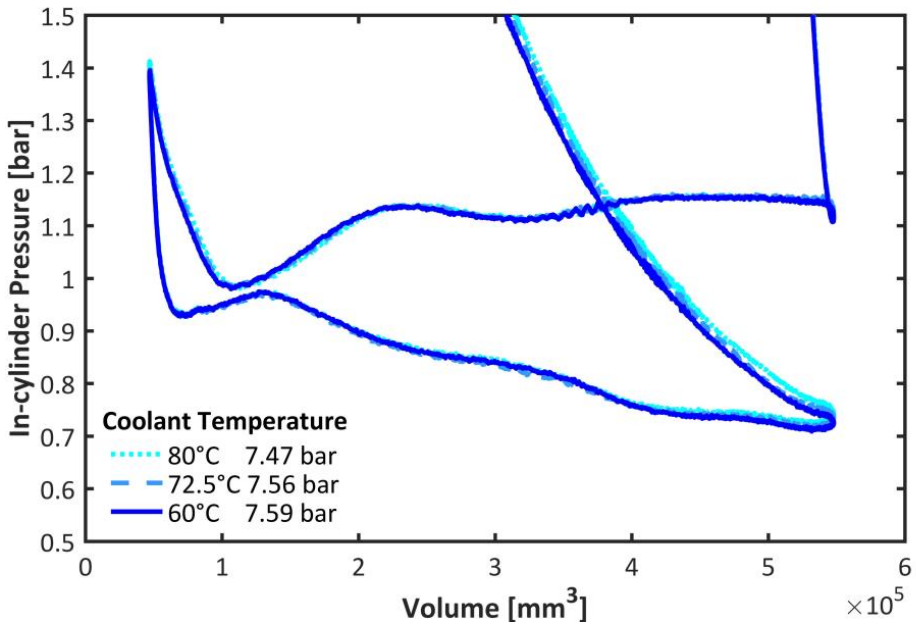
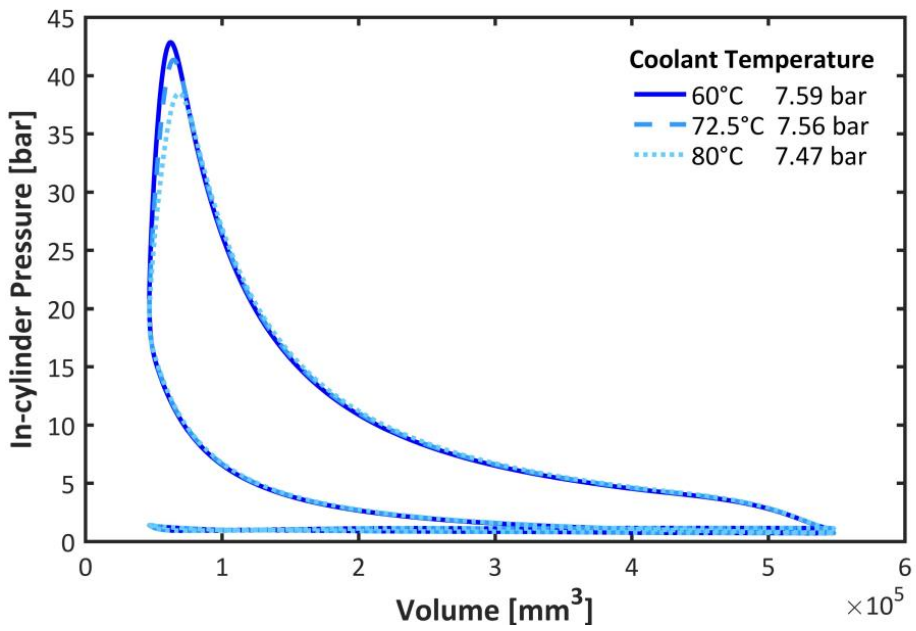


Figure 4.20 P-V diagram at 1500 rpm under cooling

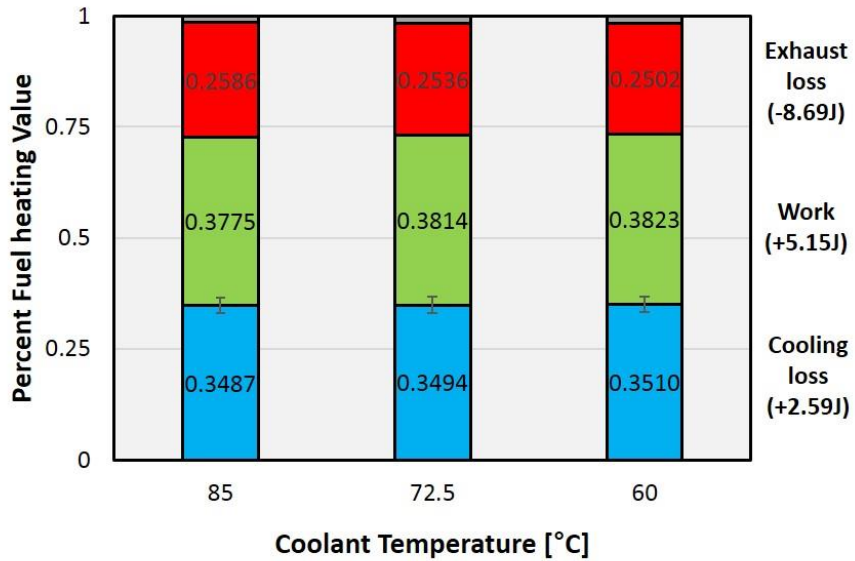


Figure 4.21 Percent fuel heating values at 1500 rpm under cooling

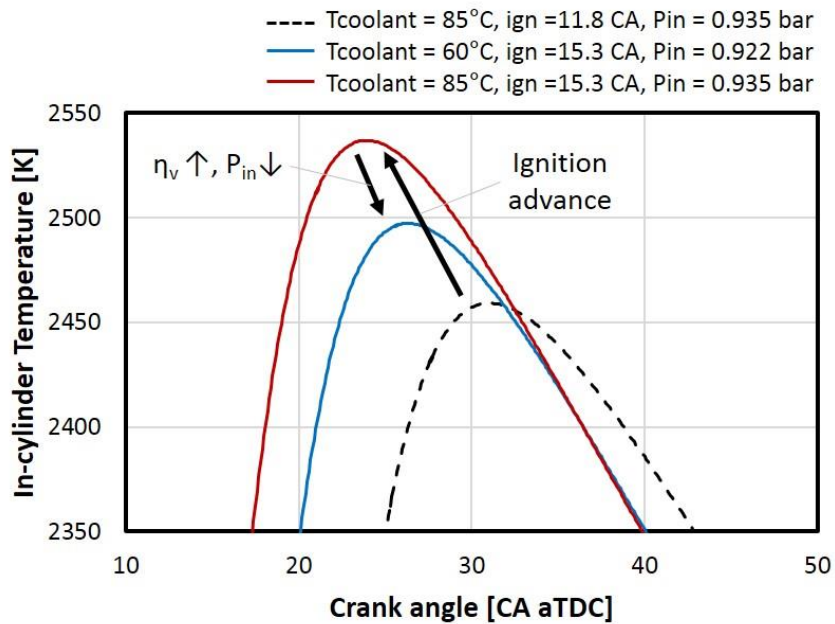


Figure 4.22 Comparison of in-cylinder temperature under cooling

#### 4.1.5.2 Efficiency increase under constant load

Engine has to be calibrated to generate an appropriate and immediate torque demanded by the driver while driving. Therefore, the main target of the engine calibration is usually the torque at a certain engine speed. In previous section, the potential of efficiency increase under the same amount of fuel input condition was discussed. In this section, very similar, but the potential of efficiency increase while maintaining the same load is investigated.

In figure 4.23, ignition timing and ISFC are shown under the same load and engine speed condition. Either PFI engine was used with compression ratio of 12, and the load was 6.9 bar of IMEP and the engine speed was fixed at 1500 rpm where the MBT timing was achieved at the load limit under 85°C coolant temperature condition. Knock incidence was 10% for all conditions in this section. While maintaining the same load, as the coolant temperature was decreased, the ignition timing could be advanced. From 17 to 22.3 CA bTDC of ignition timing advance was achieved eventually. This corresponds to 0.21 CA of advance for every unit degree of coolant temperature decrease. Combustion phasing, CA50, also showed an advance from 12.5 to 8 CA aTDC. Indicated efficiency was increased from 36.4 to 37.5% (3% increase). ISFC also showed a decrease from 230.8 to 224.1 g/kWh. In addition, the tendency seems to be very linear.

Figure 4.24 shows the case of 2000 rpm and 7.3 bar of IMEP. The target load was determined in the same manner at 1500 rpm case. Because higher engine speed is more robust for knocking, thus the load was higher in 2000 rpm case under the same knock incidence. Linear correlation between ignition timing and the coolant temperature was also observed, and so was the efficiency. ISFC was decreased from 232 to 224 g/kWh corresponding to the increase of indicated efficiency from 37.53 to 36.24% (3.56% increase) while the ignition timing could

be advanced from 25 to 18.5 CA bTDC. CA50 was moved from 12.4 to 7.8 CA aTDC. As the gas density increased followed by decrement of coolant temperature, of course, the average intake manifold pressure was decreased from 0.93 to 0.9 bar.

Figures 4.25 and 4.26 show the emission results at the 1500 and 2000 rpm, respectively. The similar result was shown with the previous section in both engine speed conditions. NO<sub>x</sub> emission showed no significant increase as the ignition timing advanced in a consequence of coolant temperature decrease. This also implies overall reduced gas temperature suppressed the NO<sub>x</sub> formation during the combustion. Slight increase THC and CO was observed but it was not significant and within the experimental error.

Figure 4.27 shows the exhaust temperature of both engine speed cases while the coolant temperature was decreased. Overall exhaust temperature is higher in 2000 rpm than 1500 rpm case mainly due to less heat transfer loss and the higher load operation. As the ignition timing increased, it is clearly shown that the exhaust temperature was decreased, which means the decrease of exhaust loss mainly converted into work increase. This was also verified in previous section.

As it is interpreted previously, demanded torque is quite important for calibration process in engine development. Effect will be larger under boosted condition where the load and operation is dominated and restricted by knocking behavior. Thus, it is meaningful to investigate the knock suppression effect under the same load condition and the result showed a larger effect than the constant fuel amount condition. This underpins as well that high efficiency achievement is highly effective though knock mitigation by wall temperature decrement.

The effect of oil jet injection was also tested under the same load conditions. As it is previously demonstrated in figure 4.7, when the oil jet was applied,

lowered piston surface temperature alleviated the knocking behavior, and contributed to an advance of ignition timing. Figures 4.28 and 4.29 shows the ignition timing advance by oil jet injection under different coolant temperature conditions at 1500 and 2000 rpm, respectively. The compression ratio was 12.5. The ignition timing could be advanced maximum 3 CA at 1500 rpm, 7.2 bar and 1.5 CA at 2000 rpm, 7.5 bar. The flow was reduced by closing oil supply valve, and the result is indicated as half injection. For example, when both coolant temperatures were 80°C, average piston surface temperature was reduced from 154.6°C, 143.7 to 133°C at full, half injection, no injection case, respectively. In average, 2.1 CA advance of ignition timing at 1500 rpm and 1.4 CA advance was obtained at 2000 rpm. It was also found that the effect of oil jet injection corresponds to 10-15°C simultaneous decrease of both coolant temperatures.

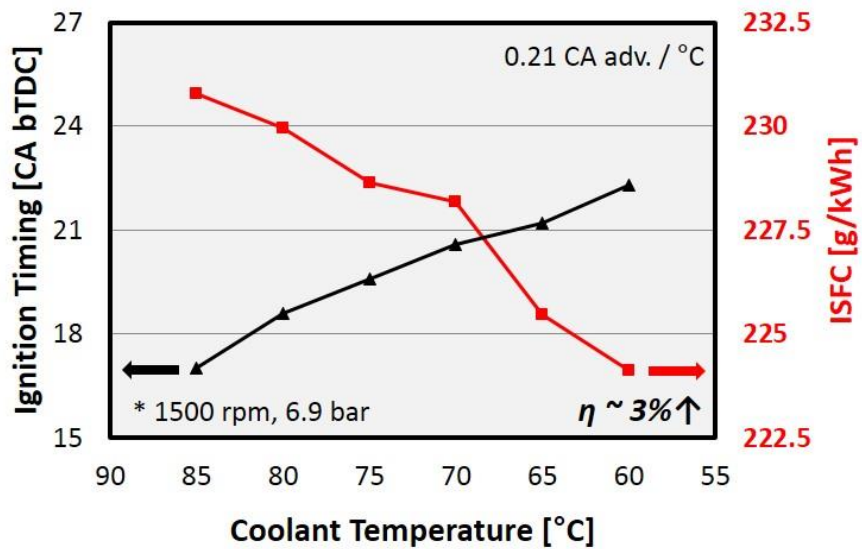


Figure 4.23 KLSA and efficiency increase at 1500 rpm, 6.9 bar under cooling

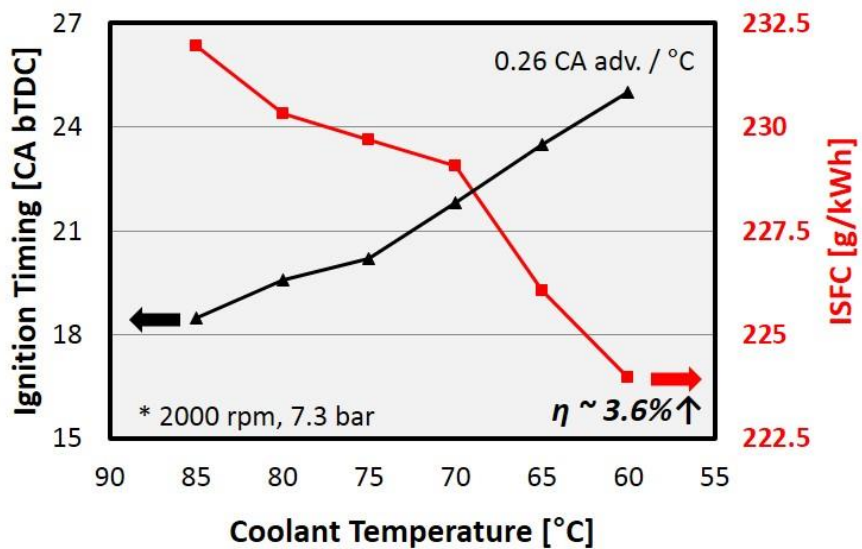


Figure 4.24 KLSA and efficiency increase at 2000 rpm, 7.3 bar under cooling

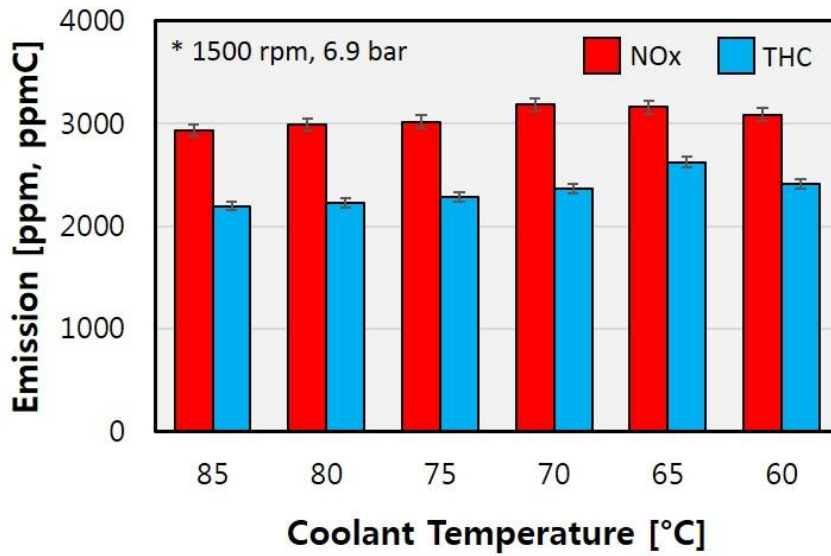


Figure 4.25 NOx and THC emissions at 1500 rpm, 6.9 bar under cooling

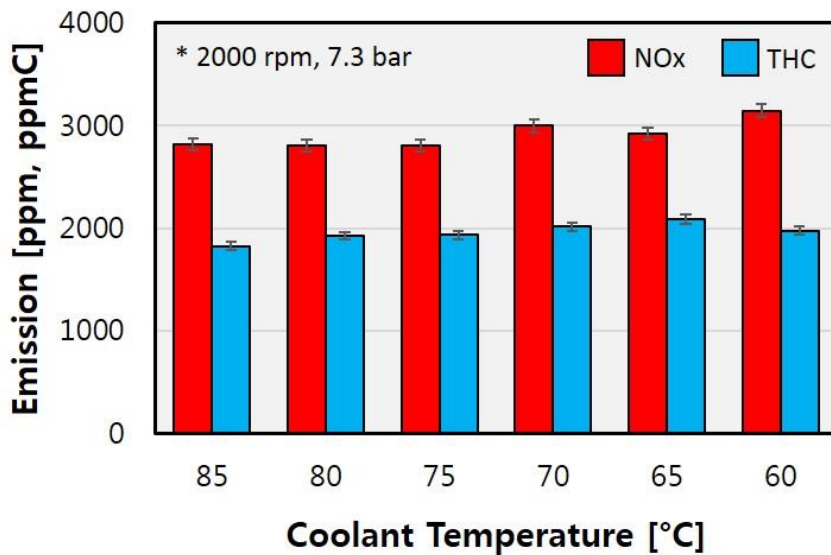


Figure 4.26 NOx and THC emissions at 2000 rpm, 7.2 bar under cooling

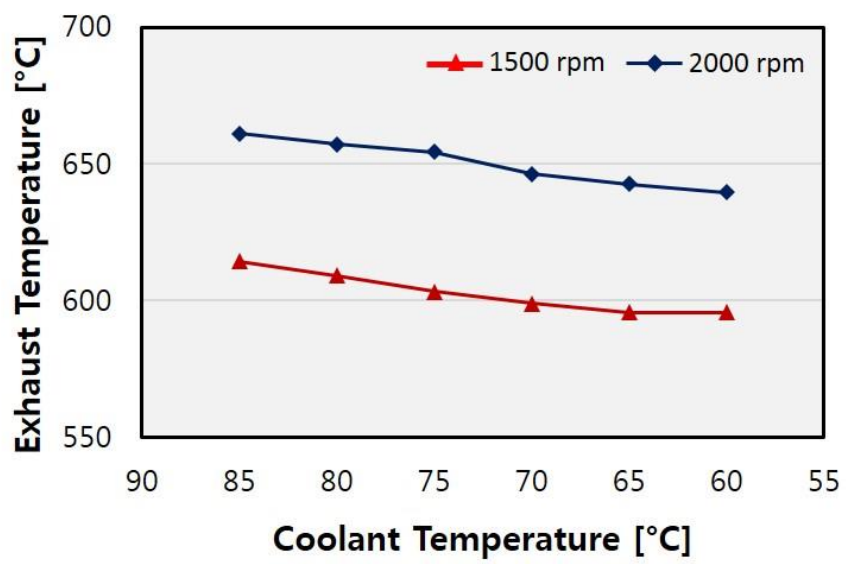


Figure 4.27 Exhaust temperature variation at 1500 and 2000 rpm under cooling

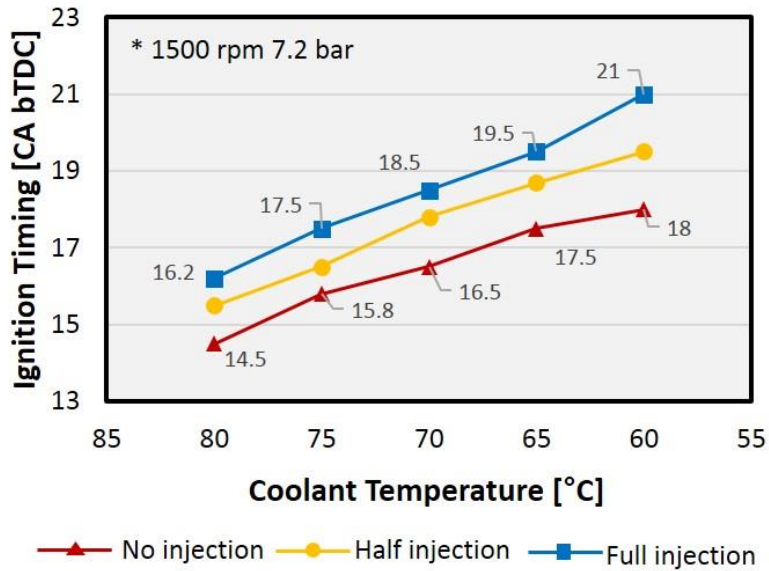


Figure 4.28 Effect of oil-jet injection to piston at 1500 rpm

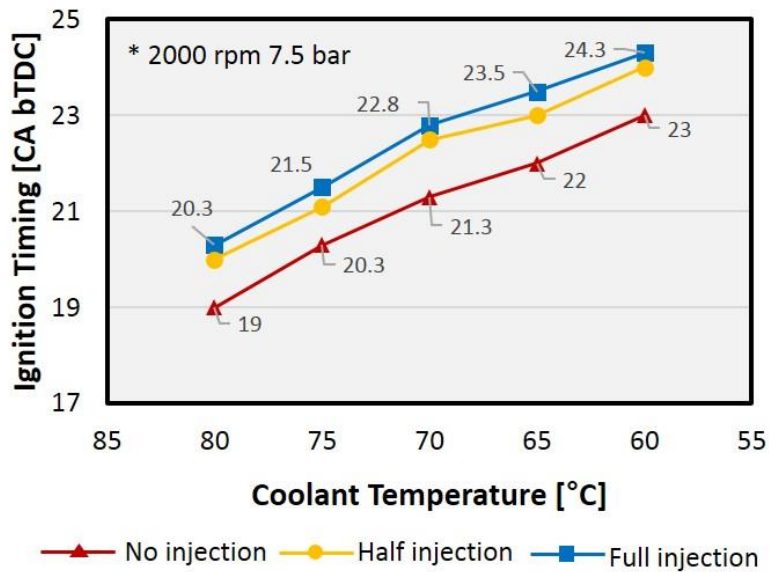


Figure 4.29 Effect of oil-jet injection to piston at 2000 rpm

## 4.1.6 Effect under different conditions

Even though the knock mitigation effect through the cooling has an advantage on efficiency increase, it needs to be verified in different engine types to be strategically used in development process. In this section, the investigations under different engine geometry are shown. Also, effects under different intake temperature were also investigated.

### 4.1.6.1 Knock mitigation effects in GDI engine

In GDI engine, due to the charge cooling effect of direct injected fuel, in-cylinder temperature can be decreased efficiently and this is one of the strengths that GDI type engine has compared to PFI engine. In every tests in this section, the knock incidence was also maintained at 10%.

In figure 4.30, the load limits of PFI and GDI engines are shown at 1500 and 2000 rpm. Knock incidence was 10% for all of the conditions and coolant temperatures were maintained at 85°C. Effective compression ratios of both engines were the same as it is previously described. CA50 was maintained at 8 CA aTDC in all cases.

Assuming the constant volume specific heat value( $C_v$ ) of air is 0.718 kJ/kg·K and HoV(heat of vaporization) of gasoline fuel is 305 kJ/kg, the effect of temperature drop was calculated. In PFI load limit condition at 1500 rpm, it was calculated that 14.3K can be decreased at IVC timing if 50% of fuel contributes to charge cooling effect (28.6K drop if a hundred percent contributes). This leads

to over 25K decrease of unburned gas temperature at averaged knock onset assuming adiabatic compression process.

Figure 4.30 shows the result of the test. The engine speed was 1500 rpm, and the injected fuel amount was fixed to 28 mg/cycle which is more than PFI case in section 4.2.2.1. Because GDI engine has the larger charge cooling effect, so it is well known to have higher knock resistance than PFI engine thus the load limit was higher than PFI engine case as it is previously mentioned. As coolant temperature decreased from 85, to 72.5 and 60°C, the load was increased from 9.16, to 9.23 and 9.3 bar of IMEP, followed by the ignition advance from 6, to 8 to 10 CA bTDC, respectively. CA50 was moved from 15.8 to 11.4 CA aTDC and ISFC was decreased from 212 to 216.9 g/kWh corresponding to the 1.4% increase of indicated efficiency as shown in figure 4.32 (38.22 → 38.5 → 38.75%). Knock mitigation effect was shown to be valid in direct injection type engine without any reversed tendency which might be caused from less fuel evaporation problem.

In addition, to verify the effect of oil jet injection to piston cooling gallery, while maintaining the coolant temperatures at the same as 85°C, test of ignition timing advance was conducted. When oil was injected, a significant enhancement was noticed. The KLSA could be moved from 3.5 to 6 CA bTDC and this led to the 1.3% of efficiency improvement which is almost similar to the effect of coolant temperature decrease to 60°C. Of course, IMEP could be increased from 9.04 to 9.16 bar.

As the piston surface has a large area among the components of combustion chamber, decreasing piston temperature is very effective to lower the gas temperature. In the intake process, the air-fuel mixture has a large heat transfer with piston, therefore, decreasing piston temperature not only has an effect decreasing the unburned gas temperature during combustion but also has an effect decreasing the intake gas temperature before IVC. This will be discussed later.

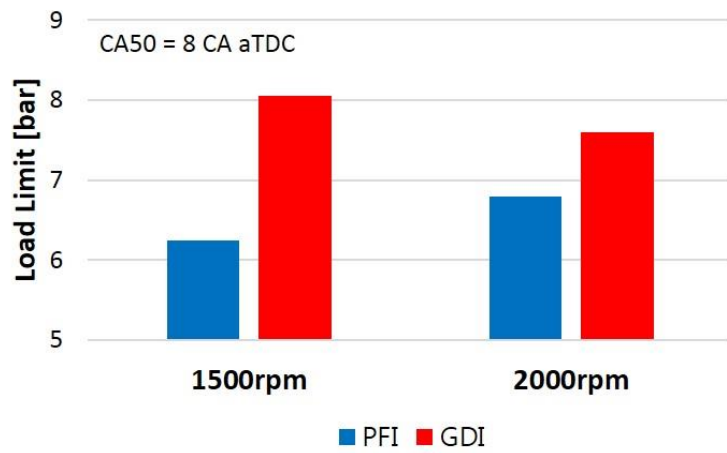


Figure 4.30 Load limit of PFI/GDI engines at 1500 and 2000 rpm

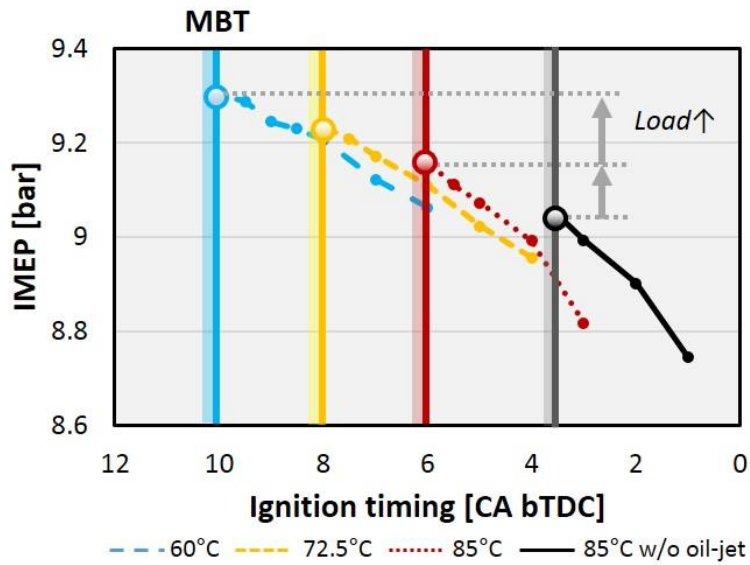


Figure 4.31 Load increase in GDI engine at 1500 rpm under cooling

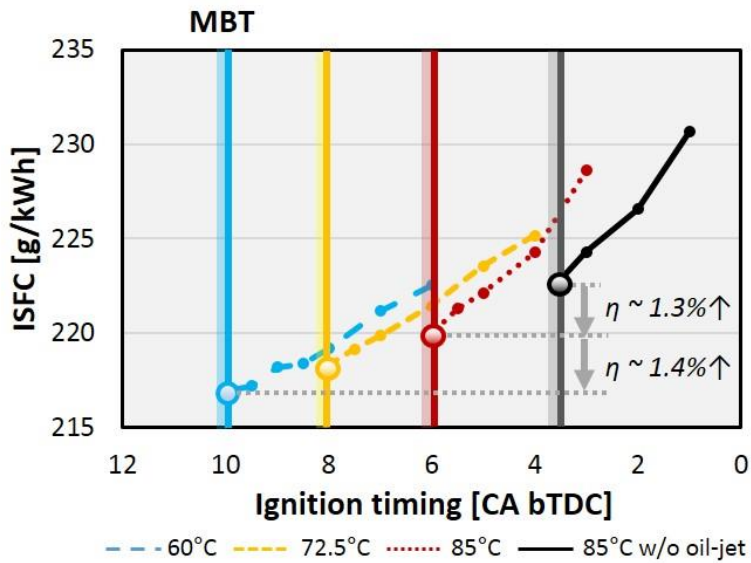


Figure 4.32 Efficiency increase in GDI engine at 1500 rpm under cooling

#### 4.1.6.2 Load limit expansion under different bore-to-stroke ratio

As it is explained in chapter 3, three different engines of different bore-to-stroke ratio (B/S), were tested. B/S 1.0 (bore: 86 mm, stroke: 86 mm), B/S 0.84 (bore: 81 mm, stroke: 97 mm) and B/S 0.68 (bore: 75.6 mm, stroke: 111 mm), three types were used and these engines have the same compression ratio. Designed compression ratio was 12, however, due to the errors in machining process, there was slight difference when they were assembled. Thus, the actual compression ratio was modified to  $12 \pm 0.1$  by adjusting the thicknesses of shim plates and it was confirmed by using an ultrasonic measurement device, CompRatio™-D3 [143]. Figure 4.32 shows the shape of chamber components of three engines. Using the same crankcase and block of GDI engine, cylinder liner and moving parts including the crankshaft, piston and connecting rod was changed.

Figures 4.33 and 4.34 show the load limits of three B/S ratios under different coolant temperatures at 1500 and 2000 rpm, respectively. As the coolant temperature decreased, the load limit was expanded while the CA50 was maintained at 8 CA aTDC. Additional mitigation effect seems to be the same by the coolant temperature decrease as it is observed as the similar slope.

Under the same coolant temperature, lower B/S ratio engine shows the highest load under the same level of knock occurrence (10% of knock incidence). The burn duration at 1500 and 200 rpm, CA10 to CA90, is shown in figures 4.35 and 4.36 respectively. The combustion is faster in lower B/S condition, and it is thought that faster mean piston velocity led to the higher turbulent velocity. Because two different heads were designed to have the same tumble ratio of 1.35, and tested on a flow tumble bench. It seems that faster flame speed by enhanced turbulent intensity contributed to further knock suppression, led to the higher knock limit. However, at 1500 rpm, in the B/S 0.68 case, the load limit was not

significantly expanded compared to B/S 0.84 case. At 2000 rpm, as B/S decreases, burn duration was clearly shortened. However, there was no significant difference in burn duration at 2000 rpm. Nevertheless, the load limit was expanded in lower B/S. It can be concluded that not only flame speed is a dominant factor in knocking tendency, but the heat transfer between walls and air-fuel mixtures also have a large effect.

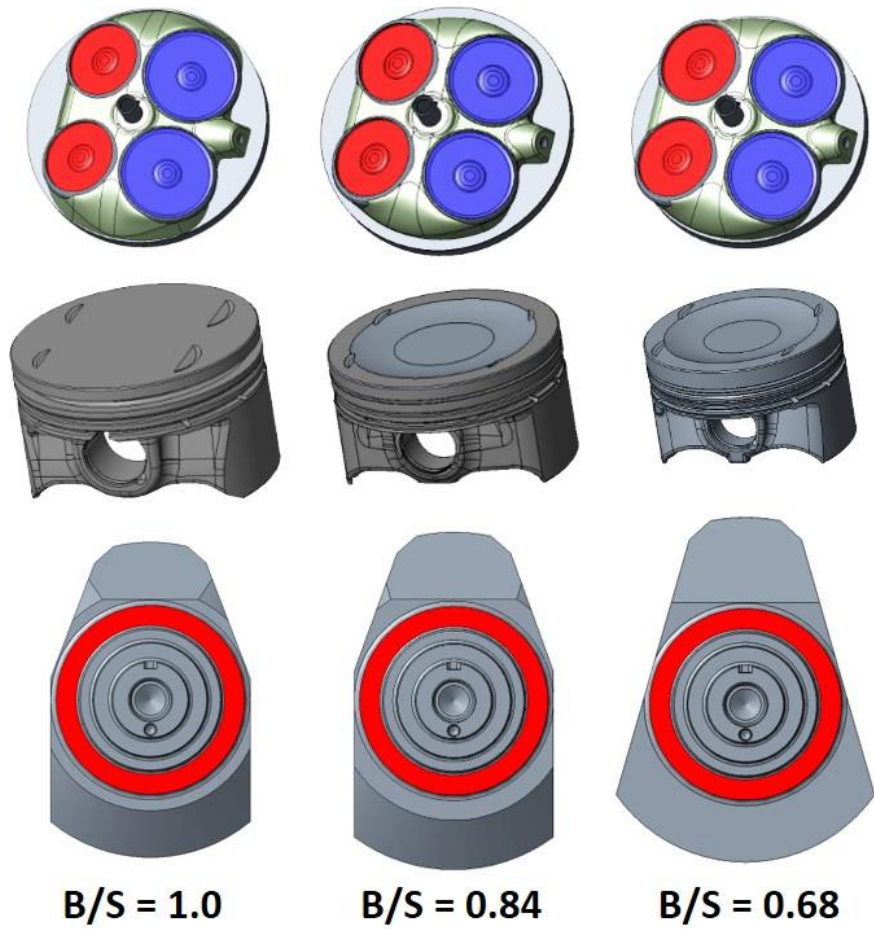


Figure 4.33 Engine designs for three bore-to-stroke ratio:  $B/S = 1.0$ ,  $0.84$  and  $0.68$

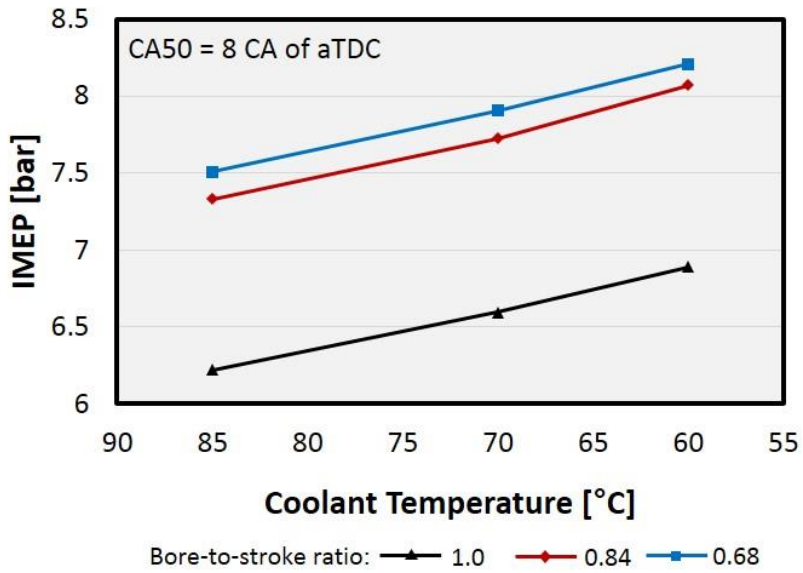


Figure 4.34 Load limit expansion at 1500 rpm, different B/S ratio under cooling

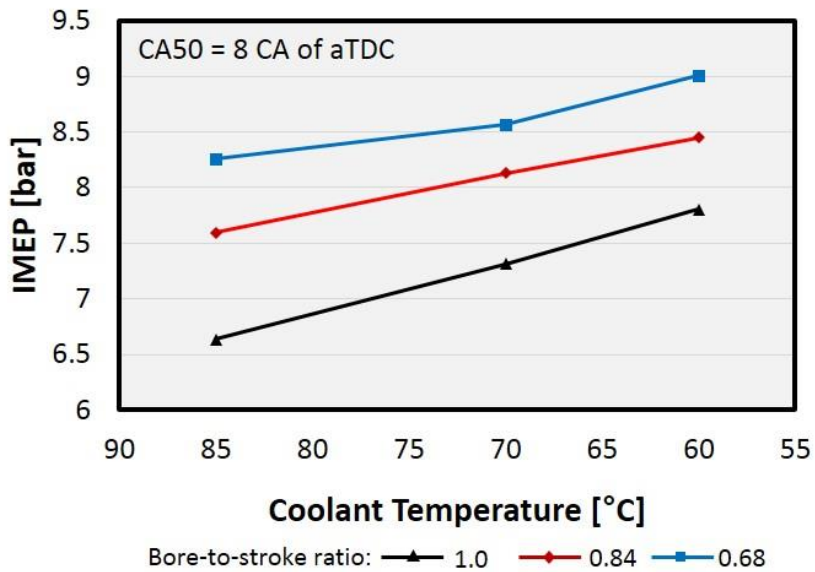


Figure 4.35 Load limit expansion at 2000 rpm, different B/S ratio under cooling

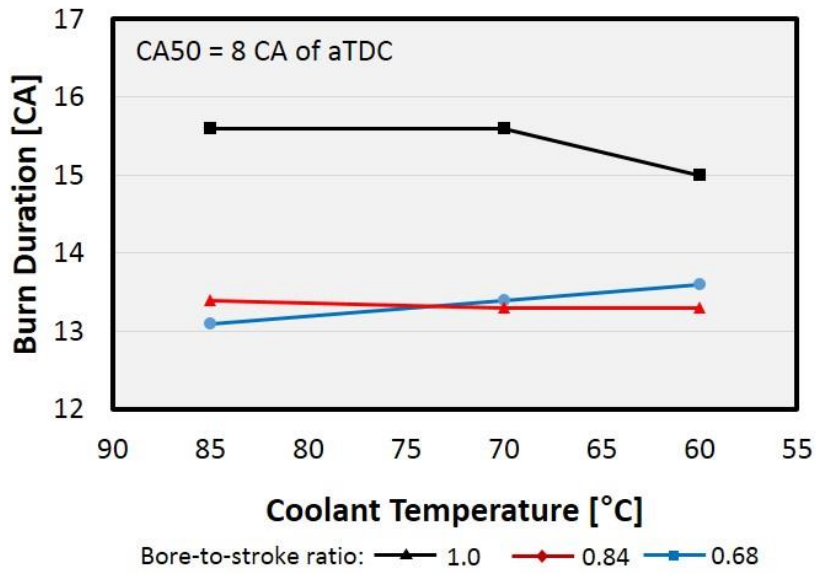


Figure 4.36 Burn duration of different B/S ratio at 1500 rpm

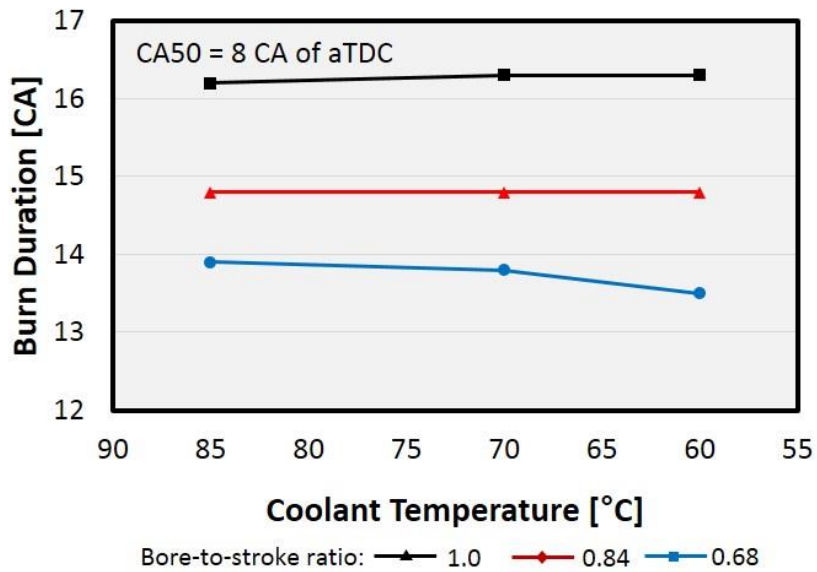


Figure 4.37 Burn duration of different B/S ratio at 2000 rpm

## **4.2 Knock Mitigation Effect of Independent Cooling**

In previous sections, load limit expansion and ignition timing advance was attempted while the coolant temperatures were simultaneously decreased. The feasibility of coolant temperature decrease was clearly achieved. Decreased wall temperatures by coolant temperature reduction led to decrease of in-cylinder gas temperature, which facilitated further advance of ignition timing resulting in higher efficiency with decreasing exhaust enthalpy while maintaining the cooling loss to the same level due to reduction of overall gas temperature.

Even though cylinder head has the largest area during combustion process among in-cylinder wall components, the area of piston is still not negligible and liner area is also large during the intake and expansion process. Therefore, there is still issues on which one has the bigger effect, in order to suggest the strategic knock suppression method. Therefore, the knock mitigation effect of each component have to be quantified.

The difference of the impact by each coolant is very small and knock has a highly stochastic behavior, comparison of each effect is not easy task under normal test environment. By establishing the test methodology as it is well described in chapter 2 and 3, the reliable test was performed under steady-state condition with weak knock thus the differences were possibly identified.

### **4.2.1 Comparison of coolant temperature effects**

In this section, to observe the different impact by each coolant temperature, wall temperature variation by segregated cooling passage was tried. Independent

wall temperature control was well achieved and verified in section 4.1.1. First, while each coolant temperature was decreased to 60°C from 85°C, IVC temperature was estimated by the individual cycle analysis. Figure 4.38 shows the result of in-cylinder gas temperature estimation at IVC timing. Engine was run at 1500 rpm and fuel amount was fixed to 24 mg/cycle where the same implementation with the constant fuel amount case (Chapter 4.2.2.1), ignition timing was 11.5 CA bTDC. While maintaining all the other conditions, each coolant temperature was decreased and the throttle was closed as the gas density increased. As a result, mean intake pressure was decreased from 0.94 bar to 0.935 bar when the liner coolant temperature decreased, and 0.94 bar to 0.929 bar when the head coolant temperature decreased, respectively. From cycle analysis, mean IVC temperature was decreased from 370.8 K to 365.2 and 361.6 K. It can be guessed that cooling head coolant shows the larger knock mitigation effect while observing the guess of IVC temperature, however, not only intake temperature of intake charge mixture but heat transfer process during compression and combustion process affects to knock behavior. Therefore, knock test was conducted.

It was implemented at 1500 and 2000 rpm. First, the load limit was observed while cooling one of the coolants of the head and liner from 85°C to 60°C. While the temperature of one coolant was decreased, the other one was fixed to 85°C. Summarized load limit test procedure was as the follows:

- 1) Increase the load until 5% knock incidence was obtained at condition that coolant temperature is 85°C. CA50 was maintained in all operating points (8 CA aTDC). Stoichiometric condition ( $\lambda = 1$ ) was maintained in all operating points.

- 2) By varying coolant temperature, knock mitigation was achieved and the load increase was possible. Expand the load limit until knock incidence reached to 5% while maintaining combustion phasing and engine speed, air-fuel ratio.

Figure 4.39 shows the effect of each coolant temperature decrease at 1500 rpm. The black line with triangle indicates the simultaneous cooling case of both coolants of the head and liner, red line with diamond indicates the head cooling case while the liner coolant temperature was fixed at 85°C. The blue line with rectangle shows the liner cooling case. As the load limit was tested, the CA50 was fixed to 8CA aTDC for all case by adjusting the ignition timing. As easily expected, the simultaneous cooling case, from 6.25 to 6.89 bar corresponding to 10.3% of the load limit expansion was achieved when the both coolant temperatures were decreased until 60°C. When only the head coolant temperature decreased, the load limit was expanded to 6.69 bar while it was increased to 6.54 bar when only the liner coolant temperature was decreased. Varying head coolant temperature showed the larger effect (7%) than cooling the liner (4.6%). And the ratio of the effect was approximately one and a half.

Figure 4.40 shows the result of the same implementation at 2000 rpm. Very similar result was achieved. The load limits were increased from 6.79 to 7.25 bar (6.8%) under simultaneous cooling condition, to 7.12 bar (4.9%) in head cooling case and to 6.96 bar (2.5%) in liner cooling. It was shown that cooling head shows approximately two times of effect than cooling liner in 2000 rpm. However, the overall effect was smaller than 1500 rpm case, mainly considered because of the shorter heat transfer time.

At 1500 rpm, 0.29% knock limit improvement was achieved for every unit temperature decrease of the head coolant. 0.19% was shown for liner cooling, 0.41%

was shown for simultaneous cooling case. Likewise, at 2000 rpm, the load increase effects of 0.27% for simultaneous cooling, 0.19% for head cooling and 0.1% for liner cooling were achieved while decreasing coolant 1°C. It is guessed that the shorter time for heat transfer brought the less temperature increase of initial gas temperature at the end of intake process in higher speed. Higher engine speed increases turbulence intensity which shortens burn rate but also convective heat transfer. However, from the result, observing the effect of coolant temperature decrement as deteriorated in higher speed condition, it can be said that temperature decrease effect by less heat transfer time is more dominant than the increase of convection coefficient.

Secondly, a comparison of each coolant temperature effect was conducted in terms of achievable KLSA, as well. The ignition timing was advanced while the engine load was maintained. Detailed test procedure is as the follows:

- 1) Determine the load limit at 60°C coolant temperature.

In this condition, by adjusting the ignition timing, the CA50 was maintained at 8 CA aTDC which was considered as combustion phasing at MBT timing. The load limit was first found for each coolant temperature condition. For example, under 1500 rpm, the load limit for simultaneous cooling was 6.89 bar, 6.69 bar for head cooling and 6.54 bar for liner cooling, and the determined load was maintained while retarding the ignition timing. The beginning load was naturally higher in simultaneous cooling case.

- 2) Determine the ignition timing at the test condition.

Maintaining the load and 5% knock incidence, the appropriate ignition timing, i.e. KLSA was determined for each condition. As the coolant temperature was increased from 60°C to 85°C, KLSA retard was necessary. This led to the deterioration of efficiency and load decrease without changing the air and fuel

amount, therefore, fuel with additional air was induced by increasing the intake pressure to maintain the load. All other conditions were maintained stoichiometric during the operation.

Approximately 0.2 CA of KLSA retard was achieved for every 1°C increase of coolant temperature in the 1500 rpm simultaneous cooling case, as shown in figure 4.41. In all, 0.12 CA was achieved when the head coolant temperature was decreased 1°C, and 0.11 CA was achieved for liner cooling. The same implementation was conducted at 2000 rpm as shown in figure 4.42 and resulted in 0.26 CA, 0.21 CA, 0.18 CA KLSA retard for simultaneous, head, and liner cooling, respectively. This result also implies the head coolant temperature has the larger impact on knock behavior.

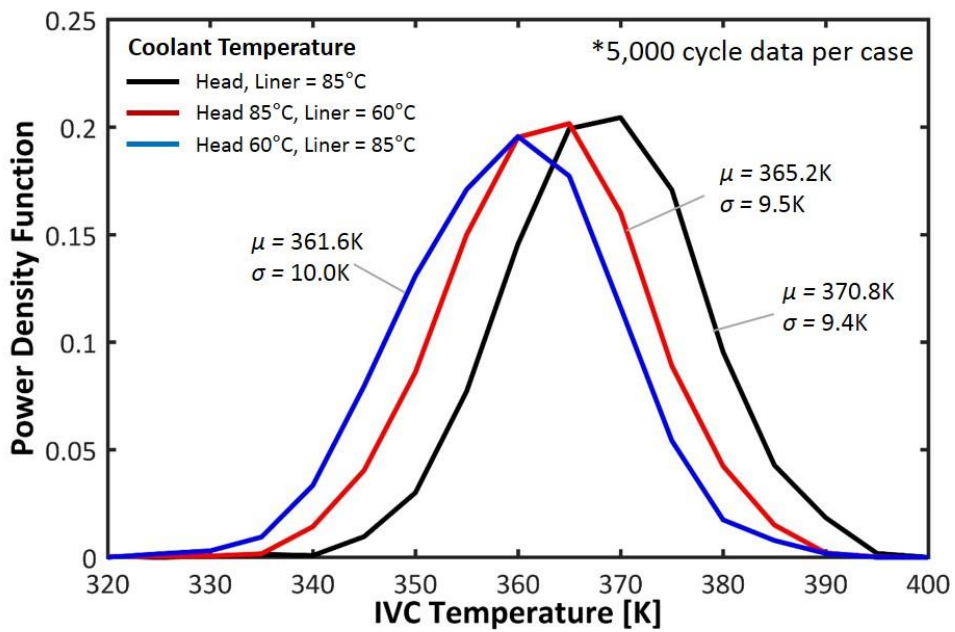


Figure 4.38 IVC temperature at different coolant temperature

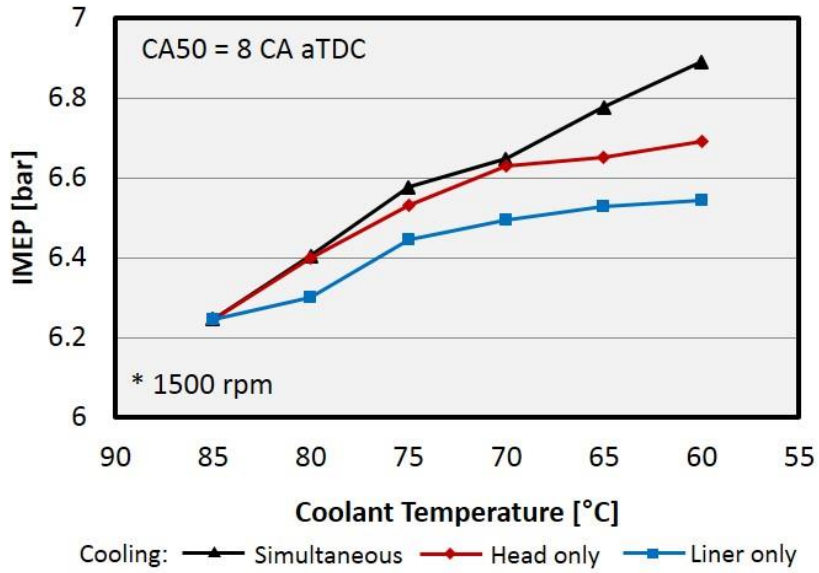


Figure 4.39 Load limit expansion at 1500 rpm under independent cooling

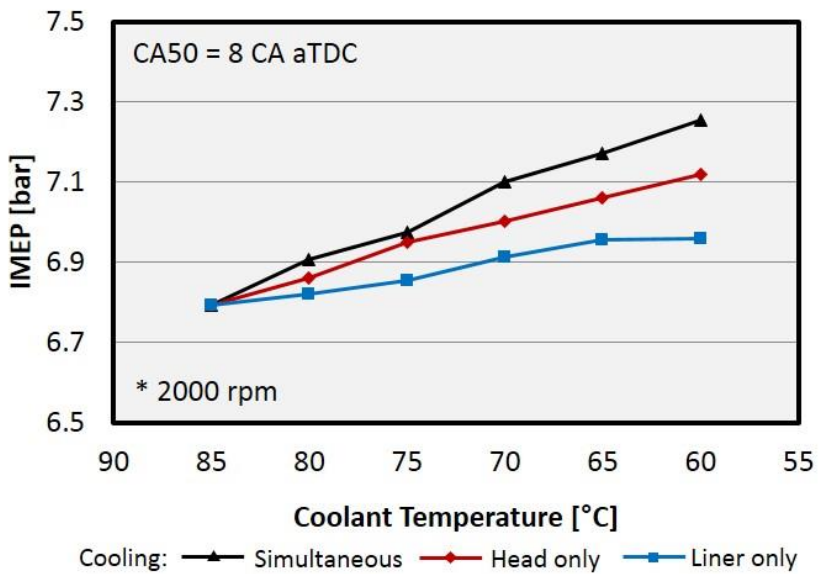


Figure 4.40 Load limit expansion at 2000 rpm under independent cooling

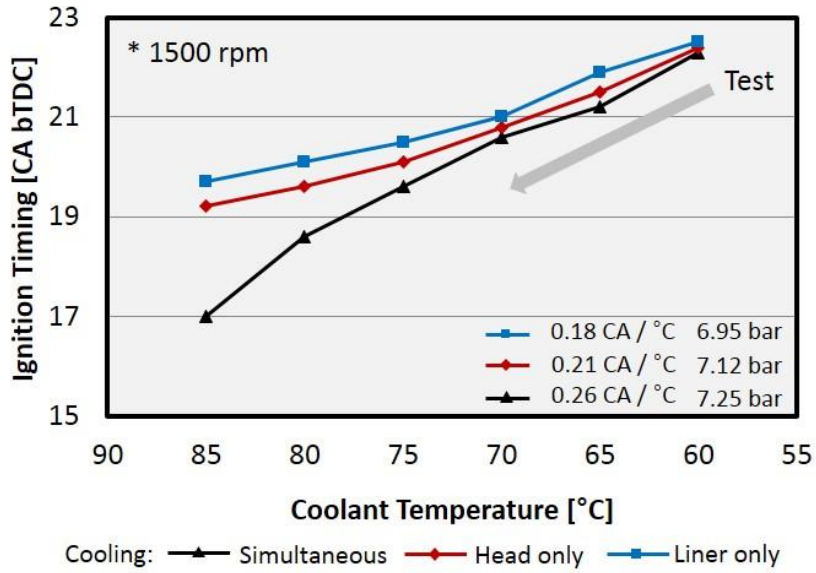


Figure 4.41 KLSA under the same load condition at 1500 rpm

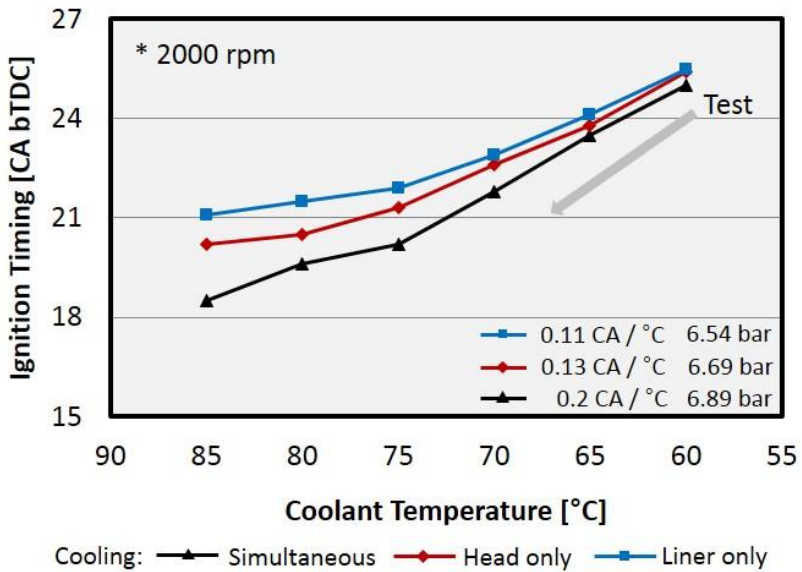


Figure 4.42 KLSA under the same load condition at 2000 rpm

## 4.2.2 Effect in different engine type

In this section, different impacts of each coolant were investigated in GDI engine. Due to direct injected fuel in GDI engine, fuel vaporization in the combustion chamber is largely affected by cylinder wall temperatures, which may affect efficiency and emission characteristics. Engine used in this section was the same engine of section 4.2.3, B/S 0.89 GDI engine, which has 97 mm of stroke and 81 mm of bore and the same dimension with PFI engine. The load limit expansion tests were conducted to verify the effects.

Figures 4.43 and 4.44 shows the results at 1500 and 2000 rpm, respectively. Overall load limit is higher than PFI engine as it is previously demonstrated. While decreasing the coolant temperature simultaneously until 60°C, 9.6% and 11.1% of load limit expansion was achieved in 1500 and 2000 rpm, respectively. It was also shown that the decrease of head coolant temperature had larger effect on the knock mitigation than that of liner coolant temperature. At 1500 rpm, 0.23% knock limit improvement for every unit temperature decrease of head coolant temperature. 0.1% was shown for liner cooling corresponding to a half effect of the head cooling, 0.42% was shown for simultaneous cooling case. Likewise, at 2000 rpm, 0.45% for simultaneous cooling, 0.22% for head cooling, 0.15% for liner cooling load increases were achieved while decreasing 1°C temperature of the coolant.

The effect by lowering head coolant temperature was approximately twice as much as that by lowering the liner coolant temperature in both PFI and GDI engines. However, the effect of simultaneous cooling of GDI engine is larger than that of PFI engine case. It is not clear why simultaneous cooling case shows additional effect in GDI engines. In addition, unlike the PFI engine case, the effect of wall temperature decrease was increased in higher engine speed condition. This

might come from the complicated mechanism by air flow motion and fuel charge, however, this still needs a further investigation.

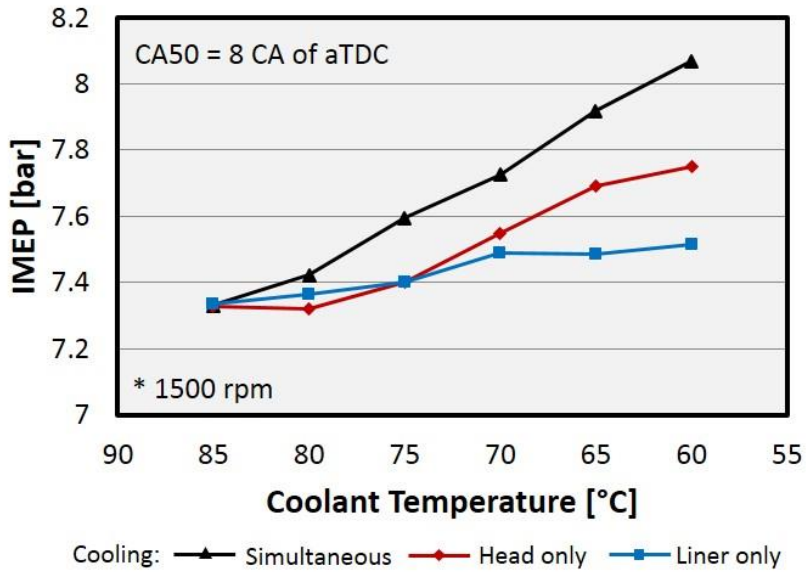


Figure 4.43 Load limit expansion at 1500 rpm (GDI) under independent cooling

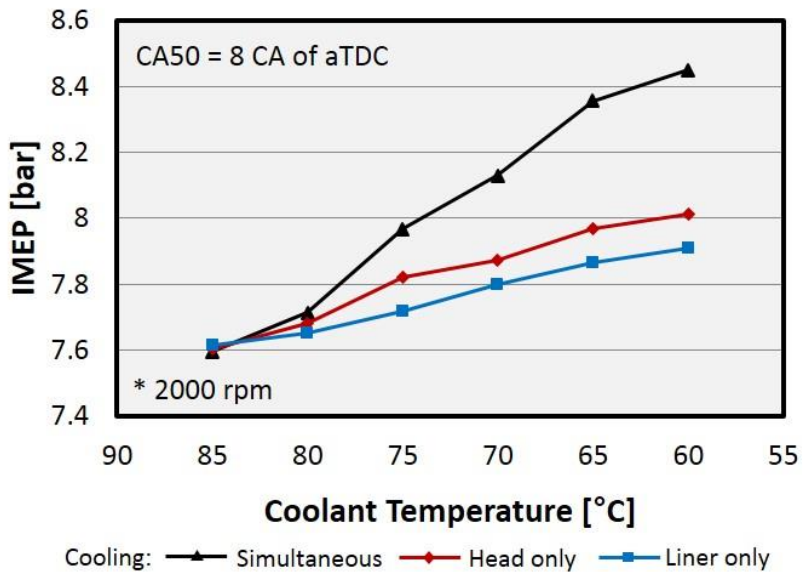


Figure 4.44 Load limit expansion at 2000 rpm (GDI) under independent cooling

### **4.3 Heat Transfer between Gas Mixture and Wall**

In previous part, it was observed that the head coolant temperature has the larger effect than others for knock mitigation. It was verified by various experimental methods, not only in terms of load expansion and ignition timing advance but also with respect to different engine type. However, as it was discussed, cooling piston surface temperature is also very effective mainly attributed to its large surface area. However, liner coolant temperature has a dominant effect on piston and it's shown in section 4.1.2. With this fact, effect of cooling the liner may have larger or even similar effect compared to head cooling. However, results still appears the head coolant is the key factor for knock suppression. This implies cooling head coolant temperature not only decrease the head surface temperature but also reduce other parts such as intake port, valves, etc. However, it is hard to separate all the effect of parts by experimental approach. Therefore, CFD simulation was applied in this part.

Unburned gas temperature is affected by many procedures, and they are categorized into following two stages in this study. In first stage, the gas temperature increase until the timing that heat transfer direction is reversed by the compression process during intake phase will be discussed. During the air induction phase, heat transfer occurs between cold intake air and intake port, first. And intake air hits the valve stems and back side of the intake valves, is heated again and goes into the combustion chamber. After the intake valves are closed, in-cylinder mixture is compressed by the piston motion and the temperature increases with being heated by walls. Heat transfer direction at certain time is reversed due to increased mixture temperature by the compression. This point is defined as 'inverse timing' and was observed at approximately 70 CA bTDC in this study.

In second stage, it will be discussed that gas temperature variation after the transition timing including the combustion. After IVC timing, in-cylinder gas mixture begins to be compressed by the piston motion. This process is usually considered as adiabatic compression process, however, heat transfer between gas and combustion chamber wall still exists. When the gas temperature exceeds wall temperature, direction of heat flux is inversed. Usually knock occurs low-end torque area where the flow is comparatively strong, therefore after the ignition, in-cylinder pressure still rises due to combustion even if piston moves down from TDC. This process keeps the unburned gas to be more pressurized, leading to the temperature increases normally over than gradient of 5 K/CA. Wall temperature decrement contributes to not only reduce the heat transfer from wall to mixture during stage one before the inverse timing, but also augment the heat transfer from mixture to gas during second stage after inverse timing. In this part, investigations on the second stage will be shown, first.

### **4.3.1 Heat transfer during combustion**

As expected from convective heat transfer denoted by equation 2.16, heat transfer predominantly relies on the convection coefficient, surface area, temperature difference between in-cylinder gas and walls. Because the unburned gas temperature generally reaches up to 700-1000K during combustion process, reducing wall temperature cannot remarkably contribute to enhancement of heat transfer.

Figure 4.45 shows the simulation results of heat transfer from in-cylinder mixture to each chamber wall during the combustion. The operating conditions for case 1 to case 4 are shown in table 3.7. For case 1, engine condition was at

1500 rpm, 8.75 bar (WOT) and the ignition timing was 4 CA bTDC. The gas mixture property was set the same for all cases at 5 CA before ignition timing of the case 1 in order to only consider the difference during combustion process. Each case shows the condition of 20°C decrease of surface temperature, but in case 4 (liner cooling case), the piston surface boundary temperature was also decreased 11°C to simulate the actual condition. It was verified formerly that piston surface temperature variation follows approximately a half of change in liner surface temperature. All of the surface temperatures were provided by the experiments.

As a result, very small change was observed. Overall combustion temperature difference was also less than 4 K in all cases at 20 CA aTDC where general knock onset appears. The difference in unburned gas temperature may be a little bit larger than difference in overall temperature due to lower gas temperature, however, it is considered not significant.

The temperature variation of unburned region is shown in figure 4.46. The figure shows the temperature distribution at 10 mm down below TDC piston position. Case 1 is no cooling condition while case 5 is an excessive cooling condition of all components. The result shows that there is no significant different in unburned gas as well; the maximum difference was less than 5K. It is apparently concluded that heat transfer enhancement by wall temperature decrement has very modest role on reducing unburned gas temperature.

Therefore, it can be concluded the temperature at ignition timing is highly important. Moreover, it can be said that it is important to enhance convection coefficient during combustion to mitigate knock efficiently. In conclusion, engine design that increases the turbulent intensity of unburned gas region at the end of compression stroke is suggested in terms of combustion. In the same time, methods for reducing overall combustion temperature is highly recommended.

Especially, reducing the unburned gas temperature during compression and combustion would remarkably enhances the knock resistance. Decreasing specific heat ratio such as introduction of cooled EGR can be a favorable option.

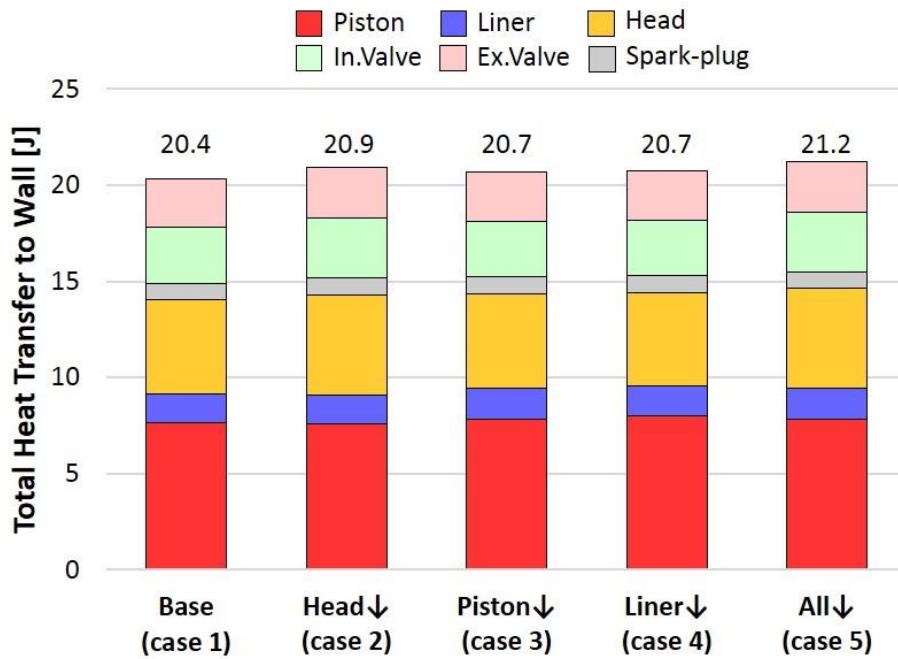


Figure 4.45 Decrease of heat transfer during combustion, case 1-5

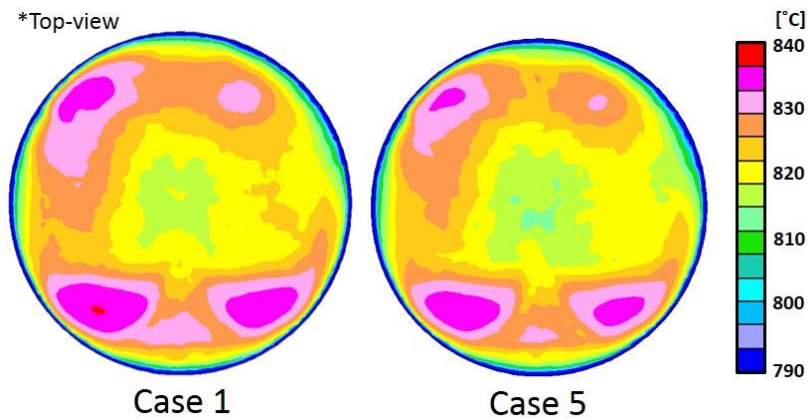


Figure 4.46 Unburned gas temperature at 20 CA aTDC: case 1 (w/o cooling) and case 5 (w/cooling)

### **4.3.2 Heat transfer until ignition timing**

As it is already described, the reduction of wall temperature does not enhance the heat transfer during combustion. It was concluded the unburned temperature during combustion is governed by the temperature at ignition timing.

In this section, the heat transfer was first investigated focused on the phase until IVC timing (phase 1). Boundary conditions for simulation are shown table 3.8. The thermal boundary condition was set with the measured temperature data. Wall boundary temperatures are varied during intake process, however, it was beyond the scope and neglected in this study.

Figure 4.47 shows the accumulated heat transfer at 1500 rpm, WOT (case 6). As it is clearly shown, heat transfer from intake port to gas mixture during the intake process takes the majority of total heat transfer amount. This already have been identified by Imaoka et al. [94] also using 3D simulation. This is attributed to the total surface area of intake port which is considerably large, and either the relatively high velocity of the flow. This supports the result in section 4.3. Because the head coolant temperature not only affects the head surface temperature but also the temperature of intake port wall, valves and other components. This is the reason why the head coolant showed the largest effect even though the head surface area is not considerable large compared to the piston during the combustion process.

Figure 4.48 shows the result at 2000 rpm (case 7). Heat transfer in intake port is also dominant. However, total heat transfer to intake gas is reduced compared to lower engine speed case, principally due to the less time. Because the convection coefficient increases as the flow speed increases, it is concluded that the effect of time reduction affected more than increase of convection in heat

transfer. This also elucidates the higher knock limits at 2000 rpm than 1500 rpm in previous sections. Slightly increased heat transfer on liner wall was observed (26.4 to 27.2%). In both figures, it is shown that the heat transfer direction is reversed at approximately -70 CA aTDC (inverse timing). As the trapped mixture is compressed after IVC timing, increased gas temperature by compression results in the heat transfer to chamber walls.

Figures 4.49 and 4.50 show the heat transfer amount from gas mixture to each component wall until TDC (after inverse timing) at 1500 rpm, 2000 rpm, respectively. It was assumed that there's no ignition. Regarding the valve temperature did not change much while decreasing the coolant temperature [2], it was found the piston has the largest impact on gas temperature reduction in both engine speed conditions while considering the ignition begins late in compression stroke in WOT condition. No remarkable difference between two engine speed was found. Regarding the gas temperature was more increased during gas induction in 1500 rpm than 2000 rpm, increased flow motion made an increase on convective heat transfer in higher engine speed. Liner showed a small contribution due to its small surface area in both cases. Head surface still contributes a lot for temperature reduction, however, in real combustion process, the unburned gas region contact to the head surface is not large due to the shape of flame propagation. Hence, the temperature decrement on piston will be favorable.

In this section, it is concluded that intake port has a significant role on heat on temperature increase during the intake process. Thus, it is suggested to modify the engine design to insulate the intake port or shorten the length to decrease the intake temperature as it is apparently shown that gas induction phase is decisive for unburned gas temperature. It was found that the head surface has no significant role paradoxically if the intake port can be decreased directly with other applications such as rapid precision cooling. Both of timeframes until IVC and

until ignition, piston showed a potential for a large role. Even though liner showed the less effect on enhancing heat transfer during compression, its role is still not negligible while conserving the heat transfer until IVC timing. Also, because the liner coolant temperature affects dominantly to liner wall and piston surface temperature, it can be said that liner cooling will be an agreeable option for future engines with intake port insulation.

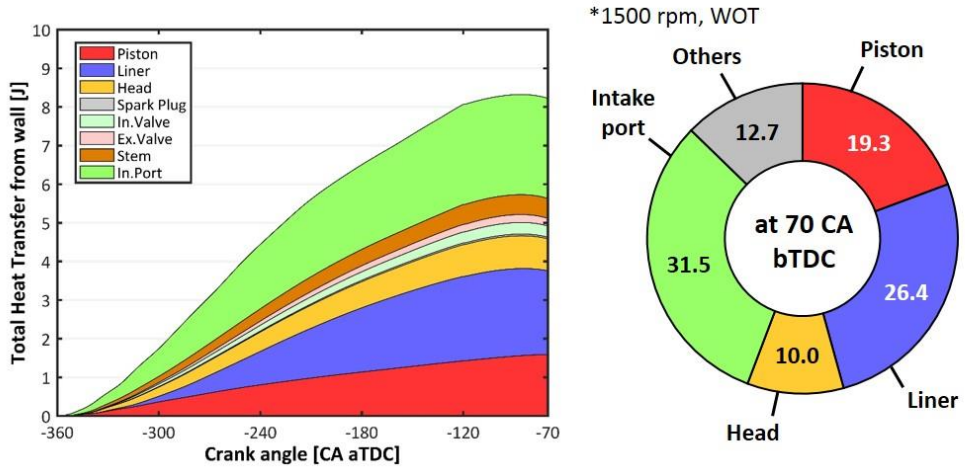


Figure 4.47 Total heat transfer from walls at 1500 rpm (case 6)

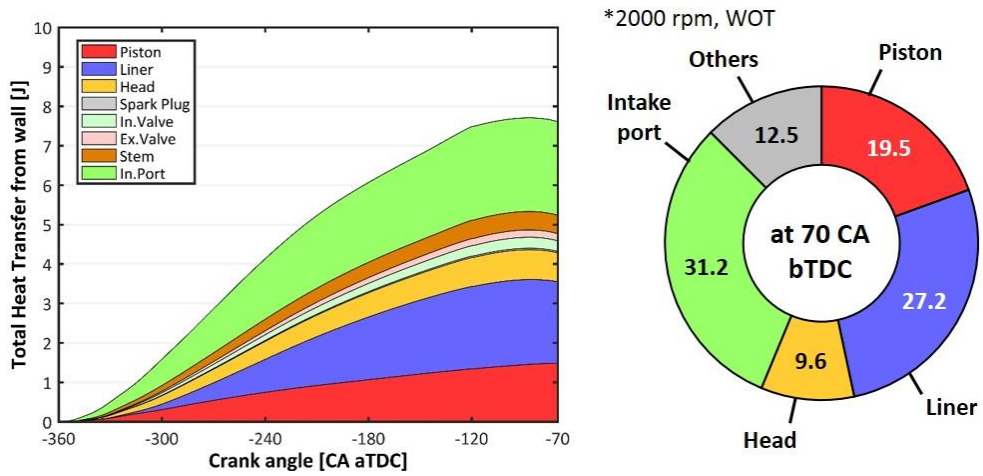


Figure 4.48 Total heat transfer from walls at 2000 rpm (case 7)

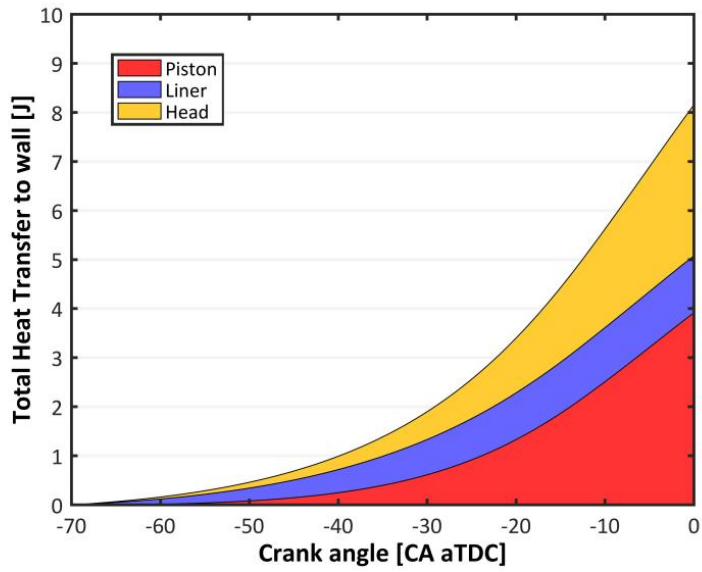


Figure 4.49 Total heat transfer from gas to wall at 1500 rpm (case 6)

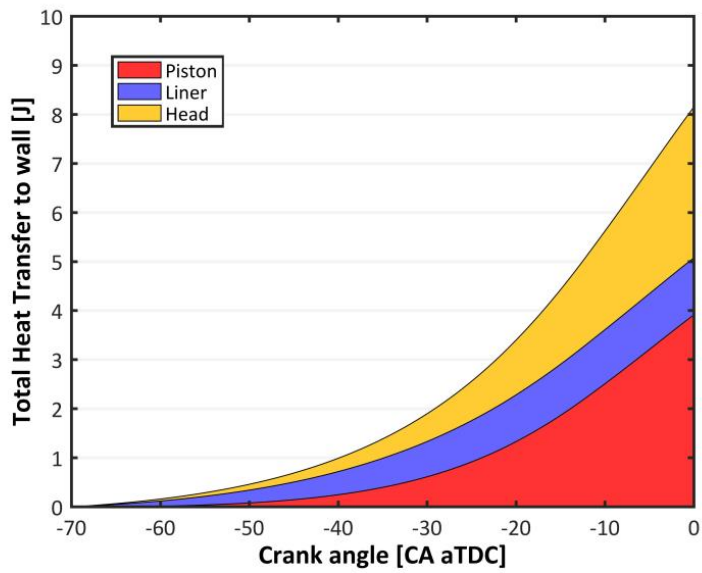


Figure 4.50 Total heat transfer from gas to wall at 2000 rpm (case 7)

## 4.4 Strategic Knock Suppression

### 4.4.1 Intake port insulation

Effect of heat insulation in the intake port was investigated in this section. As it was found that intake port has a significant role on heat transfer reduction to gas mixture during the gas induction phase until inverse timing (70 CA bTDC), it is a very reasonable option to adapt insulation in intake port. Recently studies have proposed and researched various materials such as plastic [94] or resin, polyphenylene sulfide (PPS) [96] which have remarkably low thermal conductivity than casting aluminum.

Figure 4.51 shows the total heat transfer from mixture gas to wall until the inverse timing at 1500 rpm, WOT condition. The heat transfer process was assumed to zero (adiabatic) in intake port for observation. As it is easily noticed, total heat transfer was drastically reduced from 8.2J to 5.8J while heat transfer from other components was slightly increased due to reduced gas temperature.

Interestingly, it was found that the liner cooling (case 10) has a higher effect than head cooling (case 9) on gas temperature decrease after the insulation was applied. This is attributed to the motion of intake gas flow into the cylinder. During the intake process, after intake flow pass the intake valve, it normally hits the cylinder liner wall on exhaust side. Also, a down-going plume generated by persistently incoming intake flow will fall down alongside the liner wall which eventually makes a large heat transfer by piston surface. Therefore, noting that liner surface temperature has a significant role on piston surface temperature, liner cooling strategy can be influential as there's a substantial and synergetic effect by decreasing the heat transfer of not only between its wall and gas, but also the heat

transfer between piston surface and mixture. The same result was appeared in 2000 rpm case, shown in figure 4.52.

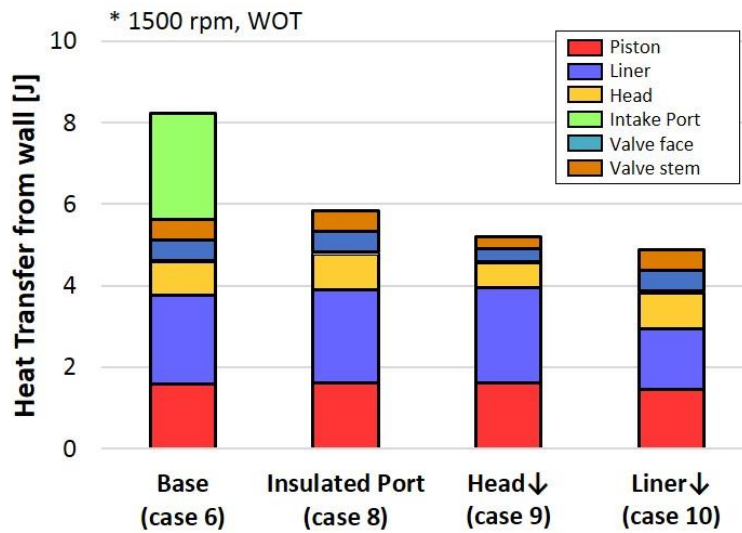


Figure 4.51 Heat transfer during gas induction phase with heat-insulated intake port at 1500 rpm, WOT (case 6, 8-10)

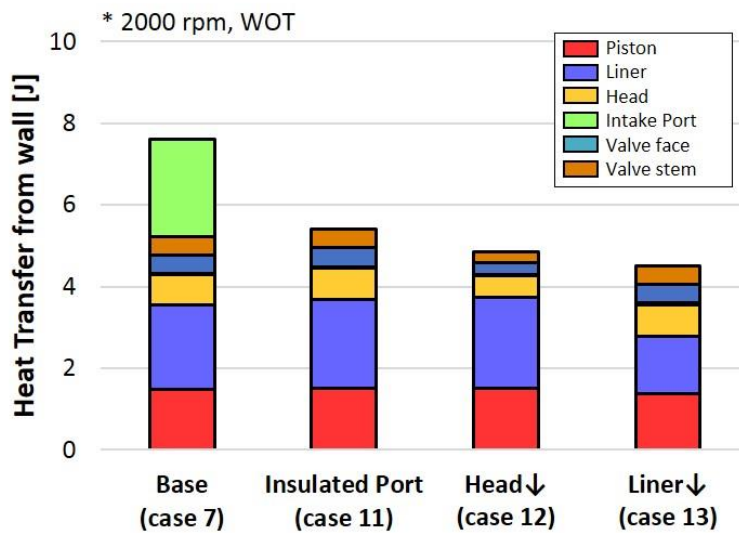


Figure 4.52 Heat transfer during gas induction phase with heat-insulated intake port at 2000 rpm, WOT (case 7, 11-13)

#### 4.4.2 Effect of intensified intake flow

Many automakers endeavor to increase in-cylinder tumble ratio as it enhances the efficiency by increasing flame speed. Increased flame speed enables the unburned gas to be consumed prior to auto-ignition, leading to higher knock resistance of engine. However, there's an issue that it also may raise the gas temperature in consequence of increased convective heat transfer during the gas induction phase. Therefore, in this section, effect of higher tumble flow was investigated.

Intake port design was modified to have a sharp edge to deliberately enhance the tumble flow as shown in figure 4.53. Design alteration may cause the variation of flow coefficient, however, the mass flow was manipulated to the same in this study to exclude the effect. As a result, higher turbulent intensity was achieved in the same condition. Figure 4.54 shows the increased in-cylinder turbulent intensity at 1500, WOT condition. Enhanced inducing intake flow towards the liner exhaust side still resulted in higher velocity at the end of compression stroke.

Figures 4.55 and 4.56 show the total heat transfer from wall to gas until the inverse timing. Due to the increased convective heat transfer, the gas mixture temperature was increased in both engine speed compared to base port design. At 1500 rpm, total heat transfer was increased from 8.2 to 8.9J, and increased from 7.61J to 8.27J at 2000 rpm. The result tells that enhanced tumble ratio can increase the gas temperature during gas induction phase. In addition, it was found that the gas temperature increase by liner becomes larger in both speed conditions. Ratio of total heat transfer for liner was increased 26.4 to 28.1% in 1500 rpm case and 27.2 to 29.2% in 2000 rpm case, respectively. This signifies that the importance of liner cooling is going to be more influential for high tumble engine, as well.

On the other hand, increased convective heat transfer exists in during the compression stroke as well as during the gas induction phase. The heat transfer amounts from gas to wall during the compression (after inverse timing) are shown in figures 4.57 and 4.58. Except three main components (cylinder, liner and head), others were excluded for clarity. In both 1500 rpm and 2000 rpm cases, substantial increase was found compared to base port design. Ignition timings were chosen from case 2 and 8 for each engine speed, WOT condition from table 3.8. Even though the effects of other components were excluded, an increase of 1.82J compared to base port design case (figure 4.49). It was also found that there's an increase of 1.56J at 2000 rpm. Regardless of choosing ignition timing, it is remarkable that the total heat transfer from the gas to wall was increased during the compression stroke due to the intensified flow. Moreover, the increased amounts in both engine speed were larger than total heat increment during the gas induction process.

Therefore, from the results, it can be concluded that high tumble design exploits the reduction of gas mixture temperature by increasing the convective heat transfer during compression, although it has an effect on gas temperature increment in gas induction phase. It is thought that design for lowering gas speed during intake process but enhancing tumble ratio in compression stroke is highly recommended. In this point of view, it is anticipated that the piston design to intensify tumble during the compression is important.

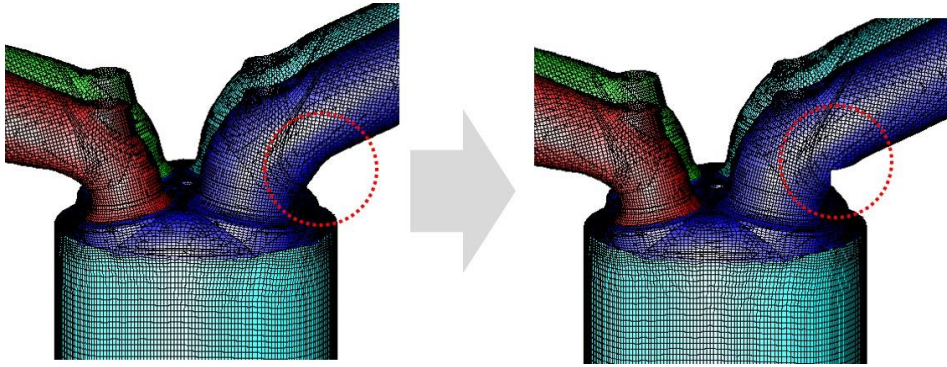


Figure 4.53 Design modification of intake port for intensified tumble flow

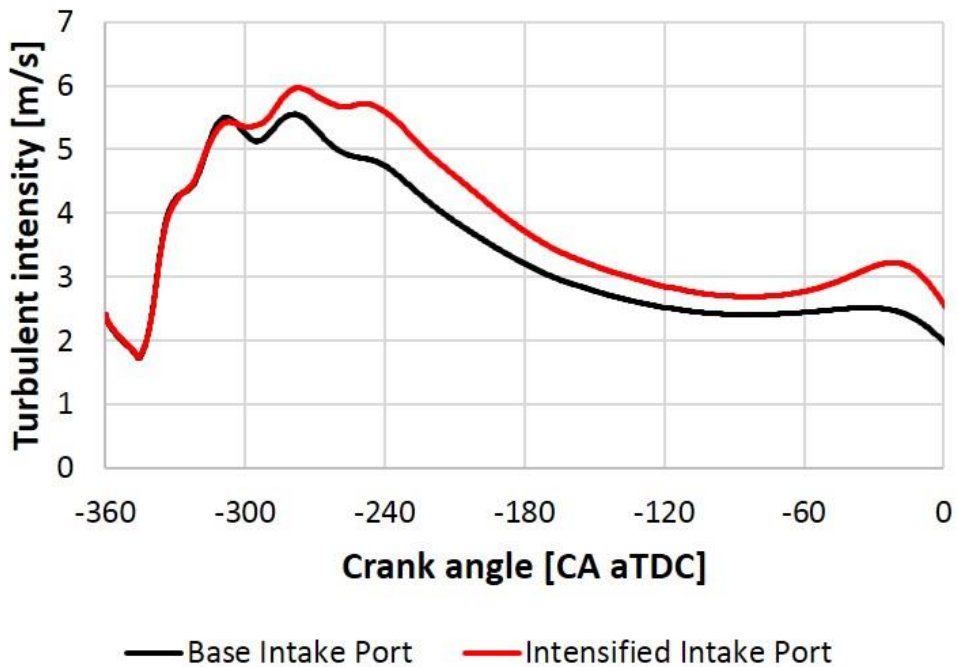


Figure 4.54 Turbulent intensity of base and intensified intake ports at 1500 rpm, WOT (case 6 and case 14)

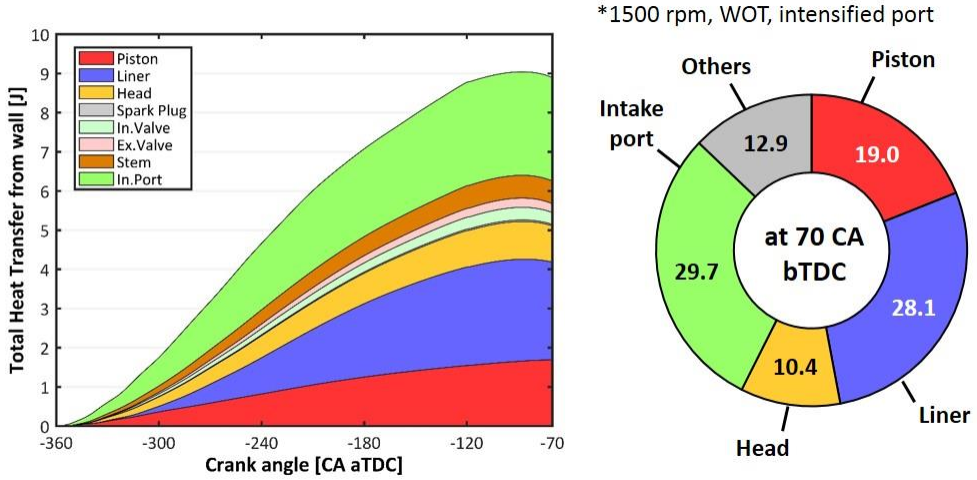


Figure 4.55 Total heat transfer from walls w/intensified port at 1500 rpm, WOT (case 14)

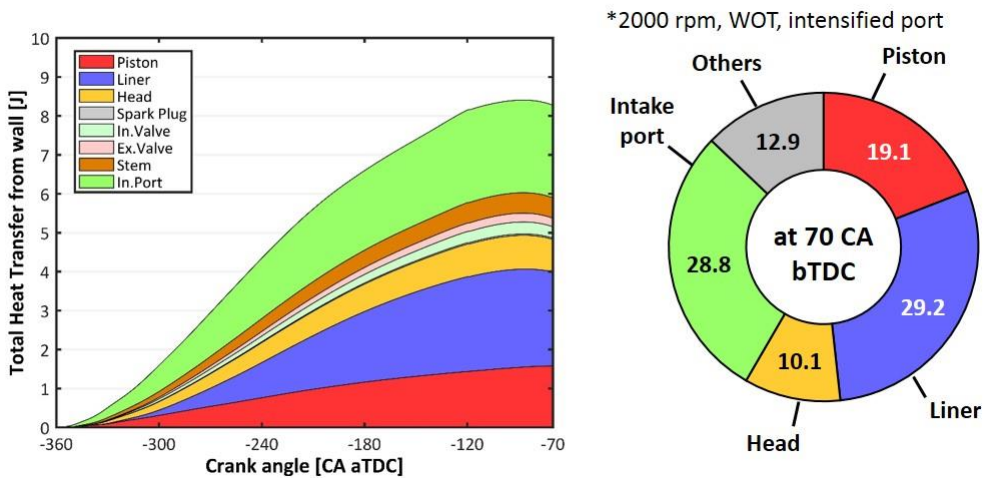


Figure 4.56 Total heat transfer from walls w/intensified port at 2000 rpm, WOT (case 15)

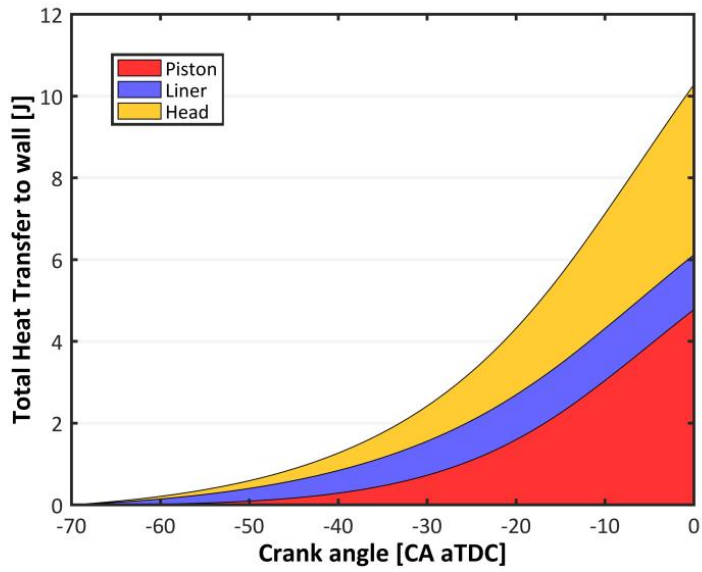


Figure 4.57 Total heat transfer from gas to wall w/ intensified port at 1500 rpm, WOT (case 14)

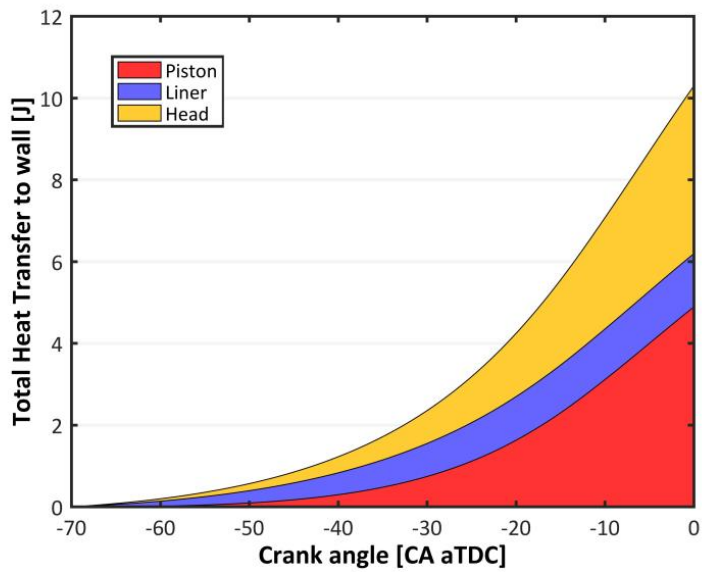


Figure 4.58 Total heat transfer from gas to wall w/ intensified port at 2000 rpm, WOT (case 15)

### 4.4.3 Knock suppression effect using liner cooling

As it was revealed that the liner cooling has a high potential on in-cylinder gas temperature reduction, the actual effect on knock phenomena was investigated. It was demonstrated using GDI engine, with two bore-to-stroke ratios of 0.84 and 0.68. B/S 0.68 engine has a higher liner surface ratio (0.69 at BDC) than B/S 0.84 engine (0.66 at BDC). It was previously shown that the lower B/S ratio engine has higher knock resistance in section 4.2.3.2, however, in this section, it was examined primarily focusing on the liner cooling effect.

Three constant fuel amount condition (26, 30 and 34 mg/cycle) was implemented at 2000 rpm, and the ignition timing was advanced until KLSA (knock incidence of 10%) in each case maintaining the stoichiometric condition. 30mg case and 34mg case were both boosted condition, thus as previously mentioned, a supercharger was used and the results are indicated with gross values.

Figure 4.59 shows the experimental result which are indicated IMEP as a function of CA50. The blue line indicates the result in B/S 0.84 engine case and the red indicates the B/S 0.68 case. Normal line indicates the trace of ignition timing advance towards the KLSA under normal coolant condition (85°C). Higher load was obtained in B/S 0.68 at KLSA in all three fuel amount cases. Because different B/S ratio engines in this study have the same head tumble ratio (1.35) this stronger knock resistance in lower B/S is thought to be attributed to the higher piston speed and smaller combustion chamber design.

Dashed lines in the figure indicate the expansion of load followed by further advance of KLSA in liner cooling condition (60°C). As it is simply noticed, the load was increased while maintaining the constant fuel amount, and this results in the efficiency increase. Figure 4.60 illustrates the efficiency and its increase in all

three cases. Overall indicated thermal efficiency is higher in B/S 0.68 than B/S 0.84. In addition, when the liner cooling is applied, the increase ratio on efficiency was found to be higher in lower B/S engine, which is mainly thought because of higher liner surface ratio.

Likewise, as the higher stroke engine is recommended for future high efficiency although it still needs an effort for friction reduction technology, liner cooling strategy has an explicit advantage for knock suppression. And the effect will be stronger if the heat insulation on intake port is adapted with intensified tumble flow as it is already discussed.

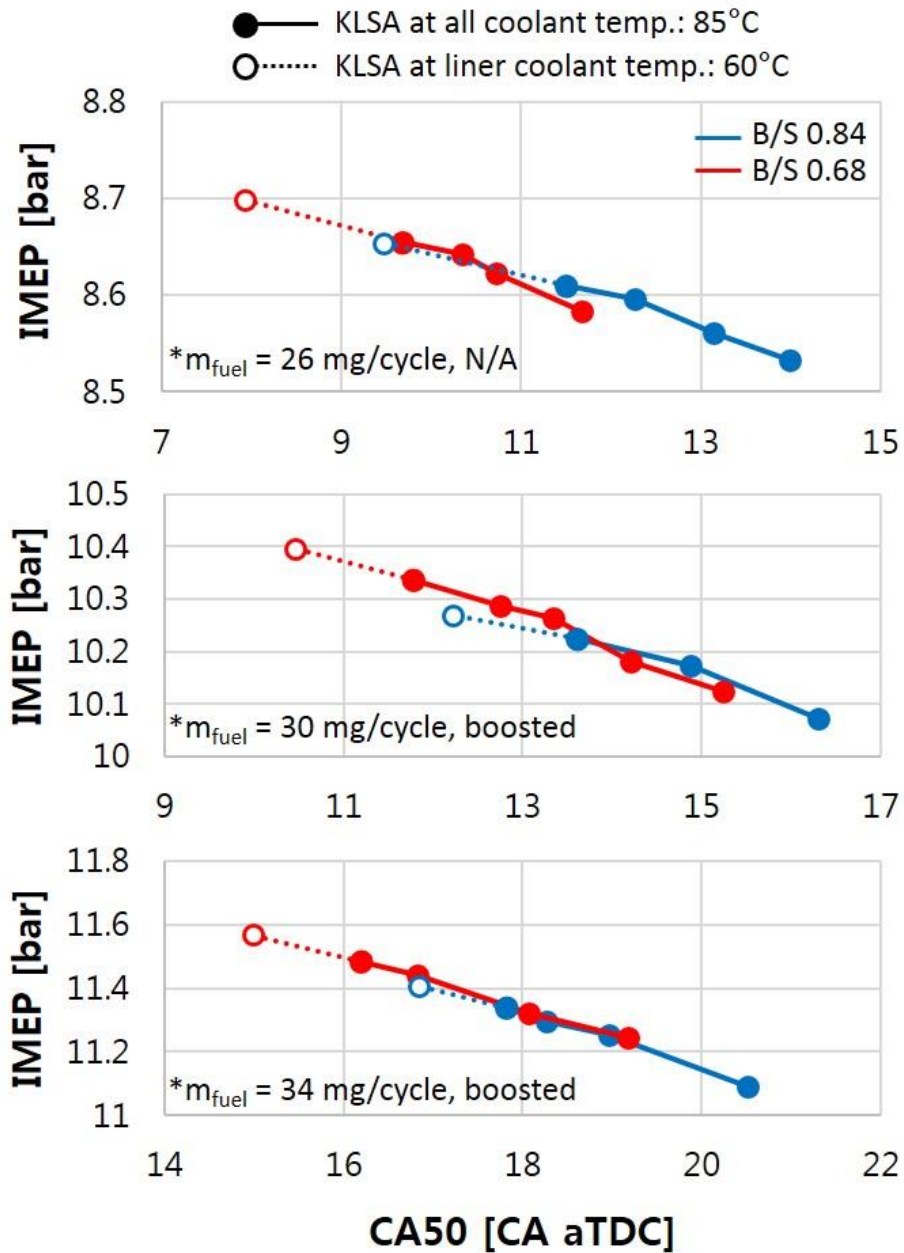
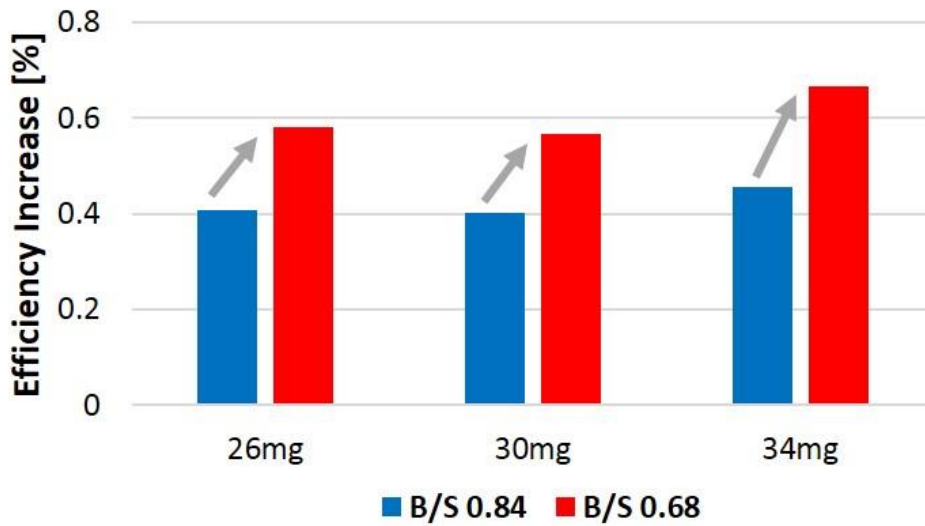


Figure 4.59 Improvement on knock resistance by liner cooling in different B/S ratio



Fuel amount [mg]	ITE at B/S 0.84		ITE at B/S 0.68	
	w/o cooling	w/ liner cooling 60°C	w/o cooling	w/ liner cooling 60°C
26 mg	38.6	38.76	38.8	39.0
30 mg	39.74	39.9	40.22	40.45
34 mg	38.92	39.09	39.41	39.67

Figure 4.60 Efficiency increase rate in different B/S ratio under liner cooling

#### 4.4.4 Knock position under liner cooling

While cooling the liner coolant temperature from 80°C to 40°C, localization of knock occurrence was performed using PCB ion-probe gasket. Cooling the liner coolant temperature includes the temperature decrease of the piston surface due to its large conduction through piston ring and skirt contact.

Figure 4.61 shows the result in weak knock condition at 80°C liner coolant temperature. Engine was operated at 1500 rpm, 6.2 bar. Ignition timing was 21 CA bTDC and knock incidence was 20%. Four individual cycles are shown in the figure for examples. As it is shown in section 3.2.2, knock location was obtained by analyzing the in-cylinder pressure and flame arrival timing simultaneously. In this condition, the flame signal arrived before the knock onset in the majority. Because under weak knock condition, although there are cycles that have high knock intensity due to stochasticity, overall flame speed is seen to be fast enough for consuming end-gas mixture before the auto-ignition occurs. It was discovered that the flame speed was slower to both the intake and exhaust side, mainly considered because of re-entering gas flow motion from the squish areas at the end of the compression stroke. This was verified with 3D simulation and shown in Figure 4.62.

Figure 4.63 shows the result of lower coolant temperature condition, 40°C. Engine was operated at 1500 rpm, 6.5 bar condition where is slightly higher load compared to 80°C condition in order to maintain the knock incidence at the same level of 20% while maintaining the same ignition timing. For comparison of knock occurrence, under different thermal boundary condition, not all of the condition can be the same. Accordingly, knock incidence was maintained in this study because the knock location highly depends on the ignition timing. It was also shown that the intake side has higher possibility of knock occurrence, however,

no remarkable difference was observed compared to 80°C of coolant temperature condition.

Figures 4.64 and 4.65 show the results of 80°C and 40°C liner coolant temperature under heavy knock condition, respectively. Ignition timing was slightly advanced until 23 CA bTDC to generate more knock-prone condition, 60% of knock incidence. Knocking sound from the engine was audible during the test in this condition, which means there is already heavy knock or thermal explosion phenomenon in the end-gas region. In both figures, there are a lot of measuring points that flame arrival timing is later than knock onset. It clearly shows that the multiple hot spots exist in high possibility. Likewise, no significant difference of coolant temperature change was revealed.

From the results, it was observed that knock normally occurs on the intake and exhaust side, and the flame propagation is slower in both sides than that of other directions around the cylinder bore. Heavy knock condition has multiple hot spots while weak knock condition showed the earlier flame arrival than knock occurrence in the most ion-probes. It can be concluded that the location of knock occurrence is mainly affected by the ignition timing rather than the thermal boundary wall temperature. This implies that effect of variation of thermal distribution is not large compared to that of overall gas temperature change by wall temperature reduction.

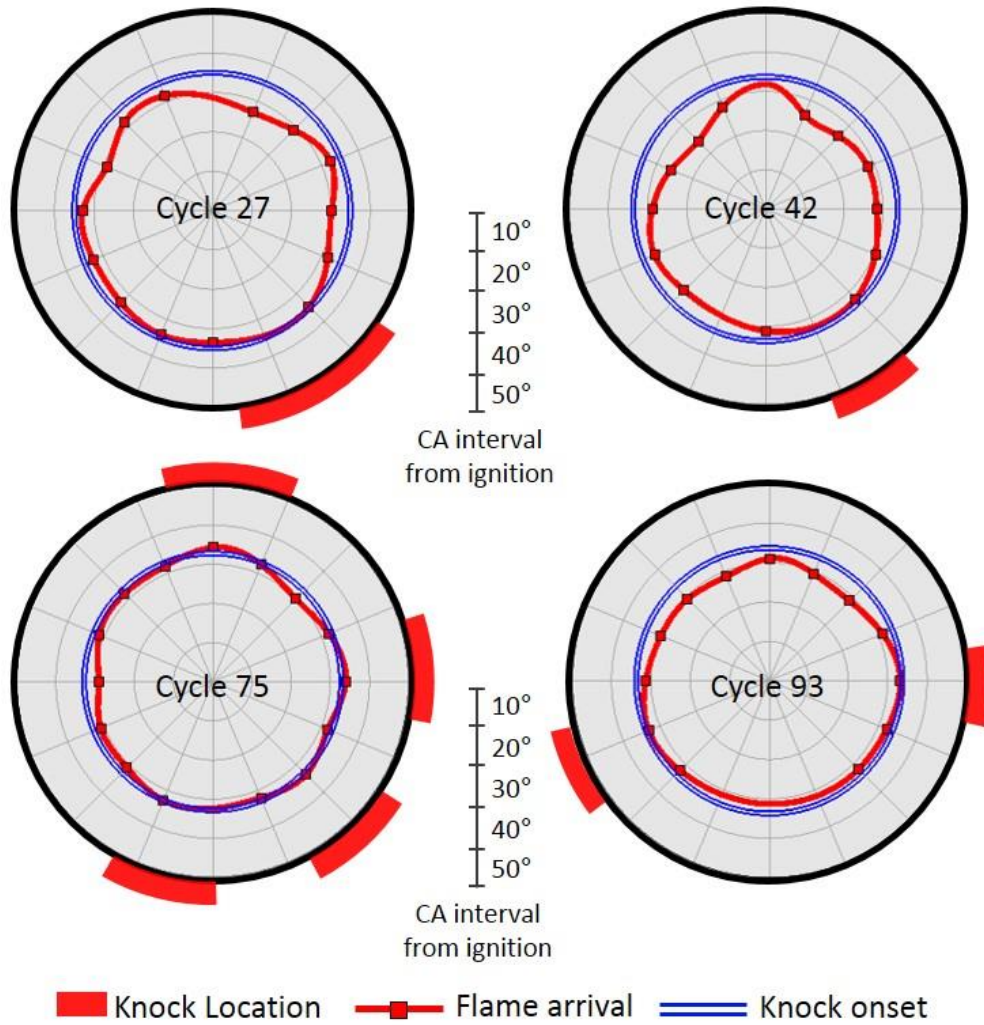


Figure 4.61 Knock locations in weak knock condition (20%)  
 at  $T_{coolant} (liner) = 80^{\circ}C$ , 1500 rpm, 6.2 bar, ign = 21 CA bTDC

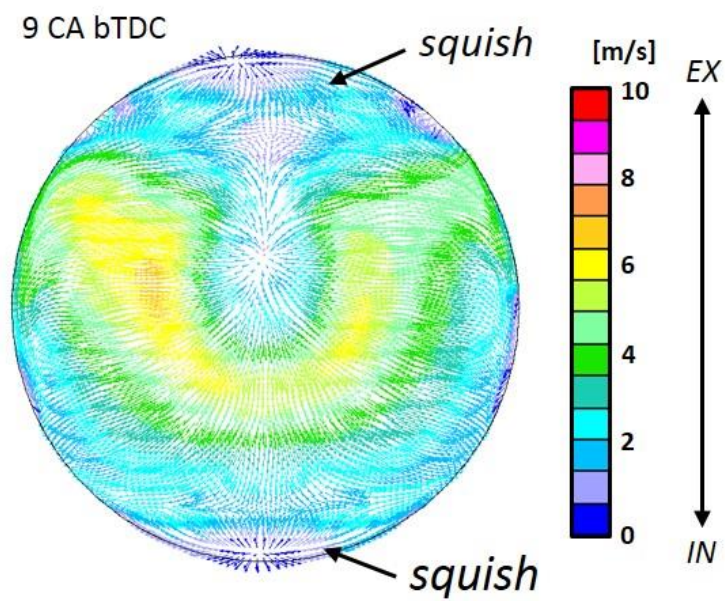


Figure 4.62 Effect of squish to air motion during compression (w/ combustion) at 1500 rpm, 6 bar, ign = 21 CA bTDC

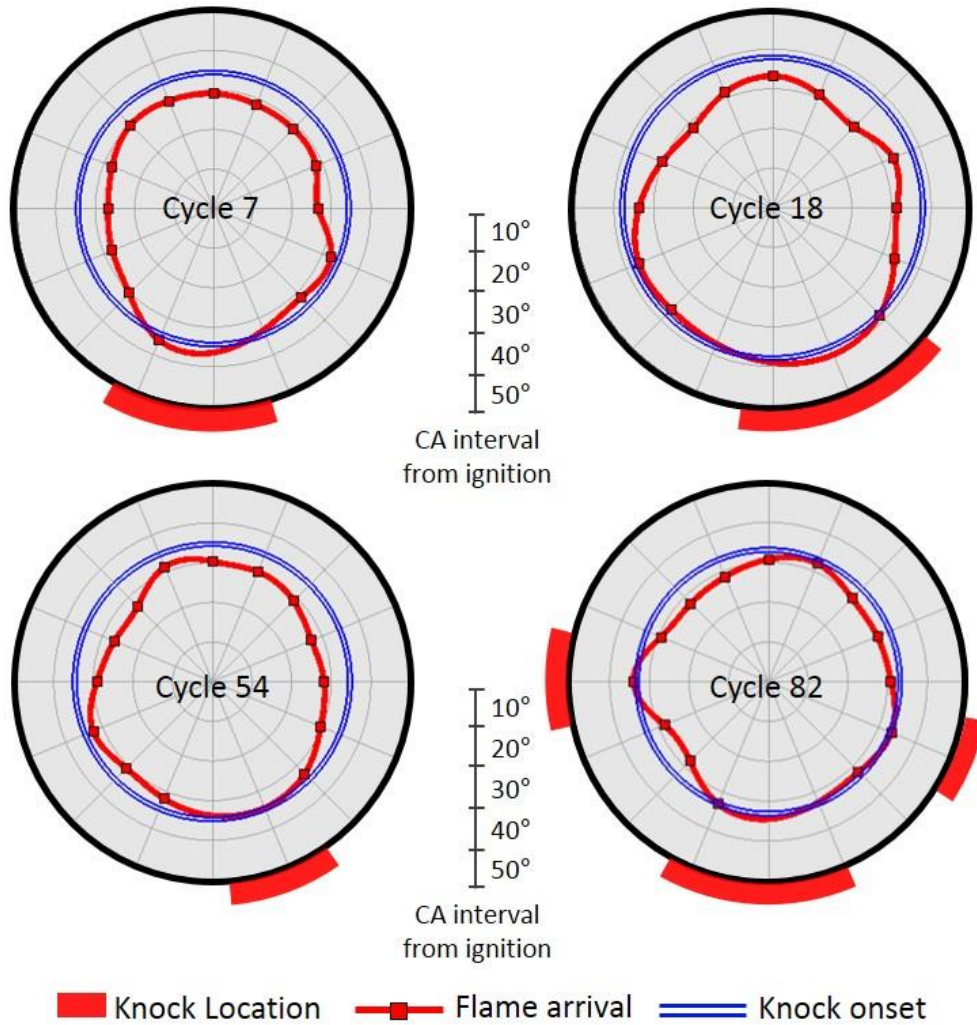


Figure 4.63 Knock locations in weak knock condition (20%)  
 at  $T_{coolant} (liner) = 40^{\circ}C$ , 1500 rpm, 6.5 bar, ign = 21 CA bTDC

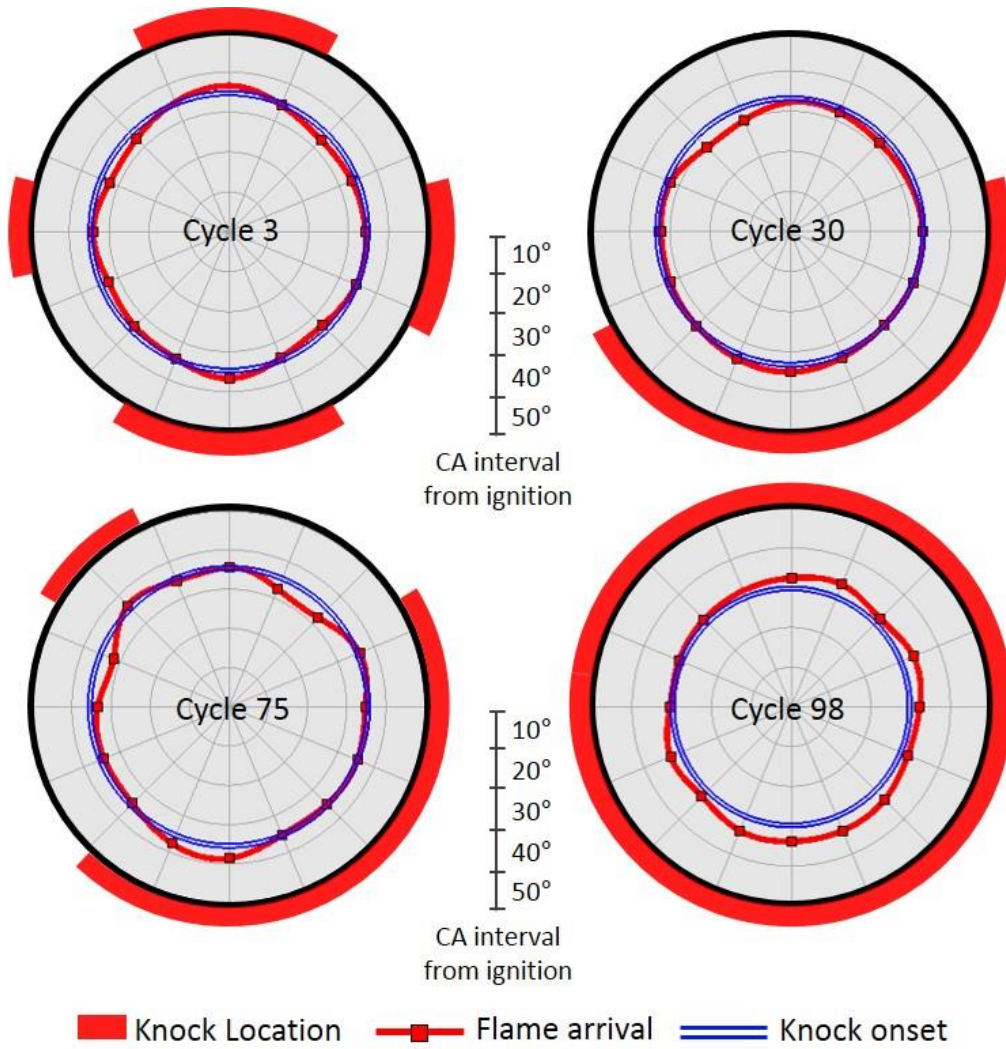


Figure 4.64 Knock locations in heavy knock condition (60%)  
 at  $T_{coolant} (liner) = 80^{\circ}C$ , 1500 rpm, 6.3 bar, ign = 23 CA bTDC

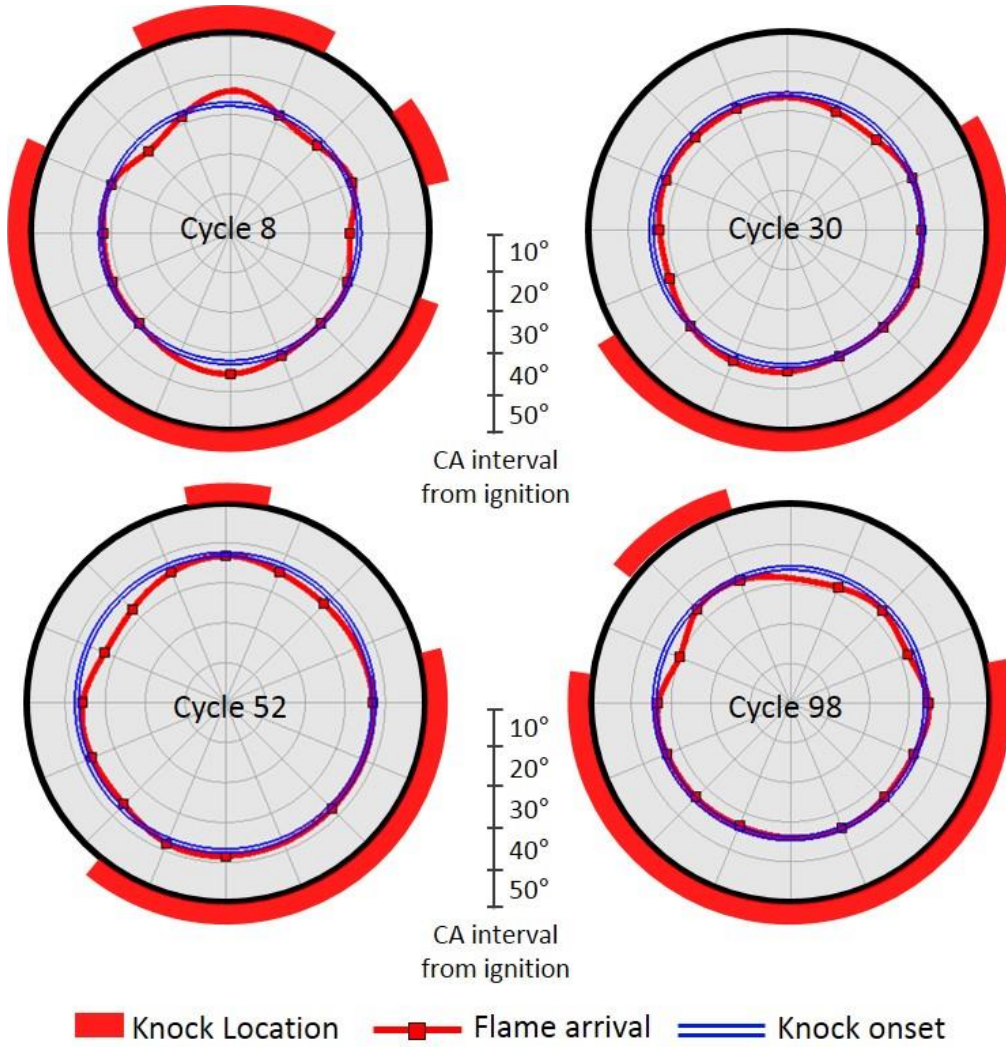


Figure 4.65 Knock locations in heavy knock condition (60%)  
 at  $T_{coolant} (liner) = 40^{\circ}C$ , 1500 rpm, 6.6 bar, ign = 23 CA bTDC

## 4.5 Evaluation of Knock Prediction Model

As it is described in chapter 1, many auto-ignition models have been proposed to date. For future high efficiency, auto-ignition might be necessary because it significantly enhances the efficiency due to faster burn duration like CAI (controlled auto-ignition) or HCCI (homogeneous charge compression ignition) combustion. For control of auto-ignition behavior during engine operating condition, cycle-by-cycle prediction is necessary because engine operation in a vehicle is not steady-state but transient condition.

However, to establish precise prediction model, previous studies have used the 1D simulation results for determination of in-cylinder condition. Pipitone et al. [37] and Beccari et al. [144, 145] used cycle-by-cycle temperature at IVC, however, it was assumed that temperature at IVC timing equals to manifold temperature. In this section, knock prediction model based on individual cycle analysis will be described for future knock control. Furthermore, as this study covers the strategic knock mitigation methods using coolant and wall temperature, the validity of knock control under different thermal boundary condition will be discussed.

Experiments were conducted at 15 different operating conditions. To obtain the universality, different conditions were tried. Engine speed, load, lambda, ignition timing and coolant temperature were varied, and detailed test conditions are listed in table 3.4. Because knock usually occurs in low-end torque region, relatively low speed was selected: 1500, 1750 and 2000 rpm. Intake pressure was varied from 0.9 bar (part load) to 1.0 bar (WOT). Additionally, boosted condition was tested using a supercharger for 1.1 bar of average intake pressure. Ignition timing was varied from 20 CA bTDC to 1 CA aTDC in accordance with knock incidence which was maintained below 50% to prevent the engine failure problem

in all condition. Different lambda conditions were tested at 1750 rpm. The engine was run in long-term timescale to achieve thermal steady-state condition and big data for knock analysis. 3,000 consecutive cycles per each condition were measured and analyzed.

Genetic algorithm was used for optimization of the coefficients in equation 2.41. An objective function was set and the coefficients was searched for minimizing RMSE in equation 4.1. Multipliers for crossover was 0.7, for mutation was 0.3 and generation limit was set to 25. Usually the minimum objective function was achieved before 20<sup>th</sup> generation. It was found that population has a big impact to this non-linear optimization problem, it was set as one thousand. This specified population showed a good repeatability and correlation.

$$RMSE = \sqrt{\frac{1}{n} * \sum (CA@onset_{model} - CA@onset_{exp})^2} \quad (4.1)$$

Depending the target operating condition, the result is different. In this study, all of the cases except the cooling conditions were optimized simultaneously. With the determined coefficients, ignition delay correlation (equation 2.34) could be written as equation 4.2.

$$\tau = 3.953 \times 10^{-5} \left(\frac{P}{T}\right)^{-2.21} \lambda^{-0.2317} \exp\left(\frac{3075}{T}\right) \quad (4.2)$$

Figure 4.66 shows the correlation of experimental knock onset and model-predicted knock onset based on equation 4.2. With individual cycle analysis of 45,000 cycles (15 cases in table 2.2), 20,513 knocking cycles were found with MAPO TVE method, and plotted on the figure including low temperature conditions (case 13-15). As a consequence, splendid correlation (1.25 of RMSE) was achieved. This tells the methodology for the individual cycle analysis is

available for future knock control or prediction in transient operation. Of course, solving ordinary differential equation during operation is not convenient, further study is needed to reduce the variables or equations in order to adapt into ECU of an engine in the future. Douaud-Eyzat ignition delay correlation in equation 4.3, was also calibrated by genetic algorithm and the result is shown in Figure 4.67. This also shows a nice correlation, however, deviation was slightly larger (overall RMSE=1.34) especially in boosted condition (top-right region).

$$\tau = 151.9 \cdot P^{-1.869} \exp\left(\frac{1817}{T}\right) \quad (4.3)$$

Figure 4.68 shows the result of the prediction model under various conditions. As it is easily noticed, higher intake pressure shows the late knock onset resulted from the ignition timing retardant. Slightly advanced knock onset was observed in higher rpm mainly due to the faster pressure rise by higher burn rate. However, no significant difference was observed in model correlation. In 1750 rpm, lambda (air-fuel ratio) was varied from 0.9 to 1.1. It is shown that the correlation works well in 1.0 and 1.1 condition, however, small discrepancy was found in lambda 0.9 condition. It is thought that the unburned gas temperature was overestimated, because 0D based calculation doesn't include the vaporization effect of rich fuel in the mixture. However, RMSE of lambda variation case was 1.05, which is not significant.

The comparison under coolant temperature 85°C and 60°C is shown in bottom right in figure 4.68. Earlier knock onset timing was observed in low temperature condition due to ignition timing advance followed by knock mitigation. However, both cases showed good correlations, no significant difference was observed. This means the developed knock prediction model can be used in different wall temperature condition if the pressure variation at IVC can be included in calculation of unburned temperature. It is expected that

pressure value predicted by manifold absolute sensor can be used for actual engine application.

$$\tau = 3.255 \times 10^{-5} \left(\frac{P}{T}\right)^{-2.183} \lambda^{-0.4408} \exp\left(\frac{3318}{T}\right) \quad (4.4)$$

Also, unburned gas can be considered to follow adiabatic process as it is previously described, the temperature calculation can be expressed as equation 2.27. Under this condition, with the experimental data, coefficients are determined with expression 4.4. Figure 4.69 shows the result of the re-calibration. Overall prediction matches well, however, as it is shown, RMSE was slightly increased, In the figure, it is noticed that points of the top right side of figure don't match well with the experimental result. The model predicts knock later than its actual onset.

Conditions under this region mainly contains the boosted conditions where the ignition timing is usually retarded by knocking behavior. Because the calculation of unburned end gas temperature is a lot affected by the calculation of heat transfer, the difference between adiabatic temperature and the temperature regarding heat transfer is larger in late timing of combustion as the total heat transfer amount increases. As it was assumed that there's no heat transfer, the temperature was predicted higher in boosted condition. This led to the uprising behavior in late timing region of the figure. However, due to the simpler calculation, it is thought to be more appropriate for future knock control.

Figure 4.70 shows the correlation result that used adiabatic temperature calculation under 85°C and 60°C coolant temperature. It includes the variation of engine speed from 1500 to 2000 rpm. The similar result is shown, no significant difference was observed for knock prediction model correlation. It can be

concluded that the established knock prediction model is still valid in variable coolant temperature condition.

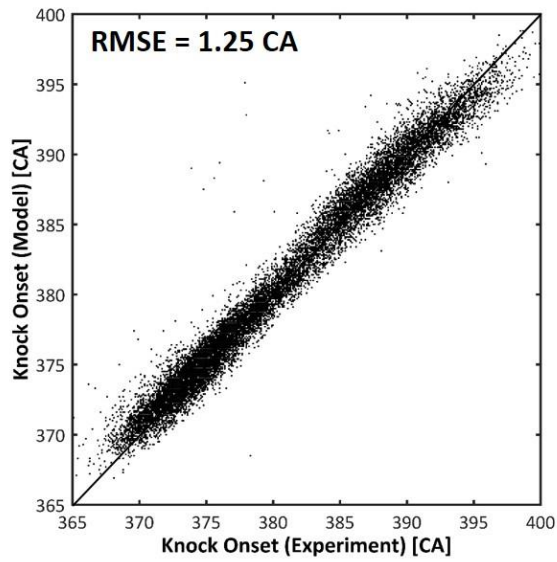


Figure 4.66 Knock prediction model (Chen)

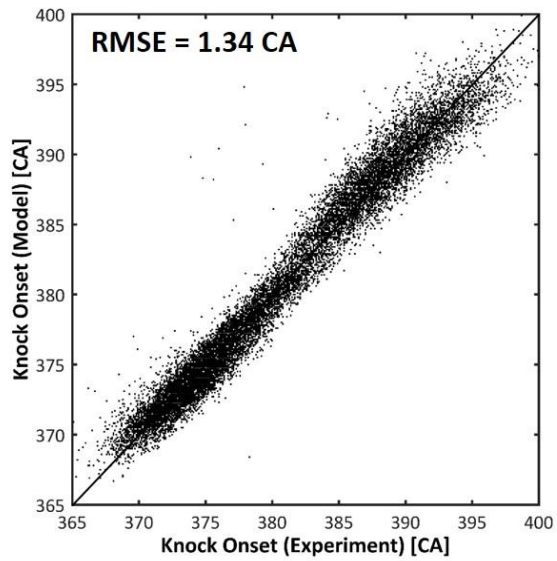


Figure 4.67 Knock prediction model (Douaud-Eyzat)

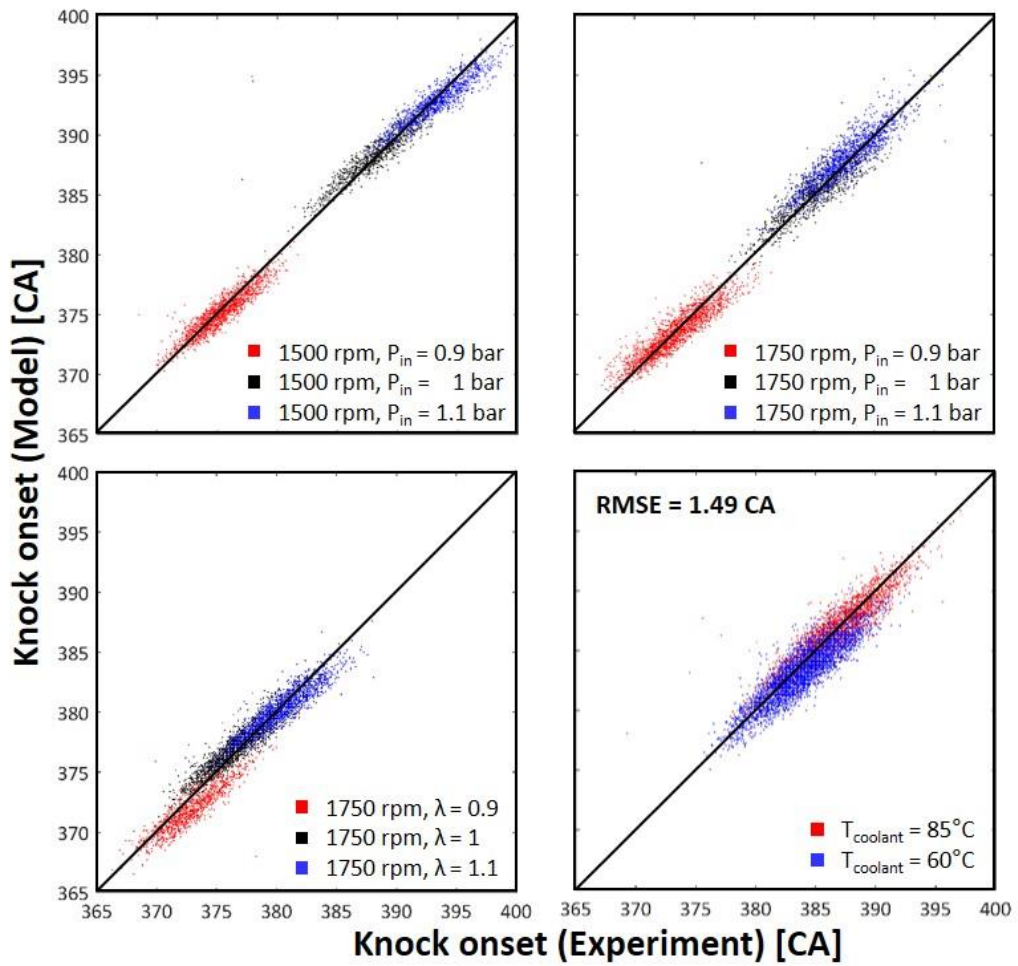


Figure 4.68 Knock prediction model validation under various conditions:  
 Engine speed, load, air-fuel ratio and coolant temperature

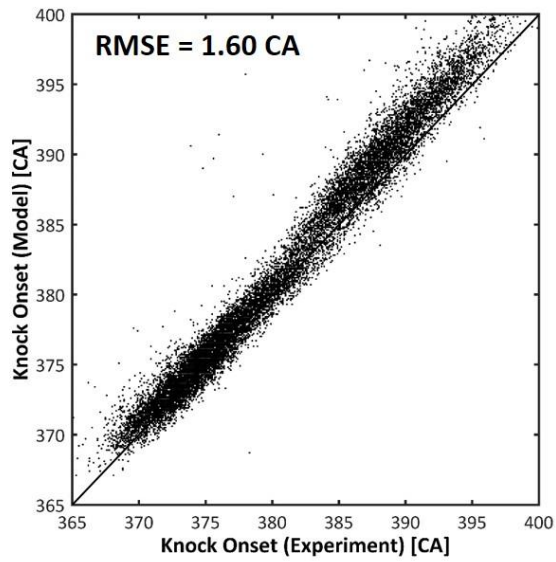


Figure 4.69 Knock prediction model with adiabatic unburned temperature

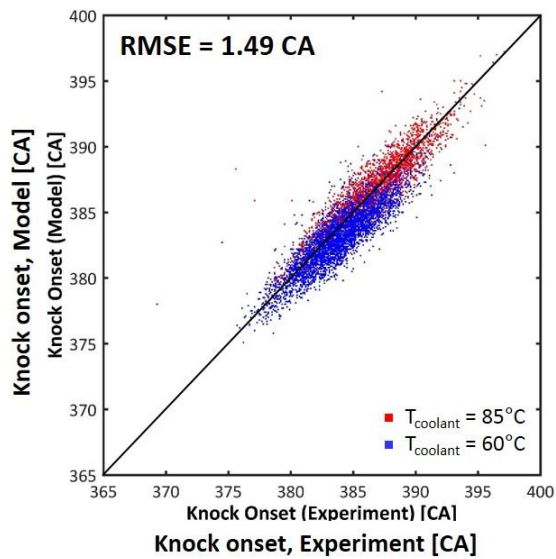


Figure 4.70 Validation of knock prediction model at different coolant temperature

## Chapter 5. Conclusions

In this study, the effect of wall temperatures on knock phenomena in spark-ignited engine was investigated. As the difference in knock propensity depending on wall temperature variation is somewhat slight and knock has highly stochastic behavior, a refined experimental methodology was necessary. Through frequency analysis and selection of appropriate filter, a statistical MAPO incidence method was introduced with high reliability. This facilitated the experimental approaches for comparison of the effect of each wall.

In order to measure wall temperatures of combustion chamber, 22 thermocouples were inserted including five on piston surface utilized by an optimized linkage system. It was verified that segregated cooling strategy can result in independent temperature control of head surface and liner surface. Introduction of oil cooling gallery was found to be very effective on piston surface temperature drop. Additionally, it was verified that piston surface temperature is significantly affected by the liner wall temperature due to its large conductive heat transfer.

The effect of coolant temperature decrease was investigated through sophisticated experiment and analysis. It was observed that no remarkable change in cooling loss while the coolant temperature was decreased. Instead, due to the increased knock suppression effect, the ignition timing could be advanced, efficiency increase was achieved by work augmentation from exhaust loss reduction. 1.5% of efficiency increase obtained during coolant temperature decrease of 25K at 1500 rpm. As the gas density was increased, the intake pressure was decreased. And due to reduction of exhaust enthalpy, thus pumping loss could be maintained at the same level. This tendency was also observed in different engine type and geometry. Specifically, 3% and 3.6% of efficiency were increased

under the same load condition at 1500 and 2000 rpm, respectively. However, additional work loss by water pump and others is inevitable for coolant temperature decrease. Therefore, it was essential to investigate the effect for strategic cooling.

The implementation under independent cooling control showed that cooling cylinder head wall has the larger effect (approximately twice) than that of liner's at both 1500 and 2000 rpm conditions. This was also verified in various conditions and engine geometries. In addition, approximately 5% load limit increase and 1.5CA of ignition timing advance were achieved by using piston oil-cooling gallery (25K overall temperature drop on piston surface). Because the piston oil-cooling gallery showed a substantial effect on knock suppression regarding the surface area of chamber components, the head effect was unexpectedly large regarding the liner cooling also decrease the piston temperature.

Therefore, for deeper understanding, 3D simulation was introduced in this study. During combustion, it was shown that wall temperature decrement cannot substantially contribute to knock mitigation due to originally large temperature difference between the combustion gas and the walls. It was found that the effect of wall temperature decrease mainly takes place in gas induction phase, where the intake port has a significant role on heat transfer to gas (31.2% at 1500 rpm and 31.5% at 2000 rpm). Insulation in intake port showed a remarkable decrease of heat transfer which can effectively mitigate the knock, and it was found the large effect of cooling head was attributed to this. Additionally, it was revealed that the liner cooling is more important than head cooling after the port insulation because of the gas flow motion. Intensification of tumble flow increased the role of liner cooling during the gas induction phase. Despite it showed increased total heat transfer before the inverse timing of heat transfer but also more enhanced the convective heat transfer from the gas to wall in the compression process.

As the importance of liner cooling was revealed, it was demonstrated examine the potential of liner cooling under different bore-to-stroke ratio. Lower B/S engine showed originally higher knock resistance under constant fuel amount condition. Lower B/S engine has a higher liner surface ratio, therefore the efficiency increase (followed by advance of KLSA) was higher than higher B/S engine under liner cooling condition. When only the liner cooling was applied for 25K decrease of coolant temperature, 0.16 and 0.24% of efficiency increments in average were observed for B/S 0.84 and 0.64, respectively (at KLSA timings under 2000 rpm).

Under liner cooling, the knock location was investigated using PCB ion-probe gasket. As the result, no significant change was observed. It was found that knock normally locates at intake or exhaust side under weak knock condition. However, by advancing the ignition timing, it was observed that knock occurs simultaneously around the cylinder bore under heavy knock condition. From the results, knock occurrence during combustion can be thought that flame propagation has dominant effect rather than variation of wall temperatures. Therefore, a design for increasing heat transfer during compression is highly recommended.

As heat transfer during intake process was found to be very important, a rapid cooling strategy or heat insulation in intake port is thought to be valid. In addition, this might be adapted for cylinder block and liner in the future. This may change the gas temperature and in-cylinder condition rapidly. Therefore, in the last, the validation of predictability of knock under cooling strategy was attempted in this study.

Individual cycle analysis including improvement of filter and knock onset determination facilitated more precise estimation of in-cylinder condition. This provided the tracing of in-cylinder condition from IVC to knock onset. Fast knock

prediction model based on 0D ignition delay correlation was established using genetic algorithm, and it was found that the prediction is still available in different temperature condition. In addition, fast calculation with assumption of adiabatic process for the estimation of core gas temperature showed an adequate result. In actual vehicle condition, with further study of simplification for variables and parameters, the established model will allow knock control or utilization of auto-ignition in the future for higher efficiency.

## Bibliography

- [1] Pulkrabek, W. W. *Engineering fundamentals of the internal combustion engine*, 1997.
- [2] Heywood, J. B. *Internal Combustion Engine Fundamentals*, 1988.
- [3] Miller, J. D. and Façanha, C., The state of clean transport policy: A 2014 synthesis of vehicle and fuel policy developments, ICCT, 2014.
- [4] United States Environmental Protection Agency (EPA), Emission Standards Reference Guide - All EPA Emission Standards.  
<https://www.epa.gov/emission-standards-reference-guide/all-epa-emission-standards>, [access date: 07-May-2018].
- [5] 中华人民共和国生态环境部, 中华人民共和国国家标准:  
轻型汽车污染物排放限值及测量方法(中国第六阶段) - Limits and measurement methods for emissions from light-duty vehicles (CHINA 6), 2016.
- [6] European Committee, Reducing CO<sub>2</sub> emissions from passenger cars.  
[access date: 07-May-2018].
- [7] United States Environmental Protection Agency (EPA), Regulations for Greenhouse Gas Emissions from Passenger Cars and Trucks.  
<https://www.epa.gov/regulations-emissions-vehicles-and-engines/regulations-greenhouse-gas-emissions-passenger-cars-and>, [access date: 07-May-2018].

- [8] United States Environmental Protection Agency (EPA), Final Rule for Model Year 2012 - 2016 Light-Duty Vehicle Greenhouse Gas Emission Standards and Corporate Average Fuel Economy Standards.  
<https://www.epa.gov/regulations-emissions-vehicles-and-engines/final-rule-model-year-2012-6-light-duty-vehicle>, [access date: 07-May-2018].
- [9] Pischinger, S. and Körfer, T., Heading towards Higher Diesel Powertrain Efficiencies - Tailored Electrification and Hybridization, 2016 SIA Powertrain Conference.
- [10] Heywood, J. B., On the Road towards 2050, 11th Concawe Symposium Brussels. 2015.
- [11] Research Association of Automotive Internal Combustion Engines (AICE), Japanese Automobile Industry Establishes Joint Research Organization, the Research Association of Automotive Internal Combustion Engines (AICE) 2014.
- [12] Director General for Science, Technology and Innovation, Cross-ministerial Strategic Innovation Promotion Program: Pioneering the Future: Japanese Science, Technology and Innovation, 2017.
- [13] EUCAR European Council for Automotive R&D, EUCAR Projects Book 2015-2016, 2015.
- [14] Wang, Z., Liu, H. and Reitz, R. D., Knocking combustion in spark-ignition engines, *Progress in Energy and Combustion Science*, 2017;61:78-112, 2017.
- [15] Zhen, X., Wang, Y., Xu, S., Zhu, Y., et al., The engine knock analysis—an overview, *Applied Energy*, 2012;92:628-36, 2012.

- [16] Nates, R. and Yates, A., Knock Damage Mechanisms in Spark-Ignition Engines, SAE Technical Paper 942064, 1994.
- [17] Fitton, J. and Nates, R., Knock Erosion in Spark-ignition Engines, SAE Technical Paper 962102, 1996.
- [18] Mckenzie, J. and Cheng, W. K., The Anatomy of Knock, SAE Technical Paper 2016-01-0704, 2016.
- [19] Shahlari, A. J., An investigation of the knock measurement, The University of Wisconsin-Madison, 2016.
- [20] Bradley, D., Kalghatgi, G., Golombok, M. and Yeo, J., Heat release rates due to autoignition, and their relationship to knock intensity in spark ignition engines, Symposium (International) on Combustion. 1996.
- [21] Zeldovich, Y. B., Regime classification of an exothermic reaction with nonuniform initial conditions, Combustion and Flame, 1980;39:211-4, 1980.
- [22] König, G., Maly, R., Bradley, D., Lau, A., et al., Role of Exothermic Centres on Knock Initiation and Knock Damage, SAE Technical Paper 902136, 1990.
- [23] Ohtomo, M., Suzuoki, T. and Yamamoto, S., Effect of Fuel-Air Mixture Dilution on Knock Intensity in an SI Engine, SAE Technical Paper 2018-01-0211, 2018.
- [24] Kalghatgi, G. *Fuel/Engine Interactions*, 2014.

- [25] Chen, L., Li, T., Yin, T. and Zheng, B., A predictive model for knock onset in spark-ignition engines with cooled EGR, *Energy Conversion and Management*, 2014;87:946-55, 2014.
- [26] Sazhin, S., Sazhina, E., Heikal, M., Marooney, C., et al., The Shell autoignition model: a new mathematical formulation, *Combustion and flame*, 1999;117:529-40, 1999.
- [27] Sazhina, E., Sazhin, S., Heikal, M. and Marooney, C., The Shell autoignition model: applications to gasoline and diesel fuels, *Fuel*, 1999;78:389-401, 1999.
- [28] Livengood, J. and Wu, P., Correlation of autoignition phenomena in internal combustion engines and rapid compression machines, *Symposium (international) on combustion*. 1955.
- [29] Douaud, A. and Eyzat, P., Four-Octane-Number Method for Predicting the Anti-Knock Behavior of Fuels and Engines, *SAE Technical Paper 780080*, 1978.
- [30] Mittal, V., Revier, B. M. and Heywood, J. B., Phenomena that Determine Knock Onset in Spark-Ignition Engines, *SAE Technical Paper 2007-01-0007*, 2007.
- [31] Kasseris, E. and Heywood, J. B., Charge cooling effects on knock limits in si di engines using gasoline/ethanol blends: part 2-effective octane numbers, *SAE International Journal of Fuels and Lubricants*, 2012;5:844-54, 2012.
- [32] Kim, K. S., Study of engine knock using a Monte Carlo method, *The University of Wisconsin-Madison*, 2015.

- [33] Worret, R., Bernhardt, S., Schwarz, F. and Spicher, U., Application of Different Cylinder Pressure Based Knock Detection Methods in Spark Ignition Engines, SAE Technical Paper 2002-01-1668, 2002.
- [34] Burluka, A., Liu, K., Sheppard, C., Smallbone, A., et al., The Influence of Simulated Residual and NO Concentrations on Knock Onset for PRFs and Gasolines, SAE Technical Paper 2004-01-2998, 2004.
- [35] Siokos, K., He, Z. and Prucka, R., Assessment of Model-Based Knock Prediction Methods for Spark-Ignition Engines, SAE Technical Paper 2017-01-0791, 2017.
- [36] Wayne, W. S., Clark, N. N. and Atkinson, C. M., Numerical Prediction of Knock in a Bi-Fuel Engine, SAE Technical Paper 982533, 1998.
- [37] Pipitone, E. and Beccari, S., Calibration of a knock prediction model for the combustion of gasoline-natural gas mixtures, ASME 2009 Internal Combustion Engine Division Fall Technical Conference. 2009.
- [38] Hoepke, B., Jannsen, S., Kasseris, E. and Cheng, W. K., EGR effects on boosted SI engine operation and knock integral correlation, SAE International Journal of Engines, 2012;5:547-59, 2012.
- [39] Mckenzie, J. and Cheng, W. K., Ignition Delay Correlation for Engine Operating with Lean and with Rich Fuel-Air Mixtures, SAE Technical Paper 2016-01-0699, 2016.
- [40] Bradley, D. and Kalghatgi, G., Influence of autoignition delay time characteristics of different fuels on pressure waves and knock in reciprocating engines, Combustion and flame, 2009;156:2307-18, 2009.

- [41] Kalghatgi, G., Algunaibet, I. and Morganti, K., On knock intensity and superknock in SI engines, SAE International Journal of Engines, 2017;10:1051-63, 2017.
- [42] Asif, M., Giles, K., Lewis, A., Akehurst, S., et al., Influence of Coolant Temperature and Flow Rate, and Air Flow on Knock Performance of a Downsized, Highly Boosted, Direct-Injection Spark Ignition Engine, SAE Technical Paper 2017-01-0664, 2017.
- [43] Draper, C. S., The physical effects of detonation in a closed cylindrical chamber, Natioanl Advisory Commitee for Aeronautics, 1934.
- [44] Millo, F. and Ferraro, C. V., Knock in S.I. Engines: A Comparison between Different Techniques for Detection and Control, SAE Technical Paper 982477, 1998.
- [45] Eng, J., Characterization of Pressure Waves in HCCI Combustion, SAE Technical Paper 2002-01-2859, 2002.
- [46] Gaeta, A., Giglio, V., Police, G. and Rispoli, N., Modeling of in-cylinder pressure oscillations under knocking conditions: A general approach based on the damped wave equation, Fuel, 2013;104:230-43, 2013.
- [47] Zucrow, M. J. and Hoffman, J. D., Gas dynamics. Volume 2- Multidimensional flow, New York, John Wiley and Sons, Inc, 1977 488 p, 1977;1977.
- [48] Shahlari, A. J. and Ghandhi, J., Pressure-Based Knock Measurement Issues, SAE Technical Paper 2017-01-0668, 2017.

- [49] Brunt, M. F., Pond, C. R. and Biundo, J., Gasoline Engine Knock Analysis using Cylinder Pressure Data, SAE Technical Paper 980896, 1998.
- [50] Bertola, A., Stadler, J., Walter, T., Wolfer, P., et al., Pressure indication during knocking conditions, Proceedings of the Seventh International AVL Symposium on Internal Combustion Diagnostics. 2006.
- [51] Ando, H., Takemura, J. and Koujina, E., A knock anticipating strategy basing on the real-time combustion mode analysis, SAE transactions: Journal of Fuels and Lubricants, 1989;98:481-93, 1989.
- [52] Kirsten, M., Pirker, G., Redtenbacher, C., Wimmer, A., et al., Advanced Knock Detection for Diesel/Natural Gas Engine Operation, SAE International Journal of Engines, 2016;9:1571-83, 2016.
- [53] Sjöberg, M., Vuilleumier, D., Yokoo, N. and Nakata, K., Effects of Gasoline Composition and Octane Sensitivity on the Response of DISI Engine Knock to Variations of Fuel-Air Equivalence Ratio, The Proceedings of the International symposium on diagnostics and modeling of combustion in internal combustion engines 20179. 2017.
- [54] Hettinger, A. and Kulzer, A., A new method to detect knocking zones, SAE International Journal of Engines, 2009;2:645-65, 2009.
- [55] Kawahara, N., Tomita, E. and Sakata, Y., Auto-ignited kernels during knocking combustion in a spark-ignition engine, Proceedings of the Combustion Institute, 2007;31:2999-3006, 2007.
- [56] Ma, X., Wang, Z., Jiang, C., Jiang, Y., et al., An optical study of in-cylinder CH<sub>2</sub>O and OH chemiluminescence in flame-induced reaction front propagation using high speed imaging, Fuel, 2014;134:603-10, 2014.

- [57] Suzuki, R., Shoji, H., Yoshida, K. and Iijima, A., Analysis of Knocking in an SI Engine based on In-cylinder: Spectroscopic Measurements and Visualization, SAE Technical Paper 2010-32-0092, 2010.
- [58] Merola, S. S. and Vaglieco, B. M., Knock investigation by flame and radical species detection in spark ignition engine for different fuels, Energy conversion and Management, 2007;48:2897-910, 2007.
- [59] Spicher, U. and Kollmeier, H.-P., Detection of Flame Propagation During Knocking Combustion by Optical Fiber Diagnostics, SAE Technical Paper 861532, 1986.
- [60] Philipp, H., Hirsch, A., Baumgartner, M., Fernitz, G., et al., Localization of Knock Events in Direct Injection Gasoline Engines, SAE Technical Paper 2001-01-1199, 2001.
- [61] Omura, T., Nakata, K., Yoshihara, Y. and Takahashi, D., Research on the Measures for Improving Cycle-to-Cycle Variations under High Tumble Combustion, SAE Technical Paper 2016-01-0694, 2016.
- [62] Cho, S., Song, C., Min, K., Kim, M., et al., The Effect of Thermal Boundary Conditions on Knock Characteristics in a Single Cylinder Spark Ignited Engine, SIA Powertrain Conference, 2017.
- [63] Matura, K., Sato, Y., Yoshida, K. and Sono, H., Proposal of Knock Mitigation Method Through Enhancement of Local Heat Transfer, International Conference on Knocking in Gasoline Engines. 2017.
- [64] AVL List GmbH G, AVL VisioKnock Application Software, AT1724E:02, 2004.

- [65] Witze, P. O. and Green, R., Determining the Location of End-Gas Autoignition Using Ionization Probes Installed in the Head Gasket, SAE Technical Paper 932645, 1993.
- [66] Borg, J. M. and Alkidas, A. C., Cylinder-pressure-based methods for sensing spark-ignition engine knock, International journal of vehicle design, 2007;45:222-41, 2007.
- [67] Shahlari, A. J. and Ghandhi, J. B., A Comparison of Engine Knock Metrics, SAE Technical Paper 2012-32-0037, 2012.
- [68] Xiaofeng, G., Stone, R., Hudson, C. and Bradbury, I., The Detection and Quantification of Knock in Spark Ignition Engines, SAE Technical Paper 932759, 1993.
- [69] Amann, M. and Alger, T., Lubricant reactivity effects on gasoline spark ignition engine knock, SAE International Journal of Fuels and Lubricants, 2012.
- [70] Breccq, G., Bellettre, J. and Tazerout, M., A new indicator for knock detection in gas SI engines, International Journal of Thermal Sciences, 2003;42:523-32, 2003.
- [71] Hudson, C., Gao, X. and Stone, R., Knock measurement for fuel evaluation in spark ignition engines, Fuel, 2001;80:395-407, 2001.
- [72] Mutzke, J., Scott, B., Stone, R. and Williams, J., The Effect of Combustion Knock on the Instantaneous Heat Flux in Spark Ignition Engines, SAE Technical Paper 2016-01-0700, 2016.

- [73] Szybist, J. P., Wagnon, S. W., Splitter, D., Pitz, W. J., et al., The Reduced Effectiveness of EGR to Mitigate Knock at High Loads in Boosted SI Engines, SAE International Journal of Engines, 2017;10:2305-18, 2017.
- [74] Lee, J.-H., Hwang, S.-H., Lim, J.-S., Jeon, D.-C., et al., A New Knock-Detection Method using Cylinder Pressure, Block Vibration and Sound Pressure Signals from a SI Engine, SAE Technical Paper 981436, 1998.
- [75] Hwang, K., Hwang, I., Lee, H., Park, H., et al., Development of New High-Efficiency Kappa 1.6L GDI Engine, SAE Technical Paper 2017-01-0667, 2016.
- [76] Niizato, T., Yasui, Y., Urata, Y., Wada, Y., et al., Honda's New Turbo-GDI Engine Series for global application, 37th International Vienna Motor Symposium, 2016;2016.
- [77] Ikeya, K., Takazawa, M., Yamada, T., Park, S., et al., Thermal efficiency enhancement of a gasoline engine, SAE International Journal of Engines, 2015;8:1579-86, 2015.
- [78] Attard, W. P., Kohn, J. and Parsons, P., Ignition Energy Development for a Spark Initiated Combustion System Capable of High Load, High Efficiency and Near Zero NOx Emissions, SAE International Journal of Engines, 2010;3:481-96, 2010.
- [79] Schenk, M., Wolf, T., Schröter, M., Zellinger, F., et al., Corona-Ignition vs. Spark Ignition: A Fundamental Comparison for varying thermodynamic conditions of modern turbocharged Gasoline Engines, SIA Powertrain Conference, 2015.

- [80] Yoshihara, Y., Nakata, K., Takahashi, D., Omura, T., et al., Development of High Tumble Intake-Port for High Thermal Efficiency Engines, SAE Technical Paper 2016-01-0692, 2016.
- [81] Takahashi, D., Nakata, K., Yoshihara, Y. and Omura, T., Combustion development to realize high thermal efficiency engines, SAE International Journal of Engines, 2016;9:1486-93, 2016.
- [82] Nakata, K. and Shimizu, R., Toyota's new combustion technology for high engine thermal efficiency and high engine output performance, 37th International Vienna Motor Symposium. 2016.
- [83] Adachi, S. and Hagihara, H. *The Renewed 4-Cylinder Engine Series for Toyota Hybrid System*, 2012.
- [84] Lee, B., Oh, H., Han, S., Woo, S., et al., Development of High Efficiency Gasoline Engine with Thermal Efficiency over 42%, 2017.
- [85] Takahashi, D., Nakata, K., Yoshihara, T., Ohta, Y., et al., Combustion technology to achieve engine thermal efficiency of 40% for HVs engine, SIA Powertrain Conference. 2016.
- [86] Matsuo, S., Ikeda, E., Ito, Y. and Nishiura, H., The New Toyota Inline 4 Cylinder 1.8L ESTEC 2ZR-FXE Gasoline Engine for Hybrid Car, SAE Technical Paper 2016-01-0684, 2016.
- [87] Kobayashi, H., Yoshimura, K. and Hirayama, T., A study on dual circuit cooling for higher compression ratio, SAE Technical Paper 841294, 1984.

- [88] Finlay, I., Gallacher, G., Biddulph, T. and Marshall, R., The Application of Precision Cooling to the Cylinder-Head of a Small, Automotive, Petrol Engine, SAE Technical Paper 880263, 1988.
- [89] Iwashita, Y., Kanda, M., Hartagiri, H. and Yokoi, Y., Improvement of Coolant Low for Reducing Knock, I Mech E Autotech Conference. 1989.
- [90] Kubozuka, T., Ogawa, N., Hirano, Y. and Hayashi, Y., The Development of Engine Evaporative Cooling System, SAE Technical Paper 870033, 1987.
- [91] Russ, S., A Review of the Effect of Engine Operating Conditions on Borderline Knock, SAE Technical Paper 960497, 1996.
- [92] Fukuda, Y., Tawa, H. and Makise, A., Increase of Knock Limit in Outboard Motor Through Employment of Dual Control Direct Cooling System, HONDA R AND D TECHNICAL REVIEW, 2004;16:121-6, 2004.
- [93] Takahashi, D., Nakata, K. and Yoshihara, Y., Engine Thermal Control for Improving the Engine Thermal Efficiency and Anti-Knocking Quality, SAE Technical Paper 2012-01-0377, 2012.
- [94] Imaoka, Y., Shouji, K., Inoue, T. and Noda, T., A Study of Combustion Technology for a High Compression Ratio Engine: The Influence of Combustion Chamber Wall Temperature on Knocking, SAE International Journal of Engines, 2016;9:768-76, 2016.
- [95] Inoue, Y., Morioka, R., Sato, K., Higashi, H., et al., Effects of heat transfer in intake ports on engine performance, JSAE 20185297, 2018;2018.

- [96] Morioka, R., Inoue, Y., Kojima, M., Hoshiya, Y., et al., Effects of heat transfer in intake ports on engine performance (Second report), JSAE 20185298, 2018;2018.
- [97] Uozumi, H., Kawamura, Y., Matsuki, H., Ikeda, T., et al., Low-heat-transfer Combustion Chamber for Improvement of Knocking, JSAE 20185348, 2018.
- [98] Brunt, M. F. and Lucas, G. G., The Effect of Crank Angle Resolution on Cylinder Pressure Analysis, SAE Technical Paper 910041, 1991.
- [99] Lancaster, D. R., Krieger, R. B. and Lienesch, J. H., Measurement and Analysis of Engine Pressure Data, SAE Technical Paper 750028, 1975.
- [100] Dan Russell, Acoustic Modes of a Circular Membrane - Acoustics, The Pennsylvania State University.  
<https://www.acs.psu.edu/drussell/demos/membranecircle/circle.html>,  
[access date: 09-May-2017].
- [101] Savitzky, A. and Golay, M. J., Smoothing and differentiation of data by simplified least squares procedures, Analytical chemistry, 1964;36:1627-39, 1964.
- [102] Gatowski, J., Balles, E. N., Chun, K., Nelson, F., et al., Heat Release Analysis of Engine Pressure Data, SAE Technical Paper 841359, 1984.
- [103] Chun, K. M. and Heywood, J. B., Estimating heat-release and mass-of-mixture burned from spark-ignition engine pressure data, Combustion Science and Technology, 1987;54:133-43, 1987.

- [104] Brunt, M. F., Rai, H. and Emtage, A. L., The Calculation of Heat Release Energy from Engine Cylinder Pressure Data, SAE Technical Paper 981052, 1998.
- [105] Ghandhi, J. B., *Pressure and heat release analysis*, 1183-95,
- [106] Brunt, M. F. and Emtage, A. L., Evaluation of Burn Rate Routines and Analysis Errors, SAE Technical Paper 970037, 1997.
- [107] Woschni, G., A Universally Applicable Equation for the Instantaneous Heat Transfer Coefficient in the Internal Combustion Engine, SAE Technical Paper 670931, 1967.
- [108] Yun, H. and Mirsky, W., Schlieren-Streak Measurements of Instantaneous Exhaust Gas Velocities from a Spark-Ignition Engine, SAE Technical Paper 7410252, 1974.
- [109] Guardiola, C., Triantopoulos, V., Bares, P., Bohac, S., et al., Simultaneous estimation of intake and residual mass using in-cylinder pressure in an engine with negative valve overlap, IFAC-PapersOnLine, 2016;49:461-8, 2016.
- [110] Gardon, R., A transducer for the measurement of heat-flow rate, Journal of Heat Transfer (US), 1960;82:1960.
- [111] Catania, A., Misul, D., Mittica, A. and Spessa, E., A refined two-zone heat release model for combustion analysis in SI engines, JSME International Journal Series B Fluids and Thermal Engineering, 2003;46:75-85, 2003.

- [112] Ferguson, C. R. and Kirkpatrick, A. T. *Internal combustion engines: applied thermosciences*, 1986.
- [113] Ibrahim, A. and Bari, S., Optimization of a natural gas SI engine employing EGR strategy using a two-zone combustion model, *Fuel*, 2008;87:1824-34, 2008.
- [114] Lounici, M. S., Loubar, K., Balistrrou, M. and Tazerout, M., Investigation on heat transfer evaluation for a more efficient two-zone combustion model in the case of natural gas SI engines, *Applied Thermal Engineering*, 2011;31:319-28, 2011.
- [115] Skoog, D. A., Holler, F. J. and Crouch, S. R. *Principles of instrumental analysis*, 2017.
- [116] Cheng, W. K., Summers, T. and Collings, N., The fast-response flame ionization detector, *Progress in Energy and Combustion Science*, 1998;24:89-124, 1998.
- [117] Lee, Y., Pae, S., Min, K. and Kim, E., Prediction of knock onset and the autoignition site in spark-ignition engines, *Proceedings of the Institution of Mechanical Engineers, Part D: Journal of Automobile Engineering*, 2000;214:751-63, 2000.
- [118] Hadjiconstantinou, N., Min, K. and Heywood, J. B., Relation between flame propagation characteristics and hydrocarbon emissions under lean operating conditions in spark-ignition engines, *Symposium (International) on Combustion*. 1996.

- [119] Jie, M.-S., Kim, M.-H. and Kim, W.-T., The Effect of Tumble Flow on Engine Performance and Flame Propagation, SAE Technical Paper 931946, 1993.
- [120] Cheng, A. S., The head gasket ionization probe as a combustion diagnostic for spark ignition engines, Massachusetts Institute of Technology, 1994.
- [121] Witze, P. O., Martin, J. K. and Borgnakke, C., Conditionally-sampled velocity and turbulence measurements in a spark ignition engine, Combustion science and technology, 1984;36:301-17, 1984.
- [122] Hadjiconstantinou, N. G., A Model for Converting SI Engine Flame Arrival Signals into Flame Contours, Massachusetts Institute of Technology, 1994.
- [123] Witze, P., Interpretation of Head-Gasket Ionization-Probe Measurements Using a Two-Zone Spherical Flame Model, COMODIA, 1994.
- [124] 이정원, 최희명, 황승환, 민경덕, LPG 엔진에서 이온프로브를 이용한 노킹 발생 위치 추정에 관한 연구, 한국자동차공학회논문집, 2003;11:42-8, 2003.
- [125] 한성주, 이용규, 민경덕, 김응서, 이온프로브 장착 점화플러그를 이용한 노크발생 판정, 한국자동차공학회논문집, 2000;8:1-8, 2000.
- [126] Furuhashi, S. and Enomoto, Y., Piston temperature of automobile gasoline engine in driving on the road, Bulletin of JSME, 1973;16:1385-400, 1973.

- [127] Furuhashi, S., Tada, T. and Nakamura, T., Some Measurements of the Piston Temperatures in a Small Type Gasoline Engine, Bulletin of JSME, 1964;7:422-9, 1964.
- [128] Tsutsumi, Y., Nomura, K. and Nakamura, N., Effect of Mirror-Finished Combustion Chamber on Heat Loss, SAE Technical Paper 902141, 1990.
- [129] Takamatsu, H. and Kanazawa, T., Piston temperature measurement method for high-speed gasoline engines, JSAE review, 1999;20:259-61, 1999.
- [130] Assanis, D. N. and Friedmann, F., A Telemetry Linkage System for Piston Temperature Measurements in a Diesel Engine, SAE Technical Paper 910299, 1991.
- [131] Hendricks, T. L., Splitter, D. A. and Ghandhi, J. B., Experimental investigation of piston heat transfer under conventional diesel and reactivity-controlled compression ignition combustion regimes, International Journal of Engine Research, 2014;15:684-705, 2014.
- [132] Continuous Acquisition of Measuring Data up to an Environmental Temperature of 180°C (Temperature, Deformation, Pressure between Piston Rings),
- [133] Ebrahimi, K. M., Lewalski, A., Pezouvanis, A. and Mason, B. A., Piston data telemetry in internal combustion engines, American Journal of Sensor Technology, 2014;2014.
- [134] Miers, S. A., Anderson, C. L., Blough, J. R. and Inal, M. K., Impingement Identification in a High Speed Diesel Engine Using Piston

- Surface Temperature Measurements, SAE Technical Paper 2005-01-1909, 2005.
- [135] Fuse, S., Contact-point method and its application for measuring temperature, Journal of JSAE, 1982;36:1982.
- [136] Cho, K., Assanis, D., Filipi, Z., Szekely, G., et al., Experimental investigation of combustion and heat transfer in a direct-injection spark ignition engine via instantaneous combustion chamber surface temperature measurements, Proceedings of the Institution of Mechanical Engineers, Part D: Journal of Automobile Engineering, 2008;222:2219-33, 2008.
- [137] Chang, J., Güralp, O., Filipi, Z., Assanis, D. N., et al., New Heat Transfer Correlation for an HCCI Engine Derived from Measurements of Instantaneous Surface Heat Flux, SAE Technical Paper 2004-01-2996, 2004.
- [138] Chang, J., Filipi, Z., Assanis, D., Kuo, T., et al., Characterizing the thermal sensitivity of a gasoline homogeneous charge compression ignition engine with measurements of instantaneous wall temperature and heat flux, International Journal of Engine Research, 2005;6:289-310, 2005.
- [139] Taylor, R. and Evans, P., In-situ piston measurements, Proceedings of the Institution of Mechanical Engineers, Part J: Journal of Engineering Tribology, 2004;218:185-200, 2004.
- [140] Mufti, R. A. and Priest, M., Experimental evaluation of piston-assembly friction under motored and fired conditions in a gasoline engine, Journal of tribology, 2005;127:826-36, 2005.

- [141] Nelder, J. A. and Mead, R., A simplex method for function minimization, The computer journal, 1965;7:308-13, 1965.
- [142] Angelberger, C., Poinso, T. and Delhay, B., Improving Near-Wall Combustion and Wall Heat Transfer Modeling in SI Engine Computations, SAE Technical Paper 972881, 1997.
- [143] corporation MS, CompRatio-D3, 05-4-17 Rev. A:
- [144] Beccari, S., Pipitone, E. and Genchi, G., Knock onset prediction of propane, gasoline and their mixtures in spark ignition engines, Journal of the Energy Institute, 2016;89:101-14, 2016.
- [145] Beccari, S., Pipitone, E. and Genchi, G., Calibration of a knock prediction model for the combustion of gasoline-LPG mixtures in spark ignition engines, Combustion Science and Technology, 2015;187:721-38, 2015.

## 국 문 초 록

강화되는 연비, 배기 규제에 따라 초고효율 가솔린 엔진의 개발이 그 어느때보다 절실하다. 가솔린 엔진은 그 특성상 압축비의 향상이 곧 기관의 효율로 직결된다. 하지만 압축비의 향상은 연소기간 중 말단가스 영역의 온도와 압력을 상승시켜 혼합기의 자발화현상을 유발하게 된다. 이는 노킹 현상으로 불리며, 운전 중 불쾌한 소음을 발생시키고 엔진내 부품의 손상을 유발하기 때문에 이를 저감하기 위한 많은 연구가 진행 중이다.

많은 선행연구에서 노킹을 저감하기 위해 미연 가스 영역의 온도를 낮추는 여러가지 방법을 시도한 바 있다. 배기 재순환, 워터 인젝션 연구 등이 활발하게 이루어지고 있으며 냉각 최적화, 이중 냉각, 단열 포트 도입 등을 통해 내부 열전달을 감소시키는 방법 등이 제안된 바 있다. 포트 벽면의 온도가 가스로의 열전달에 큰 영향을 미친다는 것이 해석을 통해 확인된 바 있으나, 그 이외 각부 온도 저감에 따른 효과의 정량적 분석이 진행된 바가 없으며, 향후 자발화 현상의 공격적인 제어 시 벽면 온도 변화에 따른 특성의 반영이 필요하다.

본 연구에서는 체계적 접근을 통해 벽면 온도가 노킹 현상 전반에 어떠한 영향을 미치는 지에 대하여 살펴보았다. 벽면 온도의 변화에 따른 간접 결과인 노킹 경향의 차이는 섬세한 실험 기법을 요구한다. 기법 정립의 필요성에 따라 주파수 분석을 통해 판정 지수를 수립하였고, 이후 다양한 실험을 통해 벽면 온도의 저감이 효율적으로 노킹 특성을 개선할 수 있음을 확인하였다.

헤드와 라이너 냉각수 분리 및 피스톤 오일 갤러리의 도입을 통해 각부의 온도를 제어하고 정립된 실험 기법을 통해 그 영향도를

평가하였다. 링키지 시스템의 최적화 설계를 통한 피스톤 온도 측정 및 엔진 각부 금속면 온도의 측정을 통하여, 연소실을 구성하는 각 벽면의 온도가 효과적으로 제어가능함을 확인하였다. 다양한 엔진 및 실험 조건 하에서 노킹 현상에 미치는 헤드 냉각수의 온도 저감에 따른 노킹억제효과가 라이너 냉각수의 온도 저감보다 큰 것으로 나타났으며, 피스톤 오일 갤러리로의 오일 주입 또한 피스톤 온도의 공격적인 하강을 통해 큰 효과를 보였다. 라이너 냉각수 온도의 하강은 피스톤 온도를 크게 낮출 수 있음이 측정을 통해 확인되었고, 이로부터 헤드 냉각수 온도 하강에는 헤드 벽면을 제외한 다른 효과의 존재가 있음을 유추하였다.

추가적으로 벽면 온도의 영향을 확인하기 위해 3D 시뮬레이션 해석을 도입하였다. 그 결과, 연소기간 중 금속면온도 저감을 통한 열전달 증대가 미연가스 영역의 온도를 하강시키는 효과는 매우 미미하게 나타났으나, 흡기 과정에서의 열전달 감소에 큰 영향을 미침을 확인하였다. 흡기 과정에서는 흡기 포트의 효과가 가장 크며, 이를 차단하기 위한 단열 포트 도입 이후에는 헤드 벽면의 온도 저감보다 라이너 벽면의 온도 저감이 혼합기 온도 감소에 더욱 큰 효과를 보일 수 있었다. 고 스트로크형 엔진에서 라이너 냉각의 효과는 더욱 커짐을 실험을 통하여 확인하였고, 고 텀블형 엔진 또한 혼합기 압축시 열전달 증대로 인해 온도 저감의 가능성이 있음이 밝혀졌다.

라이너 벽면의 온도 저감시 노킹의 위치 변화에 따른 냉각전략 수립을 위해 가스켓형 이온프로브를 도입하여 발생 위치를 확인하였다. 벽면온도의 저감에 따른 큰 변화는 관찰되지 않았으나, 노킹 강도가 강한 경우 실린더내 보어를 따라 여러위치에서 동시다발적으로 발생함을 확인하였다. 또한 노킹 은 그 강도가 약할 경우 흡기 혹은 배기 부분에서 중점적으로 나타났다. 이를 통해 노킹

발생의 위치는 벽면 온도의 영향보다는 화염 전파의 영향이 지배적임을 알 수 있었다.

실제 엔진의 트랜지언트 구동 환경하 자발화 제어를 위해서는 빠르고 정확한 노킹 시점의 예측이 필수적이다. 이를 위하여 노킹 발생시점의 판정법 개선 및 개별 사이클 분석을 수행하였다. 점화 지연 계산 및 유전알고리즘을 이용하여 강건한 개별사이클 기반 OD 노킹 예측 모델을 구성하였다. 단열 과정 가정을 통한 예측 모델은 뛰어난 정확성과 함께 계산시간 감소의 가능성을 보였다. 이러한 모델은 앞서 제시한 벽면 온도 냉각전략을 통한 노킹 제어 상황 하에서도 매우 높은 정확도로 그 시기를 예측하였다. 수립된 모델은 이후 실차환경에서 제어 알고리즘을 적용할 경우 강력한 노킹 회피 기동 혹은 자발화 유도 연소가 가능할 것으로 예상되며, 미래형 초고효율 엔진 양산에 필수적인 요소가 될 것이다.

주요어: 가솔린 엔진, 노킹, 자발화, 0 차원, 사이클 분석, 냉각수 온도, 벽면 온도, 노킹 예측 모델

학 번: 2012-20703